Acoustical Physics, Vol. 50, No. 4, 2004, pp. 363–369. Translated from Akusticheskiĭ Zhurnal, Vol. 50, No. 4, 2004, pp. 435–441.

Waves Concentrated Near Weak-Contrast Boundaries

I. V. Andronov

St. Petersburg State University, ul. Ul'yanovskaya 1, Petrodvorets, St. Petersburg, 198504 Russia
e-mail: iva@aa2628.spb.edu

Received May 15, 2003

Abstract—The excitation and propagation of acoustic waves along curvilinear boundaries between two media are investigated. Formal high-frequency asymptotic expressions practicable for approximate calculations in the case of media with slightly different velocities are derived. Dispersion equations and wave excitation coefficients at weak-contrast boundaries are investigated numerically. © *2004 MAIK "Nauka/Interperiodica".*

1. INTRODUCTION

High-frequency asymptotic expansions are practicable for efficient calculations of acoustic fields. In calculations, the common practice consists in keeping only the highest-order term of an asymptotic expansion (see, e.g., [1]). However, the accuracy of such approximate formulas may appear inadequate for some specific parameter values. In particular, the asymptotic formula for a wave concentrated near a curvilinear boundary separating two media includes, along with the frequency, a parameter proportional to the difference of sound velocities. For media with slightly different sound velocities, the standard asymptotic formulas may appear inappropriate for determining the acoustic fields. In this case, other approximate formulas with wider range of applicability are required. The new approximate formulas can be constructed in the form of asymptotic expansions in two (or more) parameters.

This paper considers waves concentrated near a curvilinear interface between two media. For these waves, such an additional parameter is the difference between the wave slownesses in the contacting media. Depending on the relationship between the parameters, one can distinguish cases of strong contrast and weak contrast. In the first case, two types of waves can be revealed. The waves of the first type resemble creeping waves traveling along the convex side of the boundary, and the waves of the second type behave as whispering gallery waves traveling along the concave side. Both types of waves are adequately described by standard asymptotic expansions. In the case of weak contrast, waves of a mixed type are formed. They satisfy a more complicated dispersion relation. New approximate formulas are derived for describing these waves. These formulas proved to be asymptotically uniform in the parameter characterizing the contrast of the media.

The first part of this paper repeats the results obtained earlier [2]. The second part considers the excitation of waves traveling along the boundary between two media by the ray field incident on the boundary. First, the excitation coefficients of the waves of the first type are calculated for the case of a strong contrast. Then, the wave excitation at a weak-contrast boundary is considered and, proceeding to the asymptotic limit of a strong contrast, the excitation coefficients of the waves of the second type are determined. If the sound velocity in the medium on the concave side of the boundary exceeds the velocity in the medium on the convex side, the approximate formulas allow sewing together with the asymptotic expansion for the head wave of the refraction type, which was obtained earlier [3]. For the case of an inverse relationship between the velocities in the media, the effect of the exponentially weak tunneling of the incident wave into the whispering gallery waves is revealed. In the final part of the paper, results of a numerical analysis of the dispersion equation for waves of the mixed type are presented and the excitation coefficients of such waves are calculated.

2. STATEMENT OF THE PROBLEM

Let a smooth surface S be the interface between two acoustic media Ω_1 and Ω_2. We assume that medium Ω_2 is convex and that the sound velocities are constant in both media. Without a loss of generality, we can consider the velocity in the first medium to be equal to unity. Let us introduce a piecewise constant slowness by the formula

$$N(\mathbf{r}) = \begin{cases} 1, & \mathbf{r} \in \Omega_1, \\ N, & \mathbf{r} \in \Omega_2. \end{cases}$$

The stationary wave field (factor $\exp(-i\omega t)$ is omitted everywhere) satisfies the Helmholtz equations

$$\Delta u(\mathbf{r}) + \omega^2 u(\mathbf{r}) = 0, \quad \mathbf{r} \in \Omega_1,$$

$$\Delta u(\mathbf{r}) + \omega^2 N^2 u(\mathbf{r}) = 0, \quad \mathbf{r} \in \Omega_2.$$

1063-7710/04/5004-0363$26.00 © 2004 MAIK "Nauka/Interperiodica"

At the boundary S, the field satisfies the continuity conditions for pressure and normal displacements:

$$\lim_{n \to +0} u = \lim_{n \to -0} u, \quad \lim_{n \to +0} \frac{\partial u}{\partial n} = \kappa \lim_{n \to -0} \frac{\partial u}{\partial n}. \qquad (2.1)$$

Here, n is the normal to the boundary and κ is the density ratio of the acoustic media.

We search for waves concentrated near the surface S and satisfying the radiation condition at infinity.

Two types of waves can be expected to propagate along the boundary. Waves of the first type travel along the boundary with a wave number ω and, within the region Ω_1, they resemble creeping waves. We represent them in the form of the formal asymptotic expansion

$$u = \exp(i\omega s + i\omega^{1/3}\varphi(s, \alpha)) \sum_{j=0}^{\infty} U_j(s, \nu_1, \alpha)\omega^{-j/3}. \qquad (2.2)$$

Here, we introduced geodesic coordinates (s, α, n), so that s is the arc length of the geodesic line at the boundary S, and performed the extension of the normal

$$\nu_1 = \begin{cases} \omega^{2/3} n, & n > 0, \\ \omega^q n, & n < 0. \end{cases} \qquad (2.3)$$

The exponent q determines the extension of the normal in the region Ω_2 and, as will be shown below, its magnitude depends on the asymptotic order of the difference $N - 1$.

Waves of the second type are mainly concentrated in the region Ω_2, and their wave number is ωN. We represent these waves in the form of the formal expansion

$$u = \exp(i(\omega N)s + i(\omega N)^{1/3}\varphi(s, \alpha)) \times \sum_{j=0}^{\infty} U_j(s, \nu_2, \alpha)(\omega N)^{-j/3}, \qquad (2.4)$$

where the extension of the normal is performed according to the formula

$$\nu_2 = \begin{cases} (\omega N)^q n, & n > 0, \\ (\omega N)^{2/3} n, & n < 0. \end{cases}$$

The procedure for determining the functions φ and U_j consists of a substitution of the expansions into the Helmholtz equations and boundary conditions (2.1), after which the terms of the same orders in the large parameter are equated. We restrict our consideration to the highest terms of asymptotic expansions (2.2) and (2.4).

3. STRONG CONTRAST

Knowledge of the asymptotic order of the quantity $N - 1$ is important for constructing asymptotic expansions (2.2) and (2.4). First, we assume that $N - 1 = O(1)$.

Consider the waves of the first type. Substituting expansion (2.2) in the Helmholtz equation for the region Ω_1 and equating the coefficients multiplying equal powers of the wave number ω, we obtain a recurrent system of equations

$$\mathcal{L}_0 U_0 = 0, \quad \mathcal{L}_0 U_1 + \mathcal{L}_1 U_0 = 0, \quad \ldots$$
$$\mathcal{L}_0 = \frac{\partial^2}{\partial \nu_1^2} + 2\left(\frac{\nu_1}{\rho} - \varphi'\right), \quad \mathcal{L}_1 = 2i\frac{\partial}{\partial s} + i\frac{h'}{h}, \qquad (3.1)$$

which is a standard system for creeping waves [4]. The radius of curvature of the geodesic line, ρ, and the divergence h depend on surface coordinates s and α, and the prime denotes the derivative with respect to s.

Carrying out similar rearrangements in the region Ω_2, in the highest order (ω^2) we obtain the equation

$$\frac{\partial^2 U_0}{\partial n^2} + \omega^2(N^2 - 1)U_0 = 0,$$

from which it follows that exponent q in Eq. (2.3) must be equal to unity. In this case, we have the following recurrent formulas:

$$\mathcal{M}_0 U_0 = 0, \quad \mathcal{M}_0 U_1 = 0, \quad \mathcal{M}_0 U_2 - 2\varphi' U_0 = 0, \ \ldots,$$
$$\mathcal{M}_0 = (N^2 - 1) + \frac{\partial^2}{\partial \nu_1^2}. \qquad (3.2)$$

The boundary conditions at $n = 0$ yield the relationships

$$U_j(s, +0, \alpha) = U_j(s, -0, \alpha),$$
$$\frac{\partial U_{j-1}(s, +0, \alpha)}{\partial \nu_1} = \kappa \frac{\partial U_j(s, -0, \alpha)}{\partial \nu_1}. \qquad (3.3)$$

Here, $j = 0, 1, \ldots$, and we set $U_{-1} \equiv 0$.

Equations (3.1) and (3.2), conditions (3.3), and radiation conditions for $\nu_1 \longrightarrow \pm\infty$ determine the recurrent system of the Sturm–Liouville problems. The solution to the first equation of system (3.1), which satisfies the radiation condition, has the form

$$U_0 = A_0(s, \alpha) w_1(\xi - \nu),$$
$$\nu = (2/\rho)^{1/3}\nu_1, \quad \xi = 2^{1/3}\rho^{2/3}\varphi'. \qquad (3.4)$$

Here, $w_1()$ is the Airy function and $\xi(s, \alpha)$ and $A_0(s, \alpha)$ are (for the moment) arbitrary functions. The solutions U_0 and U_1 to Eqs. (3.2) are the exponential functions

$$U_j = B_j \exp(-iD\nu_1), \quad D = \sqrt{N^2 - 1}, \ j = 0, 1. \qquad (3.5)$$

The minus sign in Eq. (3.5) corresponds to the radiation condition in the region Ω_2 for $\nu_1 \longrightarrow -\infty$. For $N < 1$, the branch of the radical function is specified so as to obtain $D = i\sqrt{1 - N^2}$.

Substituting (3.4) and (3.5) in boundary conditions (3.3), we obtain that $B_0 = 0$ and

$$w_1(\xi) = 0. \tag{3.6}$$

To determine the dependence of amplitude A_0 on s, we consider the equations in the following order. Using Eqs. (3.5), we exclude the interior of the region Ω_2 from consideration. For $\nu_1 > 0$, function U_1 must satisfy the inhomogeneous Airy equation

$$\mathcal{L}_0 U_1 = -\mathcal{L}_1 U_0,$$

the boundary condition (here and below, the dot denotes the derivative of the function)

$$\lim_{\nu_1 \to +0} U_1 = -i\left(\frac{2}{\rho}\right)^{1/3} \frac{1}{D\kappa} A_0 \dot{w}_1(\xi),$$

and the radiation condition for $\nu_1 \longrightarrow +\infty$. Fot this Sturm–Liouville problem to be solvable, the right-hand side of the equation must satisfy a certain compatibility condition. Eliminating the inhomogeneity from the boundary condition and using the results of paper [4], we can represent the solvability condition in the form

$$A_0' + \left(\frac{1}{6}\frac{\rho'}{\rho} + \frac{1}{2}\frac{h'}{h} - \frac{1}{\rho D\kappa}\right)A_0 = 0.$$

In the final form, the field of the wave of the first type in the region Ω_1 is expressed by the approximate formula

$$u = A_0(0)\exp\left\{i\omega s + i\left(\frac{\omega}{2}\right)^{1/3}\int_0^s \frac{\xi\, ds}{\rho^{2/3}} + \frac{1}{D\kappa}\int_0^s \frac{ds}{\rho}\right\} \times R^{1/6} H^{1/2} w_1(\xi - \nu), \tag{3.7}$$

where $R = \rho(0, \alpha)/\rho(s, \alpha)$, and

$$H = h(0, \alpha)/h(s, \alpha).$$

Waves of the second type can be considered in a similar manner. We give only the final formula for the field in the region Ω_1:

$$u = A_0(0)\sqrt{RH}\exp\left\{i(\omega N)s - \omega D n + i\left(\frac{\omega N}{2}\right)^{1/3}\int_0^s \frac{\eta\, ds}{\rho^{2/3}} + i\frac{\kappa N}{D}\int_0^s \frac{ds}{\rho}\right\}. \tag{3.8}$$

Parameter η is determined from the dispersion equation

$$v(\eta) = 0 \tag{3.9}$$

(here, v is the Airy function exponentially decreasing at $+\infty$) and is real. When $N > 1$, waves (3.8) travel along the boundary without attenuation. When $N < 1$, the field becomes an oscillatory function of n, which corresponds to waves outgoing from the boundary. In this case, the attenuation is nonzero and is described by the factor

$$\exp\left(-\frac{\kappa N}{\sqrt{1 - N^2}}\int_0^s \frac{ds}{\rho}\right). \tag{3.10}$$

4. AN ASYMPTOTICALLY LOW CONTRAST

Formulas (3.7) and (3.8) are valid for $D = O(1)$. They also remain valid for smaller D if $D > O(\omega^{-1/3})$. For $D = O(\omega^{-1/3})$, expansions (3.7) and (3.8) loose their asymptotic nature, because the orders of the two last terms in the exponents become coincident. All further terms omitted in the formulas are also of the same order.

To obtain asymptotic formulas for waves concentrated near a curvilinear boundary between media with slightly different parameters, we introduce a coefficient δ, such that $D^2 = \omega^{-2/3}\delta$, and assume that $\delta = O(1)$. In this case, the extension of the normal in the regions Ω_1 and Ω_2 must be performed using identical exponents $q = 2/3$, so that formulas (2.2) and (2.4) become similar.

Consider the formal expansion (2.2). In the region Ω_1, the recurrent system of equations remains the same as in the case of $D = O(1)$ for waves of the first type. Equating the terms with identical powers of ω in the Helmholtz equation for the region Ω_2, one can easily obtain the recurrent system

$$(\mathcal{L}_0 + \delta)U_0 = 0, \quad (\mathcal{L}_0 + \delta)U_1 + \mathcal{L}_1 U_0 = 0, \quad \ldots$$

In the highest order, the solution is the Airy function satisfying the radiation conditions at $\nu_1 \longrightarrow -\infty$:

$$U_0 = B_0 v(\xi - d - \nu), \quad d = \left(\frac{\rho}{2}\right)^{2/3}\delta. \tag{4.1}$$

Using the boundary conditions for the field u, we find

$$B_0 = A_0\frac{w_1(\xi)}{v(\xi - d)}, \qquad \frac{w_1(\xi)}{\dot{w}_1(\xi)} = \frac{1}{\kappa}\frac{v(\xi - d)}{\dot{v}(\xi - d)}. \tag{4.2}$$

To find the dependence of amplitude A_0 on arc length s, one must, as in the case of $D = O(1)$, consider the equations in the following order and formulate the conditions of their solvability. Substituting Eqs. (3.4) and (4.1) in the equation for U_1, multiplying the result by the solution to the adjoint problem

$$W(\nu) = \begin{cases} w_1(\xi - \nu), & \nu > 0, \\ \kappa\dfrac{w_1(\xi)}{v(\xi - d)}v(\xi - d - \nu), & \nu < 0, \end{cases}$$

and integrating, we find the solvability condition in the form of the differential equation in A_0 [2]:

$$A_0' + \left(\frac{1}{6}\frac{\rho'}{\rho} + \frac{1}{2}\frac{h'}{h} + \frac{1}{2}\frac{Q'}{Q}\right)A_0 = 0.$$

Here, we introduced the function

$$Q = ((1-\kappa)\xi + \kappa d)w_1^2(\xi) + \frac{1-\kappa}{\kappa}\dot{w}_1^2(\xi).$$

In the final form, the asymptotic formula for waves concentrated near the boundary can be written in the highest order as ($n > 0$)

$$u = A_0(0)\exp\left\{i\omega s + i\left(\frac{\omega}{2}\right)^{1/3}\int_0^s \frac{\xi}{\rho^{2/3}}ds\right\} \times R^{1/6}\sqrt{H\frac{Q(0,\alpha)}{Q(s,\alpha)}}w_1(\xi - \nu). \quad (4.3)$$

In asymptotic formula (4.3), parameter ξ is determined from dispersion equation (4.2) and is a function of a point at the boundary S.

A similar procedure can be used for constructing the formal asymptotic expansion in the parameter $\tilde{\omega} = \omega N$. In the highest order, we obtain for $n > 0$:

$$u = C_0(0)\exp\left\{i\tilde{\omega}s + i\left(\frac{\tilde{\omega}}{2}\right)^{1/3}\int_0^s \frac{\eta}{\rho^{2/3}}ds\right\} \times R^{1/6}\sqrt{H\frac{P(0,\alpha)}{P(s,\alpha)}}w_1(\eta + \tilde{d} - \nu), \quad (4.4)$$

$$P(s,\alpha) = (\eta(1-\kappa) + \tilde{d})w_1^2(\eta + \tilde{d}) + (\kappa^{-1} - 1)\dot{w}_1^2(\eta + \tilde{d}), \quad \tilde{d} = N^{-4/3}d.$$

Parameter η is determined from the dispersion equation

$$\frac{w_1(\eta + \tilde{d})}{\dot{w}_1(\eta + \tilde{d})} = \frac{1}{\kappa}\frac{v(\eta)}{\dot{v}(\eta)}. \quad (4.5)$$

We note that expansion (4.3) passes into (4.4) when ω is replaced by $\tilde{\omega}$, ξ by $\eta + \tilde{d}$, and d by $\tilde{d}$. In the case of asymptotically small contrasts, such replacements result in formulas differing in the terms of order $O(\omega^{-1/3})$.

It can be easily verified that formulas (4.2) and (4.3) give an asymptotic uniform in d for waves of the first type and that formulas (4.5) and (4.4) are uniform for waves of the second type. Indeed, let $D = O(1)$. Then, parameter d becomes large and the Airy functions in the dispersion equation (4.2) can be replaced with their asymptotic formulas. Assuming that $\xi = O(1)$ and replacing the Airy function $v(\xi - d)$ in Eq. (4.2) with its asymptotic, we obtain the equation

$$\kappa\sqrt{d}w_1(\xi) + i\dot{w}_1(\xi) \approx 0,$$

from which we find

$$\xi = \xi^\circ - \frac{i}{\kappa\sqrt{d}} + \ldots,$$

where ξ° is the root of Eq. (3.6). One can easily ascertain that the exponents in Eqs. (4.3) and (3.7) coincide. In addition, the quantity Q asymptotically grades into $\kappa d w_1^2(\xi^\circ)$ and ceases to depend on s. Thus, formula (4.3) grades into asymptotic formula (3.7) for large d and $\xi = O(1)$.

Now we consider asymptotic formula (4.4). Setting $\eta = O(1)$ in Eq. (4.5) and replacing the Airy function $w_1(\eta + \tilde{d})$ with its asymptotic, we obtain the equation

$$\sqrt{\tilde{d}}v(\eta) - \kappa\dot{v}(\eta) \approx 0,$$

from which we have

$$\eta = \eta^\circ + \frac{\kappa}{\sqrt{\tilde{d}}} + \ldots,$$

where η° is the root of Eq. (3.9). Function $P(s, \alpha)$ can be represented in the form

$$P \approx \frac{\tilde{d}}{\kappa}w_1^2(\eta + \tilde{d}).$$

In addition, we have

$$w_1(\eta + \tilde{d} - \nu)/w_1(\eta + \tilde{d}) \approx \exp(-\sqrt{\tilde{d}}\nu) = \exp(-\omega D n).$$

Thus, asymptotic formula (4.4) grades into (3.8) in which

$$A_0(0) = C_0(0)w_1(\tilde{d}(0) + \eta).$$

5. WAVE EXCITATION BY AN INCIDENT FIELD

Consider the excitation of waves studied in the foregoing sections. It is clear that waves of the first type originate in the Fock zone, near the point at which the tangent ray is incident on the boundary S. In addition to the normal, we also extend the coordinate s and seek the solution in the form

$$u = \exp(i\omega s)\sum_j U_j(\sigma, \nu)\omega^{-j/3}, \quad \sigma = \omega^{1/3}2^{-1/3}\rho_0^{-2/3}s. \quad (5.1)$$

Here, ρ_0 is the radius of curvature of the geodesic line on S at the light–shadow boundary.

Substitute representation (5.1) in the Helmholtz equation and equate the terms with identical powers of the large parameter ω. In the highest order, we obtain a parabolic equation. Applying the Fourier transforma-

tion to this equation, we obtain the Fourier transform $\hat{U}_0(\xi, \nu, \alpha)$ in Ω_1 in the form

$$\hat{U}_0 = \hat{A}_0(\xi, \alpha) w_1(\xi - \nu), \quad \nu > 0.$$

Within the small neighborhood of the light–shadow boundary, the incident field has, in the highest order, the form of a plane wave with some amplitude $A(\alpha)$. As is known [4], the Fourier transform of such a field is

$$A(\alpha)\frac{1}{\sqrt{\pi}} v(\xi - \nu), \quad \nu > 0.$$

Consider the case of the strong contrast $D = O(1)$. We find

$$\hat{U}_0 = \hat{B}_0(\xi, \alpha) e^{-iD\omega n}, \quad n < 0.$$

Amplitudes $\hat{A}_0$ and $\hat{B}_0$ are determined from the boundary conditions (2.1). In the highest order, the acoustic field does not penetrate into the region Ω_2, so that $\hat{B}_0 = 0$. The formula for the amplitude $\hat{A}_0$ appears to be the same as in the case of an acoustically soft boundary [4]:

$$\hat{A}_0 = -\frac{A(\alpha)}{\sqrt{\pi}} \frac{v(\xi)}{w_1(\xi)}.$$

This results in the following asymptotic representation of the field in the region Ω_1:

$$u^s \approx -\frac{A(\alpha)}{\sqrt{\pi}} e^{i\omega s} \int_{-\infty}^{+\infty} e^{i\sigma\xi} \frac{v(\xi)}{w_1(\xi)} w_1(\xi - \nu) d\xi. \qquad (5.2)$$

The integral in expression (5.2) can be calculated by the residue theorem. For asymptotically large values of coordinate σ, the main contribution to the integral is made by the pole nearest to the real axis. This contribution must be sewed together with the asymptotic representation (4.2) of the first wave. Comparing the amplitudes, we determine the excitation coefficient

$$A_0(0, \alpha) = -2A(\alpha)\sqrt{\pi} i v(\xi^\circ)/\dot{w}_1(\xi^\circ). \qquad (5.3)$$

Here, ξ° is the root of the dispersion equation (3.6).

Consider now the case of an asymptotically small contrast $D = O(\omega^{-1/3})$. Using substitution (5.1) and performing calculations as above, we obtain

$$\hat{A}_0(\xi, \alpha) = -\frac{A(\alpha)}{\sqrt{\pi}} \frac{\kappa \dot{v}(\xi - d) v(\xi) - v(\xi - d)\dot{v}(\xi)}{\kappa \dot{v}(\xi - d) w_1(\xi) - v(\xi - d)\dot{w}_1(\xi)}. \qquad (5.4)$$

Calculating the residues at zeros of the denominator in Eq. (5.4) (they coincide with the roots of the dispersion equation (4.2)) and sewing together with asymptotic expression (4.3), we find the coefficients of wave excitation

$$A_0(0, \alpha) = A(\alpha)\frac{2\sqrt{\pi} i}{Q(0, \alpha)}. \qquad (5.5)$$

Formula (5.5) holds for waves represented by both expansion (4.3) and expansion (4.4). It is not difficult to verify that it grades into Eq. (5.3) for waves of the first type with increasing parameter δ.

To find the excitation coefficients of the second-type waves described by Eq. (3.8), we apply the substitutions given at the end of the previous section to Eq. (5.5):

$$C_0(0) = A(\alpha)\frac{2\sqrt{\pi} i}{P(0, \alpha)} w_1(\eta + N^{-4/3} d),$$

after which we proceed asymptotically to $D = O(1)$. Replacing the Airy function w_1 with its asymptotic, for $N > 1$ we obtain an exponentially small amplitude

$$C \sim \frac{2\sqrt{\pi} i\kappa}{X^{3/2}} \exp\left(-\frac{2}{3}X^3 - X\eta^\circ - \kappa\right), \quad X = \left(\frac{\omega\rho}{2}\right)^{1/3} \frac{\sqrt{N^2 - 1}}{N^{2/3}}. \qquad (5.6)$$

For the case $N < 1$, we obtain

$$C \sim \frac{2\sqrt{\pi} i\kappa}{Y^{3/2}} \exp\left(-\frac{2i}{3}Y^3 - iY\eta^\circ - i\kappa - i\frac{\pi}{4}\right), \quad Y = \left(\frac{\omega\rho}{2}\right)^{1/3} \frac{\sqrt{1 - N^2}}{N^{2/3}}. \qquad (5.7)$$

Thus, in the case of a strong contrast, the incident field excites the waves of the first type, but these waves rapidly decay. Excitation of the waves of the second type is exponentially weak for $N > 1$, but, being excited, they propagate practically without attenuation. For $N < 1$, the excitation coefficients of the waves of the second type appears to be of the order of $O(\omega^{-1/2})$, but these waves decay along the boundary according to Eq. (3.10).

Asymptotic representations (5.6) and (5.7) are valid for $N \approx 1$, in which case the point of incidence of the tangent ray is close to the point of incidence of the ray incident on the surface S at the angle of total reflection. Asymptotic representation (5.7) agrees well with the results of paper [3]. In addition, the phase factor of the highest-order term in ω meets the phase difference of waves traveling along the segment $A'A$ and the arc $\breve{BA}$ in the region Ω_2 (see Fig. 1). Indeed, setting $N = 1 + \omega$, we find $\tau_1 = |A'A| = \rho_0 \sin\psi \approx \rho_0\sqrt{2\varepsilon}\,(1 - \varepsilon/4)$ and $\tau_2 = N|\breve{BA}| = N\rho_0\psi \approx \rho_0\sqrt{2\varepsilon}\,(1 - 11\varepsilon/12)$. The highest-

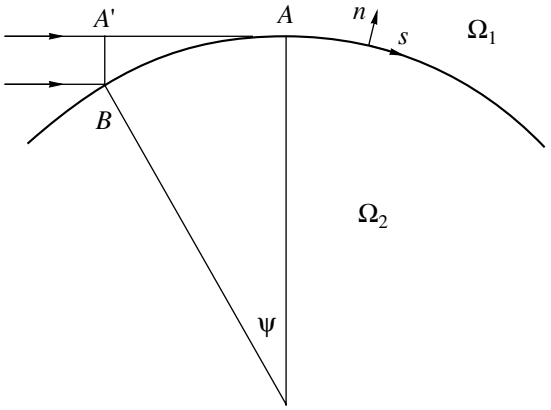

Fig. 1. Geometric interpretation of asymptotic representation (5.7).

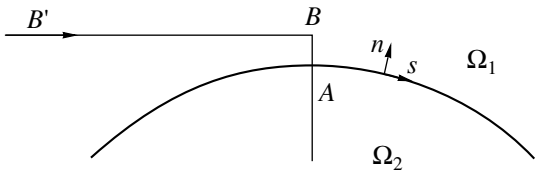

Fig. 2. Geometric interpretation of asymptotic representation (5.6).

order term in the exponent in Eq. (5.7) yields $-\frac{2}{3} iY^3 \approx -i\omega\frac{2}{3}\rho_0\sqrt{2}\,\varepsilon^{3/2} \approx i\omega(\tau_2 - \tau_1)$.

Asymptotic representation (5.6) also can be interpreted geometrically. The highest-order term in the exponent of this representation corresponds to the tunneling of the wave propagating along the ray located a distance $(N - 1)\rho_0$ from the boundary S (see Fig. 2). Consider the wave traveling in the region Ω_2 with an angular factor $i\omega N\rho_0\psi = i\omega Ns$. Note that such a wave depends in the highest order on the radius r according to the law

$$V(r) = \exp\left(\pm\omega N\int_{\rho_0}^{r}\sqrt{1-\left(\frac{\rho_0}{l}\right)^2}\,dl\right).$$

Now we mentally continue this wave beyond the boundary S. At $r = \rho_0 N$, the factor governing the dependence on the angle ψ coincides with the phase factor of the wave traveling along the ray $B'B$ in the region Ω_1. In this case,

$$V(\rho_0 N) = \pm\omega(\sqrt{1-N^{-2}} - \arccos(N^{-1})) \approx \pm\omega\frac{\sqrt{2}}{3}\left(1-\frac{1}{N}\right)^{3/2},$$

which coincides with half of the exponent in Eq. (5.6). Thus, the exponential factor in Eq. (5.6) describes an acoustic wave tunneling from point B to point A and a similar whispering gallery wave tunneling from the region Ω_2 to the region Ω_1.

6. NUMERICAL ANALYSIS OF THE FORMULAS FOR A SMALL CONTRAST

In the case of small contrast values $\delta = O(1)$, a study of the coefficients of wave excitation and dispersion equations requires a numerical analysis. We limit our consideration to media of equal densities, $\kappa = 1$. Dispersion equation (4.2) has an infinite number of solutions. As was mentioned earlier, with increasing parameter d, the roots of the dispersion equation are grouped into two semi-infinite sequences. One of them corresponds to the waves of the first type and tends to zeros of the Airy function w_1 that lie on the ray $\arg(\xi) = \pi/3$. We number these roots as –1, –2, –3, … Another sequence of roots of Eq. (4.2) corresponds to the waves of the

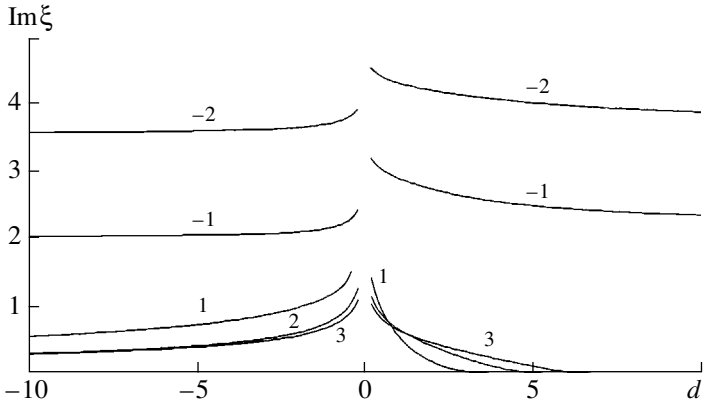

Fig. 3. Imaginary parts of solutions ξ_j of dispersion equation (4.2) as functions of parameter d.

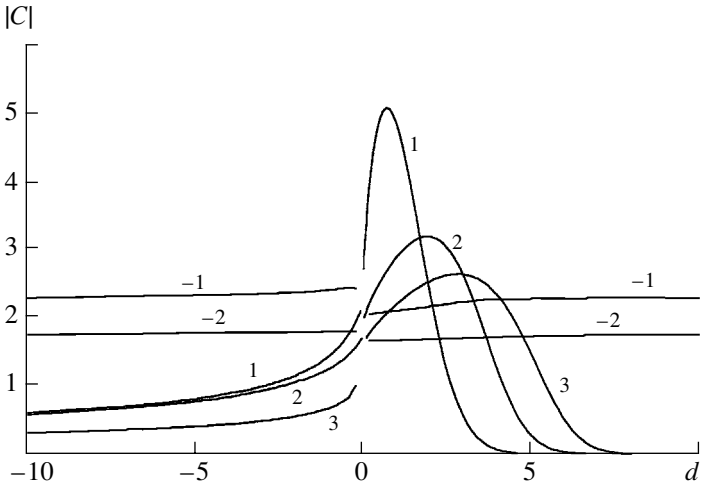

Fig. 4. Magnitudes of excitation coefficients as functions of parameter *d*.

second type and, with $d \longrightarrow \pm\infty$, tends to zeros of the function ν that lie on the negative half-axis η. We number these roots as 1, 2, 3, …. The imaginary parts of the solutions to the dispersion equation characterize the wave attenuation and are of special interest. Figure 3 shows the evolution of $\mathrm{Im}\,\xi$ with increasing parameter *d* for solutions ξ_{-2}, ξ_{-1}, ξ_1, ξ_2, and ξ_3.

Figure 4 shows the coefficients of wave excitation. In the case of the waves of the first type, the excitation coefficients depend only slightly on the contrast. For small positive values of parameter *d*, the excitation coefficients of the waves of the second type exceed the excitation coefficients of the waves of the first type. As the parameter *d* increases, the excitation coefficients exhibit characteristic maxima and then exponentially decay, which agrees well with the tunneling effect described by Eq. (5.6). Simultaneously, the imaginary parts of exponents η also decrease, i.e., the wave attenuation becomes weaker. For negative values of *d*, the excitation coefficients of the waves of the second type decrease with increasing contrast according to a power law, which agrees well with Eq. (5.7).

ACKNOWLEDGMENTS

This work was supported by the Russian Foundation for Basic Research, project no. 02-02-16560.

REFERENCES

1. V. P. Smyshlyaev, V. M. Babich, D. B. Dementiev, and B. A. Samikish, in *Fluid Mechanics and Its Applications* (Kluwer Academic, Dordrecht, 2002), Vol. 68, pp. 209–216.
2. I. V. Andronov and D. Bouche, J. Electromagn. Waves Appl. **9**, 503 (1995).
3. V. S. Buldyrev, Izv. Vyssh. Uchebn. Zaved., Radiofiz. **10** (5), 699 (1967).
4. V. M. Babich and N. Ya. Kirpichnikova, *Boundary Layer Method in Diffraction Problems* (Leningr. Gos. Univ., Leningrad, 1974).

Translated by A. Vinogradov

Acoustical Physics, Vol. 50, No. 4, 2004, pp. 370–374. Translated from Akusticheskiĭ Zhurnal, Vol. 50, No. 4, 2004, pp. 442–447.

A New Type of Acoustic Modes of Vibration of Thin Piezoelectric Plates: Quasi-Longitudinal Normal Modes

I. V. Anisimkin[†]

Institute of Radio Engineering and Electronics, ul. Mokhovaya 11, str. 7, Moscow, 125009 Russia
e-mail: anis@mail.cplire.ru

Received December 30, 2003

Abstract—Using *ST*-cut quartz crystal plates as an example, a new type of normal modes of acoustic vibrations is described. The modes propagate along the x axis with a velocity close or equal to that of longitudinal bulk waves propagating in the same direction and have a longitudinal component of elastic displacement no less than two orders of magnitude greater than the two other components (the shear-horizontal and shear-vertical ones) throughout the whole plate thickness. The domain of existence of the quasi-longitudinal modes consists of a set of limited zones that contain the "allowed" values of the plate thickness H/λ (H is the plate thickness and λ is the wavelength) and are separated by "forbidden" zones corresponding to common Lamb modes. The closeness (or coincidence) of the velocities of a quasi-longitudinal mode in the plate and a longitudinal bulk wave in an unbounded crystal is a necessary but not sufficient condition for the existence of the aforementioned type of modes in *ST*,*x* quartz. *© 2004 MAIK "Nauka/Interperiodica".*

The study of the spectrum of acoustic vibrations in solid-state structures of different geometry, materials composition, anisotropy, and piezoelectric properties is one of the most important issues of physical acoustics. By now, about ten types of acoustic vibrations [1] are known to exist in isotropic bodies, single crystals, piezoelectric crystals, layered media, periodic (Bragg) structures, and thin plates with free boundaries. They include bulk waves (longitudinal and transverse ones), surface waves (Rayleigh, shear-horizontal, Gulyaev–Bleustein electroacoustic, Sezawa, and Love waves), leaky waves (fast and slow pseudo-surface waves), normal modes (Lamb and shear-horizontal waves), and boundary (Stoneley) waves. At certain conditions, one type of wave may smoothly transform to another. For example, with a change in the propagation direction on a free surface of a piezoelectric crystal, a Rayleigh wave with an elliptic polarization may degenerate into a linearly polarized Gulyaev–Bleustein wave, and a pseudo-surface wave, into a two-partial Rayleigh or one-partial longitudinal wave. When the thickness of the plate increases, the low-order Lamb modes transform to a Rayleigh wave, and shear-horizontal (SH) waves, to a wave of the same polarization propagating in the bulk of the solid [1]. The conditions of such wave transformations are very specific and require definite combinations of elastic, piezoelectric, and other properties of the propagation medium and its crystallographic orientation [2].

[†] Deceased. This paper proved to be the last written by Ivan Vladimirovich Anisimkin shortly before his tragic death as a result of a terrorist attack on December 9, 2003, in Moscow.

The fact of existence of a new type of acoustic wave belonging to the family of normal acoustic modes was reported in [3]. The present paper is devoted to their close investigation. Unlike the well-known SH and Lamb modes, the new modes are neither elliptic nor shear-horizontal ones: they have a quasi-longitudinal polarization, i.e., are polarized along the propagation direction. Such modes represent a degeneration of certain Lamb modes, which occurs when their velocity approaches the velocity of a longitudinal bulk wave propagating in the same direction in an unbounded single crystal.

NUMERICAL CALCULATIONS

It is well known that the propagation of normal modes in thin plates is characterized by a dispersion. Their velocity v_n (n is the mode order) depends on the ratio of the thickness H of the plate to the wavelength λ [1]. In the framework of this study, the dispersion curves were calculated for the first 13 Lamb modes along the x axis of *ST*-cut quartz. The calculation was performed by the method of approximation of multilayer matrices with the use of software developed at McGill University (Canada) [4] and the materials constants from [5]. The results of calculation are shown in Fig. 1. The dotted lines in this figure indicate the velocities of purely longitudinal v_{L}, quasi-shear-horizontal v_{QSH}, and quasi-shear-vertical v_{QSV} bulk waves, which propagate in the same direction in an unbounded crystal and have energy fluxes directed along the wave vector. From Fig. 1, one can see that, at certain values of the

1063-7710/04/5004-0370$26.00 © 2004 MAIK "Nauka/Interperiodica"

plate thickness H/λ, the dispersion curves of higher-order normal modes tend to the longitudinal wave velocity v_L = 5744.43 m/s while some of the curves exhibit flat portions (weak-dispersion zones) and portions with a nonmonotone velocity decrease (flexures). Similar dispersion features were observed earlier for Lamb modes in plates made of cubic [6, 7] and tetragonal [8] crystals, but no analysis was performed for the elastic displacements of normal modes in the regions corresponding to different behavior of the dispersion curves.

Such an analysis is performed in this study for quartz plates (quartz is a crystal belonging to the trigonal system). The analysis shows that, as the relative width of the plate, H/λ, varies, the elastic polarization of all modes undergoes considerable changes: the partial components of the resulting displacements of these modes increase, decrease, or even completely disappear throughout the whole plate thickness. The change in the polarization of modes correlates with the deviation of their propagation velocity v_n from the velocities of three bulk waves, v_L, v_{QSH}, and v_{QSV} in the same direction. In the weak dispersion regions, where the mode velocities v_n approach the velocity of the longitudinal bulk wave v_L in an unbounded piezoelectric crystal, some of the higher-order modes are transformed from three-partial elliptic to linearly polarized longitudinal ones, for which the longitudinal displacement component U_1 predominates over the other two components (shear-horizontal U_2 and shear-vertical U_3 ones).

Figure 2 shows the displacements of the second-order Lamb normal mode over the cross section of the plate for the plate thickness values H/λ = 0.01, 1.1, and 0.65. At H/λ = 0.01, the dispersion curve of the mode has the first flat portion (Fig. 1), where the mode velocity v_2 = 5703.2 m/s almost coincides with the velocity of the longitudinal bulk wave v_L = 5744.43 m/s while the longitudinal displacement component U_1 is three to four orders of magnitude greater than the components U_2 and U_3 throughout the whole plate thickness (Fig. 2a). This means that the mode under consideration is a wave with an almost purely longitudinal polarization. The quasi-longitudinal nature of the mode is retained for H/λ varying within ±10% (at least) around the value specified above.

The same mode has an entirely different polarization when H/λ = 1.1, which corresponds to the second flat portion of the dispersion curve (Fig. 1) with the mode velocity approaching v_{QSH}, i.e., the velocity of the fast bulk wave of the shear-horizontal polarization. In this case, the shear-horizontal displacement component U_2 becomes dominant, although no complete degeneration of the mode into a linearly polarized wave takes place, because the longitudinal U_1 and vertical U_3 components are comparable on both surfaces of the plate (Fig. 2b).

The polarization of the second mode acquires an even more complex character at the plate thickness

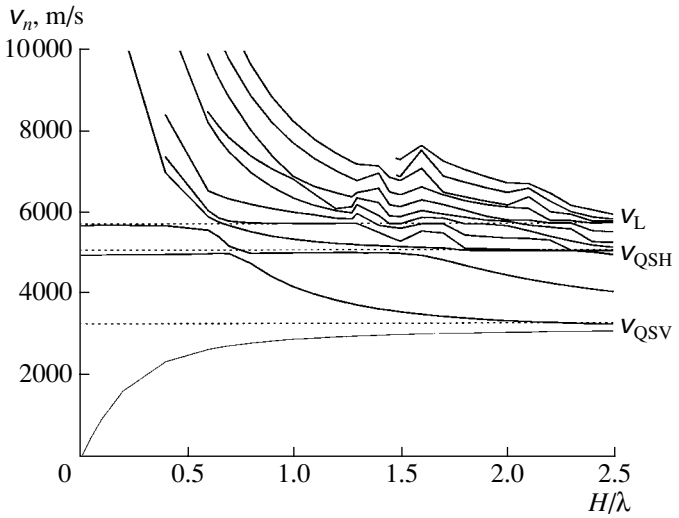

Fig. 1. Dispersion curves for the first 13 Lamb modes in an *ST*,*x*-cut quartz plate.

H/λ = 0.65, when the velocity of the mode, v_2, differs from both the longitudinal velocity v_L and the transverse velocities v_{QSH} and v_{QSV} of bulk waves (Fig. 1). In this case, the elastic displacement of the mode is formed as a sum of the longitudinal U_1 and vertical U_3 components, and the shear-horizontal component U_2 is close to zero throughout the whole plate thickness (Fig. 2c): the mode becomes elliptically polarized in the sagittal plane.

Similar changes in the elastic polarization are observed with varying plate thickness H/λ for the sixth Lamb mode. Namely, the degeneration of this mode into a quasi-longitudinal normal mode also occurs at the coincidence of the mode velocity v_6 = 5741.80 m/s with the velocity of the longitudinal bulk wave v_L = 5744.43 m/s. However, this effect takes place for other values of the plate thickness: H/λ = 1.1433–1.5 (Fig. 3).

All other 11 modes considered in this study did not undergo any degeneration into quasi-longitudinal waves: they remain two- and three-partial even when the velocities v_n and v_L are equal. Therefore, the closeness (equality) of the velocities is not a sufficient condition for the existence of normal modes of a quasi-longitudinal type, at least not in *ST*,*x*-cut quartz.

The characteristics of the modes of the new type were calculated by using the sixth Lamb mode propagating in a quartz plate with H/λ = 1.4851 as an example. The electromechanical coupling coefficient of the mode, K^2, was determined as in the case of surface acoustic waves: $K^2 = -2(v_m - v_0)/v_0$, where v_0 and v_m are the mode velocities for the plate with free surfaces and the plate with one metallized surface, respectively. The value of K_6^2 calculated in this way was found to be 0.073%.

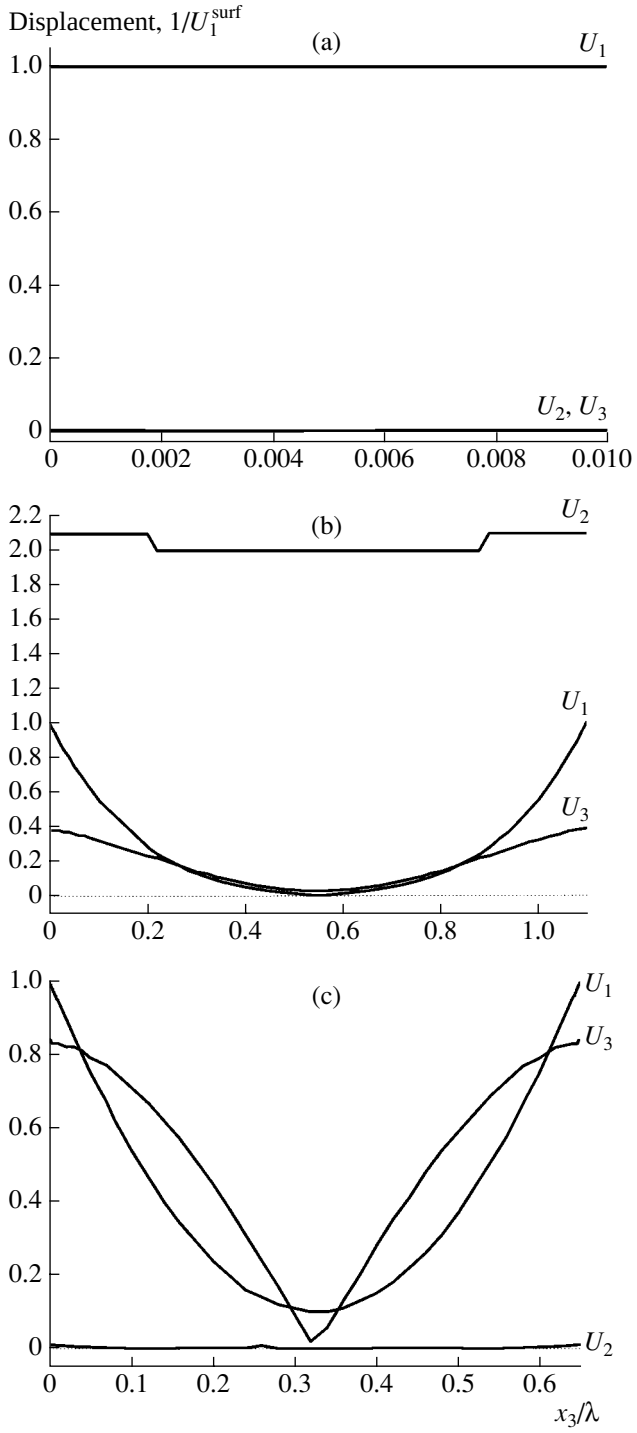

Fig. 2. Distribution of the elastic displacement components of the second Lamb mode over the depth x_3 of the *ST*,*x*-cut quartz plate: U_1^{surf} is the amplitude of the longitudinal component of the mode on the plate surface; the plate thickness is H/λ = (a) 0.01, (b) 1.1, and (c) 0.65.

The temperature coefficient of delay (TCD) of the mode was calculated by the method described in [9], as a total differential of the temperature variations of density, elastic moduli, and the linear expansion coefficient

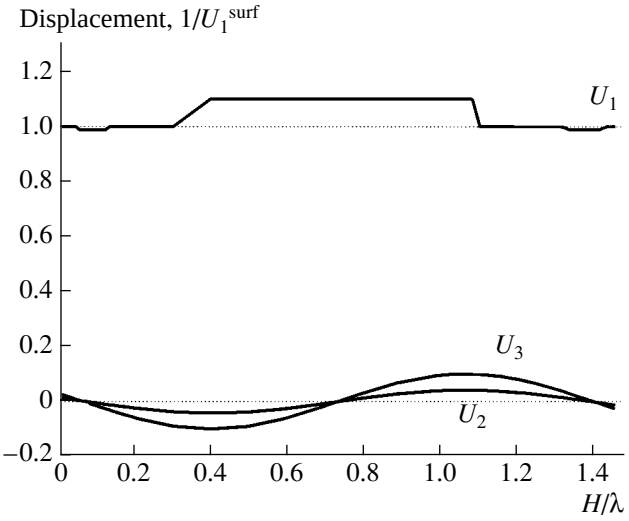

Fig. 3. Distribution of the elastic displacement components of the sixth (quasi-longitudinal) Lamb mode over the depth x_3 of the *ST*,*x*-cut quartz plate: U_1^{surf} is the amplitude of the longitudinal component of the mode on the plate surface; the plate thickness is $H/\lambda = 1.4851$.

of the plate along the propagation direction and across the plate thickness. This quantity was found to be equal to 20.2×10^{-6}°C^{-1}, which closely coincides with the TCD of the longitudinal bulk wave (19.7×10^{-6}°C^{-1}). The latter was calculated by a direct differentiation of the velocity $v_L = (C_{11}/\rho)^{1/2}$ with respect to temperature t: $TCD_L = \alpha_X - (dv_L/dt) = -0.5[\alpha_X + (1/C_{11})(dC_{11}/dt)]$, where α_X is the linear expansion coefficient along the x axis of quartz and C_{11} is the elastic modulus. The coincidence of the temperature characteristics of the quasi-longitudinal mode in a thin plate bounded by two free surfaces and the longitudinal bulk wave in an unbounded crystal presumably testifies to the almost complete identity of the two waves. In particular, this coincidence points to the possibility of representing the velocity of the quasi-longitudinal mode in the form $v_n = v_L = (C_{11}/\rho)^{1/2}$.

The sensitivity (relative velocity variation $\Delta v_n/v_n$) of the quasi-longitudinal mode to variations in the density ρ, elastic moduli C_{ij}, and thickness H/λ of the plate was studied by the method described in [9], by sequentially varying one of the aforementioned parameters of the quartz plate within ±1% around its tabular value. Unlike the common Lamb modes [10], the quasi-longitudinal mode, like the longitudinal bulk wave, proved to be sensitive to variations of only the density ρ and the elastic modulus C_{11}. This fact again points to the possibility of representing the mode velocity in the form of a simple analytical expression $v_n = (C_{11}/\rho)^{1/2}$.

EXPERIMENT

An experimental verification of the existence of quasi-longitudinal modes was carried out using a sample schematically represented in Fig. 4. The sample had the form of a plate made of *ST*-cut quartz crystal (OAO Gudvill, Aleksandrov, Russia). The plate was 0.3 ± 0.03 mm thick and was optically polished on both sides. One side of the plate carried a pair of Al/Cr interdigital transducers with a thickness of 100 nm and 16 pairs of fingers. The period, aperture, and distance between transducers were 202 μm, 12 mm, and 26.2 mm, respectively. The transducers were oriented normally to the *x* axis, along which the mode excitation occurred. The relative thickness of the plate was $H/\lambda = 1.485$: according to calculations, at this thickness, the sixth-order mode should be transformed to the quasi-longitudinal normal mode. The velocities of modes of different orders were measured, and the elastic polarization of modes was investigated.

Figure 5 shows the amplitude–frequency characteristics of the Lamb modes that were measured by an HP 8753 ES network analyzer. The vertical axis in Fig. 5 represents the mode amplitude in decibels (a scale factor of 10 dB), and the horizontal axis, the frequency in megahertz (a scale factor of 7.3 MHz). Owing to the narrow passband of the transducers, modes of different orders were well resolved. A number of modes that had a small electromechanical coupling coefficient K^2 were not observed in the experiment and not revealed by the analyzer. The identification of modes was performed according to the propagation velocity v_n. The value of the velocity was determined from the central frequency of the mode f_{no} and the period of the interdigital transducers λ: $v_n = f_{no}\lambda$. The experimental velocity values were found to coincide with the calculated values within ±5%. For example, for the sixth (quasi-longitudinal) mode (marker 1 in Fig. 5), the measured and calculated velocity values were 5800 and 5741.80 m/s, respectively.

The polarization of normal modes on the plate surface was qualitatively determined from the measurement of absorption under the effect of liquids of equal mass (378 mg) with different values of shear viscosity η. As liquids under test, we used deionized water (with $\rho = 1000$ kg/m^3, $\eta = 1.003$ mPa s, and sound velocity $v_l = 1497$ m/s) and glycerin ($\rho = 1260$ kg/m^3, $\eta = 1450$ mPa s, and $v_l = 1930$ m/s). The measurements were performed as follows. First, the amplitude of each mode, A_n^o (dB), was determined under the conditions corresponding to free surfaces of the plate (Fig. 5). Then, a drop of deionized water, 378 μl in volume, or a drop of glycerin, 300 μl in volume, was placed on one of the plate surfaces by a microdispenser. After this, the mode amplitudes A_n^l (dB) were measured anew. The difference between the amplitudes before and after the application of liquid, $A_n^o - A_n^l$, determined the desired absorption coefficient α_n for a given mode. The use of liquids with identical masses equalized the effect of the load and made it possible to study the absorption α_n only as a function of viscosity.

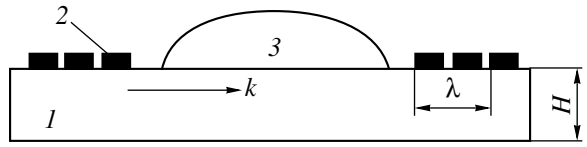

Fig. 4. Experimental sample used for studying the normal modes under the effect of a liquid: (*1*) the quartz plate, (*2*) the interdigital transducers, and (*3*) the drop of the liquid under test; *H* is the thickness of the plate, λ is the period of the transducers (the wavelength), and *k* is the wave vector.

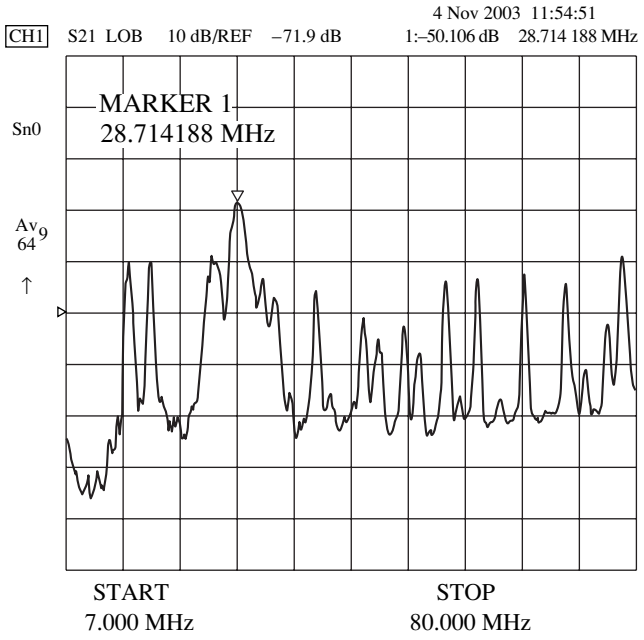

Fig. 5. Amplitude–frequency characteristics of the Lamb modes in the *ST*,*x*-cut quartz plate with free surfaces. The plate thickness is $H/\lambda = 1.485$; marker 1 indicates the quasi-longitudinal mode.

The method of determining the elastic polarization of modes from the absorption α_n is based on two experimental facts: it is well known [11] that the presence of a vertical displacement component U_3 in a wave whose velocity v_n exceeds the sound velocity in the liquid v_l leads to a reradiation of the elastic mode energy into the liquid and to its strong absorption in the propagation direction. Therefore, a weak attenuation of the normal mode under the effect of each of the two liquids under test should testify to the smallness of the vertical displacement component U_3 of this mode on the plate surface. It is also known [3, 12] that waves with a large shear-horizontal displacement component U_2, even in the absence of the vertical component U_3, experience a

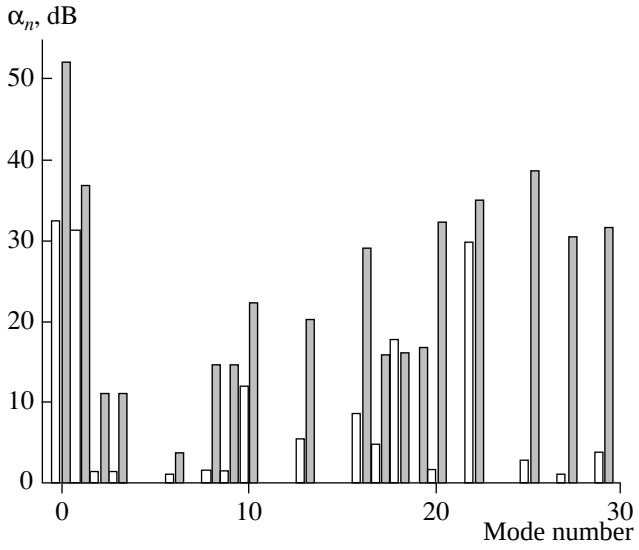

Fig. 6. Absorption coefficient α_n of the Lamb normal modes in the *ST*,*x*-cut quartz plate under the effect of (□) water and (■) glycerin. The plate thickness is $H/\lambda = 1.485$; the drop mass is 378 mg.

strong absorption under the effect of liquids with a high dynamic viscosity. Therefore, a weak absorption of the mode of interest under the effect of glycerin should testify to the smallness of both vertical component U_3 (no reradiation into the liquid) and shear-horizontal component U_2 (a weak sensitivity to viscosity) of the displacement at the plate surface. Thus, in our experiments, the mode that shows a weak absorption under the effect of both water and glycerin should be the mode with a predominantly longitudinal polarization U_1, i.e., the quasi-longitudinal mode.

The results of measuring the absorption coefficient α_n are shown in Fig. 6. One can see that, of all modes excited, only the sixth-order mode experiences a weak absorption with both water and glycerin. According to the measurements, this mode has a velocity of 5800 m/s, which is close to that of the longitudinal bulk wave (5744.43 m/s). Therefore, according to the results of calculation and experiment, precisely this mode is identified as the quasi-longitudinal one.

CONCLUSIONS

Numerical calculations and experiments show that a new type of normal modes occurs in thin plates of *ST*,*x*-cut quartz at certain values of relative thickness H/λ. These modes propagate with a velocity close or equal to that of the longitudinal bulk wave v_L in the same direction and have a predominantly longitudinal polarization. The domain of existence of quasi-longitudinal modes consists of a set of bounded zones containing the "allowed" values of the plate thickness H/λ and separated by the "forbidden" zones of common Lamb modes. The closeness (or coincidence) of the velocity of the quasi-longitudinal mode in a plate and the velocity of the longitudinal bulk wave in an unbounded crystal is a necessary but not sufficient condition for the existence of such a mode in *ST*,*x* quartz. A further development of this study should be the search for the sufficient condition of the existence of this mode and its comprehensive theoretical and experimental investigation in isotropic, anisotropic, and piezoelectric materials.

ACKNOWLEDGMENTS

This work was supported by the Presidential Grant for Scientific Schools no. 1391.2003.2 and a grant from the Foundation for Assistance to Native Science of 2003.

REFERENCES

1. *Ultrasound. Small Encyclopedia*, Ed. by I. P. Golyamina (Sovetskaya Éntsiklopediya, Moscow, 1979).
2. Yu. V. Gulyaev, Pis'ma Zh. Éksp. Teor. Fiz. **9** (2), 68 (1969) [JETP Lett. **9**, 120 (1969)].
3. I. V. Anisimkin, in *Proceedings of 2003 IEEE Ultrasonics Symposium* (Honolulu, USA, 2003).
4. E. L. Adler, J. K. Slaboszewics, G. W. Farnell, and C. K. Jen, IEEE Trans. Ultrason. Ferroelectr. Freq. Control **37**, 215 (1990).
5. A. J. Slobodnik, Jr., E. D. Conway, and R. T. Delmonico, *Microwave Acoustic Handbook* (1973), AFCRL-TR-73-0597.
6. L. P. Solie and B. A. Auld, J. Acoust. Soc. Am. **54**, 50 (1973).
7. V. I. Fedosov, V. I. Anisimkin, I. M. Kotelyanskii, *et al.*, in *Proceedings of 1996 IEEE Ultrasonics Symposium* (San Antonio, USA, 1996), p. 207.
8. V. N. Parygin, A. V. Vershoubskiy, V. G. Mozaev, and M. Weinacht, Ultrasonics **38**, 594 (2000).
9. I. V. Anisimkin, Akust. Zh. **50**, 149 (2004) [Acoust. Phys. **50**, 115 (2004)].
10. I. V. Anisimkin, F. Hickernell, and E. Verona, in *Proceedings of IEEE Ultrasonic Symposium* (Munich, Germany, 2002), p. 437.
11. B. A. Martin, S. W. Wenzel, and R. H. White, Sens. Actuators A **21–23**, 704 (1990).
12. A. J. Ricco and S. J. Martin, Appl. Phys. Lett. **50**, 1474 (1987).

Translated by E. Golyamina

Acoustical Physics, Vol. 50, No. 4, 2004, pp. 375–380. Translated from Akusticheskiĭ Zhurnal, Vol. 50, No. 4, 2004, pp. 448–453.

Filamentary Coagulation of Heavy Particles Suspended in Water in an Ultrasonic Field

S. N. Antonov and A. V. Gerus

Institute of Radio Engineering and Electronics, Fryazino Branch, Russian Academy of Sciences, pl. Vvedenskogo 1, Fryazino, Moscow oblast, 141190 Russia

e-mail: olga-ant@yandex.ru; agierus@fryazino.net

Received June 26, 2003

Abstract—A stable formation of long thin filaments involving heavy particles (heavier than water) suspended in water in an acoustic resonator was observed. The filaments consisted of regularly spaced thin disks formed by coalescent particles. The particles in the disks were tightly packed forming almost solid structures. The disks were arranged perpendicularly to the filament axis and were spaced at half-sound-wavelength intervals. The diameter of the disks was about half-wavelength. The length of the filaments was about hundreds of the sound wavelength. Experiments were performed with particles of different natures and sizes. The filaments were not destroyed under wide variations of sound frequency, acoustic power, length of resonator, size and configuration of the mirror, or its angle of rotation. The particles suspended in water not only visualized the acoustic field but also affected its configuration. The formation of filaments was explained by a nonthermal self-focusing of sound in the resonator, which was caused by the decrease in sound velocity in the region of maximum concentration of particles due to coagulation in the inhomogeneous sound field. *© 2004 MAIK "Nauka/Interperiodica".*

Nonlinear acoustic effects in liquids have long attracted the attention of researchers. These effects can appear, for example, in the coagulation [1, 2] and levitation [3] of particles suspended in liquid. A phenomenon of special interest is the self-focusing in acoustic fields (see, e.g., [4, 5]). A thermal self-focusing occurs because of the heating of liquid by ultrasound, which leads to a decrease in its velocity, bending of wave fronts toward the heated area, and a further increase in temperature. This effect is possible in any liquid except for water, where the sound velocity increases with temperature up to 74°C. Nevertheless, it was found that, in water, one can observe phenomena combining the properties of coagulation, levitation, and self-focusing determined by an entirely different mechanism, which manifests itself at much lower sound intensities than thermal self-focusing in other liquids.

EXPERIMENTAL

Figure 1 shows a schematic diagram of the experiment. A concave spherical piezoceramic transducer (transmitter) of curvature radius R = 26 mm and diameter 27 mm was placed in a rectangular quartz cell of size $30 \times 30 \times 100$ mm filled with water. The transducer produced a sound wave at a frequency of 2.5 MHz along the long side of a cell. A planar metallic mirror parallel to the short side of the cell was placed at a distance L from the transducer. An illuminator either illuminated the whole cell or provided visualization of the fine spatial structure by focusing the light into a narrow beam (~1 mm in diameter). Observations were made from above and from the cell side. The Q factor of the acoustic resonator formed by the transmitter, mirror, cell walls, and water surface, was approximately equal to 3. In the experiment, we controlled the amplitude and phase of the signal that appeared at the transducer as a result of the combination of the continuous signal from the generator and the reflected sound.

To obtain a fine-disperse suspension, we used quartz and corundum abrasive powders with particles 30 and 70 μm in size, respectively, in concentrations on the order of 5–20 g/l.

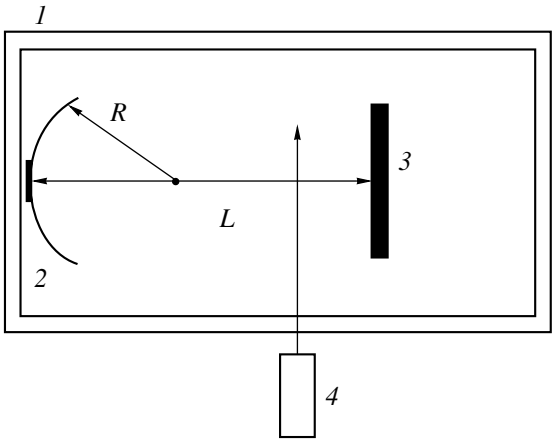

Fig. 1. Schematic diagram of the experiment: (*1*) cell, (*2*) transmitter, (*3*) mirror, and (*4*) illuminator.

1063-7710/04/5004-0375$26.00 © 2004 MAIK "Nauka/Interperiodica"

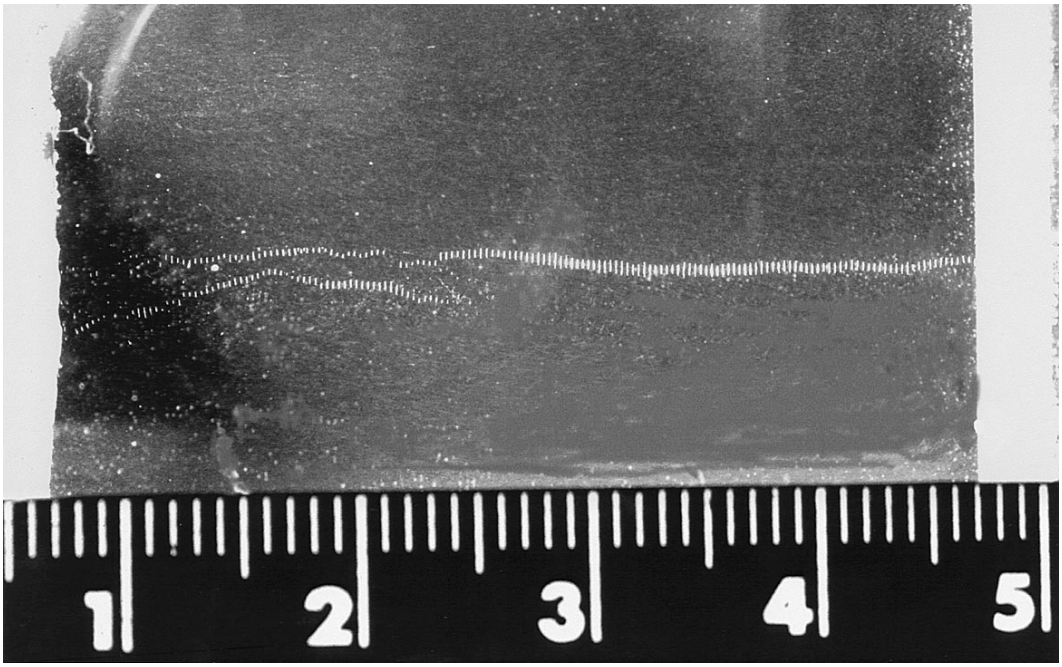

Fig. 2. Formation of filaments at medium acoustic power $W = 1$ W. Corundum particles of diameter 70 μm.

The experiments consisted in studying changes in the formation of filaments of coalescent particles depending on the power of the signal fed to the transmitter. For every experimental situation, there was an initial power (on the order of 0.1 W), above which the formation of one or several filaments of coalescent particles was observed. The filaments consisted of regularly spaced thin disks formed by coalescent particles. The particles in the disks were so tightly packed that they formed a solid structure. The disks were arranged perpendicularly to the filament axis and were spaced at a distance of half the sound wavelength from each other. The diameters of the disks were about one sound wavelength. The filament length exceeded hundreds of sound wavelengths.

Figure 2 shows the picture obtained by a uniform illumination of the whole cell. At the left, one can see a transmitter and at the right, a mirror. The figures in the photograph correspond to centimeters. Figure 3 displays a part of this picture on an enlarged scale. One can see two filaments: the first begins from the mirror in the right part of the photograph and extends practically to the transmitter, and the second is located near the transmitter. The acoustic power of the transmitter was about 1 W. At lower powers, only one filament was observed. The transverse dimension of the filament was about half the wavelength of sound in water (~0.3–0.5 mm). The filament was not homogeneous: it consisted of thin disks formed by coagulated particles. The thickness of the disks was comparable with the particle diameter (for fine quartz powder, the thickness considerably exceeded the particle size). The disks were located at antinodes of velocity of a standing sound wave, the first disk being spaced at a quarter-wavelength from the mirror. The filament usually began from the mirror and ended practically near the transmitter; i.e., its length was hundreds of sound wavelengths. In Fig. 3 it can be seen that, in addition to the stationary filament, flows of particles in a transverse direction are observed (the particles in the photograph are smeared due to their movement during exposition). The filament was very stable, it did not fail during several hours of observation. Its characteristic features were that, first, the disk sizes were approximately equal and, second, they did not increase when more particles were added to the water. This means that the potential wells in which the particles are located are equal and completely filled.

The formation of filaments in all cases led to a considerable (on the order of 20%) change in the signal amplitude at the transducer. The phase of the signal also changed. This allows us to conclude that the particles not only visualized the acoustic field but also actively modified it.

In pure water, no changes were observed in the transducer impedance with an increase in the electric power. Air bubbles, which were produced with the excitation of acoustic field in the cell, hovered over the whole volume of the cell without localization, which differs radically from the situation with heavy particles suspended in water.

In certain conditions, a simultaneous rotation of two parallel filaments about a longitudinal axis located between the filaments with a frequency of several hertz took place. In this case, the amplitude of the signal at the transducer was modulated with the same frequency.

With a further increase in the power applied to the transmitter, a considerable number of filaments were formed with their origins at both mirror and transmitter (Fig. 4). The topology of filaments was approximately the same as in the case of one filament, except that they were shorter. One can also see that, at a distance of about 30 mm from the transmitter (which is somewhat greater than its radius of curvature R), greater disks are formed with approximately a double diameter compared to other disks of the filament. In the experiment, the acoustic power radiated by the transducer reached several tens of watts.

The process of filament formation may be conventionally divided in two stages. At the first stage, the filaments were rapidly formed (within several seconds). At the second stage, within several minutes (for coarse powder, tens of seconds), changes in the distribution of particles and flows outside the filaments took place. During both these stages, the signal at the transducer was subjected to amplitude modulation with a modulation depth of about 20% and a frequency from tens to several hundreds of hertz. For fine powder, this modulation proceeded when the particles outside the filament area did not yet reach the cell bottom. For coarse powder, the modulation continued for some time after the major part of the powder mass outside the filaments fell at the bottom. The modulation frequency depended on the size of powder particles and on the applied power: the frequency usually increased with the power.

For fine quartz powder, we could observe for a long time that, besides the filaments, particles suspended over the whole volume were located in axially symmetric thin regions spaced at a distance of about half a wavelength. A detailed observation of this picture was made by using a focused beam of light, which illuminated a certain layer of the region under study (the illuminator could be moved in the vertical and horizontal directions). The observation was conducted with a microscope focused at the illuminated area. This method of visualization made it possible to see fine details not shadowed by unilluminated regions of the cell. Therefore, in Fig. 5, we schematically represent the whole picture studied by parts. Suspended particles located at the antinode surfaces of particle velocity (curved lines in Fig. 5) are displayed in areas *3*. This arrangement is also observed at sound intensities at which the filaments have not yet formed. Area *4* is the filament, in which the particles are coagulated into disks of a practically solid structure. The places of the location of disks in area *4* are the geometric extension of the places of location of particles in area *3*. Area *5* represents longitudinal flows of water with particles.

The kinetics of the filament formation were as follows. After stirring the particles and switching on the sound, the particles from area *4* began to move radially along curved lines toward the center, where the filament was formed. Then, in several seconds, the filament growth terminated and, in an area of diameter 3–4 sound wavelength around the filament, the formation of longitudinal flows of particles was observed, which later moved radially away from the center. Then, all the particles, except for those gathered in the filament, fell to the bottom of the cell.

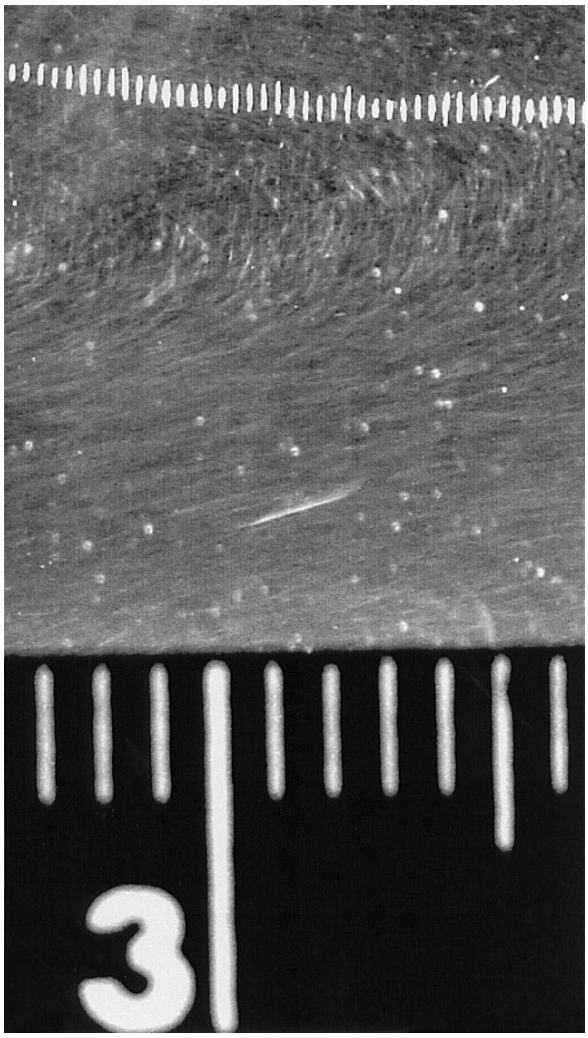

Fig. 3. Formation of filaments at medium acoustic power (a fragment).

At a slight slope of the mirror relative to the vertical axis, the kinetics changed. At first, the radial motion of particles to the center also took place, but only on one side; on the other side of the filament in the course of its formation, only longitudinal flows of particles were observed. Then, after the filament was formed, the particles from the side of longitudinal flows passed through the filament, keeping close to the disks from the side of the mirror, and then moved radially from the center. With coarse corundum particles, the picture of the phenomenon was about the same, but the process of the formation of a visible stationary picture was much faster because of the higher density and greater size of the particles; for the 70-μm corundum powder, it took several seconds.

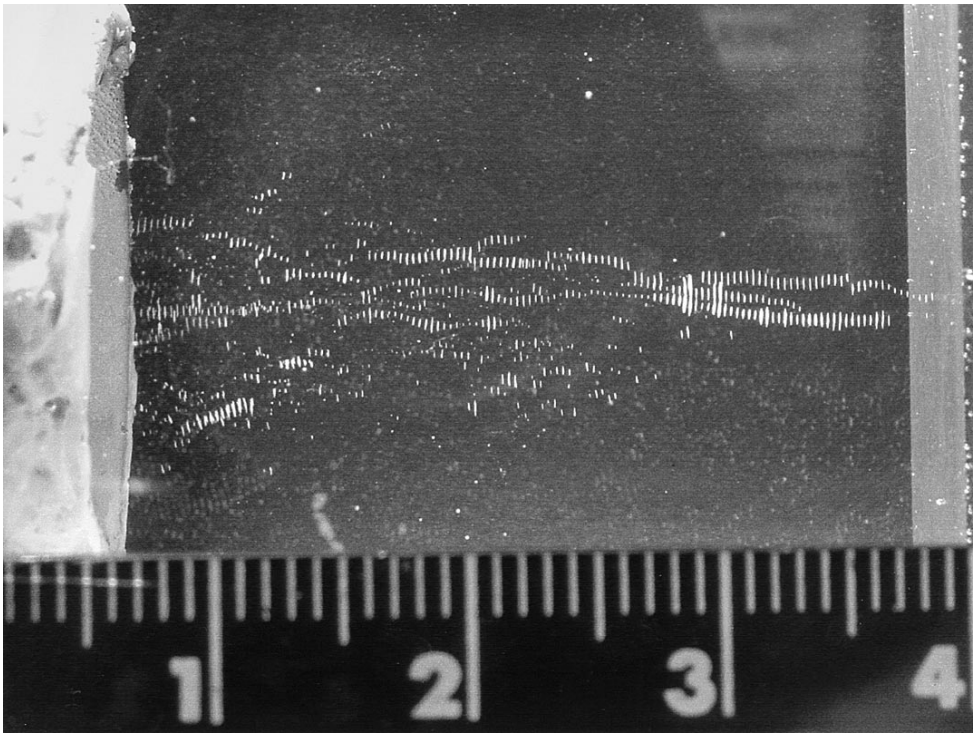

Fig. 4. Formation of filaments at high acoustic power $W = 20$ W. Corundum particles of diameter 30 μm.

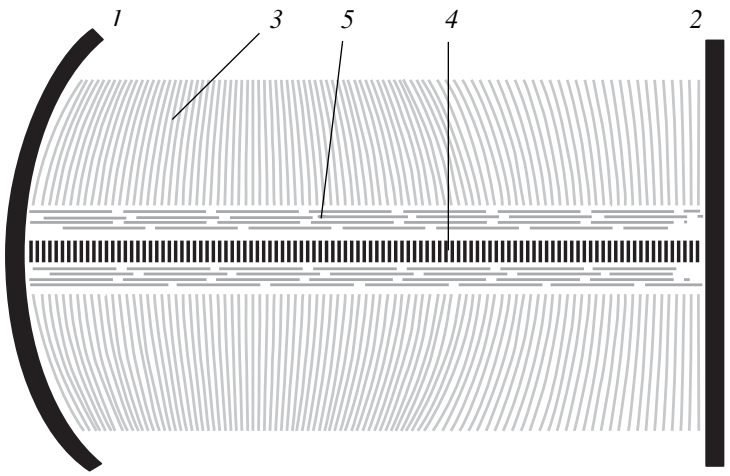

Fig. 5. A filament and the coagulation of fine particles of the quartz powder: (*1*) transmitter, (*2*) mirror, (*3*) region of coagulation, (*4*) filament, and (*5*) longitudinal flows.

A distinctive feature of the phenomena studied was that they were extraordinary stable to changes in experimental conditions. The formation of a filament could be observed with various distances between the mirror and transducer, from several millimeters to about triple the radius of curvature of the mirror (70 mm). The filament stability also manifested itself in the fact that the filament was not destroyed with changes in the frequency of sound. The change in frequency corresponded to several intermode distances of the resonator. When the mirror was rotated through greater angles (on the order of 10°) in both the horizontal and vertical planes, the filament appeared as if it was tied to the mirror: it rotated with the mirror without being destroyed. The formation of filaments occurred with various sizes and materials of the mirror. Furthermore, filaments were formed after a plane mirror was replaced by a convex cylindrical one with the directrix lying in either the

horizontal or vertical plane. In this case, everywhere, except for the filament, intense flows of small particles were clearly visible (until the particles dropped to the bottom of the cell).

The fact that the formation of long thin filaments consisting of coalescent particles in an acoustic resonator was not observed previously can presumably be explained as follows. Experimental conditions in the present study differ from the conditions in other studies, for example in [1, 2], in that we used a spherical transducer, which made it possible to produce more inhomogeneous fields in the resonator.

THEORY

The phenomena observed in our experiment can be qualitatively explained in the following way. In pure water, the acoustic field consists of the near field of the transmitter and a field of standing waves. Away from the transmitter, this field in the cross section has a form close to Gaussian with a maximum lying on the axis. As is shown in [3], spherical particles of radius R located in the standing wave experience a mean acoustic force applied in the longitudinal direction r:

$$F = 4\pi EkR^3 \sin(2kr)\left(\frac{\rho + 2/3(\rho - \rho_0)}{\rho_0 + 2\rho} - \frac{\rho c_0^2}{2\rho c^2}\right), \quad (1)$$

where k is the wave vector of sound; E is the energy density of standing waves; and ρ, c and ρ_0, c_0 are the density and sound velocity of longitudinal waves for a particle and water, respectively. For particles heavier than water, from Eq. (1) it follows that they should gather in antinodes of velocity. In a standing wave, the whole space of the resonator represents potential wells (velocity antinodes) divided by long barriers, the wells being deeper and the barriers higher for higher energy densities. Thus, the particles first fall to the nearest wells and then move along them to the places where the total force acting on them (acoustic and gravitational, with consideration for buoyancy force) is equal to zero; that is, they are drawn to the region near the maximum energy density. The locus where this condition is satisfied for not too high powers of the transmitter resembles a circle with the center (for particles heavier than water) lying slightly below the symmetry axis. Figure 6 shows the transverse profile of the total force acting on a particle for one of the wells for six equidistant levels. The second line from above (a straight line) corresponds to the distribution of the force in the middle of the cell height. The asterisks show the points where the total force acting on the particles vanishes. As the particles gather near these circles, the sound velocity in these areas decreases, because, as is known, for example, from [7], the sound velocity in a liquid with suspended particles of volume concentration α is determined by the expression

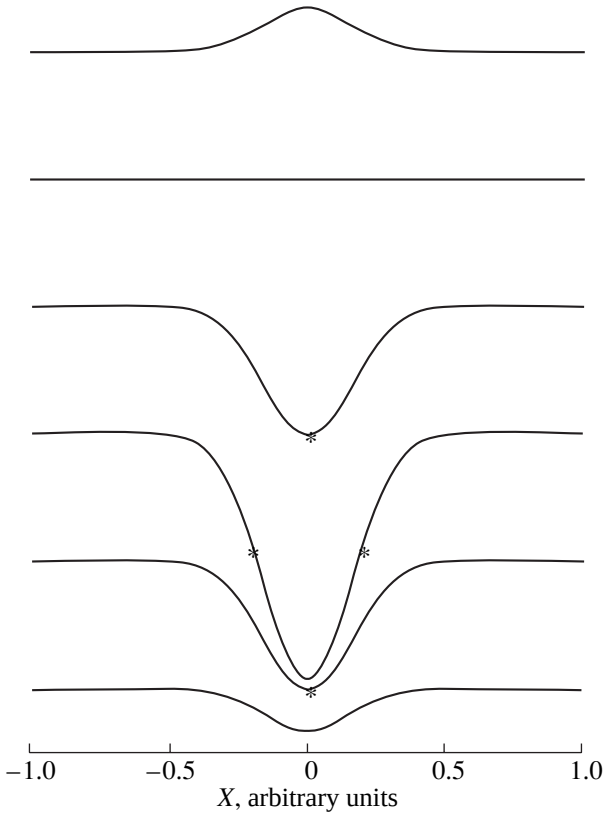

Fig. 6. Calculation of the transverse profile of total force acting on a particle in various cross sections of the field.

$$c = \frac{c_0}{\sqrt{\left(1 + \alpha\frac{\rho - \rho_0}{\rho_0}\right)\left(1 + \alpha\frac{\beta - \beta_0}{\beta_0}\right)}}, \quad (2)$$

where c and c_0 are the sound velocities in the mixture and in pure water, and β and β_0 are the compressibilities of particles and water, respectively. According to Eq. (2), the velocity c reaches its minimum (for quartz, at $\alpha \approx 20\%$, and for corundum, at $\alpha \approx 30\%$) and then grows. In this case, the wave fronts are curved so that, in the regions with large numbers of particles, the energy density increases. The circle shrinks to a disk of small diameter, which is determined by the inverse processes: by the local heating of water, which leads to an increase in sound velocity, violation of resonance conditions for water oscillation between the disks consisting of solid particles, and the growth of the sound velocity after the concentration α exceeds the value minimizing Eq. (2). Note that Eq. (2) may be satisfied only qualitatively, since it was derived for the case of uniformly suspended particles, which in our case is not true. The particles gather into thin disks near these circles also due to the mutual attraction in the field of the sound wave [3]. With a further increase in the power

produced by the transmitter, the strong inhomogeneity of the near field leads to the situation where the condition of equilibrium for suspended particles becomes also fulfilled in other regions, near the mirror and near the transmitter. In this case, new filaments of a similar configuration, which is determined not by the initial distribution of the field but by the developing nonlinear processes, are formed. The experiment showed that the particles do not necessarily constrict into one filament but may split in two filaments rotating around an axis over the aforementioned circles. In addition, in the process of equilibrium establishment (until the particles outside the filaments fall to the bottom), due to the interaction with the flows of particles, oscillations of filaments as a whole are possible, which results in similar oscillations of the voltage at the transducer.

Thus, the phenomenon observed in the experiment, namely, the stable formation of thin long filaments consisting of suspended heavy particles, is qualitatively explained by a special type of self-focusing of sound due to the decrease in its velocity by the particles that appear in the region of maximum acoustic energy density. This phenomenon may be useful for the concentration of sound energy in an acoustic resonator with low electric power supply, as well as for the separation of particles suspended in a liquid.

ACKNOWLEDGMENTS

We are grateful to O.A. Sapozhnikov and V.I. Mirgorodskii for their useful discussions.

REFERENCES

1. K. Soliner and C. Bondy, Trans. Faraday Soc. **32**, 616 (1936).
2. A. G. Avetisyan, V. S. Arakelyan, O. V. Bagdasaryan, and A. K. Dudoyan, Akust. Zh. **31**, 385 (1985) [Sov. Phys. Acoust. **31**, 227 (1985)].
3. V. A. Krasil'nikov and V. V. Krylov, *Introduction to Physical Acoustics* (Nauka, Moscow, 1984).
4. V. G. Andreev, A. A. Karabutov, O. V. Rudenko, and O. A. Sapozhnikov, Pis'ma Zh. Éksp. Teor. Fiz. **41**, 381 (1985) [JETP Lett. **41**, 466 (1985)].
5. V. Yu. Armeev, A. A. Karabutov, and O. A. Sapozhnikov, Akust. Zh. **33**, 177 (1987) [Sov. Phys. Acoust. **33**, 109 (1987)].
6. L. K. Zarembo and V. A. Krasil'nikov, *Introduction to Nonlinear Physical Acoustics* (Nauka, Moscow, 1966).
7. L. Bergmann, *Ultrasonics* (Bell, London, 1938; Inostrannaya Literatura, Moscow, 1957).

Translated by A. Svechnikov

Acoustical Physics, Vol. 50, No. 4, 2004, pp. 381–387. Translated from Akusticheskiĭ Zhurnal, Vol. 50, No. 4, 2004, pp. 454–461.

Sound Radiation from a Cylindrical Transducer Filled with an Elastic Medium

V. E. Glazanov and A. V. Mikhaĭlov

Morfizpribor Central Research Institute, Chkalovskiĭ pr. 46, St. Petersburg, 197376 Russia

e-mail: eugenia@dg3409.spb.edu

Received July 22, 2003

Abstract—An approximate method is proposed for calculating the acoustic field produced by a finite-height cylindrical piezoceramic transducer with allowance for the radiation from the ends of its inner volume that is filled with an elastic medium characterized by an arbitrary Poisson's ratio. Structural features of the transducer (the presence of a sealing compound and an inner baffle) are taken into account. Good agreement is obtained between calculations and experiment for two transducers (a short one with a height-to-radius ratio $h/a \approx 1$ and a long one with $h/a \approx 3$) whose inner cavities are filled with either water or foam plastic. © *2004 MAIK "Nauka/Interperiodica".*

Water-filled cylindrical piezoceramic transducers [1] are widely used in designing transmitting hydroacoustic arrays. The inner cavity of such a transducer may contain an acoustic baffle, which has the form of a cylinder made of a material with a wave resistance smaller than that of water. Exact methods for calculating the parameters of such transducers with allowance for their structural features (the presence of a sealing compound, an inner baffle, etc.) do not exist. The theoretical models developed in some publications describe some idealized cases. For example, a rigorous solution was obtained in [2] to the problem of sound radiation caused by axisymmetric vibrations of a finite open tube whose wall thickness was small compared to its other dimensions. In [3], the acoustic properties of an array of open cylindrical piezoceramic shells were calculated by solving an infinite system of equations of shell vibration. However, the use of these results for analyzing the behavior of real transducers is difficult. An approximate method was proposed in [4] for calculating the field produced by a cylinder of finite height with allowance for the radiation from the ends of its inner volume filled with an isotropic elastic medium with an arbitrary Poisson's ratio. The method is based on the results reported in [5, 6]. In [5], expressions were obtained for calculating the input impedance of a radially excited solid elastic cylinder of finite height. It was assumed that the lateral surface of the cylinder was excited by a force uniform along the cylinder height and that, for the height-to-radius ratio $h/a \geq 1$ in the region before the first resonance, the axial displacement at the ends weakly depends on the radius, so that, under the transformation of radial vibrations to longitudinal ones, they vibrate as one-sided flat pistons without a baffle. The validity of these assumptions was confirmed by the results obtained in [6], where it was shown that the exact values obtained in [2] for the active and reactive components of the radiation resistance of a thin water-filled cylinder coincide with these results in positions of resonances and maximal values.

In this paper, we use the aforementioned approaches to determine the acoustic characteristics of a water-filled cylindrical transducer or a transducer with a foam-plastic inner baffle (Fig. 1). In solving this problem, we do not take into account the interaction between the ends of the inner cavity and the outer lateral surface of the cylinder, which is considered as an opaque cylinder enclosed in perfectly rigid, semi-infinite cylindrical baffles. In addition, we ignore the contributions of the ends of the thin-walled cylindrical transducer and the gap between the cylinder and the inner baffle to the total radiation field.

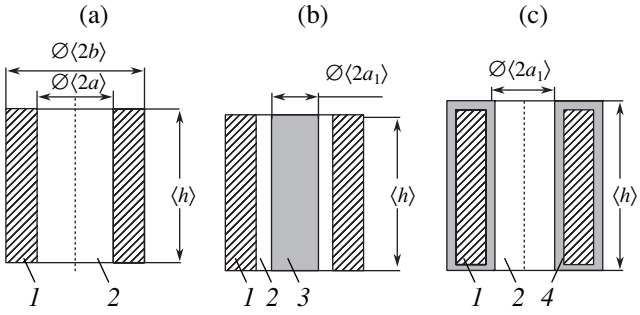

Fig. 1. Types of transducers under study: (a) a water-filled cylinder, (b) a cylinder with an inner baffle, and (c) a compound water-filled cylinder. (*1*) Piezoceramic ring, (*2*) water, (*3*) inner baffle, and (*4*) sealing compound.

1063-7710/04/5004-0381$26.00 © 2004 MAIK "Nauka/Interperiodica"

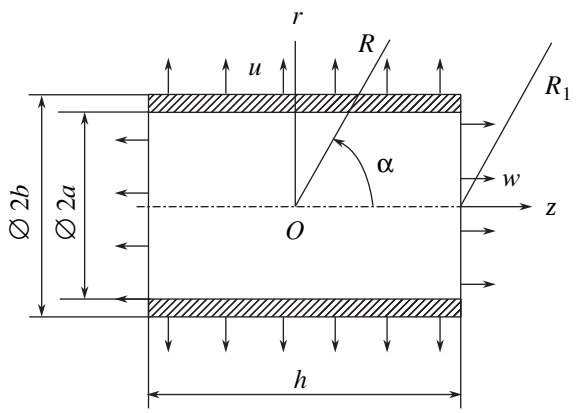

Fig. 2. Determination of the radiation field of a cylindrical transducer with an inner cavity.

To clarify the principle of calculation, we follow the previous publication [4] and first consider a simplified model (Fig. 2). If we assume that the piezoceramic cylinder and the ends of the inner cavity vibrate with velocities $\dot{u}$ and $\dot{w}$, respectively, the pressures p_u and p_w produced in the far field at any angle α are expressed by the formulas [2, 7, 8]

$$p_u(\alpha) = -i(\rho c)_{\text{wat}}\dot{u}\frac{kh\sin\left(\frac{kh}{2}\cos\alpha\right)e^{ikR}}{i\pi\sin\alpha H_1(kb\sin\alpha)\frac{kh}{2}kR\cos\alpha}; \quad (1)$$

$$p_w(\alpha) = -i(\rho c)_{\text{wat}}\dot{w}\frac{(ka)^2}{2}\left\{\frac{(1+\delta)}{2}\frac{2J_1(ka\sin\alpha)}{ka\sin\alpha}\right. \quad (2)$$
$$\left. + (1-\delta)\frac{4}{3\pi}ka\left[1+\left(\frac{ka}{5}\right)^2\right]\right\}\frac{e^{ikR_1}}{kR_1},$$

where a and b are the inner and outer radii of the cylinder and $(\rho c)_{\text{wat}}$ is the wave resistance of water. In Eq. (2), for $ka \le 2$ we set $\delta = 0$, which, to sufficient accuracy, corresponds to the radiation from a flat piston without a baffle; for $ka > 2$, we have $\delta = 1$ and, in this case, the pressure produced by a piston without a baffle coincides with the pressure produced by a piston in a perfectly rigid baffle [2].

Now, we obtain an expression for the pressure produced by the transducer in the direction $\alpha = 90°$:

$$p_r = p_u(90°) + 2p_w(90°). \quad (3)$$

The factor "2" that appears before p_w is explained by the fact that the radiation is produced by both ends of the inner cavity. From Eq. (3) with allowance for Eqs. (1) and (2), we obtain

$$p_r = p_u\left[1 + \frac{\dot{w}}{\dot{u}}\frac{a}{h}\frac{a_1}{a}J_1\left(ka\frac{a_1}{a}\right)i\pi H_1(kb)\right], \quad (4)$$

where

$$p_u = -i(\rho c)_{\text{wat}}\dot{u}kh\frac{1}{i\pi H_1(kb)} \quad (5)$$

is the pressure produced by a cylinder enclosed in perfectly rigid cylindrical baffles. The factor a_1/a is introduced to allow for the decrease in the radius of the end surface of the inner cavity (see Fig. 1c) or baffle (Fig. 1b) relative to the radius of the piezoceramic element of the transducer.

Formula (4) involves the ratio of the particle velocity $\dot{w}$ to the radial velocity of the outer cylindrical surface of the transducer $\dot{u}$. If the cylinder is thin-walled [9, 10], its inner surface vibrates with velocity $\dot{u}$. The ratio $\dot{w}/\dot{u}$ and the specific input impedance Z_{inp} of the radially excited elastic cylinder are determined on the basis of refined expressions derived in [4–6]. Assuming for generality that the ends are loaded with different impedances Z_{I} and Z_{II}, we represent Z_{inp} in the form

$$Z_{\text{inp}} = Z' + Z''. \quad (6)$$

Dividing the impedance components by the wave resistance of water, we obtain

$$\frac{Z'}{(\rho c)_{\text{wat}}} = im\left[\frac{J_0(k_l a_1)}{J_1(k_l a_1)} - \frac{1-2\nu}{1-\nu}\frac{1}{k_l a_1}\right]; \quad (7)$$

$$\frac{Z''}{(\rho c)_{\text{wat}}} = -im\left(\frac{\nu}{1-\nu}\right)^2\frac{2\frac{a}{h}\frac{a_1}{a}}{(k_l a_1)^2}\frac{\frac{1}{m}\left[\frac{Z_{\text{I}}}{(\rho c)_{\text{wat}}}+\frac{Z_{\text{II}}}{(\rho c)_{\text{wat}}}\right]-2i\tan\frac{k_l h}{2}}{\frac{1}{m}\cot k_l h\left[\frac{Z_{\text{I}}}{(\rho c)_{\text{wat}}}+\frac{Z_{\text{II}}}{(\rho c)_{\text{wat}}}\right]-i\left[1+\frac{1}{m}\frac{Z_{\text{I}}}{(\rho c)_{\text{wat}}}\frac{Z_{\text{II}}}{(\rho c)_{\text{wat}}}\right]}. \quad (8)$$

In Eqs. (1), (2), (4), (7), and (8), k and k_l are the wave numbers in water and in the baffle, ν is Poisson's ratio of the elastic medium filling the inner cavity (or the baffle), $m = \rho c_l/(\rho c)_{\text{wat}}$ is the relative wave resistance of the medium, and J_0 and J_1 are Bessel functions.

From Eqs. (6)–(8), we derive the expressions for the active and reactive components of the input impedance $Z_{\text{inp}} = R_{\text{inp}} + iX_{\text{inp}}$ in the case of identical loads at the ends of the cavity, which corresponds to Fig. 2; i.e., we set $Z_{\text{I}} = Z_{\text{II}} = Z_T$, where $Z_T = R_T - iX_T$ is the impedance of a flat piston without a baffle:

$$\frac{R_{\text{inp}}}{(\rho c)_{\text{wat}}} = \frac{R''}{(\rho c)_{\text{wat}}} = \frac{R_T}{(\rho c)_{\text{wat}}} \frac{\dfrac{a}{h}\dfrac{a_1}{a}\left(\dfrac{\nu}{1-\nu}\right)^2\left(\dfrac{2}{k_l a_1}\right)^2}{\left[\dfrac{R_T}{(\rho c)_{\text{wat}}}\dfrac{1}{m}\right]^2 + \left[\dfrac{X_T}{(\rho c)_{\text{wat}}}\dfrac{1}{m} - \cot\dfrac{k_l h}{2}\right]^2}; \tag{9}$$

$$\frac{X_{\text{inp}}}{(\rho c)_{\text{wat}}} = \frac{Z'}{(\rho c)_{\text{wat}}} + \frac{X''}{(\rho c)_{\text{wat}}} = -m\left[\frac{J_0(k_l a_1)}{J_1(k_l a_1)} - \frac{1-2\nu}{1-\nu}\frac{1}{k_l a_1}\right] + \frac{m\dfrac{a}{h}\dfrac{a_1}{a}\left(\dfrac{2}{k_l a_1}\right)^2\left(\dfrac{\nu}{1-\nu}\right)^2\left[\cot\dfrac{k_l h}{2} - \dfrac{X_T}{(\rho c)_{\text{wat}}}\dfrac{1}{m}\right]}{\left[\dfrac{R_T}{(\rho c)_{\text{wat}}}\dfrac{1}{m}\right]^2 + \left[\dfrac{X_T}{(\rho c)_{\text{wat}}}\dfrac{1}{m} - \tan\dfrac{k_l h}{2}\right]^2}. \tag{10}$$

The ratio between particle velocities that appears in Eq. (4) is determined as

$$\frac{\dot{w}}{\dot{u}} = \text{Re}\left(\frac{\dot{w}}{\dot{u}}\right) + \text{Im}\left(\frac{\dot{w}}{\dot{u}}\right), \tag{11}$$

where

$$\text{Re}\left(\frac{\dot{w}}{\dot{u}}\right) = \frac{2}{k_l a_1}\frac{\nu}{1-\nu}\frac{\dfrac{R_T}{(\rho c)_{\text{wat}}}\dfrac{1}{m}}{\left[\dfrac{R_T}{(\rho c)_{\text{wat}}}\dfrac{1}{m}\right]^2 + \left[\dfrac{X_T}{(\rho c)_{\text{wat}}}\dfrac{1}{m} - \cot\dfrac{k_l h}{2}\right]^2};$$

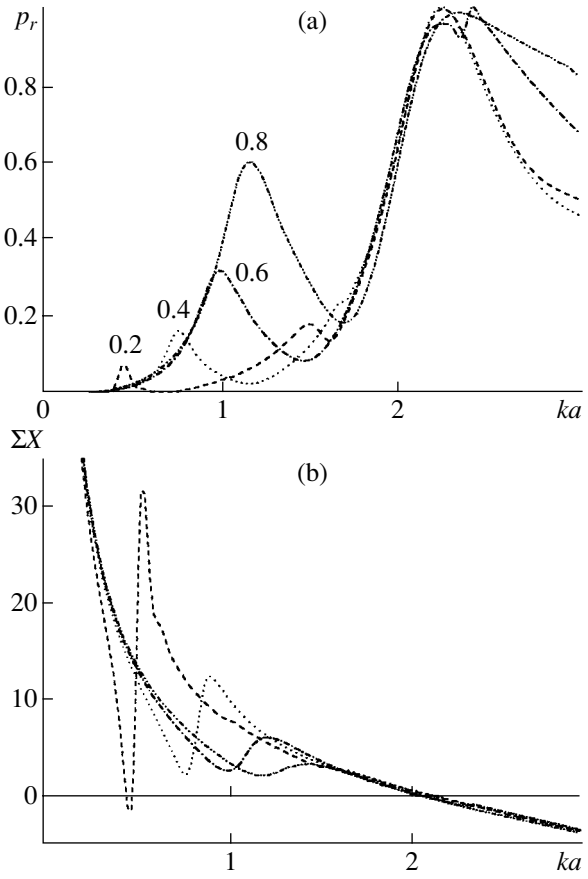

Fig. 3. Frequency dependences of (a) the pressure produced by a cylindrical transducer along its radius and (b) the sum of reactive impedance components of the transducer–inner cavity system. The numbers near the curves indicate the ratio of the inner radius of the piezoceramic ring a to its height h.

$$\text{Im}\left(\frac{\dot{w}}{\dot{u}}\right) = \frac{2}{k_l a_1}\frac{\nu}{1-\nu}\frac{\dfrac{X_T}{(\rho c)_{\text{wat}}}\dfrac{1}{m} - \cot\dfrac{k_l h}{2}}{\left[\dfrac{R_T}{(\rho c)_{\text{wat}}}\dfrac{1}{m}\right]^2 + \left[\dfrac{X_T}{(\rho c)_{\text{wat}}}\dfrac{1}{m} - \cot\dfrac{k_l h}{2}\right]^2}.$$

To calculate the dependences $p_r(ka)$ as functions of the wave radius in water, we introduce the following relations in Eqs. (9)–(11):

$$k_l a_1 = ka\frac{c_{\text{wat}}}{c_l}\frac{a_1}{a}; \quad k_l h = ka\frac{c_{\text{wat}}}{c_l}\frac{h}{a}, \tag{12}$$

where c_l is the velocity of longitudinal waves in the baffle.

Expression (5) for P_u involves the radial particle velocity $\dot{u}$. For a piezoceramic transducer, its value is

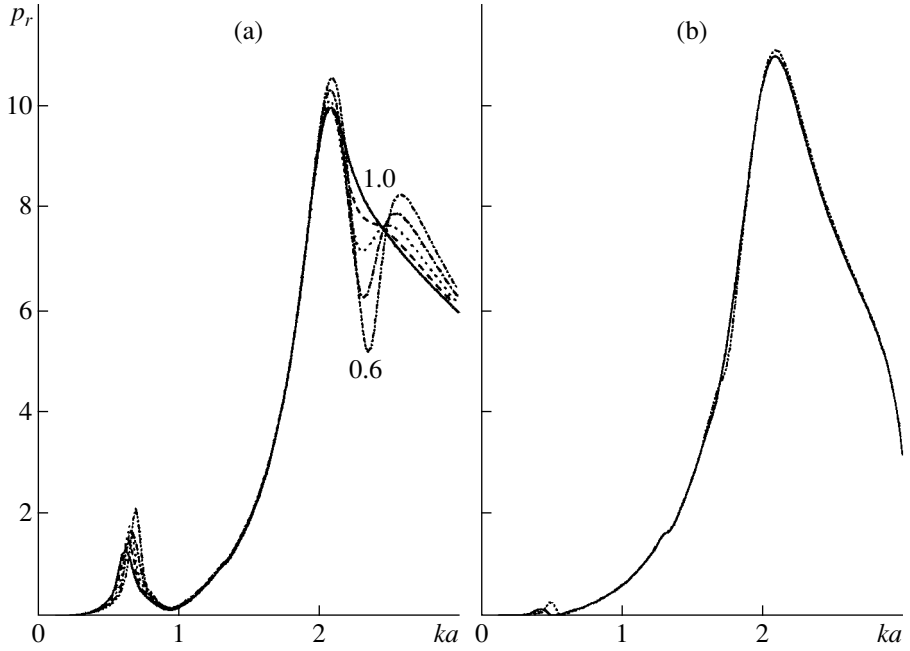

Fig. 4. Influence of the ratio a_1/a (from 1 to 0.6) on the dependence $p_r(ka)$ for the cases of a (a) water-filled and (b) foam-plastic-filled inner cavity. The numbers near the curves show the ratio a_1/a.

determined from the theory of transducers [11] according to the formula

$$\dot{u} = B/Z_{\text{sp}}, \tag{13}$$

where

$$Z_{\text{sp}} = Z_{MC} + \frac{Z_{\text{inp}}}{(\rho c)_{\text{wat}}} + \frac{z_s}{(\rho c)_{\text{wat}} S_b} \tag{14}$$

is the sum of the specific impedances of the transducer itself Z_{MC}, its inner cavity Z_{inp}, and the outer cylinder surface (of area S_b) – z_s; B is a coefficient that depends on the constants of piezoelectric ceramics, the thickness of the piezoceramic ring, and the voltage supplied to the transducer. In subsequent calculations, we assume that $B = 1$. According to [12], we write the expression for Z_{MC} in the form

$$Z_{MC} = R_{MC} - iX_{MC}$$
$$= m_{cer}\frac{1-\varepsilon}{\varepsilon}\left\{\frac{1}{Q} - i\left[\frac{ka}{(ka)_0} - \frac{(ka)_0}{ka}\right]\right\}, \tag{15}$$

where $m_{\text{cer}} = (\rho c)_{\text{cer}}/(\rho c)_{\text{wat}}$ is the relative wave resistance of piezoelectric ceramics, Q is the Q factor of the transducer in air, $\varepsilon = a/b$ is the ratio of the inner radius of the transducer to its outer radius (of piezoceramics), and $(ka)_0 = \dfrac{c_{\text{cer}}}{c_{\text{wat}}}\dfrac{2\varepsilon}{1+\varepsilon}$ is the resonant wave radius of the piezoceramic ring in air.

With allowance for Eqs. (13) and (14), the quantity $|\dot{u}|$ can be represented as

$$|\dot{u}| = \frac{1}{\sqrt{\left[\dfrac{R_{\text{inp}}}{(\rho c)_{\text{wat}}} + R_{MC} + \dfrac{r_S}{\varepsilon}\right]^2 + \left[\dfrac{X_{\text{inp}}}{(\rho c)_{\text{wat}}} + X_{MC} + \dfrac{x_S}{\varepsilon}\right]^2}}. \tag{16}$$

Formulas (4), (5), and (9)–(16) allow us to calculate the radiation field of the cylinder and to analyze the dependences $P_r(ka)$ by varying the parameters of the transducer and the inner cavity. To reveal the general trends, we plotted a family of curves normalized to unity for different ratios a/h at $a_1/a = 1$ (Fig. 3a). Calculations were performed with the following parameters: the ratio of the velocity in piezoceramics to the velocity in water $c_{\text{cer}}/c_{\text{wat}} = 2.33$, $m_{\text{cer}} = 16.8$, $Q = 20$, and the parameters of the foam plastic (see [13]) $m = 0.35$ and $\nu = 0.3$. Let us indicate two resonances in the characteristic of p_r: one of them, at $(ka)_2$, is caused by radial vibrations of the piezoceramic cylinder, and the other, at $(ka)_1$, corresponds to lower frequencies and is mainly determined by the vibrations of the inner cylindrical cavity. As the relative height of the cylinder h/a increases, the low-frequency resonance shifts to the left along the ka axis and its level decreases relative to the pressure level reached at the main (radial) resonance frequency $(ka)_2$. The positions of both resonances are governed by the function ΣX (Fig. 3b), i.e., by the sum

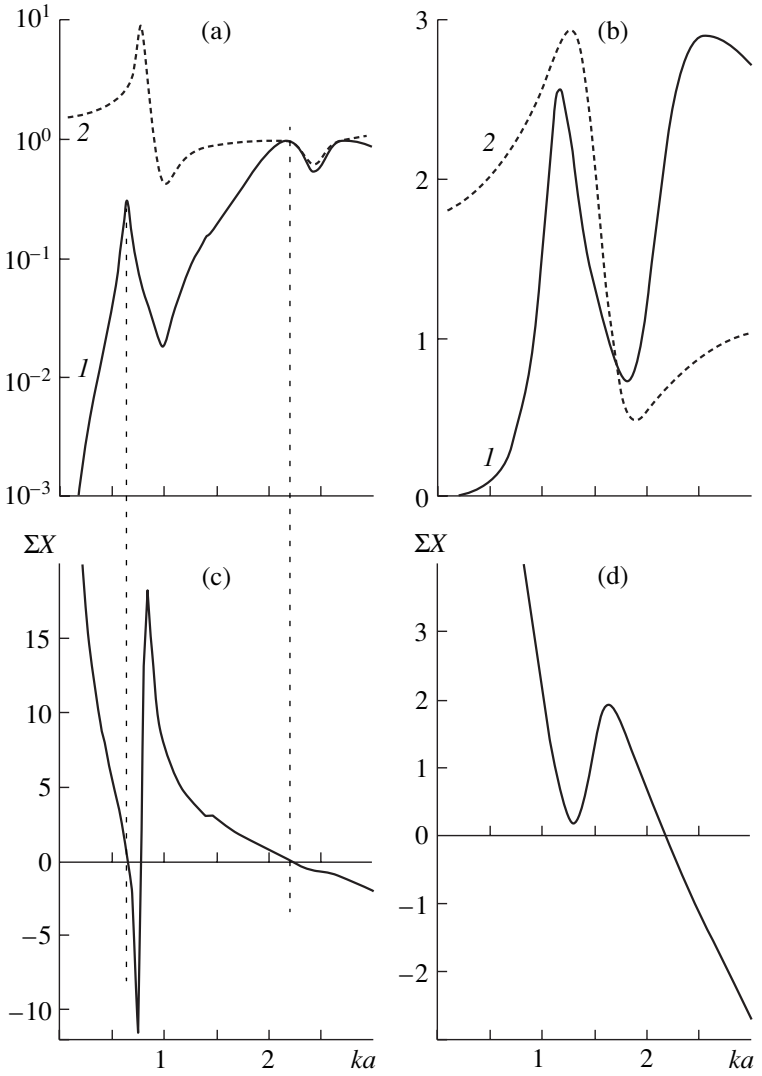

Fig. 5. Characteristics of (*1*) pressure $p_r(ka)$ and (*2*) ratio p_r/pu (upper plots) and the dependences $\Sigma X(ka)$ (lower plots) for (a, c) transducer no. 1 and (b, d) transducer no. 2 (see table).

of the reactive impedance components of the transducer–inner cavity system (see the second term in the denominator of expression (16)). From Fig. 3, one can see that, at certain values of $(ka)_1$, when the pressure characteristic $p_r(ka)$ has its first maximum, the quantity ΣX reaches its minimum. Near $(ka)_2$, the second resonance is observed at $\Sigma X \cong 0$.

The positions of the maxima of p_r depend on the ratio a_1/a (Fig. 4). As a_1/a decreases, the frequency characteristic of pressure begins to exhibit an additional resonance (see Fig. 4a), which (as will be shown below) is caused by the change in the contribution of the radiation of the cavity end to the total radiation field of the transducer. In the case of a cavity with an inner foam-

Dimensions of the transducers and their elements

Parameters	a (cm)	b (cm)	h (cm)	ε	a/h	a_1 (cm)	b_1 (cm)	h_1 (cm)
Transducer no. 1	5.1	5.7	16.5	0.89	0.31	3.75	7	20.3
Transducer no. 2	16.75	19.25	18.5	0.87	0.9	15	20.5	23

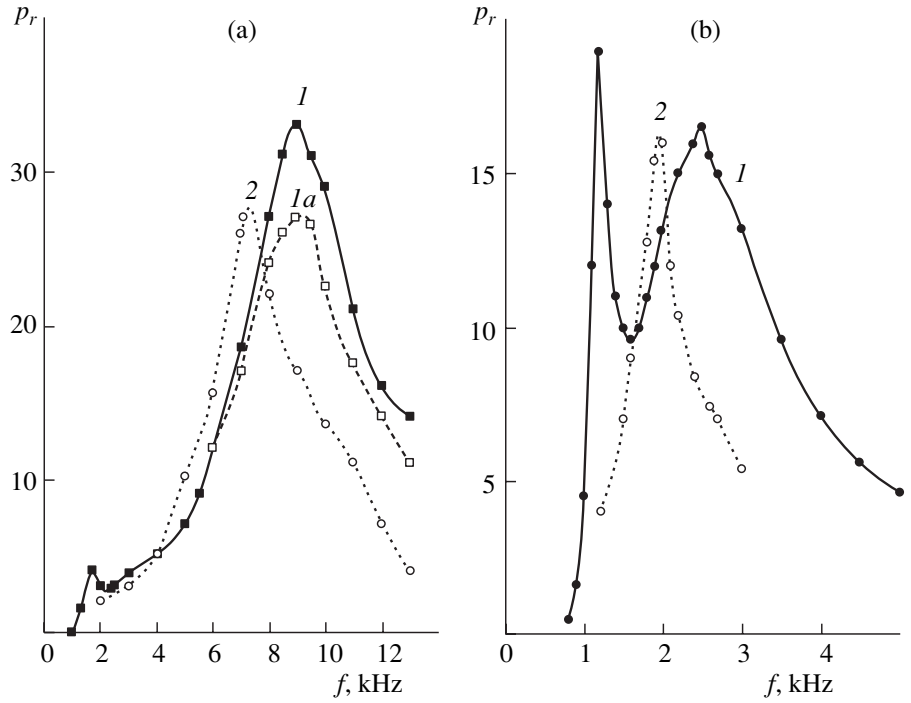

Fig. 6. Experimental frequency dependences of pressure p_r (Pa × m/V) produced by (a) transducer no. 1 and (b) transducer no. 2 along the radius when the cavity is filled with (*1*, *1a*) water or (*2*) foam plastic.

plastic baffle, this effect does not occur (Fig. 4b). (Note that the curves in Fig. 4 are not normalized and the absolute values of pressure p_r can be estimated; for the cases of water and foam plastic, these values are almost the same.)

Let us analyze the characteristics $p_r(ka)$ for two cases of cylindrical transducers: a long transducer (no. 1) with $a/h = 0.31$ and a short transducer (no. 2) with $a/h \cong 1$. For these specific transducers, we compare theory and experiment. The dimensions of the transducers and their components are given in the table.

We compare the characteristics $p_r(ka)$ with the ratio p_r/p_u between the pressure produced by a transducer with an inner cavity and the pressure produced by a cylinder in perfectly rigid cylindrical baffles (i.e., without considering the ends of the cavity), which was calculated by Eq. (6) (see the upper plots in Fig. 5). One can see that, in the low-frequency region near the first resonance, for the long cylinder (transducer no. 1), the aforementioned ratio is $p_r/p_u \geq 1$. This means that the predominant radiation is that from the ends of the cavity in the direction $\alpha = 90°$ (along the radius). In the region of the second resonance, the dependence $p_r(ka)$ reproduces the behavior of the characteristics of p_r/p_u, which testifies to the negligibly small influence of the cavity properties on the total radiation field. (In calculating the characteristic $p_r(ka)$, we used the value $a_1/a = 0.73$, which corresponds to the geometric dimensions of the transducer (see table).) Hence, for the long cylinder, when $a_1/a < 1$, the frequency characteristic of sound radiation exhibits two humps. The first of them occurs at $\Sigma X = 0$, and the second, in the case when the effect of the cavity becomes insignificant. In this case, radiation of a cylinder in perfectly rigid cylindrical baffles predominates in the main resonance region. Note that, at $a_1/a = 1$, the pressure curve exhibits only one resonance. For the short cylinder (transducer no. 2), the characteristic $p_r(ka)$ exhibits the first and second resonances in the region of $\Sigma X \cong 0$ and the characteristic of p_r/p_u does not affect to any considerable extent the pressure value near the second resonance, unlike the case of transducer no. 1.

Experimental frequency characteristics of pressure, $p_r(f)$, produced by transducers nos. 1 and 2 with different relative heights and different materials filling their inner cavities (water or foam plastic), are presented in Fig. 6. To compare them with the calculated dependences $p_r(ka)$, it is necessary to recalculate the scale of the f axis (given in kHz) to the scale of the ka axis through a coefficient M, i.e., to set $ka = Mf$. A numerical analysis showed that, for both cases of inner cavity filling (water or foam plastic), good agreement between the calculated and experimental characteristics of p_r (see Figs. 4–7) is achieved when the value of M is approximately equal to the ratio of the inner radius of the piezoceramic transducer to its height: $M \cong a/h$.

The results obtained in this paper may serve for estimating the characteristics of transducers with geomet-

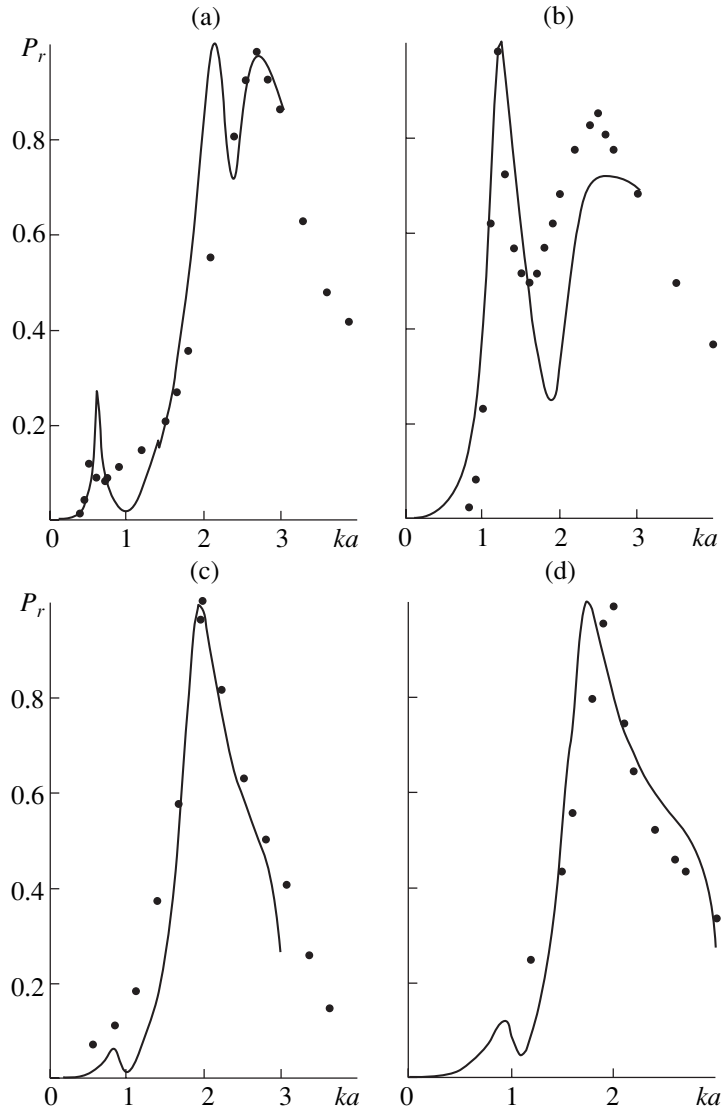

Fig. 7. Pressure produced along the radius by (a, c) transducer no. 1 and (b, d) transducer no. 2 (pressure is normalized to unity): calculation (solid line) and experiment (dots); the cavity is filled with (a, b) water or (c, d) foam plastic.

ric parameters within the limits of $a/h = 0.2–1.0$ and $\varepsilon = a/b = 0.8–0.9$ and with a wave radius of $ka \le 3$.

REFERENCES

1. *Underwater Electroacoustic Transducers. Calculation and Design: A Handbook*, Ed. by V. V. Bogorodskiĭ (Sudostroenie, Leningrad, 1983).
2. E. L. Shenderov, *Sound Radiation and Scattering* (Sudostroenie, Leningrad, 1989).
3. I. V. Vovk, Akust. Zh. **38**, 427 (1992) [Sov. Phys. Acoust. **38**, 234 (1992)].
4. V. E. Glazanov, *Screening of Hydroacoustic Arrays* (Sudostroenie, Leningrad, 1986).
5. V. E. Glazanov, Akust. Zh. **14**, 532 (1968) [Sov. Phys. Acoust. **14**, 447 (1968)].
6. V. E. Glazanov, Akust. Zh. **35**, 801 (1989) [Sov. Phys. Acoust. **35**, 467 (1989)].
7. M. D. Smaryshev, *Directivity of Hydroacoustic Arrays* (Sudostroenie, Leningrad, 1973).
8. L. Ya. Gutin, in *Selected Works* (Sudostroenie, Leningrad, 1977), pp. 95–105.
9. D. D. Ebenzer and A. J. Sujatha, J. Acoust. Soc. Am. **102**, 1540 (1997).
10. D. D. Ebenezer, J. Acoust. Soc. Am. **102**, 1549 (1997).
11. G. M. Sverdlin, *Hydroacoustic Transducers and Arrays* (Sudostroenie, Leningrad, 1980).
12. V. E. Glazanov and A. V. Mikhaĭlov, Akust. Zh. **42**, 609 (1996) [Acoust. Phys. **42**, 537 (1996)].
13. I. N. Zavalina, V. E. Glazanov, and V. I. Orlova, Vopr. Sudostr., Ser. Obshchetekh. **11**, 77 (1975).

Translated by E. Golyamina

Acoustical Physics, Vol. 50, No. 4, 2004, pp. 388–393. Translated from Akusticheskiĭ Zhurnal, Vol. 50, No. 4, 2004, pp. 462–468.

The Effect of Electrical Boundary Conditions on the Characteristics of Surface Acoustic Waves Propagating in Potassium Niobate

B. D. Zaĭtsev, I. E. Kuznetsova, and I. A. Borodina

Institute of Radio Engineering and Electronics, Russian Academy of Sciences (Saratov Branch), ul. Zelenaya 38, Saratov, 410019 Russia

e-mail: zaitsev@ire.san.ru

Received April 8, 2003

Abstract—The study of the effect of a perfectly conducting plane placed at a certain distance from the surface of a potassium niobate crystal on the characteristics of the generalized Rayleigh and Gulyaev–Bleustein surface waves is continued. In addition, the effect of an infinitely thin conducting layer applied to the surface of the piezoelectric on the characteristics of these waves is analyzed. It is found that a variation in the conductance of this layer can produce a result that completely differs from the result obtained when a perfectly conducting plane is moved toward the surface, although the extreme states of these actions (electrically open and short-circuited surfaces) are identical. A possible physical explanation of this difference is proposed. © *2004 MAIK "Nauka/Interperiodica".*

INTRODUCTION

Until recently, it was believed that, for surface acoustic waves (SAWs) propagating in piezoelectric crystals, an electrical short-circuiting of the surface does not affect the wave type but causes insignificant changes in the wave structure and reduces the wave velocity. This statement was corroborated by numerous calculations and experiments [1, 2]. However, a number of recent publications reported that it is not always valid for strong piezoelectrics [3–6]. In particular, it was theoretically predicted that there exist crystallographic orientations for which metallization of the surface of a semi-infinite potassium niobate crystal [3, 4] or a piezoelectric structure based on it [5] can produce an unusual phenomenon, namely, an increase in the velocity of the surface acoustic waves. The possibility of this effect was also demonstrated experimentally for the Rayleigh SAWs propagating along the X axis of the Y + 128°-cut lithium niobate crystal [6]. The lithium niobate crystals were specially processed, after which lithium ions were found to be partially replaced by protons in a thin surface layer. To explain the effect of the SAW velocity increase by the metallization of the surface, a hypothesis was put forward: it was presumed that either the type of the surface wave changes or hybrid coupled waves are generated.

A work is also known [7] that theoretically analyzes the effect of a perfectly conducting plane placed a distance d apart from the surface of a Y-cut potassium niobate crystal on the characteristics of generalized surface acoustic waves propagating in the X + 15° direction. Another unusual phenomenon was predicted, namely, it was shown that, as this plane is moved away from the piezoelectric surface, the structure of the wave may significantly change and a generalized Gulyaev–Bleustein wave may transform into a generalized Rayleigh wave.

This paper continues the analysis of the behavior of the characteristics of SAWs propagating in $Y - X$ + 15°-cut potassium niobate under a smooth variation of the electrical boundary conditions. The boundary conditions can be varied in two ways: by moving the perfectly conducting plane away from the piezoelectric surface or by changing the conductance of an infinitely thin conducting layer applied to the potassium niobate surface. Results obtained with these methods of smoothly transforming an electrically short-circuited surface into an electrically open surface are compared. A specific feature of our calculations is that the absolute value of the determinant of the matrix of boundary conditions was minimized using the representation of the velocity as a complex quantity [8]. Its real part is the phase velocity, while the imaginary part allows for the attenuation associated with either the leaky nature of the wave being analyzed [8] or the presence of the conducting layer. The calculations employed materials constants of potassium niobate borrowed from [9].

It should be noted that, in our opinion, the generalized Gulyaev–Bleustein waves must be distinguished from the generalized Rayleigh waves. By a "generalized Gulyaev–Bleustein wave," we mean a piezoactive surface wave with three mechanical displacement components, whose polarization ellipse is closest to the crystal surface [7]. If this ellipse is closest to the sagittal

1063-7710/04/5004-0388$26.00 © 2004 MAIK "Nauka/Interperiodica"

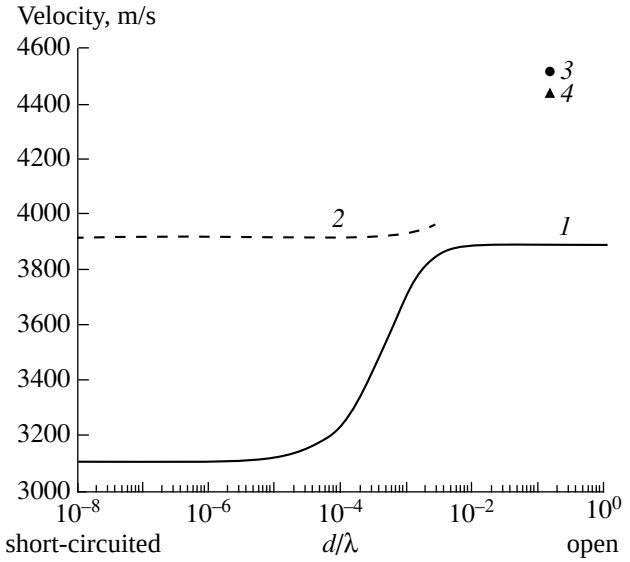

Fig. 1. Phase velocity of the generalized Gulyaev–Bleustein SAW—generalized Rayleigh wave (branch *1*) and the generalized Rayleigh wave (branch *2*) in a $Y - X + 15°$-cut potassium niobate crystal versus the vacuum gap d/λ between the perfectly conducting plane and the surface of the crystal; dots *3* and *4* refer to the fast and slow quasi-shear bulk waves.

plane, the wave will be referred to as a generalized Rayleigh wave.

1. CHARACTERISTICS OF SAWS IN A PERFECTLY CONDUCTING PLANE–VACUUM–PIEZOELECTRIC STRUCTURE

Let us consider in more detail the results of analyzing the effect of an infinitely thin, perfectly conducting plane placed a distance d apart from the free surface of a piezoelectric material on the characteristics of generalized surface acoustic waves. As shown in [7], as the distance d increases from 0 to ~0.1λ, where λ is the wavelength, the surface of the piezoelectric crystal smoothly goes over from the electrically short-circuited state to the electrically free state. As a result of the theoretical analysis, the velocity and mechanical particle displacement components of the generalized surface waves propagating in an $Y - X + 15°$-cut potassium niobate crystal were determined as functions of the normalized vacuum gap d/λ. The phase velocity and the normalized components u_1/u, u_2/u, and u_3/u ($u = \sqrt{u_1^2 + u_2^2 + u_3^2}$) of the mechanical displacement on the surface of the piezoelectric versus the normalized vacuum gap d/λ are plotted in Figs. 1 and 2, respectively. Here, the x_1 axis coincides with the wave propagation direction, the x_3 axis is orthogonal to the surface, and the x_2 axis lies on the surface and is orthogonal to the propagation direction. An analysis of the plots shows that, in this crystallographic situation, two branches of

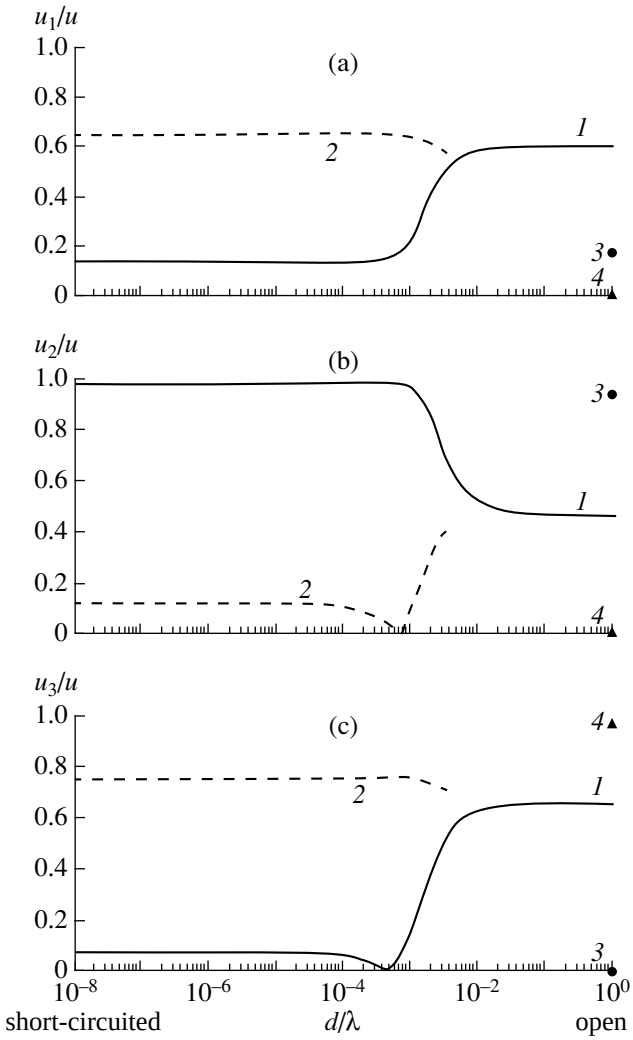

Fig. 2. Normalized mechanical particle displacement components (a) u_1/u, (b) u_2/u, and (c) u_3/u of the (*1*) generalized Gulyaev–Bleustein and (*2*) Rayleigh SAWs in a $Y - X + 15°$-cut potassium niobate crystal on its surface versus the vacuum gap d/λ between the perfectly conducting plane and the crystal surface; dots *3* and *4* refer to the fast and slow quasi-shear bulk waves.

the solution are possible. As can be seen in Fig. 2 (curve *1*), the first branch refers to the generalized Gulyaev–Bleustein wave when the surface is short-circuited, because the second component u_2 of the mechanical displacement in this wave is much greater than the first u_1 and third u_3 components. The second branch of the solution (curve *2*) refers to the generalized Rayleigh wave, in which the first u_1 and third u_3 components of the mechanical displacement are the greatest. Further analysis of the plots given in Fig. 2 shows that, as the distance d increases from 0 to λ, the generalized Gulyaev–Bleustein wave (curve *1*) smoothly transforms into the generalized Rayleigh wave. As for the second branch of the solution, which refers to the generalized Rayleigh wave (curve *2*), its

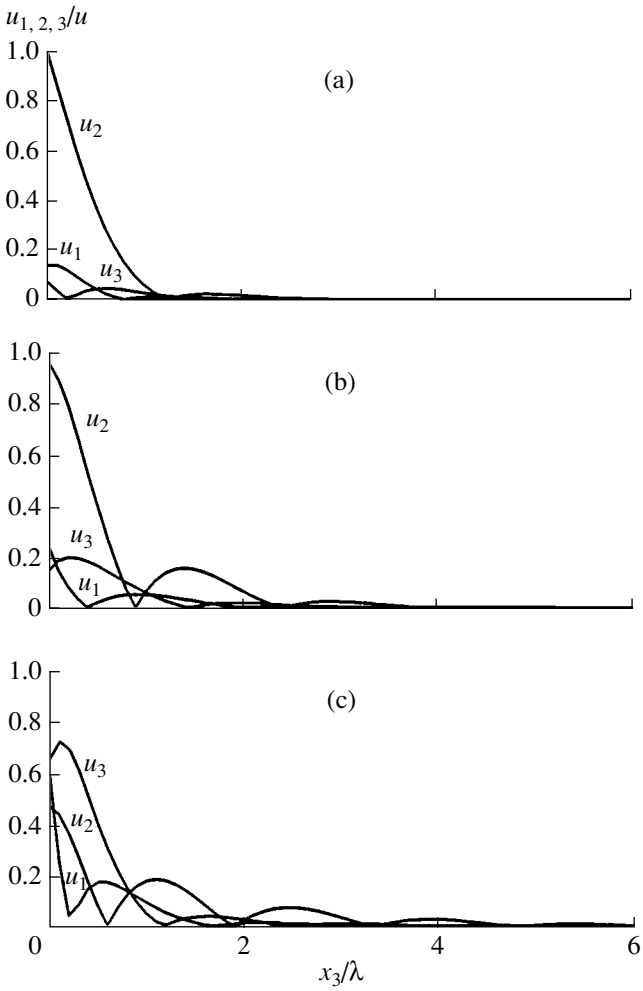

Fig. 3. Normalized mechanical particle displacement components u_1/u, u_2/u, and u_3/u of the generalized Gulyaev–Bleustein wave in a $Y - X + 15°$-cut potassium niobate crystal on its surface versus the depth x_3/λ of the crystal for different values of the vacuum gap between the perfectly conducting plane and the crystal surface: d/λ = (a) 10^{-8}, (b) 10^{-3}, and (c) 10^{-1}.

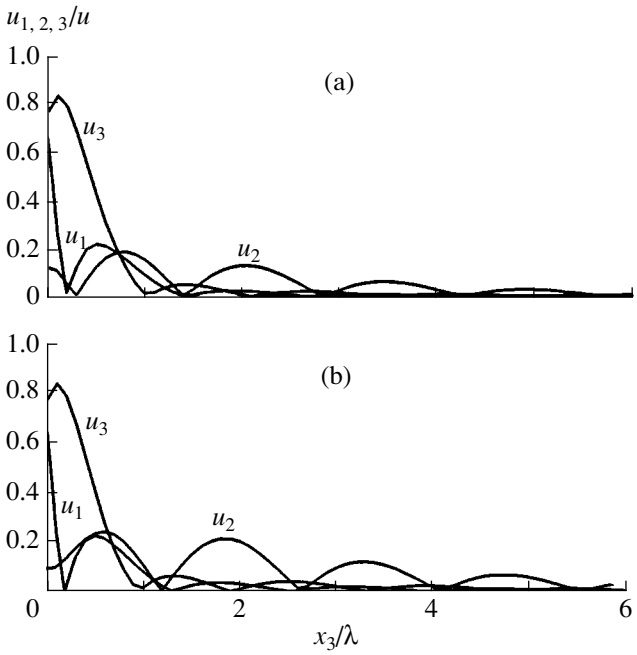

Fig. 4. Normalized mechanical particle displacement components u_1/u, u_2/u, and u_3/u of the generalized Rayleigh wave in a $Y - X + 15°$-cut potassium niobate crystal on its surface versus the depth x_3/λ of the crystal for different values of the vacuum gap between the perfectly conducting plane and the crystal surface: d/λ = (a) 10^{-8} and (b) 10^{-3}.

structure remains almost unchanged, but its damping constant grows with increasing distance d. At $d = 0.002\lambda$, this wave ceases to be a propagating wave and the second solution disappears. Figures 3 and 4 show the distributions of normalized mechanical displacement components throughout the thickness of the crystal at different gaps d for the first and second branches, respectively. Both waves are seen to be relatively strongly localized near the surface. However, on branch *1* (Fig. 3), when the gap is $d/\lambda \in [10^{-8}, 10^{-3}]$, the greatest component is u_2, which decreases with increasing d/λ and, at $d/\lambda = 10^{-2}$, the component u_3 becomes the greatest. This behavior also corroborates the above conclusion that the generalized Gulyaev–Bleustein wave smoothly transforms into the generalized Rayleigh wave. As for branch *2* (Fig. 4), the distribution of the displacement amplitude in depth remains almost unchanged over the entire range of the gap d. Figures 1 and 2 also show the velocities and normalized components of the mechanical displacement for the fast and slow quasi-shear waves propagating in the same direction.

Thus, potassium niobate has a crystallographic orientation, for which the motion of a perfectly conducting plane away from the crystal surface may lead to a smooth transformation of the generalized Gulyaev–Bleustein wave into the generalized Rayleigh wave.

2. CHARACTERISTICS OF SAWS IN A THIN CONDUCTING LAYER–PIEZOELECTRIC STRUCTURE

Now let us consider the other possibility of a smooth variation of electrical boundary conditions, namely, let us study the behavior of the velocity and mechanical displacement components of the surface Rayleigh and Gulyaev–Bleustein waves as a function of the conductance of an infinitely thin conducting layer applied to the surface of potassium niobate crystal. As in the previous case, we study the $X + 15°$ direction of propagation on an Y cut potassium niobate crystal. Figure 5 shows the phase velocity of SAWs versus the conductance of the thin conducting layer. The curve was obtained by numerically solving the boundary-value problem specified by standard elasticity and electrostat-

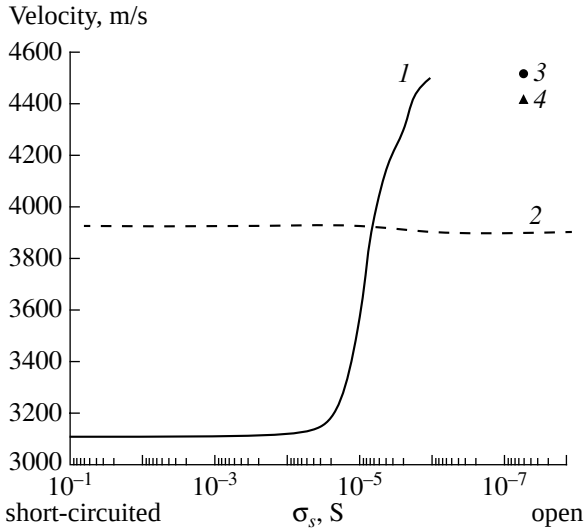

Fig. 5. Phase velocities of (*1*) generalized Gulyaev–Bleustein and (*2*) Rayleigh SAWs propagating in the direction $X + 15°$ of a *Y*-cut potassium niobate crystal versus the conductance of the thin layer on the crystal surface; dots *3* and *4* refer to the fast and slow quasi-shear bulk waves.

ics equations and standard mechanical and electrical boundary conditions, which are described in detail in [10]. Figure 6 shows the normalized components of the mechanical displacement of particles on the surface of the piezoelectric versus the conductance of the layer. It can be seen that, in this case, the solution also has two branches. An analysis of the results shows that, as in the previous case, for a short-circuited surface, the first branch refers to the Gulyaev–Bleustein wave, because $u_2/u > u_1/u$ and $u_2/u > u_3/u$ (Fig. 6). As the conductance decreases, the velocity and the damping constant of this wave increase up to $\sigma_s = 10^{-6}$ S when the wave ceases to be a propagating wave and, subsequently, the first branch of the solution disappears. Presumably, this branch, on the electrically open surface, transforms into a fast quasi-shear bulk wave ($V = 4531$ m/s) with the polarization (–0.133; 0.991; 0) (Figs. 5 and 6). As for the structure of the wave on the surface of the crystal, it remains almost unchanged (Fig. 6); i.e., the type of wave remains the same. Figure 7 shows the distribution of the normalized components of the mechanical particle displacement in the depth of the crystal for different surface conductivities. It can be seen that the second component u_2 of the mechanical displacement remains the greatest over the entire range of conductance variation. As for the penetration depth (δ) of the wave under study, it increases as the surface conductance decreases and reaches $\delta \approx 500\lambda$ at $\sigma_s = 10^{-6}$ S. This fact supports the assumption made above that this wave can be transformed into a fast quasi-shear bulk wave.

The second branch of the solution (curve *2* in Fig. 5) refers to the generalized Rayleigh wave, because the second component u_2 of the mechanical displacement

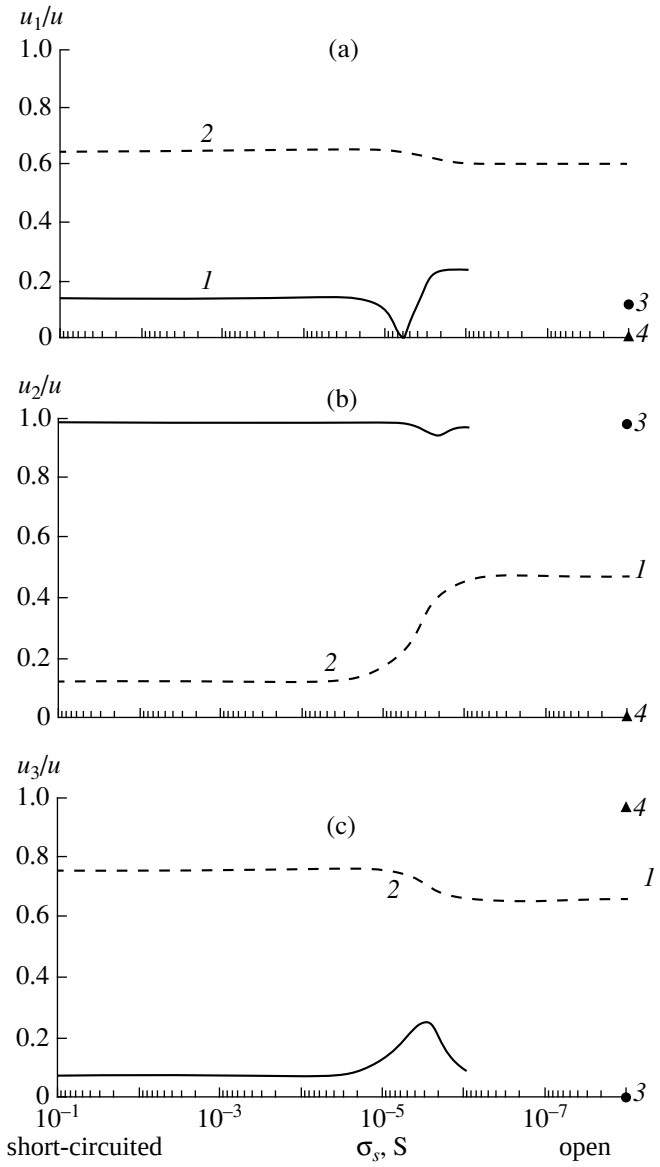

Fig. 6. Normalized mechanical particle displacement components (a) u_1/u, (b) u_2/u, and (c) u_3/u of the (*1*)generalized Gulyaev–Bleustein and (*2*) Rayleigh SAWs in a $Y - X + 15°$-cut potassium niobate crystal on its surface versus the conductance of the thin layer on the crystal surface; dots *3* and *4* refer to the fast and slow quasi-shear bulk waves.

in this case is the smallest, as shown in Fig. 6. As the conductance decreases, the structure of the wave remains almost unchanged. Figure 8 shows the distributions of normalized components of the mechanical particle displacement in the depth of the crystal for different surface conductivities. It can be seen that the wave is strongly localized and its third component of mechanical displacement, u_3, is always the greatest. The velocity of this wave increases with the conductance and, at high layer conductivities (electrically short-circuited surface), it proves to be higher than at a zero surface conductance (electrically open surface). In

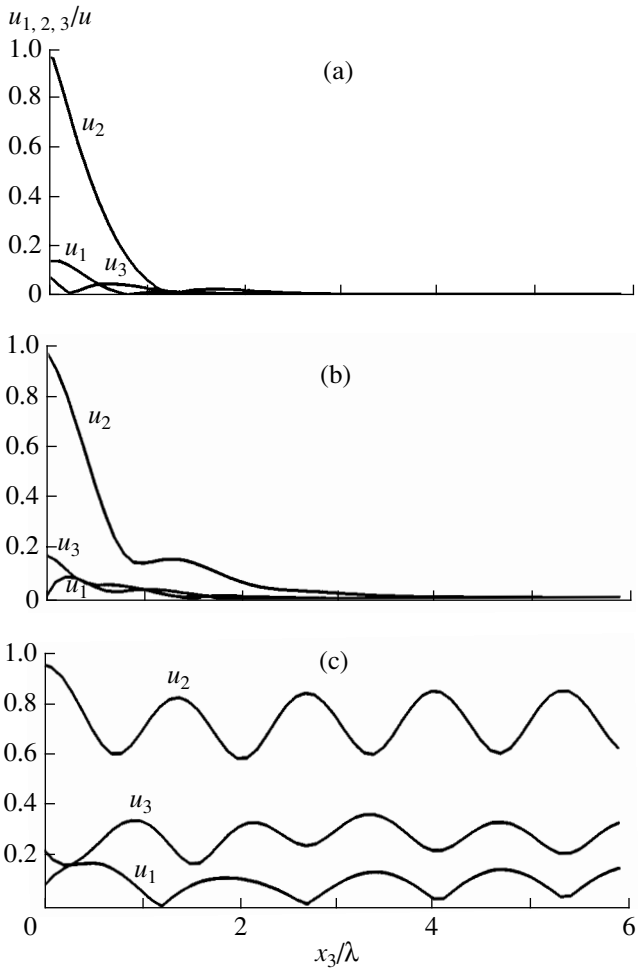

Fig. 7. Normalized mechanical particle displacement components u_1/u, u_2/u, and u_3/u of the generalized Gulyaev–Bleustein wave in a $Y-X+15°$-cut potassium niobate crystal versus the depth x_3/λ of the crystal for different values of surface conductance: σ_s = (a) 10^{-1}, (b) 5.8×10^{-6}, and (c) 10^{-6} S.

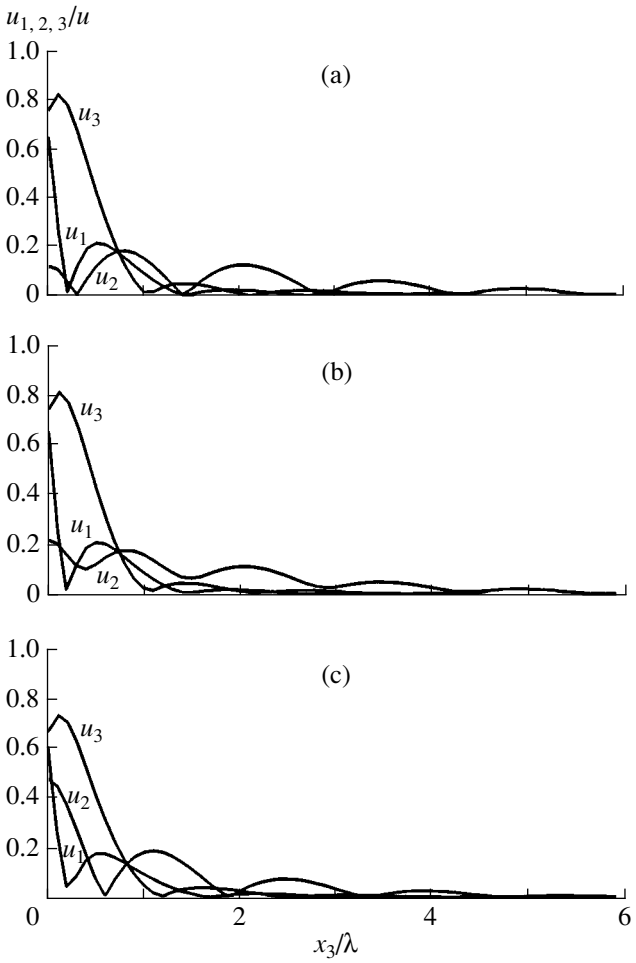

Fig. 8. Normalized mechanical particle displacement components u_1/u, u_2/u, and u_3/u of the generalized Rayleigh wave in a $Y-X+15°$-cut potassium niobate crystal versus the depth x_3/λ of the crystal for different values of surface conductance: σ_s = (a) 10^{-1}, (b) 5.8×10^{-6}, and (c) 10^{-8} S.

this case, the electromechanical coupling coefficient $K_2 = 2\Delta v/v$ becomes negative.

Figure 5 also shows that a situation is possible in which, at a certain conductance of the surface layer ($\sigma_s = 5.8 \times 10^{-6}$ S), two piezoactive waves propagate with the same phase velocity in the same direction. However, these waves differ in the degree of their localization and in the magnitude of their mechanical displacement components, both on the surface of the crystal and in its depth (Figs. 6, 7b, 8b). It should also be noted that the generalized Gulyaev–Bleustein wave features a noticeably higher attenuation than the generalized Rayleigh wave (Fig. 9). The smooth behavior of the characteristics of the waves under study versus the surface conductance in the region where the curves in Fig. 5 intersect rules out a wrong transition from one type of the solution to another. A comparison of Figs. 1 and 5 also shows that, when the perfectly conducting layer is moved toward the surface, the maximum velocity of the generalized Gulyaev–Bleustein wave is 3851 m/s; when the conductance of the surface layer is varied, the corresponding velocity value is 4500 m/s.

Thus, the study performed above leads us to a completely unexpected conclusion. It was found that a variation in the conductance of the layer applied to the piezoelectric surface can produce a result different from that obtained when a perfectly conducting plane is moved toward the surface, although the initial and terminal states of these actions (electrically open and electrically short-circuited surfaces) are fully identical. The analysis has shown that, unlike the case of moving a perfectly conducting plane away from the surface of the piezoelectric, the variation of the conductance of a thin layer applied to the surface does not lead to a transformation of the type of waves under study. In this case, a

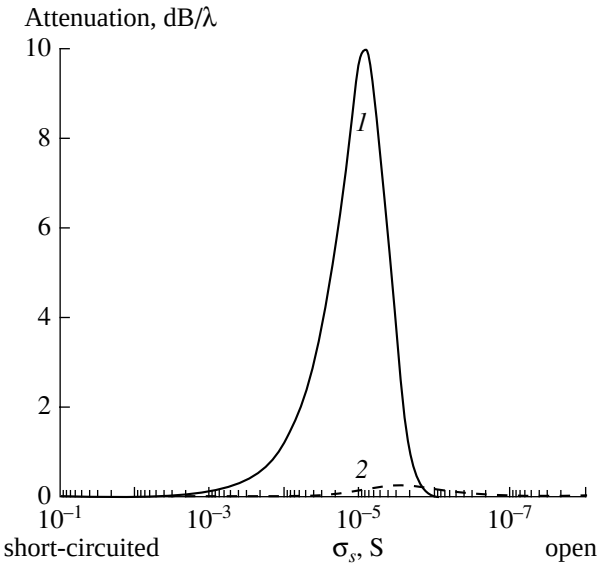

Fig. 9. Attenuation per wavelength for the (*1*) generalized Gulyaev–Bleustein and (*2*) Rayleigh SAWs propagating in the $X + 15°$ direction of an *Y*-cut potassium niobate crystal versus the conductance of the thin layer applied to the crystal surface.

situation is realized in which a metallization of the surface causes an increase in the velocity of surface acoustic waves.

CONCLUSIONS

A theoretical analysis of generalized surface acoustic waves propagating in a $Y - X + 15°$-cut potassium niobate crystal has shown that different methods of bringing a semi-infinite crystal from the state with an electrically short-circuited surface to the state with an electrically open surface may produce different results. If this transition is realized by moving a perfectly conducting plane away from the surface of the crystal, a transformation of the generalized Gulyaev–Bleustein wave into the generalized Rayleigh wave is possible. As a result, the velocity of the wave increases; i.e., the wave is characterized by a positive electromechanical coupling coefficient defined in terms of the relative velocity variation. Conversely, if the transition between the states is accomplished by varying the conductance of a thin layer applied to the piezoelectric surface, no transformation of the wave type is observed. However, the velocity of the generalized Rayleigh surface wave for the electrically short-circuited surface proves to be greater than that for the electrically open surface, and the electromechanical coupling coefficient defined in terms of the relative velocity variation looks as if it were negative.

Presumably, the reason why the above methods of changing the crystal state from an electrically short-circuited one to an electrically open state produce different results is as follows. When the conducting surface is moved away from the surface of the piezoelectric crystal, an external force must do work to increase the total energy of the surface wave and change its polarization. Conversely, when the conductance of the thin surface layer is varied, the external force seems to be absent and the polarization of the wave does not change.

ACKNOWLEDGMENTS

This work was supported by the Russian Foundation for Basic Research, project no. 01-02-16266a.

REFERENCES

1. A. J. Slobodnik, *Microwave Acoustic Handbook* (Microwave Phys. Lab., Bedford, 1973).
2. A. Wixforth, J. Scriba, M. Wassermeier, *et al.*, J. Appl. Phys. **64**, 2213 (1988).
3. V. G. Mozhaev and M. Weihnacht, Ultrasonics **37**, 687 (2000).
4. V. G. Mozhaev and M. Weihnacht, in *Proceedings of IEEE Ultrasonics Symposium* (IEEE, 1999), p. 73.
5. B. D. Zaitsev, I. E. Kuznetsova, and S. G. Joshi, J. Appl. Phys. **86**, 6868 (1999).
6. Sh. Kakio, H. Nakamura, Y. Kanmori, and Y. Nakagava, Jpn. J. Appl. Phys., Part 1 **38** (5B), 3261 (1999).
7. B. Zaitsev, I. Kuznetsova, and S. Joshi, Electron. Lett. **35** (14), 1205 (1999).
8. M. K. Balakirev and I. A. Gilinskiĭ, *Waves in Piezoelectric Crystals* (Nauka, Novosibirsk, 1982), pp. 96–100.
9. M. Zgonik, R. Schlesser, I. Biaggio, *et al.*, J. Appl. Phys. **74** (2), 1287 (1993).
10. I. E. Kuznetsova, S. G. Joshi, and B. D. Zaĭtsev, Akust. Zh. **47**, 336 (2001) [Acoust. Phys. **47**, 282 (2001)].

Translated by A. Khzmalyan

Acoustical Physics, Vol. 50, No. 4, 2004, pp. 394–400. Translated from Akusticheskiĭ Zhurnal, Vol. 50, No. 4, 2004, pp. 469–475.

Focused Antenna Array in a Strongly Inhomogeneous Medium

V. A. Zverev

Institute of Applied Physics, Russian Academy of Sciences, ul. Ul'yanova 46, Nizhni Novgorod, 603600 Russia
e-mail: zverev@hydro.appl.sci-nnov.ru

Received September 16, 2002

Abstract—A focused acoustic antenna array is considered in a strongly inhomogeneous stationary medium. An opportunity is indicated to determine the coordinates of a number of objects by active location. It is assumed that, in insonifying the objects by a wave with an arbitrary wave front, they scatter spherical waves and are sufficiently separated in distance and angle to be resolved by the same array in a homogeneous medium. The procedure of determining the coordinates of the objects involves a wave front inversion for distinguishing between the signals from different objects. The coordinates are determined by estimating the parameters for each individual object. The parameter estimation procedure is shown to provide a high efficiency of extracting the argument of a complex signal. The results of the numerical modeling and solution of the problem are presented. *© 2004 MAIK "Nauka/Interperiodica".*

A focused antenna array is especially efficient when its aperture is large and the number of receiving elements is great. However, such arrays are very sensitive to inhomogeneities of the medium. The inhomogeneities can be sufficiently smooth to cause no substantial energy loss due to multiple scattering but, at the same time, they can dramatically spoil the image produced by a focused array of large aperture. In [1], a method was proposed for eliminating the distortions caused by wave propagation through a thin layer with rather intense inhomogeneities. The layer thickness was assumed to be so small that the distortions were independent of the range and angle of the objects. The method can be also applied to a focused array. In [2], a problem was considered on acoustical imaging by an array positioned in a thick layer of inhomogeneous medium where the signals of objects with different coordinates underwent different distortions. However, this consideration was based on the assumption that all objects were in the far field of the array, and the specificity of a focusing array was neglected. The present paper considers an array placed in a thick layer of inhomogeneities, so that different distortions are obtained for different objects.

The imaging of objects by an array placed in a thick inhomogeneous layer is based on the concept that different objects can be distinguished from each other by the wave front inversion (WFI) [3]. In acoustics, the WFI procedure consists of two steps. In the first step, a single array element is used to transmit a pulse. This pulse passes through the inhomogeneous medium, reaches the objects, and undergoes scattering by them. It is assumed that the field scattered by each object is a spherical wave. These waves pass through the inhomogeneous medium again and arrive at the array. The second step consists of memorizing the signals that arrived at the array and then transmitting them in the form of signals that are complex conjugated, that is, time-inverted with respect to the received signals. As a result, waves with an inverted wave front are transmitted into the medium. Upon passing through the same medium again, the WFI waves compensate the newly accumulated distortions by the old ones and arrive at the objects in the form of spherical waves.

These waves are scattered by the objects again and arrive at the array through the inhomogeneous medium. The latter signal differs from the previous one in that a signal of doubled level arrives from each object because, upon scattering, the waves again acquire factors that are determined by the scattering strengths of the objects. This procedure constitutes the basis of detecting every individual scattered signal by the WFI method.

At first the strongest signal is extracted. The corresponding procedure is described in detail and experimentally illustrated in [3]. The procedure consists of multiply using WFI (iterations). At each iteration, the received signals acquire additional factors that are equal to the amplitudes of the corresponding scattered signals. As a result, in every consecutive iteration, the strongest signal becomes enhanced in comparison with the remaining signals. In this way, one can select a single signal by performing a required number of iterations. This signal is memorized for its subsequent processing to determine its parameters.

In [2], a WFI method for eliminating the strongest signal and, by multiple iterations, selecting the signal next in intensity is described and numerically illustrated. The method also allows one to estimate the level

1063-7710/04/5004-0394$26.00 © 2004 MAIK "Nauka/Interperiodica"

of the eliminated signal. Now, the WFI procedure is performed with the difference between signals of two iterations: first, the initial iteration multiplied by the amplitude of the signal to be eliminated and, second, the subsequent iteration in which the signal to be eliminated predominates. The value of the multiplying factor that determines the amplitude of the signal to be eliminated is chosen to minimize the level of the difference signal averaged over the array, because this level strongly depends on the extent to which the strongest signal is suppressed. Now, the second-in-intensity signal becomes the strongest one. After a number of iterations, this signal proves to be governing, and it is memorized for subsequent processing. The procedure can be repeated until all the signals are detected whose parameters have to be estimated.

One can find a more detailed description of the signal separation process in [2]. Here we do not consider this process, because it is the same for both ordinary and focused antenna arrays. To obtain true amplitudes of all signals in the case at hand, a number of additional iterations are required, as compared to the case considered in [2].

Let us consider the procedure for estimating the parameters [4, 5] of already detected signals produced by individual objects. Numerical modeling is advantageous to illustrate the processing technique.

Let a linear array have 256 receiving and transmitting elements spaced at 0.5λ (λ is the wavelength). Let us suppose that pulses with a monochromatic carrier are transmitted, many periods of the carrier fitting within the pulse duration. Such signals can be treated as monochromatic ones. Let the objects meet the conditions for the WFI method to be successful. These objects scatter regular spherical waves when they are excited by an arbitrary wave field. The distances separating the objects are supposed to be sufficient to reliably distinguish between them in a medium without inhomogeneities. Let us specify the positions of the objects and the corresponding amplitudes of the scattered waves according to Table 1.

In Table 1, n is the ordinal number of the object, W_n is the amplitude of the scattered signal (in arbitrary units), and U_n is the spatial frequency of the object position (in units of quantization). The spatial frequency (in the quantization units) is related to the angle θ_n at which the object is seen from the array (the angle between the direction to the object from the array center and the normal to the array aperture at the array center) according to the formula [6]

$$\arcsin(\theta_n) = \frac{\lambda}{L}U_n, \tag{1}$$

where L is the length of the array. The distances to the objects are presented in the R_n row of the table (in units of L). The lower row shows the parameter that determines the wave front curvature for the wave scattered by the object. This parameter is expressed as values y_n that are the numbers of a set of functions describing the phase front of a spherical wave (see below).

Table 1

n	1	2	3
W_n	6	2	0.5
U_n	12	38	57
R_n	6.15L	8.9L	16L
y_n	24	16	8

Note that, in the case of a strongly inhomogeneous medium, one cannot use the ordinary technique [6, 7] for processing the signals of a focused array to obtain the parameters of the signals received. Figure 1 shows the result of such a processing of a signal separated from other ones by WFI in the absence and presence of inhomogeneities of the medium. The ordinary processing procedure is based on the concept that the waves received by the array have spherical wave fronts. Hence, the ordinary processing of the signals received by a focused array is performed in two steps. In the first step, the sphericity of the wave front is eliminated; in the second step, the spatial frequency of the resulting harmonic signal is determined as a function of the coordinate (ordinal number) of a receiving element of the array. (Such a procedure is completely described in [7].) However, in our case, the wave front produced by each object has a complicated unpredictable shape because of the influence of the inhomogeneities. Therefore, the ordinary processing of the signals of a focused array cannot serve to obtain the array field of view similar to that in a homogeneous medium. Figure 1 illustrates this fact. Hence, other ways of signal processing should be found for focused antenna arrays.

For this purpose, let us consider the structure of the signals received by a focused array in an inhomogeneous medium. Such signals, as functions of spatial coordinate x, have the form

$$Af(x) = \sum_n A_n(x)\exp(iF_n(x)). \tag{2}$$

Here, $A_n(x)$ represents the signals received by the array in a homogeneous medium and $F_n(x)$ represents the phase changes introduced by the medium into the signals. These changes are assumed to be much greater than π.

Suppose that the signal sources are in the near field of the array, so that, for a homogeneous medium, the signals at the array can be represented as spherical waves [6]:

$$A_n(x) = W_n\exp\left(i\frac{2\pi}{L}xU_n + S_n(x)\right). \tag{3}$$

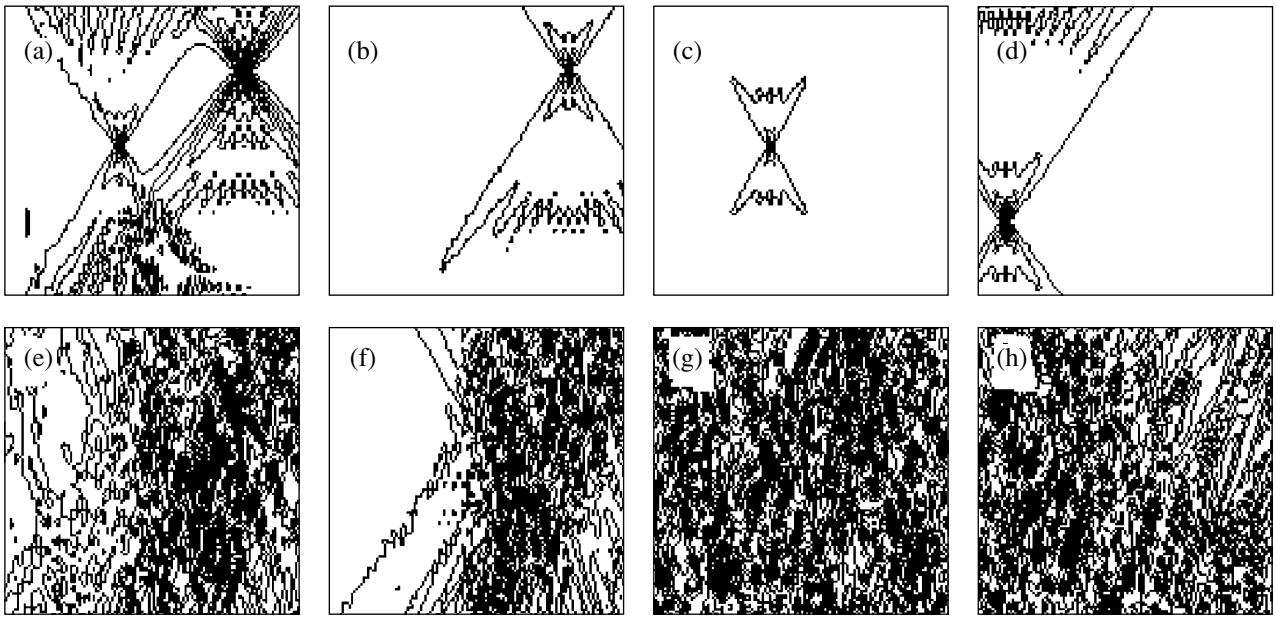

Fig. 1. Field of view of a focused array in range (vertical) versus angle (horizontal) coordinates. The upper (a–d) and lower (e–h) rows of data correspond to the homogeneous and inhomogeneous media, respectively. The whole signal is shown in plots (a) and (e). The remaining plots show the signals reflected by individual objects and separated by the WFI procedure: (b, f) the first, (c, g) second, and (d, h) third signals.

Here, W_n is the wave amplitude; U_n is the spatial frequency; and $S_n(x)$ is a function taking into account the sphericity of the wave front:

$$S_n(x) = \frac{2\pi}{\lambda}\sqrt{(x-0.5L)^2 + R_n^2} - R_n, \qquad (4)$$

where R_n is the distance to the nth object.

To determine the value of R_n both with the ordinary processing of the focused-array signal (like in a homogeneous medium) and with the parameter estimation procedure, one should exhaust the set of functions that describe the shape of the phase front of the spherical wave. The set of admissible distances R is related to a set of integers y starting from zero [7–9]:

$$R(y) = \frac{(0.5L)^2 - (0.4 + 0.2y)^2}{2(0.4 + 0.2y)}. \qquad (5)$$

This way of forming the set of distances results in a uniform distribution of the ranges selected by the array from set (5).

According to Eq. (2), each selected signal is described by the function

$$Q_n(x) = W_n \exp\left(i\frac{2\pi}{L}xU_n + iS_n(x) + iF_n(x)\right). \qquad (6)$$

The main idea of constructing the system for estimating the parameters of objects consists in extracting the argument of function (6). Such a technique was used in our earlier studies [8, 9]. The technique underlies the method of separating multiplicatively related signal spectra [11], i.e., the method of a complex cepstrum. In [11] it is shown that the role of extracting the arguments of complex signals is not restricted to selecting the spectra of the arguments obtained or the logarithms of the complex signals. This procedure offers another opportunity, which has so far remained unnoticed: the opportunity to efficiently estimate the parameters of the signal. It is important that the estimation can be also performed if the spectra of logarithms of the signals cannot be separated.

The arguments of all detected signals $Q_n(x)$, as calculated according to [10], are shown in Fig. 2. The following features can be noticed in this figure: a general slope that increases as the spatial frequency of the signal increases, a bend of the wave front (Fig. 2a), and signal distortions that are governed by the quantity $F_n(x)$.

From the argument of function (6), one should estimate the angular position of the source and the distance from the source to the array. This problem can be solved in two steps: first, the angular positions of the sources are determined, and, second, the distances are estimated. First of all, let us estimate the angular position of the source, because such an estimate allows one to compensate for the slope of the argument of function (6), this slope masking the curvature of the wave front. To do so, we multiply Eq. (6) by a factor of the form

$$M(x, H) = \overline{\exp\left(i\frac{2\pi}{L}xH\right)}, \qquad (7)$$

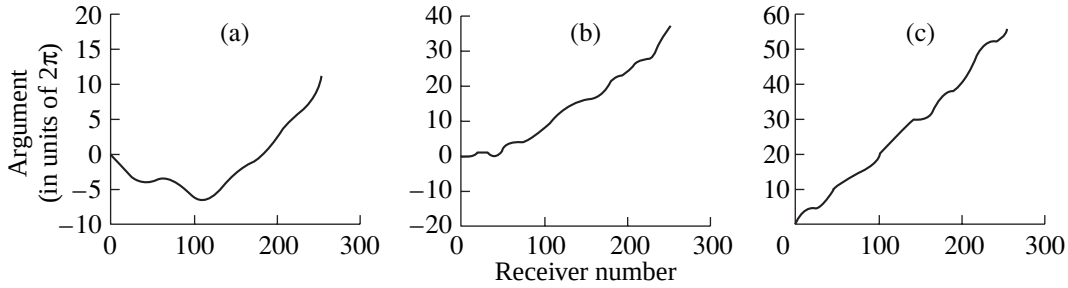

Fig. 2. Argument of function (6) versus the number of receiving element: n = (a) 1, (b) 2, and (c) 3.

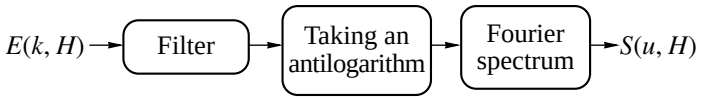

Fig. 3. Flowchart of transformation of argument (8) for using filtration to estimate the angular position of the signal.

where the overbar denotes complex conjugation and H is the parameter whose value is varied. For each nth signal, the product of quantities (6) and (7) can be expressed as

$$E_n(x, H) = \frac{2\pi}{L}x(U_n - H) + S_n(x) + F_n(x). \quad (8)$$

Equation (8) shows that the slope is minimal at $H = U_n$. To confirm this statement, one can consider the standard deviation of quantity (8):

$$\sigma_n(H) = \sqrt{\left(\sum_x E_n(x, H)^2 - \left(\sum_x E_n(x, H)\right)^2\right)}. \quad (9)$$

The minimum of deviation (9) is reached at the value of H that can serve as the estimate of U_n. In the numerical experiment carried out, this estimate for $n = 1$ differs by unity from U_1 presented in Table 1; for other values of n, the estimate coincides with the value presented in Table 1. The difference can be greater or smaller, depending on the specific shape and level of the noise realization used in modeling the inhomogeneous medium. One can attain better accuracy by introducing a filtration of random noise into the estimation procedure. Figure 3 shows the flowchart of this kind of signal processing. The filter shown rejects the lower frequencies, at which the noise occurs in argument (8).

Thus, one parameter of the signal is estimated. Then, by multiplying Eq. (6) by Eq. (7) with the substitution of $H = U_n$, we obtain the basis for determining the second parameter: the curvature of the wave front at the array. Equation (6) is then reduced to

$$AF_n(x) = W_n \exp(iS_n(x) + iF_n(x)). \quad (10)$$

The argument of function (10), as a function of the array receiver's number, is a sum (additive mixture) of the regular wave field $S_n(x)$, which has the form of Eq. (4), and random noise. It would be advantageous to subtract the noise from this mixture. Unfortunately, one cannot perform such a subtraction, because the form of noise is unknown. However, we know the admissible form of the regular signal. Let us give such a form to the regular signal that is depends on a single numerical parameter. To do so, let us use the set of distances (5) that depends on parameter y. In view of the above considerations and Eq. (4), the regular signal can be expressed as

$$RS_n(x, y_n) = \frac{2\pi}{\lambda}(\sqrt{(x - 0.5\lambda)^2 + R(y_n)^2} - R(y_n)), \quad (11)$$

where $R(y_n)$ is defined for a set of integer numbers y_n according to Eq. (5). The set of regular functions (11) is composed in view of the ability of the array to distinguish between the waves that have different curvatures of the wave front. The waves that can be resolved in their front curvatures over the array aperture have numbers y differing by more than one [7]. This fact means that, among all admissible functions (4) within the ranges at hand, a single function can be found that coincides with one of functions (11) to the accuracy of the array. If one subtracts the regular signal with y_n close to the true value from the argument of Eq. (10), only noise will remain in this argument. The noise is independent of what exactly is subtracted from the argument, and, hence, the trial method can be used to arrive at the situation when pure noise remains in the argument of Eq. (10). In this case, the mean square of the argument must be minimum. This can be done by considering the following function:

$$PS_n(x, y_n) = E(x, U_n) - RS(x, y_n) + RS(0, y_n). \quad (12)$$

In Eq. (12), function $E(x, U_n)$ is defined by Eq. (8). The last term of Eq. (12) accounts for the initial phase.

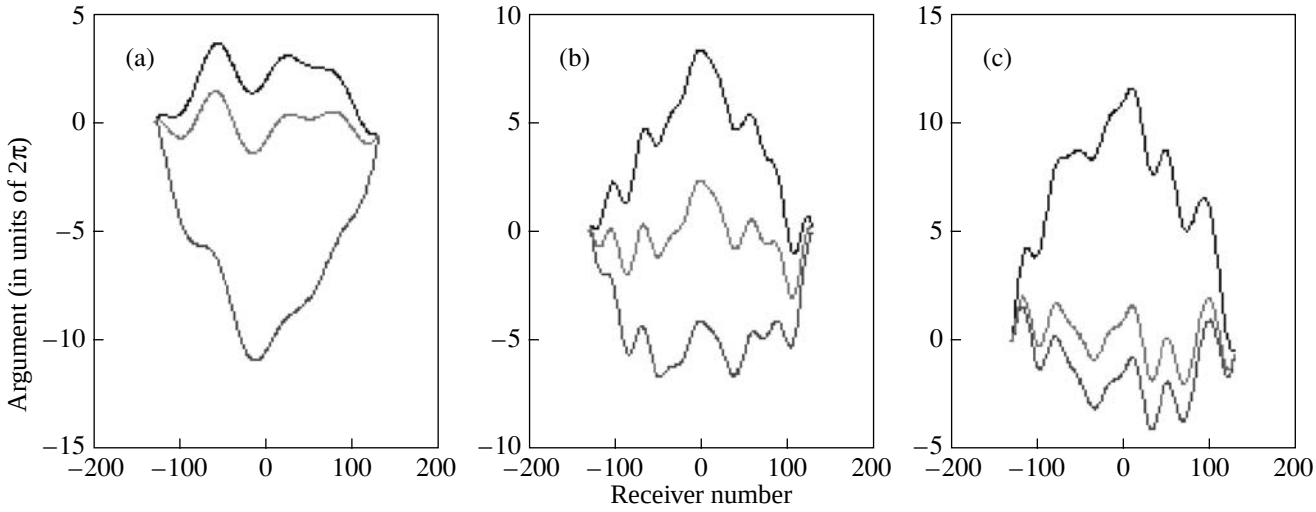

Fig. 4. Function (12) versus parameter *y*. The limiting values of the parameter correspond to the upper and lower parts of the plots. The center of the plots corresponds to the parameter value at which the least mean square of function (12) is obtained; i.e., only noise remains in the signal. The plots refer to n = (a) 1, (b) 2, and (c) 3.

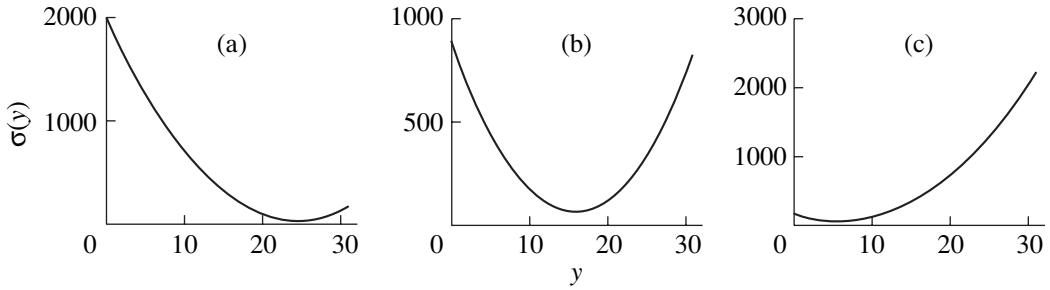

Fig. 5. Mean square of function (12) versus the parameter *y* for n = (a) 1, (b) 2, and (c) 3.

Figure 4 presents function (12) for all three desired signals, with three values of parameter y_n in each case. The figure shows how the fraction of the regular summand in Eq. (12) varies when functions from the set depending on parameter y_n are added. To estimate the parameter, let us use Eq. (12) to construct the expression for the standard deviation (as in Eq. (10)) and then find the minimum of this expression as a function of y_n. Such a dependence is shown in Fig. 5.

The results of signal processing are graphically represented in Fig. 6. The fluctuations of the arguments are shown for each signal. These fluctuations are caused by the inhomogeneities of the medium that influence the process of wave propagation. The fluctuations are found by subtracting the values of functions (11) from the arguments of function (10). The dotted curves show the true values of the same functions that were specified in the modeling. In the regions where the dotted curves cannot be seen, they fully coincide with the solid curves. The same figure also shows the array fields of view, which are determined as a result of dividing Eq. (6) by the exponential of the fluctuations found. Using such plots, one cannot refine the signal parameters, namely, the angle and distance. As these parameters change, the pattern of the array field of view is shifted as a whole, without deformations. The patterns do not change if one substitutes the true arguments shown by the dotted curves in Fig. 6 for the values found. Nevertheless, the patterns of the array field of view are quite different in Figs. 6 and 1. The latter fact indicates that some inaccuracy exists in our signal processing.

The source of the inaccuracy is known. If one divides Eq. (6) by the noise defined as an exponential function rather than by the exponential of the true value of the argument, the field of view of the focused array will have the same pattern as the one shown in Fig. 1 for the homogeneous medium. In so doing, one excludes the procedure of determining the argument without phase jumps and precisely this procedure causes the inaccuracy. For the processing to yield the same patterns as in Fig. 1 (without inhomogeneities), one should improve the procedure of extracting the argument without π-periodic phase jumps. The source of errors in this method, along with the ways to improve the accuracy, are considered in [10]: one should increase the fre-

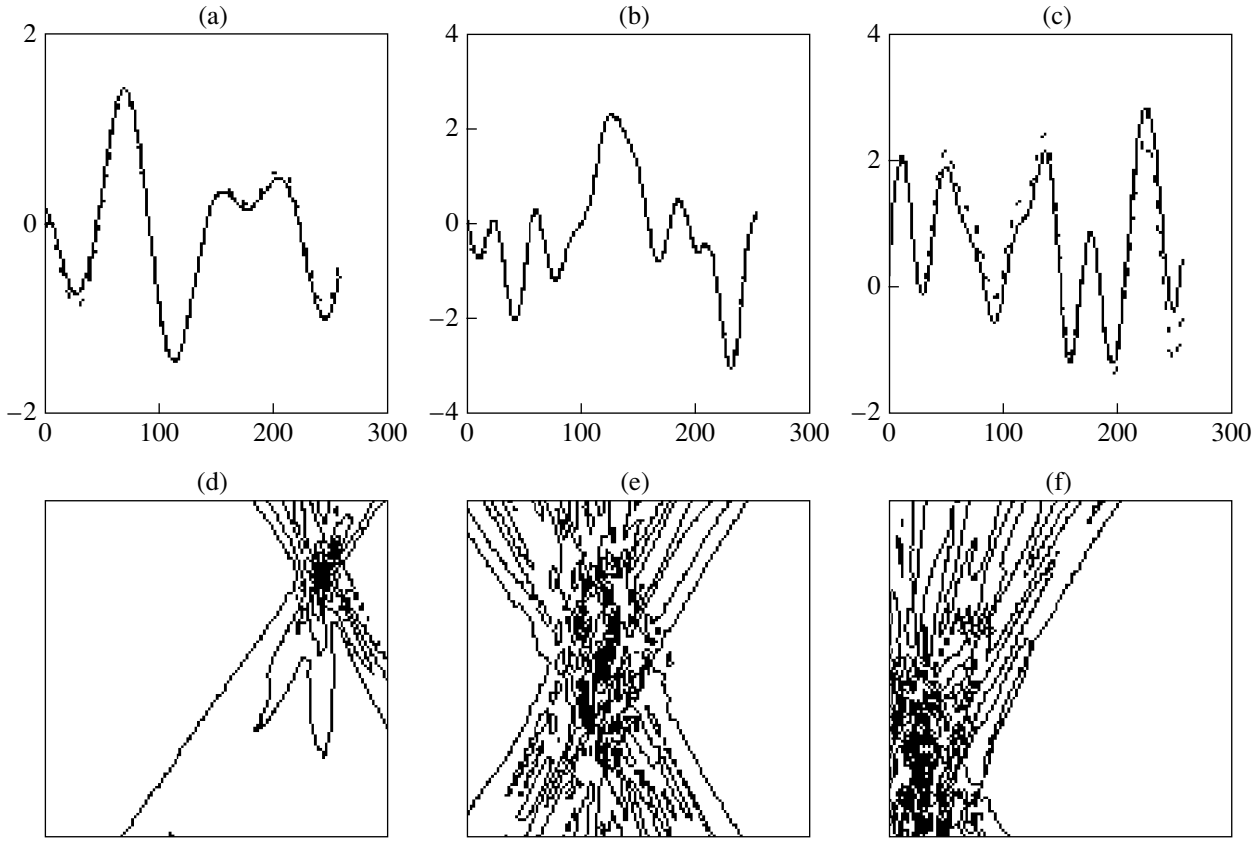

Fig. 6. The upper (a–c) row of data shows the argument of noise (in units of 2π) as a function of the receiver number. The solid curve is the result of extracting the noise from the argument of function (10). The dotted curve is the true value of this noise. The lower (d–f) row of data shows the field of view of the focused array, in range (vertical) versus angle (horizontal) coordinates, in the inhomogeneous medium after eliminating noise from signal (6): (a, d) the first, (b, e) second, and (c, f) third signals.

quency of quantization. In the case of the focused array, these recommendations mean an increase in the number of receiving elements of the array. Figure 6 confirms the validity of this recommendation: the signal (Fig. 6d) of the lowest frequency has the best shape, and the high-frequency signal (Fig. 6f) is the worst. The point is that the accuracy is influenced by the ratio of the quantization frequency to the full width of the signal spectrum [10] rather than by the quantization frequency itself. This ratio takes the highest value for the lowest-frequency signal.

The parameters of the objects determined by the WFI procedure of separating individual signals are summarized in Table 2.

Table 2

n	1	2	3
W_n	6	2	0.5
U_n	12	38	57
R_n	6.15L	8.9L	20L
y_n	24	16	6

The values shown in Tables 1 and 2 nearly coincide in spite of the strong inhomogeneities that cause random object-independent distortions of the phases of signals received by the array (the value of the distortions is much greater than π). The only difference occurs in determining the curvature of the wave front (range) for the farthest (third) signal.

The method proposed allows one to determine the parameters of the objects in a thick layer of a medium with strong large-scale inhomogeneities to a high accuracy. The consideration presented above also shows the efficiency of the procedure consisting in taking a complex logarithm of multiplicatively related signals to estimate their parameters. The technique allows one to distinguish between multiplicatively related signals with overlapping spectra of their logarithms. The signals can be separated on the basis of using the structure of one of them. One of the signals should be defined by a certain parameter.

ACKNOWLEDGMENTS

This work was supported by the Russian Foundation for Basic Research, project nos. 00-15-96741 and 02-02-17056.

REFERENCES

1. V. A. Zverev, Akust. Zh. (in press).
2. V. A. Zverev, Akust. Zh. (in press).
3. M. Fink, D. Cassereau, A. Derode, *et al.*, Rep. Prog. Phys. **63**, 1933 (2000).
4. Y. Bard, *Nonlinear Parameter Estimation* (Academic, New York, 1974; Mir, Moscow, 1979).
5. V. A. Zverev, Akust. Zh. **46**, 796 (2000) [Acoust. Phys. **46**, 676 (2000)].
6. V. A. Zverev, *Physical Fundamentals of Image Formation by Wave Fields* (Inst. Prikl. Fiz., Ross. Akad. Nauk, Nizhni Novgorod, 1998).
7. V. A. Zverev, A. L. Matveev, M. M. Slavinskiĭ, and A. A. Stromkov, Akust. Zh. **43**, 501 (1997) [Acoust. Phys. **43**, 429 (1997)].
8. V. A. Zverev and A. A. Pavlenko, Akust. Zh. **47**, 355 (2001) [Acoust. Phys. **47**, 297 (2001)].
9. V. A. Zverev and A. A. Stromkov, *Selection of Signals from Noise by Numerical Methods* (Inst. Prikl. Fiz., Ross. Akad. Nauk, Nizhni Novgorod, 2001).
10. V. A. Zverev and A. A. Pavlenko, Izv. Vyssh. Uchebn. Zaved., Radiofiz. **43**, 652 (2000).
11. A. V. Oppenheim, R. W. Schafer, and T. G. Stockham, IEEE Trans. Audio Electroacoust. **16** (3), 437 (1968).

Translated by E. Kopyl

Acoustical Physics, Vol. 50, No. 4, 2004, pp. 401–405. Translated from Akusticheskiĭ Zhurnal, Vol. 50, No. 4, 2004, pp. 476–480.

Measurement of the Moments of the Relaxation Time Spectrum of a Liquid by Pulsed Acoustic Spectroscopy

P. V. Zozulya and O. M. Zozulya

Andreev Acoustics Institute, Russian Academy of Sciences, ul. Shvernika 4, Moscow, 117036 Russia

e-mail: zozulya@mail.ru

Received December 29, 2001

Abstract—On the basis of theoretical results describing the propagation of short acoustic pulses in relaxation media, the temporal characteristics of a signal that carry the information on the first five moments of the relaxation time spectrum (RTS) are determined. The measurement of these characteristics forms the basis of the proposed variant of pulsed acoustic spectroscopy of relaxation media. An experimental setup was developed in which short acoustic pulses were excited by a neodymium glass laser. Test measurements of RTS moments for an acetic acid, the liquid with a single relaxation time, are carried out. © *2004 MAIK "Nauka/Interperiodica".*

Traditionally, acoustic spectroscopy of relaxation media was based on the determination of the phase velocity and attenuation coefficient as functions of frequency for harmonic signals. These data make it possible to determine the dispersion jump and the mean relaxation time in a medium. Theoretical foundations of pulsed spectroscopy were recently formulated in [1], where relaxation properties of a medium were determined from the evolution of the shape of a short pulse during its propagation. The consideration of the change in the pulse shape makes spectroscopy more informative: it becomes possible to characterize the relaxation properties of a medium in more detail by determining not only the first but also other moments of the relaxation time spectrum (RTS) of the medium.

The change in the shape of a short signal in a medium with an arbitrary RTS is determined in [1] from the low-frequency and high-frequency asymptotics of the fundamental solution describing the propagation of a δ-pulse. Generally, the RTS $g(\tau)$ is determined as a weighting function in the dispersion relation for a relaxation medium:

$$k(\omega) = \frac{\omega}{c_\infty}\left(1 + \frac{\Delta}{\langle\tau\rangle}\int\frac{\tau g(\tau)}{1 - i\omega\tau}d\tau\right),$$

where $\langle\tau\rangle$ is the mean relaxation time in the medium and $\Delta = (c_\infty - c_0)/c_\infty$ is the dispersion jump of the phase velocity. The high-frequency asymptotics of the fundamental solution have the form

$$G(t, x) = \left[\delta(t') + \beta\langle\tau^{-1}\rangle\theta(t') - \left(\beta\langle\tau^{-2}\rangle - \frac{1}{2}\beta^2\langle\tau^{-1}\rangle^2\right)t'\theta(t') + \ldots\right]\exp(-\beta), \quad (1)$$

where $t' = t - x/c_\infty$, $\beta = \alpha_\infty x$, $\alpha_\infty = \Delta/c_\infty\langle\tau\rangle$, and $\langle\tau^n\rangle$ is the moment of the RTS function of the nth order. The low-frequency asymptotics satisfy the condition $\beta \gg 1$ and have the form

$$G(t, x) = \frac{1}{2\sqrt{\pi\beta\langle\tau^2\rangle}}\left(1 - \beta\langle\tau^3\rangle\frac{d^3}{dt^3}\right)\exp\left(-\frac{(t - x/c_0)^2}{4\beta\langle\tau^2\rangle}\right). \quad (2)$$

Thus, as a short forerunning pulse propagates in a relaxation medium, a relaxation tail is formed behind it, which then transforms into a long pulse of Gaussian form, the body of the signal (Fig. 1). If the duration of the forerunner is short compared to the minimal relaxation time, it propagates without changing its shape with a velocity c_∞. This pulse undergoes exponential attenuation with distance with an attenuation coefficient α_∞. The body of pulse propagates with a velocity c_0 and, at a distances of $\alpha_\infty x \gg 1$, its evolution is similar to the evolution of a signal in a conventional viscous medium; i.e., its amplitude decreases and its duration

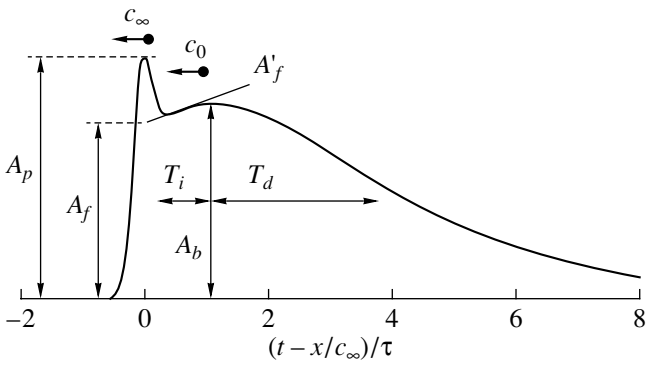

Fig. 1. Characteristics of the signal in a relaxation medium.

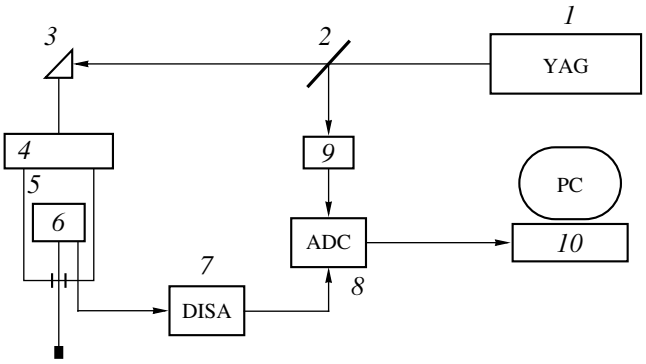

Fig. 2. Flow chart of the experimental setup for investigating the relaxation properties of liquids.

grows as a root of the distance traveled. From these results it follows that:

(i) by measuring the time of arrival of the forerunner and the body of the signal (by their maxima), it is possible to determine the velocities c_∞ and c_0 and the dispersion Δ;

(ii) by measuring the forerunner amplitude at two distances, it is possible to determine the attenuation coefficient α_∞ and, hence, the mean relaxation time $\langle\tau\rangle$;

(iii) by measuring such characteristics of the body of the signal as the amplitude A_b, the jump A_f at its front, the front derivative A'_f, the duration T_b, and the asymmetry ξ, it is possible to determine four more moments of the RTS from the expressions

$$\begin{aligned} T_b &= 2\sqrt{\beta\langle\tau^2\rangle}, \\ \xi &= \frac{(T_d - T_i)}{T_b} = \frac{3}{2}\frac{\langle\tau^3\rangle}{(\sqrt{\beta\langle\tau^2\rangle})^3}, \\ \frac{A_f}{A_b(T_b)} &= \sqrt{\pi}\beta\langle\tau^{-1}\rangle\exp(-\beta), \\ \frac{A'_f}{A_f} &= \frac{1}{2}\beta\langle\tau^{-1}\rangle - \frac{\langle\tau^{-2}\rangle}{\langle\tau^{-1}\rangle}, \end{aligned} \tag{3}$$

where T_i and T_d are the rise and fall times, respectively, and $T_i + T_d = 2T_b$. All five moments of the RTS, $\langle\tau^n\rangle$, where $n = -2\ldots3$, are determined from the signal parameters in the time domain. If the forerunner has a finite duration, a more precise determination of $\langle\tau\rangle$ can be achieved using the spectral approach, in which α_∞ is computed from the frequency spectra of the signal at two distances (compare with statement (ii)).

The solution given by Eqs. (1), (2) is obtained for a one-dimensional case disregarding the diffraction. In fact, the signal is recorded at distances satisfying the condition $c_0 T_b x/a^2 > 1$, where a is the initial radius of the sound beam, i.e., beyond the projection zone for the pulse body. If we assume that the transverse distribution of the field in the sound beam is Gaussian and the signal is recorded at the beam axis, we can eliminate from the signal the influence of diffraction by using the transformation

$$p_d(t', x) = p(t') - 2\frac{c_\infty x}{a^2}\int_{-\infty}^{t'} p(t)dt. \tag{4}$$

A flow chart of the experimental setup for studying relaxation properties of liquids is shown in Fig. 2. A short acoustic pulse is excited in liquid by a mercury photoacoustic generator *4* consisting of two parallel-aligned glass plates, the space between which is filled with mercury. The thickness of the plates and the size of the gap between them are chosen to avoid distortion by multiple reflection in recording the signal in a time window of 0–4 μs. The signal is excited through the absorption of the radiation of a YAG:Nd^{3+} laser 1 in mercury, the duration and energy of the laser pulse being 30 ns and 30 mJ, respectively. The energy of the laser pulse is monitored by a photodiode gauge *9*. To reduce the diffraction divergence of the sound beam, the diameter of the laser beam is increased by a telescope. For smoothing out the nonuniformity of the laser radiation, the mercury generator is covered with a light-scattering plate. The intensity distribution behind the light-scattering plate is measured by scanning the beam with an 8-digit photodiode gauge with a sensitive element 1×1 mm in size. The measurements show that the distribution of radiation approaches the Gaussian distribution and that the beam diameter is 11 mm. With these parameters of laser radiation, the amplitude of the acoustic pulse at the output of the mercury generator did not exceed 3 atm and its duration was 35 ns. The vessel for the liquid studied is a tube (*5*), in which a piston (*6*) with a built-in diaphragm pressure gauge and a

Table 1. Characteristics of the signal in acetic acid according to the waveforms shown in Fig. 3

Distance, mm	t_p, μs	t_b, μs	T_i, ns	T_d, ns	ξ	A_f/A_b	A_f/A_f, 10^6 s^{-1}
33.3	30.609	30.880	434	578	0.286	0.68	3.3
42.4	38.902	39.327	479	694	0.365	0.40	6.4

Table 2. Moments of the RTS for acetic acid: results of measurements at a temperature of 35°C

Distance, mm	$\langle\tau^2\rangle^{1/2}$, ns	$\langle\tau^3\rangle^{1/3}$, ns	$\langle\tau^{-1}\rangle^{-1}$, ns	$\langle\tau^{-2}\rangle^{-1/2}$, ns	
33.3	136 ± 7	97	132 ± 9	113	137
42.4	137 ± 7	110	124 ± 9	102	128

preamplifier can freely move. At the top, the tube is closed by the mercury photoacoustic generator (*4*). By moving the piston, it is possible to detect the signal at distances within 2–10 cm with an accuracy of 0.2 mm in gauge positioning. The strong dependence of the RTS on temperature ($\langle\tau\rangle \sim \exp(W/kT)$, where W is the activation energy of the relaxation transition) requires a thermostating of the liquid under investigation and an accurate measurement of its temperature. The temperature of the liquid is monitored to within 0.1°C with a mercury thermometer built into the tube *5*. The sensor of the pressure gauge is a piece of a PVDF film 9 μm thick and 2×2 mm in area. To provide the acoustic matching, the PVDF film is loaded with a glycerin layer, whose impedance is close to the impedance of polyvinylidene fluoride. The signal from the gauge is fed to a wide-band amplifier (*7*) and then to an A/D converter (*8*) to save the signal in the memory of a computer (*10*). The sampling frequency is 200 MHz, and the word length is 8 bit. The data processing channel, including the gauge, the amplifier, and the A/D converter, provides an undistorted measurement of the signal in the range of 0.05–100 MHz (by the 3-dB level) with the flatness of the frequency response within 0.35 dB.

In this paper, we present the results of the test measurements aimed at determining the accuracy of measurement of the RTS moments and revealing the shortcomings of both the method and the experimental setup realizing it. The testing was carried out with a simple liquid whose relaxation properties are well understood: concentrated acetic acid. This liquid is characterized by a single relaxation time τ_0 corresponding to the monomer–dimer molecular transition. The RTS and its moments have a simple form: $g(\tau) = \delta(\tau - \tau_0)$ and $\langle\tau^n\rangle = \tau_0^n$. In addition, for a medium with a single relaxation time, the exact expression for the fundamental solution is known:

$$G_0(x, t) = \left[\delta(t') + \theta(t')\sqrt{\frac{\beta}{t'\tau_0}} I_1(2\sqrt{\beta t'/\tau_0})\right]\exp(-\beta), \quad (5)$$

where $I_1(t)$ is the Bessel function of an imaginary argument. This relation makes it possible to determine at what distances asymptotic representation (1), (2) adequately describes the evolution of the pulse shape. The detection of the signal in acetic acid was performed at a temperature of 35°C, which corresponds to a relaxation time $\tau_0 = 140$ ns and a dispersion $\Delta = 1.79\%$ [2, 3]. To increase the signal-to-noise ratio, the signal was stored and averaged over 50 realizations. Figure 3 shows the averaged waveforms of signals recorded in acetic acid at three distances from the source (curves *1*). The same figure displays the transformed waveforms, in which the influence of diffraction is eliminated according to Eq. (4) (curves *2*), and their approximations obtained using the exact expression (5) (curves *3*) and asymptotics (1), (2) (curves *4*). The velocity c_∞ and the absorption coefficient α_∞, which are completely determined by the dynamics of the forerunner, are calculated from the waveforms obtained for the distances of 22.4 and 33.3 mm, at which the forerunner is clearly observed. The calculations give the values $c_\infty = 1089 \pm 3$ m/s and $\alpha_\infty = 108 \pm 5$ m^{-1}. The remaining calculations were performed for the distances of 33.3 and 42.4 mm, at which the maximum of the signal body is clearly seen. The signal characteristics for these distances are given in Table 1, where t_p and t_b designate the arrival times of the forerunner and body of the pulse, respectively. At the initial moment, the signal body is ahead of the forerunner by a distance $d = \beta_0\Delta/\alpha_\infty$, where $\beta_0 = 2\langle\tau^{-2}\rangle/\langle\tau^{-1}\rangle^2$. Therefore, the calculation of the velocity c_0, unlike the calculation of c_∞, cannot be performed using the absolute value of the time of arrival. Determining c_0 from the difference in t_b for two distances, we

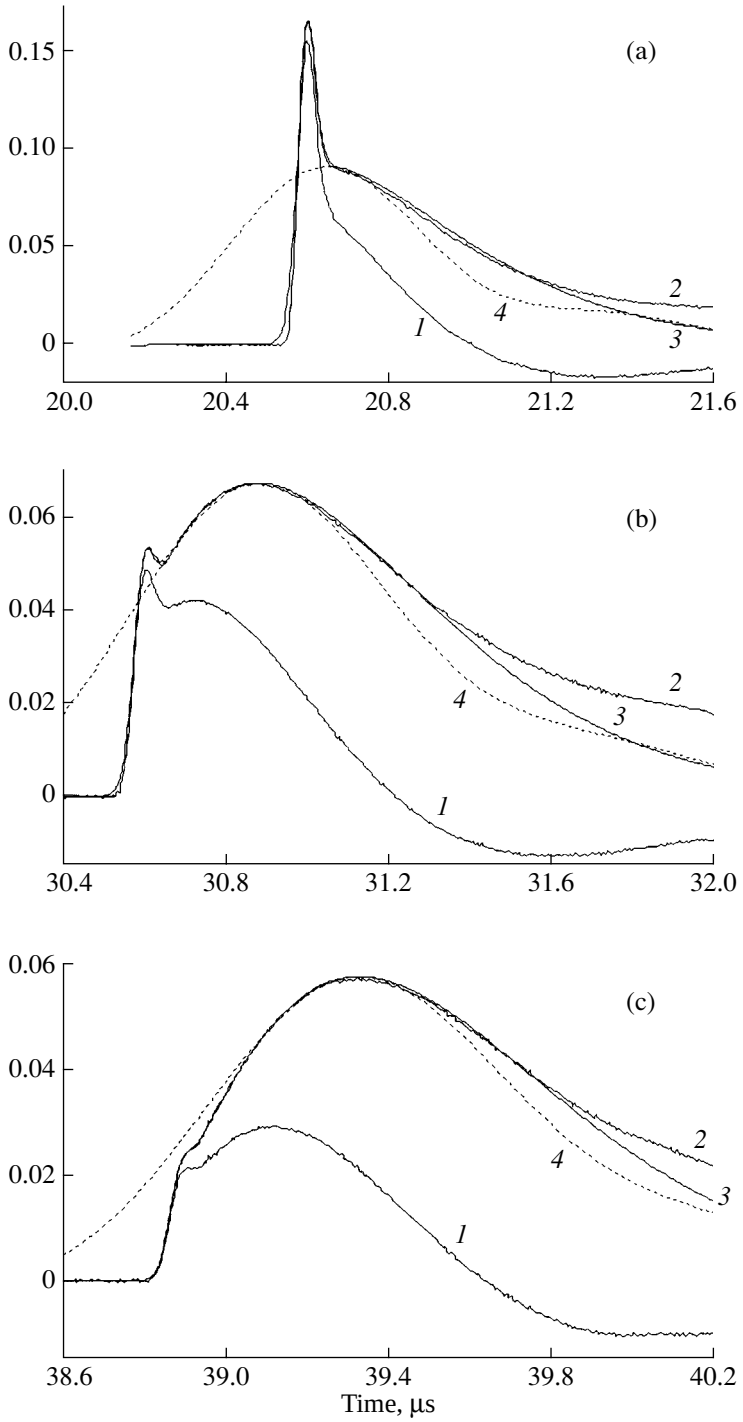

Fig. 3. Waveforms of the signals that traveled the distances x = (a) 22.4, (b) 33.3, and (c) 42.4 mm in acetic acid and their approximations.

obtain $c_0 = 1069 \pm 9$ m/s (the relative error has become greater because the path length was reduced by a factor of three). The corresponding dispersion and the first moment are $\Delta = 1.83 \pm 0.02\%$ and $\langle\tau\rangle = 158 \pm 8$ ns. The values of higher moments calculated from Eqs. (3) are given in Table 2. The large error in calculating the moment $\langle\tau^{-2}\rangle$ is explained by the considerable inaccuracy in determining the derivative A_f'. This moment can be computed with higher accuracy (the second value in Table 2) by using the relation $(1 - \beta_0/\beta)\Delta = (t_b - t_p)/t_b$. In this case, the error is determined by the errors in measuring $\langle\tau^{-1}\rangle$ and α_∞, and proves to be equal to 7%.

An appreciable error in calculating $\langle\tau^3\rangle$ is caused by the fact that, at the distances under consideration, asymptotics (1), (2) give a too rough approximation of the shape of the pulse body, as one can see from the comparison of curves *3* and *4* in Fig. 3. The results obtained in our study suggest that the proposed method of pulsed acoustic spectroscopy should be promising for studying the relaxation properties of liquids.

ACKNOWLEDGMENTS

This work was supported by the Russian Foundation for Basic Research, project no. 00-02-16556.

REFERENCES

1. G. A. Maksimov, Akust. Zh. **42**, 541 (1996) [Acoust. Phys. **42**, 478 (1996)].
2. *Physical Acoustics: Principles and Methods*, Ed. by W. P. Mason (Academic, New York, 1965; Mir, Moscow, 1968), Vol. 2, Part A.
3. L. Bergmann, *Der Ultraschall und seine Anwendung in Wissenschaft und Technik* (Hirzel, Zürich, 1954; Inostrannaya Literatura, Moscow, 1957).

Translated by A. Svechnikov

Acoustical Physics, Vol. 50, No. 4, 2004, pp. 406–419. Translated from Akusticheskiĭ Zhurnal, Vol. 50, No. 4, 2004, pp. 481–495.

Principle of an *A Priori* Use of Symmetries in the Theory of Nonlinear Waves

N. H. Ibragimov* and O. V. Rudenko**

** Research Center ALGA: Advances in Lie Group Analysis, Blekinge Institute of Technology, 37179 Karlskrona, Sweden*

e-mail: nib@bth.se

*** Faculty of Physics, Moscow State University, Vorob'evy gory, Moscow, 119992 Russia*

e-mail: rudenko@acs366.phys.msu.ru

Received February 10, 2004

Abstract—The principle of an *a priori* use of symmetries is proposed as a new approach to solving nonlinear problems on the basis of a reasonable complication of mathematical models. Such a complication often causes an additional symmetry and, hence, opens up possibilities for finding new analytical solutions. The application of group analysis to the problems of nonlinear acoustics is outlined. The potentialities of the proposed approach are illustrated by exact solutions, which are of interest for wave theory. © *2004 MAIK "Nauka/Interperiodica".*

1. INTRODUCTION

The mathematical models of physical processes that are constructed on the basis of general concepts (from first principles) often have a rather complex form. Examples of such models are the systems of equations of mechanics of continua or electrodynamics, which are difficult to solve in the general form by common analytical and numerical methods, especially if the nonlinearity, inhomogeneity, hereditary and other properties of real media are taken into account. Therefore, it is expedient to simplify as much as possible the model equations with due regard for the specificity of the problem under study. It is seemingly evident that, for simpler models, an appropriate method of solution can be most readily found. The simplification is achieved by neglecting the less important features of a given phenomenon and concentrating on its most important properties. A comprehensive description of the ideas underlying this approach was given by A.A. Andronov, A.A. Vitt, and S.É. Khaĭkin in their classical monograph on the theory of oscillations [1]. A historically significant example of applying these ideas to the wave theory is the development of the method of a slowly varying profile by R.V. Khokhlov [2, 3]. This method considerably extended the possibilities for the analytical solution of nonlinear wave problems [4].

Another approach, namely, a complication of the model with the aim to find the desired solutions of a simpler problem, seems to be logically absurd. However, sometimes a complex model proves to be more simple to analyze. An example of such a "useful" complication in acoustics is the Burgers equation (see, e.g., [4] and the notation accepted there):

$$\frac{\partial V}{\partial z} - V\frac{\partial V}{\partial \theta} = \Gamma\frac{\partial^2 V}{\partial \theta^2}.$$

The presence of the additional "viscous" term proportional to the higher (second-order) derivative on the right-hand side of this equation surprisingly does not complicate the initial first-order equation but, on the contrary, provides the possibility to solve the problem. With the transformation

$$V = 2\Gamma\frac{\partial}{\partial \theta}\ln U,$$

the Burgers equation can be linearized and reduced to the heat conduction equation for U. Then, by passing to the limit $\Gamma \longrightarrow 0$, one obtains a physically correct solution to the problem of interest for the "nonviscous" medium.

Evidently, this example is accidental and does not give any general approach. However, the experience gained from the group classification of differential equations shows that, in many cases, a complication of the initial model supplies it with new symmetries. By contrast, a simplification may lead to the loss of a number of symmetry properties inherent in the more general model and to the loss of physically important solutions.

A well-known regular and effective method of symmetry determination is the theory of continuous Lie groups [5, 6]. The conventional method of using Lie groups for finding analytical solutions to differential equations is as follows. Specific equations or systems of equations are considered. For them, symmetry

groups are calculated. Then, these groups are used to construct exact particular solutions, conservation laws, and invariants. A more complicated and interesting problem is the group classification of equations involving unknown parameters or functions. The group classification is understood as the choice of such parameters (or functions) at which the allowed group is wider than the symmetry group of the initial general equation. Many equations with physically interesting solutions have already been obtained in this way (see, e.g., [7–10]). The approach described above can be called an *a posteriori* one, because it is based on analyzing given systems of equations.

In this paper, we propose a fundamentally new and fairly simple approach providing new symmetric models. The approach is based on a reasonable complication of a given model without any loss of its physical content. The basis of the approach, which we call the principle of an *a priori* use of symmetries, is the N.H. Ibragimov's theorem on projections of equivalence groups (see Section 4.2).

For a better understanding of the problem, we begin by describing the standard methods of the group analysis of differential equations by adapting it to the models of nonlinear wave theory and nonlinear acoustics.

2. A BRIEF DESCRIPTION OF THE METHODS OF GROUP ANALYSIS

2.1. Calculation of the Symmetries of Differential Equations

Consider the second-order partial differential evolution equation:

$$u_t = F(t, x, u, u_x, u_{xx}), \quad \frac{\partial F}{\partial u_{xx}} \neq 0. \tag{1}$$

Definition. A set of G reversible transformations of variables t, x, and u that is given by the formulas

$$\bar{t} = f(t, x, u, a), \quad \bar{x} = g(t, x, u, a), \quad \bar{u} = h(t, x, u, a), \tag{2}$$

and depends on a continuous parameter a is called the single-parameter group allowed by equation (1), or the symmetry group of Eq. (1), if Eq. (1) retains its form in terms of the new variables $\bar{t}$, $\bar{x}$, and $\bar{u}$ and also if G contains all inverse transformations, the identity transformation

$$\bar{t} = t, \quad \bar{x} = x, \quad \bar{u} = u,$$

and compositions of any two sequential transformations, i.e.,

$$\bar{\bar{t}} \equiv f(\bar{t}, \bar{x}, \bar{u}, b) = f(t, x, u, a + b),$$

$$\bar{\bar{x}} \equiv g(\bar{t}, \bar{x}, \bar{u}, b) = g(t, x, u, a + b),$$

$$\bar{\bar{u}} \equiv h(\bar{t}, \bar{x}, \bar{u}, b) = h(t, x, u, a + b).$$

Thus, the group G is allowed by Eq. (1) if transformation (2) of the group G transforms any solution $u = u(t, x)$ to Eq. (1) into a solution $\bar{u} = \bar{u}(\bar{t}, \bar{x})$ to the equation

$$\bar{u}_{\bar{t}} = F(\bar{t}, \bar{x}, \bar{u}, \bar{u}_{\bar{x}}, \bar{u}_{\bar{x}\bar{x}}), \tag{3}$$

where F is the same function as that involved in Eq. (1).

According to the Lie theory, the determination of the symmetry group G is equivalent to calculating its infinitesimal transformation

$$\bar{t} \approx t + a\tau(t, x, u), \quad \bar{x} \approx x + a\xi(t, x, u), \quad \bar{u} \approx u + a\eta(t, x, u), \tag{4}$$

which is obtained from the general formulas (2) by expanding them in a Taylor series with respect to the parameter a and retaining only the linear terms. According to Lie, it is convenient to introduce a symbol of transformation (4) in the form of a differential operator:

$$X = \tau(t, x, u)\frac{\partial}{\partial t} + \xi(t, x, u)\frac{\partial}{\partial x} + \eta(t, x, u)\frac{\partial}{\partial u}. \tag{5}$$

The action of this operator on any differentiable function $J(t, x, u)$ is given by the formula

$$X(J) = \tau(t, x, u)\frac{\partial J}{\partial t} + \xi(t, x, u)\frac{\partial J}{\partial x} + \eta(t, x, u)\frac{\partial J}{\partial u}. \tag{6}$$

Operator (5) is also called the infinitesimal operator or the generator of the group G.

Transformation (2) corresponding to operator (5) is found as a solution to the Lie equations

$$\frac{d\bar{t}}{da} = \tau(\bar{t}, \bar{x}, \bar{u}), \quad \frac{d\bar{x}}{da} = \xi(\bar{t}, \bar{x}, \bar{u}), \quad \frac{d\bar{u}}{da} = \eta(\bar{t}, \bar{x}, \bar{u}) \tag{7}$$

with the initial conditions

$$\bar{t}\big|_{a=0} = t, \quad \bar{x}\big|_{a=0} = x, \quad \bar{u}\big|_{a=0} = u.$$

Now, let us return to Eq. (3). Expressions for the derivatives $\bar{u}_{\bar{t}}$, $\bar{u}_{\bar{x}}$, and $\bar{u}_{\bar{x}\bar{x}}$ involved in Eq. (3) are obtained by transformation (2) considered as a simple change of variables. Then, expanding the expressions for these derivatives in a series with respect to parameter a, we obtain an infinitesimal form of the transformations:

$$\bar{u}_{\bar{t}} \approx u_t + a\varsigma_0(t, x, u, u_t, u_x),$$

$$\bar{u}_{\bar{x}} \approx u_x + a\varsigma_1(t, x, u, u_t, u_x), \tag{8}$$

$$\bar{u}_{\bar{x}\bar{x}} \approx u_{xx} + a\varsigma_2(t, x, u, u_t, u_x, u_{tx}, u_{xx}),$$

where the functions ζ_0, ζ_1, ζ_2 are given by the following prolongation formulas:

$$\begin{aligned}\zeta_0 &= D_t(\eta) - u_t D_t(\tau) - u_x D_t(\xi),\\ \zeta_1 &= D_x(\eta) - u_t D_x(\tau) - u_x D_x(\xi),\\ \zeta_2 &= D_x(\zeta_1) - u_{tx} D_x(\tau) - u_{xx} D_x(\xi).\end{aligned} \tag{9}$$

Here, D_t and D_x denote the total derivatives with respect to t and x:

$$D_t = \frac{\partial}{\partial t} + u_t\frac{\partial}{\partial u} + u_{tt}\frac{\partial}{\partial u_t} + u_{tx}\frac{\partial}{\partial u_x},$$

$$D_x = \frac{\partial}{\partial x} + u_x\frac{\partial}{\partial u} + u_{tx}\frac{\partial}{\partial u_t} + u_{xx}\frac{\partial}{\partial u_x}.$$

Substituting expressions (4) and (8) into Eq. (3), we obtain

$$\bar{u}_{\bar{t}} - F(\bar{t}, \bar{x}, \bar{u}, \bar{u}_{\bar{x}}, \bar{u}_{\bar{x}\bar{x}}) \approx u_t - F(t, x, u, u_x, u_{xx}) + a\left(\zeta_0 - \frac{\partial F}{\partial u_x}\zeta_1 - \frac{\partial F}{\partial u_{xx}}\zeta_2 - \frac{\partial F}{\partial t}\tau - \frac{\partial F}{\partial x}\xi - \frac{\partial F}{\partial u}\eta\right).$$

Therefore, by virtue of Eq. (1), Eq. (3) leads to the condition

$$\zeta_0 - \frac{\partial F}{\partial u_x}\zeta_1 - \frac{\partial F}{\partial u_{xx}}\zeta_2 - \frac{\partial F}{\partial t}\tau - \frac{\partial F}{\partial x}\xi - \frac{\partial F}{\partial u}\eta = 0, \tag{10}$$

where u_t is replaced by $F(t, x, u, u_x, u_{xx})$ in the expressions for ζ_0, ζ_1, ζ_2.

Equation (10) determines all infinitesimal symmetries of Eq. (1) and therefore is called the determining equation. It can be represented in a convenient compact form as

$$X[u_t - F(t, x, u, u_x, u_{xx})] = 0. \tag{11}$$

Here, X denotes the prolongation of operator (5) to the first- and second-order derivatives:

$$X = \tau\frac{\partial}{\partial t} + \xi\frac{\partial}{\partial x} + \eta\frac{\partial}{\partial u} + \zeta_0\frac{\partial}{\partial u_t} + \zeta_1\frac{\partial}{\partial u_x} + \zeta_2\frac{\partial}{\partial u_{xx}}.$$

Determining equation (10) (or its equivalent (11)) is a homogeneous linear second-order partial differential equation in the unknown functions τ, ξ, and η. Therefore, the set L of all solutions to the determining equation forms a vector space. Moreover, it is closed with respect to applying a commutator; i.e., the space L together with operators $X_1, X_2 \in L$ also contains their commutator $[X_1, X_2] = X_1X_2 - X_2X_1$. This property means that the set of all solutions of the determining equation forms a Lie algebra. In particular, if L is a finite-dimensional space L_r with a basis $X_1, \ldots, X_r$, we have $[X_i, X_j] = c_{ij}^k X_k$, where c_{ij}^k are the numbers called structural constants of the Lie algebra L_r.

Note that Eq. (10) should be identically satisfied with respect to all variables involved in it, i.e., t, x, u, u_x, u_{xx}, and u_{tx}, which should be considered as six independent variables. As a result, the determining equation falls into a system of several equations, and we obtain an overdetermined system (it contains more than three equations and three unknown functions: τ, ξ, and η). Hence, the determining equation can almost always be easily solved. To simplify the calculations, we use the following lemma.

Lemma. In the case of an equation of the type of Eq. (1), the symmetry transformation (2) has the form

$$\bar{t} = f(t, a), \quad \bar{x} = g(t, x, u, a), \quad \bar{u} = h(t, x, u, a). \tag{12}$$

This means that infinitesimal symmetries can be sought in the form

$$X = \tau(t)\frac{\partial}{\partial t} + \xi(t, x, u)\frac{\partial}{\partial x} + \eta(t, x, u)\frac{\partial}{\partial u}. \tag{13}$$

Proof. In Eq. (10), we separate the terms containing the variable u_{tx}. According to prolongation formulas (9), u_{tx} is involved only in ζ_2, namely, in its last term $u_{tx}D_x(\tau)$. Since the determining equation (10) is identically satisfied with respect to all variables t, x, u, u_x, u_{xx}, and u_{tx}, we can conclude that $D_x(\tau) \equiv \tau_x + u_x\tau_u = 0$, which yields $\tau_x = \tau_u = 0$. Thus, we have $\tau = \tau(t)$, and generator (5) takes the form of Eq. (13), which proves the theorem. Thus, prolongation formulas (9) can be represented in the form

$$\begin{aligned}\zeta_0 &= D_t(\eta) - u_x D_t(\xi) - \tau'(t)u_t,\\ \zeta_1 &= D_x(\eta) - u_x D_x(\xi),\\ \zeta_2 &= D_x(\zeta_1) - u_{xx} D_x(\xi)\\ &\equiv D_x^2(\eta) - u_x D_x^2(\xi) - 2u_{xx} D_x(\xi).\end{aligned} \tag{14}$$

2.2. Exact Solutions Obtained by Using Symmetry Groups

The methods of group analysis open two main ways to constructing exact solutions: by group transformations of the known solutions and by finding invariant solutions.

Group transformations of the known solutions. This way is based on the fact that a symmetry group transforms any solution of the equation under investigation to a solution of the same equation. Namely, let Eqs. (2) represent a group of symmetry transformations for Eq. (1) and let the function

$$u = \Phi(t, x)$$

be a solution to Eq. (1). Since transformation (2) is a symmetry transformation, solution (12) can be represented in terms of the new variables

$$\bar{u} = \Phi(\bar{t}, \bar{x}).$$

Replacing $\bar{u}$, $\bar{t}$, and $\bar{x}$ according to Eqs. (2), we obtain

$$h(t, x, u, a) = \Phi(f(t, x, u, a), g(t, x, u, a)). \tag{15}$$

Solving this equation for u, we obtain a single-parameter (with the parameter a) family of new solutions to Eq. (1). Hence, any known solution can serve as a source of a multiparameter class of new solutions on the condition that the differential equation under consideration allows a multiparameter symmetry group. In the following section, the procedure described above is illustrated in application to the Burgers equation taken as an example.

Invariant solutions. If the group transformation transforms the solution into itself, we obtain the so-called invariant solution. When the infinitesimal symmetry (5) of Eq. (1) is known, the invariant solution is obtained as follows. Two independent invariants, $J_1 = \lambda(t, x)$ and $J_2 = \mu(t, x, u)$, are calculated by solving the equation $X(J) = 0$ (see Eq. (6)) or its characteristic system of equations

$$\frac{dt}{\tau(t, x, u)} = \frac{dx}{\xi(t, x, u)} = \frac{du}{\eta(t, x, u)}. \tag{16}$$

Then, one of the invariants is expressed as a function of the other:

$$\mu = \phi(\lambda). \tag{17}$$

Equation (17) is solved for u, and the resulting expression is substituted into Eq. (1). As was shown by Lie, one obtains an ordinary differential equation for the unknown function $\phi(\lambda)$ of a single variable. This procedure reduces the number of independent variables by one. A further simplification can be achieved by considering invariant solutions generated by two infinitesimal symmetries.

3. BURGERS EQUATION USED AS AN EXAMPLE

The methods described in the previous section are illustrated below in application to the Burgers equation [11] taken as an example:

$$u_t = uu_x + u_{xx}. \tag{18}$$

3.1. Calculation of the Infinitesimal Symmetries

The determining equation (10) has the form

$$\zeta_0 - \zeta_2 - u\zeta_1 - \eta u_x = 0, \tag{19}$$

where ζ_0, ζ_1, ζ_2 are given by Eqs. (14). Let us separate the terms involving u_{xx} and set them equal to zero. Taking into account that u_t should be replaced by $uu_x + u_{xx}$ and substituting the expressions

$$\begin{aligned} D_x^2(\xi) &= D_x(\xi_x + \xi_u u_x) \\ &= \xi_u u_{xx} + \xi_{uu}u_x^2 + 2\xi_{xu}u_x + \xi_{xx}, \\ D_x^2(\eta) &= D_x(\eta_x + \eta_u u_x) \\ &= \eta_u u_{xx} + \eta_{uu}u_x^2 + 2\eta_{xu}u_x + \eta_{xx} \end{aligned} \tag{20}$$

into ζ_2, we arrive at the equation

$$2\xi_u u_x + 2\xi_x - \tau'(t) = 0.$$

From this equation, we obtain two other ones: $\xi_u = 0$ and $2\xi_x - \tau'(t) = 0$. Hence, ξ only depends on t and x and has the form

$$\xi = \frac{1}{2}\tau'(t)x + p(t). \tag{21}$$

From Eq. (21) it follows that $D_x^2(\xi) = 0$. Now the determining equation (19) is reduced to the form

$$u_x^2\eta_{uu} + \left[\frac{1}{2}\tau'(t)u + \frac{1}{2}\tau''(t)x + p'(t) + 2\eta_{xu} + \eta\right]u_x + u\eta_x + \eta_{xx} - \eta_t = 0$$

and falls into three equations:

$$\begin{gathered} \eta_{uu} = 0, \\ \frac{1}{2}\tau'(t)u + \frac{1}{2}\tau''(t)x + p'(t) + 2\eta_{xu} + \eta = 0, \\ u\eta_x + \eta_{xx} - \eta_t = 0. \end{gathered} \tag{22}$$

The first equation of Eqs. (22) yields $\eta = \sigma(t, x)u + \mu(t, x)$, and the second equation of Eqs. (22) takes the form

$$\left(\frac{1}{2}\tau'(t) + \sigma\right)u + \frac{1}{2}\tau''(t)x + p'(t) + 2\sigma_x + \mu = 0,$$

which yields

$$\sigma = -\frac{1}{2}\tau'(t), \quad \mu = -\frac{1}{2}\tau''(t)x - p'(t).$$

Thus, we have

$$\eta = -\frac{1}{2}\tau'(t)u - \frac{1}{2}\tau''(t)x - p'(t). \tag{23}$$

Finally, the substitution of Eq. (23) into the third equation of Eqs. (22) yields

$$\frac{1}{2}\tau'''(t)x + p''(t) = 0.$$

From this equation, we obtain $\tau'''(t) = 0$ and $p''(t) = 0$ and, therefore,

$$\tau(t) = C_1t^2 + 2C_2t + C_3, \quad p(t) = C_4t + C_5.$$

Taking into account Eqs. (21) and (23), we finally arrive at the following general solution to the determining equation (19):

$$\begin{gathered} \tau(t) = C_1t^2 + 2C_2t + C_3, \quad \xi = C_1tx + C_2x + C_4t + C_5, \\ \eta = -(C_1t + C_2)u - C_1x - C_4. \end{gathered}$$

This solution contains five arbitrary constants C_i. This means that the infinitesimal symmetries of the Burgers equation (18) form a five-dimensional Lie algebra

"stretched" over the following linearly independent operators:

$$X_1 = \frac{\partial}{\partial t}, \quad X_2 = \frac{\partial}{\partial x}, \quad X_3 = t\frac{\partial}{\partial x} - \frac{\partial}{\partial u},$$
$$X_4 = 2t\frac{\partial}{\partial t} + x\frac{\partial}{\partial x} - u\frac{\partial}{\partial u}, \tag{24}$$
$$X_5 = t^2\frac{\partial}{\partial t} + tx\frac{\partial}{\partial x} - (x + tu)\frac{\partial}{\partial u}.$$

3.2. Solutions Obtained Using a Symmetry Group

One can easily find the group transformation (12) that is allowed by the Burgers equation by solving the Lie equations for the basic infinitesimal symmetries (24). For generators (24), the Lie equations (7) have a "triangular" form

$$\frac{d\bar{t}}{da} = \tau(\bar{t}), \quad \frac{d\bar{x}}{da} = \xi(\bar{t}, \bar{x}), \quad \frac{d\bar{u}}{da} = \eta(\bar{t}, \bar{x}, \bar{u}), \tag{25}$$

which is convenient for a sequential integration with the use of the initial conditions (see Eqs. (7)).

For example, let us consider the generator X_5 from Eqs. (24). For this case, the Lie equations (25) have the form

$$\frac{d\bar{t}}{da} = \bar{t}^2, \quad \frac{d\bar{x}}{da} = \bar{t}\bar{x}, \quad \frac{d\bar{u}}{da} = -(\bar{x} + \bar{t}\bar{u}).$$

The integration of the first of these equations yields

$$\bar{t} = -\frac{1}{a + C_1}.$$

According to the initial condition for the Lie equations, we require that $\bar{t} = t$ at $a = 0$. Then, we determine the value of the constant C_1 (constant with respect to the variable a in the Lie equations): $C_1 = -1/t$. Thus, we have

$$\bar{t} = \frac{t}{1 - at}. \tag{26}$$

Substituting Eq. (26) into the second Lie equation we obtain

$$\bar{x} = \frac{x}{1 - at}. \tag{27}$$

Equations (26) and (27) determine a special group of the projective transformation (the Möbius transformation) on the plane. Substituting Eqs. (26) and (27) into the third Lie equation, we arrive at an inhomogeneous linear equation

$$\frac{d\bar{u}}{da} + \frac{t}{1 - at}\bar{u} + \frac{x}{1 - at} = 0.$$

Integrating this equation with the initial condition $\bar{u} = u$ at $a = 0$, we obtain

$$\bar{u} = u(1 - at) - ax. \tag{28}$$

Using projective transformations (26)–(28) and applying Eq. (15) to any known solution $u = \Phi(t, x)$ of the Burgers equation, we obtain the following single-parameter family of new solutions:

$$u = \frac{ax}{1 - at} + \frac{1}{1 - at}\Phi\left(\frac{t}{1 - at}, \frac{x}{1 - at}\right). \tag{29}$$

Expression (29) has an important physical meaning. It describes the interaction of the signal $u = \Phi(t, x)$ with the linear part of a sawtooth wave profile. For example, if a high-frequency train of a quasi-harmonic signal occurs on the rear "slope" of the sawtooth profile, whose steepness decreases in the course of the wave propagation (negative values of the constant a), the amplitude of the signal and its frequency decrease. By contrast, on the steepening front slope of the low-frequency wave (the constant a is positive), the signal is amplified and its frequency increases. These phenomena were described theoretically and observed in experiments (see [12, 13]).

Example 1. One can obtain a multitude of new solutions by choosing any invariant solution as the initial one $u = \Phi(t, x)$. For example, let us take a solution that is invariant with respect to a shift along the x coordinate axis and is generated by the operator X_2 from Eqs. (24). In this case, the invariants are $\lambda = t$ and $\mu = u$, and Eq. (17) takes the form $u = \phi(t)$. The substitution of this expression into the Burgers equation leads to a trivial solution in the form of a constant: $u = k$. According to Eq. (29), this solution is transformed to the following single-parameter family of solutions:

$$u = \frac{k + ax}{1 - at},$$

which are used in nonlinear acoustics to describe the smooth parts of sawtooth wave profiles [4].

Example 2. From the physical point of view, one of the most interesting solutions is the stationary solution

$$u = \Phi(x)$$

obtained from the condition of invariance with respect to the time translation group generated by the operator X_1. The substitution into the Burgers equation leads to an ordinary differential equation

$$\Phi'' + \Phi\Phi' = 0. \tag{30}$$

Integrating this equation once, we obtain $\Phi' + \Phi^2/2 = C_1$, and integrating it again for different values of the

constant, namely, $C_1 = 0$, $C_1 = \nu^2 > 0$, and $C_1 = -\nu^2 < 0$, we obtain

$$\Phi = \frac{2}{x + C}, \quad \Phi = \nu\tanh\left(C + \frac{\nu}{2}x\right), \quad \Phi = \nu\tan\left(C - \frac{\nu}{2}x\right). \tag{31}$$

Note that the Galilean transformation, i.e., $\bar{t} = t$, $\bar{x} = x + at$, $\bar{u} = u - a$, which is generated by the operator X_3, maps X_1 into the sum $X_1 + cX_2$. Correspondingly, it maps the stationary solution into a travelling wave $u = u(x - ct)$, which is easily obtained from solutions (31).

As is known, the solution in the form of a hyperbolic tangent describes a single shock wave with a finite shock wave thickness [4, 14]. The profiles of the two other stationary waves given by Eqs. (31) contain singularities, and, therefore, these solutions are rarely used in physical problems.

Example 3. If we apply transformation (29) to stationary solutions (31), we obtain new nonstationary solutions:

$$u = \frac{ax}{1 - at} + \frac{2}{x + C(1 - at)},$$

$$u = \frac{1}{1 - at}\left[ax + \nu\tanh\left(C + \frac{\nu x}{2(1 - at)}\right)\right], \tag{32}$$

$$u = \frac{1}{1 - at}\left[ax + \nu\tan\left(C - \frac{\nu x}{2(1 - at)}\right)\right].$$

Example 4. Let us find invariant solutions for the projective group generated by the operator X_5. In this case, the characteristic system of equations (16) can be represented as

$$\frac{dt}{t^2} = \frac{dx}{tx} = -\frac{du}{x + tu}.$$

Solving this system, we find two invariants: $\lambda = x/t$ and $\mu = x + tu$. Thus, the general expression (17) for the invariant solution takes the form

$$u = -\frac{x}{t} + \frac{1}{t}\Phi(\lambda), \quad \lambda = \frac{x}{t}. \tag{33}$$

Substituting this expression into Burgers equation (18) we obtain Eq. (30) for $\Phi(\lambda)$. Hence, the general solution is obtained from Eqs. (31) by replacing x with λ. The corresponding invariant solutions are found by substituting the result obtained for $\Phi(\lambda)$ into Eq. (33). For example, using the second formula from Eqs. (31) and assuming that $\nu = \pi$, we arrive at the solution

$$u = \frac{1}{t}\left[-x - \pi\tanh\left(C + \frac{\pi x}{2t}\right)\right]. \tag{34}$$

This solution was obtained earlier by R.V. Khokhlov from physical considerations (see, e.g., Paragraph 4, Chap. 9 in [14]). Note that formula (34) can also be derived from the second formula of Eqs. (32) by setting $\nu = -\pi a$ and assuming that a tends to infinity.

Example 5. Solutions invariant with respect to the dilation group generated by the operator X_4 are often called self-similar solutions in the literature. In this case, the characteristic system of equations

$$\frac{dt}{2t} = \frac{dx}{x} = -\frac{du}{u}$$

yields the invariants $\lambda = x/\sqrt{t}$ and $\mu = \sqrt{t}\,u$. Hence, the invariant solution should be sought in the form

$$u = \frac{1}{\sqrt{t}}\Phi(\lambda), \quad \lambda = \frac{x}{\sqrt{t}}.$$

As a result, we obtain an equation [4] for determining self-similar solutions to the Burgers equation:

$$\Phi'' + \Phi\Phi' + \frac{1}{2}(\lambda\Phi' + \Phi) = 0. \tag{35}$$

Integrating this equation once, we obtain

$$\Phi' + \frac{1}{2}(\Phi^2 + \lambda\Phi) = C.$$

At $C = 0$, this equation is easily integrated and yields a solution that vanishes at $\pm\infty$ (see Paragraph 4, Chap. 9 in [14] or Sect. 11.4 in Vol. 1 of [10]):

$$u = \frac{2}{\sqrt{\pi t}}\frac{\exp\left(-\frac{x^2}{4t}\right)}{B + \operatorname{erf}\left(\frac{x}{2\sqrt{t}}\right)}, \quad \operatorname{erf}(z) = \frac{2}{\sqrt{\pi}}\int_0^z \exp(-s^2)\,ds,$$

where B is an arbitrary constant and erf is the error function.

Example 6. The construction of exact solutions may be based not only on the basic infinitesimal symmetries (24) but also on their linear combinations. For example, consider the operator

$$X_1 + X_5 = (1 + t^2)\frac{\partial}{\partial t} + tx\frac{\partial}{\partial x} - (x + tu)\frac{\partial}{\partial u}. \tag{36}$$

The characteristic system of equations yields the following invariants:

$$\lambda = \frac{x}{\sqrt{1 + t^2}}, \quad \mu = \frac{tx}{\sqrt{1 + t^2}} + u\sqrt{1 + t^2}.$$

Thus, the invariant solution has the form

$$u = -\frac{tx}{1 + t^2} + \frac{1}{\sqrt{1 + t^2}}\Phi(\lambda), \quad \lambda = \frac{x}{\sqrt{1 + t^2}}.$$

Substituting this expression into the Burgers equation, we arrive at the following equation for $\Phi(\lambda)$:

$$\Phi'' + \Phi\Phi' + \lambda = 0. \tag{37}$$

Integrating Eq. (37) once, we obtain

$$\Phi' + \frac{1}{2}(\Phi^2 + \lambda^2) = C_1.$$

When the constant is $C_1 = 0$, the solution to this equation can be expressed in terms of the Bessel functions:

$$\Phi = 2\frac{d}{d\lambda}\ln\left[\sqrt{\lambda}J_{1/4}\left(\frac{\lambda^2}{4}\right) + C\sqrt{\lambda}Y_{1/4}\left(\frac{\lambda^2}{4}\right)\right],$$

where C is the second constant.

4. METHOD OF THE *A PRIORI* USE OF SYMMETRY

In Section 3, we described examples of using symmetry groups. However, in many problems, a symmetry group is absent or is insufficiently wide to solve the given model equation. The method proposed below is aimed at constructing models with an elevated symmetry without the loss of the physical contents of the initial model. The essence of the method is as follows.

If the model contains "arbitrary elements" and allows a sufficiently wide equivalence group (see Definition 2 in Sect. 4.2 of this paper), the symmetry group is determined as a suitable subgroup of the equivalence group. Otherwise, the nonlinear model under consideration is generalized by means of its "immersion" into a wider model in a "reasonable" way, i.e., so as not to lose the initial physical meaning but, at the same time, to achieve the desired expansion of the equivalence group. In this case, the nonlinearity of the model is essential, because it provides the necessary flexibility in choosing the model and ensures the generality of the method.

4.1. Immersion and the Application of Laplace Invariants

Consider the Earnshaw equation (see, e.g., [15])

$$\frac{\partial^2 v}{\partial t^2} - c^2\left(1 + \frac{\partial v}{\partial \xi}\right)^{-(\gamma+1)}\frac{\partial^2 v}{\partial \xi^2} = 0, \qquad (38)$$

which describes the one-dimensional motion of a compressible gas in terms of the Lagrange variables. The physical meaning of the variables are as follows: v is the displacement of particles of the medium, c is the velocity of sound, and γ is the adiabatic exponent in the equation of state.

Equation (3) can be linearized by the hodograph transformation:

$$x = v_\xi, \quad y = v_t, \quad \xi = X(x, y), \quad t = u(x, y); \qquad (39)$$

i.e., the Lagrangian coordinate ξ and time t are considered as functions of the new independent variables x and y, which are the first derivatives of the desired function v. The corresponding linearized equation has the form

$$\frac{\partial^2 u}{\partial x^2} - c^2(1 + x)^{-(\gamma+1)}\frac{\partial^2 u}{\partial y^2} = 0. \qquad (40)$$

At a small acoustic Mach number $|v_x| = |x|$, Eq. (40) can be approximated by a simpler equation

$$\frac{\partial^2 u}{\partial x^2} - c^2[1 - (\gamma + 1)x]\frac{\partial^2 u}{\partial y^2} = 0. \qquad (41)$$

However, neither Eq. (40) nor its simplified version (41) are solvable because of the lack of a sufficiently wide symmetry group.

Therefore, we choose an approximating equation not for the simplicity of its form but for the presence of symmetry sufficient to make it solvable. Namely, we consider a hyperbolic equation

$$\frac{\partial^2 u}{\partial x^2} - c^2\psi^2(x)\frac{\partial^2 u}{\partial y^2} = 0 \qquad (42)$$

generalizing Eqs. (40) and (41) and undertake a search for such a function $\psi(x)$ that, first, coincides with the corresponding function in the initial equation at small $|x|$ and, second, opens up a possibility to find a general solution to Eq. (42). Let us choose $\psi(x)$ so as to make Eq. (42) allow the widest possible symmetry group.

It is well known that the hyperbolic equation

$$\frac{\partial^2 u}{\partial\alpha\partial\beta} + A(\alpha, \beta)\frac{\partial u}{\partial\alpha} + B(\alpha, \beta)\frac{\partial u}{\partial\beta} + P(\alpha, \beta)u = 0 \qquad (43)$$

allows the widest possible symmetry group [16, 17] and, hence, can be solved by reducing it to a conventional wave equation if the Laplace invariants [18] for Eq. (43),

$$h = \frac{\partial A}{\partial\alpha} + AB - P, \quad k = \frac{\partial B}{\partial\beta} + AB - P, \qquad (44)$$

are equal to zero. Therefore, we calculate the Laplace invariants of Eq. (42) by rewriting it in terms of the characteristic variables

$$\alpha = c\int\psi(x)dx - y, \quad \beta = c\int\psi(x)dx + y. \qquad (45)$$

With these variables, Eq. (42) takes the canonic form of Eq. (43),

$$\frac{\partial^2 u}{\partial\alpha\partial\beta} + \frac{\psi'(x)}{4c\psi^2(x)}\left(\frac{\partial u}{\partial\alpha} + \frac{\partial u}{\partial\beta}\right) = 0, \qquad (46)$$

with the coefficients

$$A = B = \frac{\psi'(x)}{4c\psi^2(x)}, \quad P = 0, \qquad (47)$$

where x is expressed through α and β according to Eqs. (45), namely:

$$x = \Psi^{-1}(z), \quad z = \frac{\alpha+\beta}{2c} = \Psi(x) \equiv \int \psi(x)dx. \quad (48)$$

From Eqs. (47) and (48), we obtain

$$\frac{\partial A}{\partial \alpha} = \frac{\partial A}{\partial x}\frac{z_\alpha}{z_x} = \frac{1}{2c\psi(x)}\frac{\partial A}{\partial x} = \frac{\psi''}{8c^2\psi^3} - \frac{\psi'^2}{4c^2\psi^4} = \frac{\partial B}{\partial \beta}.$$

Using this relation, we calculate the Laplace invariants (44) for Eq. (46):

$$h = k = \frac{1}{8c^2\psi^4}\left(\psi\psi'' - \frac{3}{2}\psi'^2\right). \quad (49)$$

Hence, the conditions $h = k = 0$ are reduced to a single equation, the solution to which is

$$\psi(x) = (l + sx)^{-2}, \quad s, l = \text{const}.$$

Thus, Eq. (42) with the widest possible symmetry group has the form

$$\frac{\partial^2 u}{\partial x^2} - c^2[l + sx]^{-4}\frac{\partial^2 u}{\partial y^2} = 0.$$

Comparing it with Eq. (41), we see that the constants should be set as $l = 1$ and $s = (\gamma + 1)/4$. As a result, we obtain the desired solvable equation

$$\frac{\partial^2 u}{\partial x^2} - c^2\left[1 + \frac{\varepsilon}{2}x\right]^{-4}\frac{\partial^2 u}{\partial y^2} = 0, \quad \varepsilon = \frac{\gamma+1}{2}, \quad (50)$$

which approximates Eq. (40) with a sufficient accuracy for $\varepsilon|x| \ll 1$.

To solve Eq. (50), we represent it in the canonical form of Eq. (46):

$$\frac{\partial^2 u}{\partial\alpha\partial\beta} + \frac{1}{\alpha+\beta}\left(\frac{\partial u}{\partial\alpha} + \frac{\partial u}{\partial\beta}\right) = 0. \quad (51)$$

According to the general theory, Eq. (51) is reduced to the simplest wave equation $w_{\alpha\beta} = 0$ by the substitution $w = (\alpha + \beta)u$. Therefore, the general solution to Eq. (51) is given by the formula

$$u(\alpha, \beta) = \frac{1}{\alpha+\beta}[\Phi_1(\alpha) + \Phi_2(\beta)] \quad (52)$$

with two arbitrary functions Φ_1 and Φ_2. Now, we return to variables x, y in Eq. (52). Formulas (45) yield

$$\alpha = -\left[\frac{2c}{\varepsilon(1+\varepsilon x/2)} + y\right], \quad \beta = -\left[\frac{2c}{\varepsilon(1+\varepsilon x/2)} - y\right],$$

$$\alpha + \beta = -\frac{4c}{\varepsilon(1+\varepsilon x/2)}.$$

The substitution of these expressions into Eq. (52) with the changing of the inessential sign in the arbitrary functions provides the following general solution to Eq. (50):

$$u(x, y) = \frac{\varepsilon(1+\varepsilon x/2)}{4c} \times \left[\Phi_1\left(\frac{2c}{\varepsilon(1+\varepsilon x/2)} + y\right) + \Phi_2\left(\frac{2c}{\varepsilon(1+\varepsilon x/2)} - y\right)\right]. \quad (53)$$

Summarizing, we conclude that solution (53) was found by way of "immersion" of the model of interest given by Eq. (38) into the more general model

$$\frac{\partial^2 v}{\partial t^2} - c^2\psi^2\left(\frac{\partial v}{\partial \xi}\right)\frac{\partial^2 v}{\partial \xi^2} = 0. \quad (54)$$

However, it should be emphasized that the possibility of constructing solution (53) essentially depends on the accidental fact that Eq. (38) and its generalization (50) are linearized by transformation (39). Therefore, although this example clearly illustrates the idea of immersion and shows how the generalization of a model can make it solvable, it still does not provide any practical method for selecting the most symmetric equations from the generalized model. Such a method is discussed in the following section using a specific example.

4.2. Method Based on the Theorem on Projections

The theorem on projections was proved by N.H. Ibragimov in 1987 [19] and then used in the group classification problems [20] as the basis for the preliminary group classification (see also [21–23]).

Now, we proceed to the main examples illustrating the potentialities of the proposed approach. These examples are of interest by themselves, because new nonlinear equations are considered. Their physical content is discussed in the following section.

We begin with the nonlinear equation

$$\frac{\partial}{\partial t}\left[\frac{\partial u}{\partial x} - u\frac{\partial u}{\partial t}\right] = -\beta u, \quad \beta = \text{const} \neq 0. \quad (55)$$

It allows a three-dimensional Lie algebra with the basis

$$X_1 = \frac{\partial}{\partial t}, \quad X_2 = \frac{\partial}{\partial x}, \quad X_3 = t\frac{\partial}{\partial t} - x\frac{\partial}{\partial x} + 2u\frac{\partial}{\partial u}. \quad (56)$$

Hence, Eq. (55) is not rich in invariant group solutions. Their class is limited to the travelling-wave solutions that are constructed using the translation generators X_1 and X_2, and the self-similar solutions constructed using the dilation generator X_3.

Therefore, we use the immersion approach and consider two types of models generalizing Eq. (55). The first of them has the form

$$\frac{\partial}{\partial t}\left[\frac{\partial u}{\partial x} - P(u)\frac{\partial u}{\partial t}\right] = F(x, u), \quad (57)$$

and, as the second, we take

$$\frac{\partial}{\partial t}\left[\frac{\partial u}{\partial x} - Q(x, u)\frac{\partial u}{\partial t}\right] = F(x, u). \quad (58)$$

Calculations show that the second generalization is more appropriate and is the source of a symmetry group much richer than that of Eqs. (55) and (57). Therefore, we use model (58) to illustrate the main tenets of the *a priori* symmetry method.

Definition 2. A group of transformations (2) is called an equivalence group if each equation of the given family (in the case under consideration, family (58) with any functions Q, F) is transformed to an equation of the same family; i.e.,

$$\frac{\partial}{\partial \bar{t}}\left[\frac{\partial \bar{u}}{\partial \bar{x}} - \bar{Q}(\bar{x}, \bar{u})\frac{\partial \bar{u}}{\partial \bar{t}}\right] = \bar{F}(\bar{x}, \bar{u}),$$

where, generally speaking, the functions $\bar{Q}$, and $\bar{F}$ do not coincide with Q and F. The generators of the equivalence group have the form

$$Y = \xi^1\frac{\partial}{\partial t} + \xi^2\frac{\partial}{\partial x} + \eta\frac{\partial}{\partial u} + \mu^1\frac{\partial}{\partial Q} + \mu^2\frac{\partial}{\partial F}, \quad (59)$$

where

$$\xi^i = \xi^i(t, x, u), \quad \eta = \eta(t, x, u),$$
$$\mu^i = \mu^i(t, x, u, Q, F), \quad i = 1, 2.$$

They form a Lie algebra, which is called the equivalence algebra and is denoted as L_ε. In operator (59) and its coordinates, the functions Q and F are considered as new variables along with the physical variables t, x, and u.

As was shown by L.V. Ovsyannikov [8], the equivalence algebra can be found using the infinitesimal Lie technique (see Section 2.1) by determining the equivalence group as the group allowed by the following extended system of equations equivalent to the family of equations of type (58):

$$u_{tx} - Qu_{tt} - Q_u u_t^2 - F = 0, \quad Q_t = 0, \quad F_t = 0. \quad (60)$$

Despite the fundamental similarity to the classical Lie theory, considerable technical differences occur between the calculation of infinitesimal symmetries and that of generators (59) of the equivalence group. Detailed calculations can be found in [20, 21].

Using this approach, one can obtain by calculation that, for Eq. (58), generators (59) of the equivalence group have the coordinates

$$\xi^1 = C_1 t + \varphi(x), \quad \xi^2 = \psi(x),$$
$$\eta = (C_1 + C_2)u + \lambda(x), \quad (61)$$
$$\mu^1 = -\varphi'(x) + [C_1 - \psi'(x)]Q, \quad \mu^2 = [C_2 - \psi'(x)]F,$$

where φ, ψ, and λ are arbitrary functions of x. This means that Eq. (58) has an infinite-dimensional algebra L_ε with the basis

$$Y_1 = \varphi(x)\frac{\partial}{\partial t} - \varphi'(x)\frac{\partial}{\partial Q},$$
$$Y_2 = \psi(x)\frac{\partial}{\partial x} - \psi'(x)Q\frac{\partial}{\partial Q} - \psi'(x)F\frac{\partial}{\partial F},$$
$$Y_3 = \lambda(x)\frac{\partial}{\partial u}, \quad Y_4 = t\frac{\partial}{\partial t} + u\frac{\partial}{\partial u} + Q\frac{\partial}{\partial Q}, \quad (62)$$
$$Y_5 = u\frac{\partial}{\partial u} + F\frac{\partial}{\partial F}.$$

Note 1. Analogously, Eq. (57) can be shown to have a seven-dimensional algebra L_ε stretched over the operators

$$Y_1 = \frac{\partial}{\partial t}, \quad Y_2 = \frac{\partial}{\partial x}, \quad Y_3 = \frac{\partial}{\partial u},$$
$$Y_4 = t\frac{\partial}{\partial t} + u\frac{\partial}{\partial u} + P\frac{\partial}{\partial P}, \quad Y_5 = u\frac{\partial}{\partial u} + F\frac{\partial}{\partial F}, \quad (63)$$
$$Y_6 = x\frac{\partial}{\partial t} - \frac{\partial}{\partial P}, \quad Y_7 = x\frac{\partial}{\partial x} - P\frac{\partial}{\partial P} - F\frac{\partial}{\partial F}.$$

The following calculations are based on the theorem on projections, which was mentioned at the beginning of Section 4.2. We introduce the notation X and Z for the projections of generator (59) of the equivalence group onto the physical variables t, x, and u and the variables x, u, Q, and F of arbitrary elements, respectively:

$$X = pr_{(t, x, u)}(Y) \equiv \xi^1\frac{\partial}{\partial t} + \xi^2\frac{\partial}{\partial x} + \eta\frac{\partial}{\partial u}, \quad (64)$$

$$Z = pr_{(x, u, Q, F)}(Y) \equiv \xi^2\frac{\partial}{\partial x} + \eta\frac{\partial}{\partial u} + \mu^1\frac{\partial}{\partial Q} + \mu^2\frac{\partial}{\partial F}. \quad (65)$$

Substituting Eqs. (61) into Eqs. (64) and (65), we obtain the projections correctly determined in the sense that the coordinates of X only depend on t, x, and u while the coordinates of Z depend on x, u, Q, and F:

$$X = [C_1 t + \varphi(x)]\frac{\partial}{\partial t} + \psi(x)\frac{\partial}{\partial x} + [(C_1 + C_2)u + \lambda(x)]\frac{\partial}{\partial u}, \quad (66)$$

$$Z = \psi(x)\frac{\partial}{\partial x} + [(C_1 + C_2)u + \lambda(x)]\frac{\partial}{\partial u} + [-\varphi'(x) + (C_1 - \psi'(x)Q)]\frac{\partial}{\partial Q} + (C_1 - \psi'(x))F\frac{\partial}{\partial F}. \quad (67)$$

As applied to Eq. (58), the theorem on projections is formulated as follows.

Theorem on projections. Operator X defined by formula (66) represents the infinitesimal symmetry of equation (58) with the functions

$$Q = Q(x, u), \quad F = F(x, u) \tag{68}$$

if and only if the system of equations (68) is invariant with respect to the generator Z defined by formula (67); i.e., if

$$Z[Q - Q(x, u)] = 0, \quad Z[F - F(x, u)] = 0, \tag{69}$$

where the variables Q and F should be replaced by the functions $Q(x, u)$ and $F(x, u)$ according to Eqs. (68). In view of Eq. (67), Eqs. (69) can be represented in the form of a system of linear first-order partial differential equations for the functions $Q(x, u)$ and $F(x, u)$:

$$\psi(x)\frac{\partial Q}{\partial x} + [(C_1 + C_2)u + \lambda(x)]\frac{\partial Q}{\partial u} + [\psi'(x) - C_1]Q + \varphi'(x) = 0, \tag{70}$$

$$\psi(x)\frac{\partial F}{\partial x} + [(C_1 + C_2)u + \lambda(x)]\frac{\partial F}{\partial u} + [\psi'(x) - C_2]F = 0.$$

Note 2. This theorem is analogously formulated for Eq. (57) by replacing operators (62) with operators (63) and also replacing Eqs. (68) with

$$P = P(u), \quad F = F(x, u).$$

Example 1. Let us choose the constants and functions involved in Eq. (61) as

$$C_1 = 1, \quad \varphi(x) = 0, \quad \psi(x) = k - x,$$
$$C_2 = 0, \quad \lambda(x) = 0,$$

i.e., choose $Y' \in L_\varepsilon$ of a specific form:

$$Y' = t\frac{\partial}{\partial t} + (x - k)\frac{\partial}{\partial x} + u\frac{\partial}{\partial u} - F\frac{\partial}{\partial F}. \tag{71}$$

Then, by solving the system of equations (70), we obtain the functions

$$Q = \Phi\left(\frac{u}{x - k}\right), \quad F = \frac{1}{x - k}\Gamma\left(\frac{u}{x - k}\right), \tag{72}$$

where Φ and Γ are arbitrary functions of the same argument. From the theorem on projections, it follows that, in addition to the evident time transfer generator $X_0 = \partial/\partial t$, Eq. (58) of the form

$$\frac{\partial}{\partial t}\left[\frac{\partial u}{\partial x} - \Phi\left(\frac{u}{x - k}\right)\frac{\partial u}{\partial t}\right] = \frac{1}{x - k}\Gamma\left(\frac{u}{x - k}\right) \tag{73}$$

allows one more operator

$$X' = t\frac{\partial}{\partial t} + (x - k)\frac{\partial}{\partial x} + u\frac{\partial}{\partial u}. \tag{74}$$

From the equation $X'(J) = 0$, we determine the invariants

$$\lambda = \frac{t}{x - k}, \quad \mu = \frac{u}{x - k}.$$

The invariant solution $u = (x - k)G(\lambda)$ to Eq. (73) should satisfy the ordinary differential equation

$$\lambda G'' + (\Phi(G)G')' + \Gamma(G) = 0.$$

The particular case of interest is that of Eq. (73) with linear functions Φ and Γ, when a quadratic nonlinear term appears on the left side of Eq. (73):

$$\frac{\partial}{\partial t}\left[\frac{\partial u}{\partial x} - \alpha\frac{u}{k - x}\frac{\partial u}{\partial t}\right] = -\beta\frac{u}{(k - x)^2}. \tag{75}$$

This case is considered separately in Section 5.

Example 2. Now let us consider an equation with two additional symmetries. For this purpose, we take two equivalence generators forming a two-dimensional algebra. We again take the first of them in the form given by Eq. (71), while to determine the second generator Y'', we set

$$C_1 = 0, \quad C_2 = 1, \quad \varphi(x) = \psi(x) = \lambda(x) = x - k$$

in Eqs. (61); i.e. we choose

$$Y'' = (x - k)\left(\frac{\partial}{\partial t} + \frac{\partial}{\partial x}\right) + (u + x - k)\frac{\partial}{\partial u} - (1 + Q)\frac{\partial}{\partial Q}.$$

Operators Y' and Y'' commute and, hence, form an Abelian Lie algebra. Applying the theorem on projections to both these operators, i.e., in fact, solving Eqs. (70) with the coordinates of the operator Y'' and with the functions Q and F in the form of Eqs. (72), we obtain

$$Q = -1 + A\exp\left(-\frac{u}{x - k}\right), \quad F = \frac{B}{x - k}\exp\left(\frac{u}{x - k}\right),$$

where A, B = const.

According to the theorem on projections, the equation

$$\frac{\partial}{\partial t}\left[\frac{\partial u}{\partial x} + \left(1 - A\exp\left(-\frac{u}{x - k}\right)\right)\frac{\partial u}{\partial t}\right] = \frac{B}{x - k}\exp\left(\frac{u}{x - k}\right) \tag{76}$$

allows two additional operators:

$$X' = t\frac{\partial}{\partial t} + (x - k)\frac{\partial}{\partial x} + u\frac{\partial}{\partial u},$$
$$X'' = (x - k)\left(\frac{\partial}{\partial t} + \frac{\partial}{\partial x}\right) + (u + x - k)\frac{\partial}{\partial u}. \tag{77}$$

In particular, we can find a solution that is invariant with respect to the two-parameter symmetry group with two generators (77). For this purpose, it is necessary to

solve the system of equations $X'(J) = 0$, $X''(J) = 0$. From the first equation, we obtain two invariants

$$\lambda = \frac{x-k}{t}, \quad \mu = \frac{u}{t},$$

and the second equation yields

$$\mu = L\lambda + \lambda\ln\left(\frac{\lambda}{1-\lambda}\right), \quad L = \text{const}.$$

Substituting the values of μ and λ into these expressions, we obtain the invariant solution in the form

$$u = (x-k)\left[L + \ln\left(\frac{x-k}{t-x+k}\right)\right].$$

The constant L is determined by substituting the solution into Eq. (76).

Example 3. Now, let us consider Eq. (57) and apply the theorem on projections to the combination $Y = Y_3 + Y_5 + Y_6 + Y_7$ of the basis operators (63), i.e., to the equivalence operator

$$Y = x\frac{\partial}{\partial t} + x\frac{\partial}{\partial x} + (1+u)\frac{\partial}{\partial u} - (1+P)\frac{\partial}{\partial P}.$$

Using formulas similar to Eqs. (64) and (65), we obtain the projections

$$X = x\frac{\partial}{\partial t} + x\frac{\partial}{\partial x} + (1+u)\frac{\partial}{\partial u}, \tag{78}$$

$$Z = x\frac{\partial}{\partial x} + (1+u)\frac{\partial}{\partial u} - (1+P)\frac{\partial}{\partial P}. \tag{79}$$

Solving the equations $Z[P(u) - P] = 0$, $Z[F(x, u) - F] = 0$ (compare with Eqs. (69) and see Note 2), whose specific form is

$$(1+u)\frac{dP}{du} + (1+P) = 0, \quad x\frac{\partial F}{\partial x} + (1+u)\frac{\partial F}{\partial u} = 0,$$

we obtain

$$F = \Gamma\left(\frac{x}{1+u}\right), \quad P = \frac{K}{1+u} - 1,$$

where K = const.

Hence, the equation

$$\frac{\partial}{\partial t}\left[\frac{\partial u}{\partial x} + \left(1 - \frac{K}{1+u}\right)\frac{\partial u}{\partial t}\right] = \Gamma\left(\frac{x}{1+u}\right) \tag{80}$$

of the form of Eq. (57), allows not only the operator $X_0 = \partial/\partial t$ but also an additional operator X determined by Eq. (78). We use this operator to construct the invariant solution. Determining the invariants $\lambda = t - x$ and $\mu = (u+1)/x$ of the operator X, we arrive at the invariant solution

$$u = x\Phi(\lambda), \quad \lambda = t - x.$$

Substituting it into Eq. (80), we obtain the ordinary differential equation

$$K(\Phi'/\Phi)' + \Phi' = \Gamma(\Phi). \tag{81}$$

Note that, for small values of u, Eq. (80) is a good approximation with an additional symmetry for the models described by equations of the type of Eq. (55).

5. DERIVATION OF EQUATIONS AND DISCUSSION OF THE PHYSICS OF PROCESSES

Model (55) appears in several problems. Let us first consider the oscillations of a compressible gas inside a cylinder with a cross section S. The cylinder is closed with a moving piston of mass m. The bottom of the cylinder is fixed at $x = 0$ (the x coordinate is measured along the generatrix, from the bottom upwards). The piston can perform oscillations with a displacement ζ relative to its mean position at $x = H$. The system of equations describing the piston motion with allowance for the nonlinear gas movements has the form

$$\rho c\frac{\partial\zeta}{\partial t} = p(t_-) - p(t_+), \quad \frac{m}{S}\frac{\partial^2\zeta}{\partial t^2} = p(t_+) + p(t_-). \tag{82}$$

Here, ρ and c are the density of the gas and the sound velocity in it and $p(t)$ is the form of any of the two acoustic pressure waves propagating toward each other. The arguments contain the time shift determined by the length H of the resonator and by the nonlinear properties of the gas:

$$t_\pm = t \pm \frac{H}{c}\left(1 - \varepsilon\frac{p}{c^2\rho}\right).$$

Using the method [24] of transforming functional equations of the type of Eq. (82) to differential evolution equations, for the region near the acoustic resonance $\omega H/c = \pi + \Delta$ (where Δ is a small frequency detuning), we obtain [25]

$$\frac{\partial}{\partial\xi}\left[\frac{\partial U}{\partial T} + \Delta\frac{\partial U}{\partial\xi} - \pi\varepsilon U\frac{\partial U}{\partial\xi}\right] = -\beta U. \tag{83}$$

In Eq. (83), we used the dimensionless quantities:

$$U = \frac{p}{c^2\rho}, \quad \xi = \omega t + \pi, \quad T = \frac{\omega t_1}{\pi}, \quad \beta = \frac{1}{\pi}\frac{m_g}{m},$$

where t_1 is the "slow" time describing the settling of steady-state oscillations in the resonator and $m_g = \rho SH$ is the mass of gas in the cylinder. It is evident that, by changing the variables and renaming the constants as

$$t = \xi - \Delta T, \quad T = x, \quad u = \pi\varepsilon U,$$

Eq. (83) can be transformed to Eq. (55).

Approximate solutions to Eq. (83) were obtained in [25] for the problem statements of physical interest. However, some exact solutions also have important

physical meanings. For example, let us consider the exact solution obtained by using the dilation operator X_3 from Eqs. (56). The corresponding invariants and the self-similar form are expressed as

$$\lambda = xt, \quad \mu = ux^2, \quad u(x,t) = \frac{1}{x^2}\Phi(\lambda).$$

The substitution of the last expression into Eq. (55) leads to an ordinary differential equation

$$\Phi\Phi'' + \Phi'^2 - \lambda\Phi'' + \Phi' - \beta\Phi = 0.$$

Its particular solution, which in the limit $\beta \longrightarrow 0$ takes the form of the solution $u = -x/t$ for Riemann waves, is

$$\Phi(\lambda) = -\lambda + \frac{\beta}{6}\lambda^2, \quad u(x,t) = \frac{\beta}{6}t^2 - \frac{t}{x}. \qquad (84)$$

By analogy with the known procedure of constructing a sawtooth signal [4], in which the periodically continued solution $u = -x/t$ is used to describe smooth linear portions of the profile (see the dashed curves in Fig. 1), we continue solution (84) with a period of 2π. The shock fronts are localized at the points

$$t_n = \pi(2n+1) + \frac{3}{\beta x} - \sqrt{\left(\frac{3}{\beta x}\right)^2 - \frac{\pi^2}{3}},$$
$$n = 0, \pm 1, \pm 2, \ldots,$$

whose coordinates are calculated from the condition that the period-average value of the function $u(x, t)$ be zero.

As shown in Fig. 1, the inclusion of a low-frequency dispersion ($\beta \neq 0$) leads to an asymmetric distortion of the waveform. The duration of the compression phase proves to be shorter, and the duration of the rarefaction phase, longer. The curves shown in Fig. 1 are plotted for $\beta = 3$ and two dimensionless distances $x = 0.2$ and 0.5 (curves *1*, *1*' and *2*, *2*', respectively). Evidently, the construction is valid up to the distances $x \le 3\sqrt{3}/\pi\beta$.

The waveform distortion shown in Fig. 1 is similar to that observed in experiments with high-intensity diffracted beams. The same behavior is predicted by the theory [26, 14]. Therefore, the second physical problem associated with model (55) belongs to the theory of nonlinear acoustic beams [26]. Let us consider the Khokhlov–Zabolotskaya equation in the form (see p. 346 in [14])

$$\frac{\partial}{\partial\tau}\left[\frac{\partial p}{\partial x} - \frac{\varepsilon}{c^3\rho}p\frac{\partial p}{\partial\tau} - \frac{1}{c}\frac{\partial p}{\partial\tau}\left(\frac{\partial\Psi}{\partial x} + \frac{1}{2}\left(\frac{\partial\Psi}{\partial r}\right)^2\right) + \frac{\partial p}{\partial r}\frac{\partial\Psi}{\partial r} + \frac{p}{2}\Delta_\perp\Psi\right] = \frac{c}{2}\Delta_\perp p. \qquad (85)$$

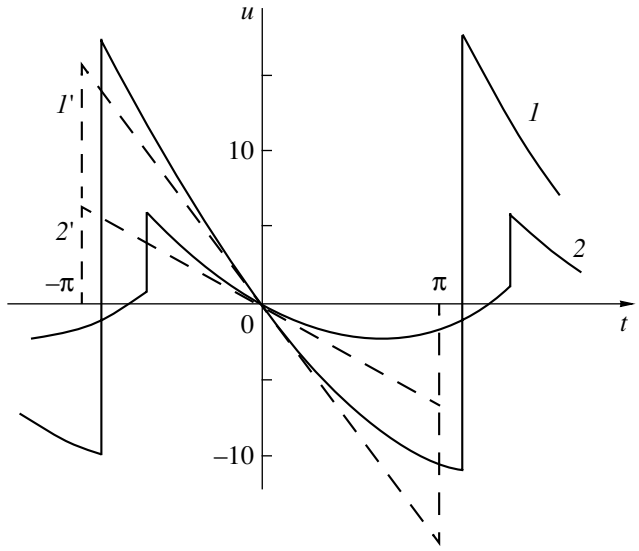

Effect of a low-frequency dispersion on the wave distortion process. The profiles are plotted for the distances $x = (1, 1')$ 0.2 and $(2, 2')$ 0.5. The solid curves are described by the self-similar solution (84) for $\beta = 3$. The dashed curves are plotted with allowance for the nonlinearity alone ($\beta = 0$, the dispersion is absent) and are presented for the sake of comparison with the profiles shown by the solid curves.

Equation (85) describes circular beams for which the relations

$$\Delta_\perp = \frac{\partial^2}{\partial r^2} + \frac{1}{r}\frac{\partial}{\partial r}, \quad \tau = t - \frac{x}{c} - \frac{1}{c}\Psi(x, r)$$

are valid, where $\varepsilon = (\gamma + 1)/2$ is the nonlinear parameter and Ψ is the eikonal. In a homogeneous medium, the distance traveled by a wave is measured along some straight line, while in an inhomogeneous medium, x may be measured along the ray representing the axis of the beam [27]. Limiting our consideration to the near-axis region, in Eq. (85) we set

$$\frac{\partial\Psi}{\partial x} + \frac{1}{2}\left(\frac{\partial\Psi}{\partial r}\right)^2 = \frac{r^2}{2}f(x) + q'(x), \qquad (86)$$

where f and q' are known functions describing the behavior of the refraction index in the medium. Determining the eikonal from Eq. (86),

$$\Psi = \frac{r^2}{2}\Phi(x) + q(x), \quad \Phi' + \Phi^2 = f,$$

we reduce Eq. (85) to the form

$$\frac{\partial}{\partial\tau}\left[\frac{\partial p}{\partial x} + \frac{f}{\Phi}\nu\frac{\partial p}{\partial\nu} - \frac{1}{c}\frac{\partial p}{\partial\tau}\left(\frac{\nu^2}{2}\frac{f}{\Phi^2} + q'\right) - \frac{\varepsilon}{c^3\rho}p\frac{\partial p}{\partial\tau} + \Phi p\right] = \frac{c}{2}\Phi^2\left(\frac{\partial^2 p}{\partial\nu^2} + \frac{1}{\nu}\frac{\partial p}{\partial\nu}\right), \qquad (87)$$

where $\nu = r\Phi(x)$. In the nonlinear geometric acoustics approximation, the right-hand side of Eq. (85) or Eq. (87) is assumed to be equal to zero. This approximation can be refined by taking into account the diffraction corrections, if we use the following model for the right-hand side of Eq. (87):

$$\left(\frac{\partial^2 p}{\partial \nu^2} + \frac{1}{\nu}\frac{\partial p}{\partial \nu}\right) \longrightarrow -\frac{2}{a^2}p, \tag{88}$$

where a is the initial beam width. Note that, for a transverse structure described by the Bessel function $J_0(\sqrt{2}\,\nu/a)$, representation (88) proves to be exact. Now, varying the right-hand side of Eq. (87) according to Eq. (88) and letting ν tend to zero, we obtain an equation describing the field of an acoustic beam near its axis:

$$\frac{\partial}{\partial \tau}\left[\frac{\partial p}{\partial x} - \frac{q'(x)}{c}\frac{\partial p}{\partial \tau} - \frac{\varepsilon}{c^3\rho}p\frac{\partial p}{\partial \tau} + \Phi(x)p\right] = -\frac{c}{a^2}\Phi^2(x)p. \tag{89}$$

In particular, for a focused wave, setting $\Phi = 1/(x - k)$ and $q' = 0$ (k is the focal distance), we reduce Eq. (89) to Eq. (75), in which $u = p(x - k)$, $\alpha = \varepsilon/c^3\rho$, and $\beta = c/a^2$.

By the change of variables

$$t = c\left[\tau + \frac{1}{c}q(x)\right], \quad u = \frac{\varepsilon}{c^3\rho}\exp\left(\int \Phi(x)dx\right),$$

Eq. (89) is reduced to a simpler form

$$\frac{\partial}{\partial t}\left[\frac{\partial u}{\partial x} - Q(x)u\frac{\partial u}{\partial t}\right] = -\frac{\Phi^2(x)}{a^2}u, \tag{90}$$

where

$$Q(x) = \exp\left(-\int \Phi(x)dx\right).$$

In the general case, when all characteristics of the medium, including the nonlinearity parameter, may depend on the x coordinate, the generalized equation can be written in the form

$$\frac{\partial}{\partial t}\left[\frac{\partial u}{\partial x} - Q(x,u)\frac{\partial u}{\partial t}\right] = F(x,u). \tag{91}$$

Equation (91) also takes into account the possibility of a more complex nonlinear response of the medium that cannot be described by a common quadratic nonlinearity.

If in Eq. (91) we set

$$Q = -\frac{\alpha}{k-x}, \quad F = -\frac{\beta}{(k-x)^2}u,$$

it takes the form of Eq. (75) and describes the focusing of a beam in a homogeneous medium. The invariant solution corresponding to operator (74) is

$$u = (k-x)G(\lambda), \quad \lambda = \frac{t}{k-x}.$$

The function $G(\lambda)$ satisfies the equation

$$\lambda G'' - \alpha(GG')' + \beta G = 0. \tag{92}$$

The exact solution to Eq. (92) at $\alpha = 0$ is expressed in terms of the Bessel functions

$$G = \sqrt{\lambda}\left[C_1 J_1(2\sqrt{\beta\lambda}) + C_2 Y_1(2\sqrt{\beta\lambda})\right],$$

and, at $\beta = 0$, it has the form

$$\lambda = -\alpha D_1 + D_2(G + D_1) - \alpha(G + D_1)\ln|G + D_1|.$$

Evidently, the two problems discussed above are not the only ones that lead to models (55), (57), and (58). For any distributed linear system with a low-frequency dispersion described by the law

$$k(\omega) = \frac{\omega}{c} - \frac{\beta}{\omega},$$

a corresponding differential equation of the form

$$\frac{\partial^2 u}{\partial t \partial x} = -\beta u \tag{93}$$

can be written. If the nonlinearity is weak, the nonlinear term is added to the evolution equation in an additive way, and Eq. (93) is transformed to, for example, Eq. (55).

Note that the "general" form (91) is still specific enough. Its symmetry properties reflect the physics of the processes under study with a higher accuracy than, for example, the symmetries of the simplified model (55) or the most general model

$$\frac{\partial^2 u}{\partial t \partial x} = G\left(x, t, u, \frac{\partial u}{\partial t}, \frac{\partial^2 u}{\partial t^2}\right),$$

which could be studied by the proposed method without any strong limitations on the class of problems under consideration.

6. CONCLUSIONS

The present study is based on the seemingly paradoxical statement that it is expedient to analyze nonlinear problems by way of their "immersion" into the class of more general and, hence, more complex models. The experience in studying the theory of nonlinear oscillations and waves on the basis of physically justified simplification of models seems to contradict the proposed approach based on the *a priori* use of symmetries. However, behind the external differences, one can discover the single nature of the two approaches. Evidently, the higher-symmetry model should contain more exact solutions. How one could obtain a higher

symmetry? On the one hand, one can follow the conventional simplification method by rejecting the elements of the model that violate its symmetry (neglecting some of the terms in the equation or modifying them in some way). On the other hand, one can complement the model to make it more symmetric by complicating the initial model. If the complex model allows a suitable exact solution, the necessary simplification can be performed at the last step of calculation, i.e., in the final formulas.

ACKNOWLEDGMENTS

This work was performed under the Cooperation Agreement between the Acoustics Department of the Faculty of Physics of Moscow State University and the ALGA BTH Center. The work was supported in part by the Russian Academy of Sciences (under the Leading Scientific Schools program) and the Russian Foundation for Basic Research.

REFERENCES

1. A. A. Andronov, A. A. Vitt, and S. É. Khaĭkin, *Theory of Oscillations*, 3rd ed. (Nauka, Moscow, 1981; Pergamon Press, Oxford, 1966).
2. R. V. Khokhlov, Radiotekh. Élektron. (Moscow) **6**, 917 (1961).
3. S. A. Akhmanov, Usp. Fiz. Nauk **149**, 917 (1986).
4. O. V. Rudenko and S. I. Soluyan, *Theoretical Foundations of Nonlinear Acoustics* (Nauka, Moscow, 1975; Consultants Bureau, New York, 1977).
5. S. Lie, *Gesammelte Abhandlungen* (Teubner, Leipzig, 1922–1937), Vols. 1–6.
6. S. Lie, *Forlesungen uber Differentialglechungen mit bekannten infinitesimalen Transformationen*, Ed. by Dr. Georg Scheffers (Teubner, Leipzig, 1891).
7. L. V. Ovsyannikov, *Group Properties of Differential Equations* (Sib. Otd. Akad. Nauk SSSR, Novosibirsk, 1962).
8. L. V. Ovsyannikov, *Group Analysis of Differential Equations* (Nauka, Moscow, 1978; Academic, New York, 1982).
9. N. H. Ibragimov, *Group Transformation in Mathematical Physics* (Nauka, Moscow, 1983; Reidel, Dordrecht, 1985).
10. *CRC Handbook of Lie Group Analysis of Differential Equations*, Vol. 1: *Symmetries, Exact Solutions and Conservation Laws*, Vol. 2: *Applications in Engineering and Physical Sciences*, Vol. 3: *New Trends in Theoretical Developments and Computational Methods*, Ed. by N. H. Ibragimov (CRC Press, Boca Raton, FL, 1994, 1995, 1996).
11. E. Hopf, Commun. Pure Appl. Math. **3**, 201 (1950).
12. O. V. Rudenko, Usp. Fiz. Nauk **149**, 413 (1986) [Sov. Phys. Usp. **29**, 620 (1986)].
13. Yu. N. Makov and O. V. Rudenko, Akust. Zh. **42**, 824 (1996) [Acoust. Phys. **42**, 728 (1996)].
14. M. B. Vinogradova, O. V. Rudenko, and A. P. Sukhorukov, *The Theory of Waves*, 2nd ed. (Nauka, Moscow, 1990).
15. *Acoustics in Problems*, Ed. by S. N. Gurbatov and O. V. Rudenko (Nauka, Moscow, 1996).
16. N. H. Ibragimov, *Elementary Lie Group Analysis and Ordinary Differential Equations* (Wiley, Chichester, 1999).
17. N. H. Ibragimov, Differ. Uravn. **29**, 1739 (1993).
18. P. S. Laplace, *Traite de Mechanique Celeste* (Gauthier-Villars, Paris, 1878; Chelsea, Bronx, N.Y., 1966), Vol. 1.
19. N. H. Ibragimov, *Theorem on Projections of Equivalence Lie Algebras* (unpublished, 1987).
20. I. Sh. Akhatov, R. K. Gazizov, and N. H. Ibragimov, *Nonlocal Symmetries: Heuristic Approach* (VINITI, Moscow, 1989); Itogi Nauki Tekh., Ser.: Sovrem. Probl. Mat. Noveishie Dostizh. **34**, 3 (1989); J. Sov. Math. **55**, 1401 (1991).
21. N. H. Ibrabimov, M. Torrisi, and A. Valenti, J. Math. Phys. **32**, 2988 (1991).
22. N. H. Ibragimov and M. Torrisi, J. Math. Phys. **33**, 3931 (1992).
23. N. H. Ibragimov and N. Safstrom, Commun. Nonlinear Sci. Numer. Simul. **9** (1), 61 (2004).
24. O. V. Rudenko and A. V. Shanin, Akust. Zh. **46**, 392 (2000) [Acoust. Phys. **46**, 334 (2000)].
25. O. V. Rudenko and C. M. Hedberg, Nonlinear Dyn. **32**, 405 (2003).
26. O. V. Rudenko, S. I. Soluyan, and R. V. Khokhlov, Dokl. Akad. Nauk SSSR **225** (5), 1053 (1975) [Sov. Phys. Dokl. **20**, 836 (1975)].
27. O. V. Rudenko, A. K. Sukhorukova, and A. P. Sukhorukov, Akust. Zh. **40**, 294 (1994) [Acoust. Phys. **40**, 264 (1994)].

Translated by E. Golyamina

Acoustical Physics, Vol. 50, No. 4, 2004, pp. 420–426. Translated from Akusticheskiĭ Zhurnal, Vol. 50, No. 4, 2004, pp. 496–503.

Localization of Nonlinear Waves in Elastic Bodies with Inclusions

D. A. Indeĭtsev and E. V. Osipova

Institute of Problems in Machine Science, Russian Academy of Sciences, Vasil'evskiĭ Ostrov, Bol'shoĭ pr. 61, St. Petersburg, 199178 Russia

e-mail: oav@phase.ipme.ru

Received June 10, 2003

Abstract—By the example of the problem of the motion of a semi-infinite string lying on an elastic base, a method for describing wave localization near inclusions is proposed for the case of a cubic nonlinearity of the base. The method applies the perturbation technique to the amplitude of a localized mode. The nature of the divergences is revealed, and the secular terms are found to belong to one of two types: inphase or antiphase with the localized wave. It is shown that a combination of the renormalization method and multiscale method provides a convergence of the solutions, which are sought for in the form of power series in the amplitude of the localized mode. It is found that the localization process is determined by the type of the discrete spectrum, type of the nonlinearity, and type of dispersion. The nonlinearity of the elastic base produces two characteristic effects. First, the frequency of the localized wave becomes dependent on the wave amplitude. Second, the system can generate traveling waves at multiple frequencies, which withdraw energy from the localized wave and cause it to decay. The decay behavior is determined by the minimum frequency of these traveling waves (because it must be higher than the cutoff frequency). The lifetime of the localized wave as a function of the mass of a dynamic inclusion exhibits a number of maxima. In particular, the first maximum corresponds to the minimum amplitude of the traveling wave at the triple frequency.

INTRODUCTION AND FORMULATION OF THE PROBLEM

As is known, in elastic bodies that have an infinite boundary with a continuous eigenfrequency spectrum displaced from zero, a discrete spectrum may appear if the body contains dynamic inclusions [1–8]. When a time-harmonic force acts on such a body, resonance phenomena may be observed. The reason is that the frequency of the perturbing force may coincide with frequencies of the discrete spectrum. Investigations into wave processes evolving in displaced-spectrum systems are presently very topical [9–15]. In particular, deceleration of an elastic wave traveling near mass inclusions has been reported by many authors [1, 2, 7, 16]. The effect was accompanied by the localization of the strain wave, which sometimes caused the structure to lose its stability and even collapse. The deceleration of the wave near inclusions is explained within the linear theory by the fact that the spectrum of modes, in which the propagating elastic wave can be expanded, contains standing waves localized near the inclusions. It is intuitively clear that nonlinear effects must distort the localization effect through changes in the "trapped" frequencies, generation of modes at multiple frequencies, interaction with the continuous spectrum, and so on. At small wave amplitudes, these effects must be insignificant. That is why the localization effect is observed in practice. Nevertheless, the effect of nonlinearity on the trapped modes in systems of elastic bodies has attracted considerable interest. In particular, one of the most important issues is the question as to how the amplitude of the elastic wave affects the frequency of the trapped modes. Another important issue is the estimation of the life time of a trapped mode.

To study these effects, this paper considers a nonstationary motion of a semi-infinite string that lies on a base with a stiffness k and a cubic nonlinearity and has a lumped mass M at its end (Fig. 1). As the load $P(\xi, \tau)$, we use a point force $P_0\delta(\xi - \xi_0)\delta(\tau)$, where δ is the Dirac delta-function, ξ is the spatial coordinate, and τ is the time. Wave processes in the string are described by the Klein–Gordon equation with a cubic nonlinearity and a delta-like right-hand side:

$$Ty_{\xi\xi} - \rho y_{\tau\tau} - ky - \nu y^3 = P_0\delta(\xi - \xi_0)\delta(\tau - 0). \quad (1)$$

The initial and boundary conditions can be represented as

$$y(\xi, 0) = y_\tau(\xi, 0) = 0, \quad (2)$$

$$y(\infty, \tau) = y_\xi(\infty, \tau) = 0, \quad (3)$$

$$Ty_\xi\big|_{\xi = 0} = (My_{\tau\tau})_{\xi = 0}. \quad (4)$$

Here, T is the string tension, ρ is its linear density, and the term νy^3 is the nonlinear contribution of the elastic base. Equation (4) is nothing but Newton's second law written for the lumped mass inclusion M. When $M > 0$, the inclusion decelerates the reflected wave and absorbs part of its energy proportional to M. These

effects are convenient to study by changing to the dimensionless variables and constants:

$$u = \frac{\sqrt{\rho T}}{P} y, \quad x = \sqrt{\frac{k}{T}}\xi, \quad t = \sqrt{\frac{k}{\rho}}\tau, \tag{5}$$

$$m = \frac{M}{\rho}\sqrt{\frac{k}{T}}, \quad \varepsilon = \frac{\nu P^2}{k\rho T}. \tag{6}$$

Then, we have

$$\begin{cases} u_{xx} - u_{tt} - u - \varepsilon u^3 = \delta(x - x_0)\delta(t) \\ u(x, 0) = u_t(0, x) = 0 \\ u(\infty, t) = u_x(\infty, t) = 0 \end{cases} \tag{7}$$

$$u_x\big|_{x=0} = (mu_{tt})_{x=0}. \tag{8}$$

It is this nonlinear problem that will be studied in this paper.

TRAPPED MODES OF OSCILLATION IN A SEMI-INFINITE STRING WITH A LUMPED MASS

First, it is necessary to find a solution to the corresponding linear problem with $\varepsilon = 0$, because we will use it in constructing the nonlinear solution in terms of the perturbation theory. In this case, Eqs. (7) and (8) have the form

$$u_{xx} - u_{tt} - u = \delta(x - x_0)\delta(t), \tag{9}$$

$$u_x\big|_{x=0} = mu_{tt}\big|_{x=0}. \tag{10}$$

To determine the physical origin of the localization effect, let us analyze the problem using the method of expansion in eigenfunctions. We will also use this method below to analyze the nonlinear problem. The eigenfunctions are found from the auxiliary spectral problem

$$u_{xx} - (1 - \omega^2)u = 0, \tag{11}$$

$$u_x\big|_{x=0} = -m\omega^2 u\big|_{x=0}. \tag{12}$$

We assume that functions u and u_x are finite at infinity. At frequencies below the boundary frequency ($\omega < 1$), a solution to Eq. (11) has the form $u = qe^{-\sqrt{1-\omega^2}x}$, which, being substituted into boundary condition (12), yields the equation for eigenfrequency of the linear problem, $\sqrt{1-\omega_0^2} - m\omega_0^2 = 0$. The solution to this equation is

$$\omega_0 = \frac{1}{m}\sqrt{\sqrt{m^2 + \frac{1}{4}} - \frac{1}{2}}. \tag{13}$$

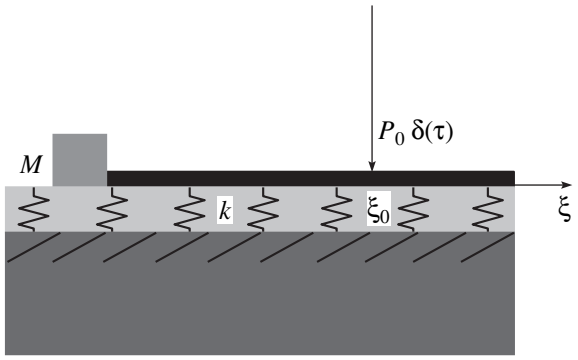

Fig. 1. Schematic diagram of a semi-infinite string with a lumped mass M at its end. The spring lies on a base with a stiffness k and is loaded by point force $P_0\delta(\xi - \xi_0)\delta(\tau)$.

Formula (13) describes a function decreasing from $\omega = 1$ at $m = 0$ to $\omega = 0$ as $m \longrightarrow \infty$. The corresponding eigenfunction has the form of the standing wave

$$u = qe^{-m\omega_0^2 x}. \tag{14}$$

Therefore, it is the presence of the discrete trapped frequency ω_0 in the spectrum that causes the wave localization effect.

At frequencies above $\omega = 1$, the solution to spectral problem (11), (12) has the form

$$u = p\left[\cos(\sqrt{\omega^2 - 1}x) - \frac{m\omega^2}{\sqrt{\omega^2 - 1}}\sin(\sqrt{\omega^2 - 1}x)\right]. \tag{15}$$

Eigenvalues ω form a continuous spectrum, which occupies the entire axis from 1 to ∞. The discrete frequency ω_0 is separated from the lower boundary $\omega_b = 1$ (referred to as the cutoff frequency) of the continuous spectrum by a certain nonzero region.

Therefore, we seek a solution to the original problem (9), (10) in the form of an expansion in terms of the eigenfunctions:

$$u(x, t) = q(t)e^{-m\omega_0^2 x} + \int_1^\infty p(\omega, t) \times \left[\cos(\sqrt{\omega^2 - 1}x) - \frac{m\omega^2}{\sqrt{\omega^2 - 1}}\sin(\sqrt{\omega^2 - 1}x)\right] d\omega. \tag{16}$$

Eigenfunctions (14), (15) are orthogonal with weight $1 + m\delta(x)$. This property can be used to obtain equations for $q(t)$ and $p(\omega, t)$. In fact, by multiplying Eq. (9) by $[1 + m\delta(x)]e^{-m\omega_0^2 x}$ and integrating the result with

respect to x from 0 to ∞, we obtain (with allowance for the boundary conditions)

$$\ddot{q}(t) + \omega_0^2 q(t) = -\frac{2m\omega_0^2 e^{-m\omega_0^2 x_0}}{1 + 2m^2\omega_0^2}\delta(t). \quad (17)$$

The solution to this equation at $q(x_0) = \dot{q}(x_0) = 0$ has the form

$$q(t) = -\frac{2m\omega_0 e^{-m\omega_0^2 x_0}}{1 + 2m^2\omega_0^2}\sin\omega_0(t - x_0)H(t - x_0), \quad (18)$$

where $H(t)$ is the Heaviside step function. The equation for p is derived in a similar manner:

$$\begin{aligned}\ddot{p} + \omega^2 p &= -\frac{2\omega}{\pi}\frac{1}{m^2\omega^4 + \omega^2 - 1} \\ &\times [\sqrt{\omega^2 - 1}\cos(\sqrt{\omega^2 - 1}x_0) \\ &- m\omega^2\sin(\sqrt{\omega^2 - 1}x_0)]\delta(t).\end{aligned} \quad (19)$$

Its solution has the form

$$\begin{aligned}p(\omega, t) &= \frac{-2/\pi}{m^2\omega^4 + \omega^2 - 1} \\ &\times [\sqrt{\omega^2 - 1}\cos(\sqrt{\omega^2 - 1}x_0) \\ &- m\omega^2\sin(\sqrt{\omega^2 - 1}x_0)]\sin\omega(t - x_0)H(t - x_0).\end{aligned} \quad (20)$$

Expressions (16), (18), and (20) completely determine the evolution of the wave. As $t \longrightarrow \infty$, the integral in Eq. (16) approaches zero and the wave is determined by the first term alone:

$$\begin{aligned}u(x, t) &= -\frac{2m\omega_0}{1 + 2m^2\omega_0^2}e^{-m\omega_0^2(x + x_0)} \\ &\times \sin\omega_0(t - x_0)H(t - x_0).\end{aligned} \quad (21)$$

This expression shows that the localized wave performs harmonic oscillations at a trapped frequency (13), which depends on the mass of the inclusion alone. Next, let us study how the nonlinearity changes the localization effect.

NONLINEAR EFFECTS

Let us seek a solution to the system of equations (7), (8) in the form of a power series in ε:

$$u(x, t) = u_0(x, t) + \varepsilon u_1(x, t) + \varepsilon^2 u_2(x, t) + \ldots. \quad (22)$$

Substituting expression (22) into Eqs. (7) and (8) and equating the coefficients of equal powers of ε, we obtain

$$\begin{cases}u_{0xx} - u_{0tt} - u_0 = \delta(x - x_0)\delta(t) \\ u_{0x}\big|_{x=0} = mu_{0tt}\big|_{x=0},\end{cases} \quad (23)$$

$$\begin{cases}u_{1xx} - u_{1tt} - u_1 = u_0^3 \\ u_{1x}\big|_{x=0} = mu_{1tt}\big|_{x=0},\end{cases} \quad (24)$$

$$\begin{cases}u_{2xx} - u_{2tt} - u_2 = 3u_0^2 u_1 \\ u_{2x}\big|_{x=0} = mu_{2tt}\big|_{x=0}\end{cases} \quad (25)$$

.....

Each of these linear equations can be solved by the technique described above; specifically, by expanding the solution in eigenfunctions of the corresponding spectral problem. In this procedure, secular terms will appear beginning already with u_1. Let us analyze them in more detail.

It can easily be seen that the secular terms are produced by the right-hand sides of Eqs. (24), (25), etc., which originate from the cubic nonlinearity. Solution (16), (18), (20) to Eq. (23) was found in the previous section. It consists of undamped and damped wave components:

$$u_0(x, t) = \tilde{u}_0(x, t) + \hat{u}_0(x, t), \quad (26)$$

where $\tilde{u}_0$ is the undamped "trapped" term (21), which describes the localized wave, and $\hat{u}_0$ is the damped term, which describes the traveling waves. Therefore, term u_0^3 on the right-hand side of Eq. (24) can be represented as

$$u_0^3 = \tilde{u}_0^3 + 3\tilde{u}_0^2\hat{u}_0 + 3\tilde{u}_0\hat{u}_0^2 + \hat{u}_0^3. \quad (27)$$

The term $\tilde{u}_0^3 = A_0^3(x)\sin^3\omega_0 t$ gives rise to secular terms, because $\sin^3\omega_0 t = (3/4)\sin\omega_0 t - (1/4)\sin 3\omega_0 t$. The term containing $\sin\omega_0 t$ causes the resonance and gives the specific solution of the form $\tilde{u}_1 \sim t\cos\omega_0 t$. This divergence can be removed using, for example, the renormalization technique [17].

The term $3\tilde{u}_0^2\hat{u}_0$ does not cause any divergence, because $\tilde{u}_0^2 \sim \cos 2\omega_0 t$.

The term $3\tilde{u}_0\hat{u}_0^2$ may cause a logarithmic divergence of the solution, which can also be removed by the renormalization technique [16] (causing the phase to logarithmically increase with time). Below we ignore this effect because it is much weaker than the effect that causes the frequency renormalization (in this case, the phase grows with time as a linear function).

The last term does not cause a divergence and can therefore be neglected just as the term $3\tilde{u}_0^2\hat{u}_0$. Now let us consider the next order of the perturbation theory. The equation for u_1 has the form

$$u_{1xx} - u_{1tt} - u_1 = -\frac{1}{4}A_0^3(x)\sin 3\omega_0 t. \quad (28)$$

Here, for the sake of simplicity, we omit all terms that cause no divergence or can be removed through frequency renormalization (or by changing the phase). The solution for u_1 also consists of two components: localized, $\tilde{u}_1$, and traveling, $\hat{u}_1$, ones. It can also be found using the eigenfunction expansion (see Eqs. (14) and (15)). The property that they are orthogonal with weight $1 + m\delta(x)$ allows us to separate equations for $\tilde{u}_1$ and $\hat{u}_1$. The $\tilde{u}_1$ solution is a correction to the localized and renormalized wave $\tilde{u}_0$; $\hat{u}_1$ determines traveling waves among which there are waves at the triple frequency:

$$\hat{u}_1 \sim \sin(3\omega_0 t - \sqrt{(3\omega_0)^2 - 1}x). \quad (29)$$

This term produces a new divergence in the second-order term in ε, because $u_0^2 \sim -\cos 2\omega_0 t$. Term $u_0^2 u_1$ contains $-\sin(\omega_0 t - \sqrt{(3\omega_0)^2 - 1}x)$ and it in turn produces secular terms $\tilde{u}_2 \sim -t\sin\omega_0 t$. This divergence cannot be removed through the frequency renormalization, because it has a different phase. It can only be removed by the multiscale method [16] or by the Krylov–Bogolyubov–Mitropol'skiĭ method, which allow for the amplitude variation of the localized wave in time. Due to the nonlinearity, the localized wave produces traveling waves at the triple frequency (only when $\omega_0 > 1/3$) with an amplitude on the order of ε. Therefore, the energy E withdraws from the localized wave at a rate of $\sim\varepsilon^2$ (i.e., $E \sim \varepsilon^2 t$), and the amplitude of the localized wave must decrease with a characteristic time of $t_0 \sim \varepsilon^{-1/2}$. If $1/5 < \omega_0 \le 1/3$, the localized wave will excite the traveling wave only at a frequency that is five times higher with an amplitude of ε^2. The energy will decrease as $\varepsilon^3 t$, and the maximum lifetime of the localized wave will therefore be on the order of $\varepsilon^{-1/3}$ (secular terms will be present in the equation for $\tilde{u}_3$). In the general case, if

$$\frac{1}{2n+1} < \omega_0 \le \frac{1}{2n-1}, \quad (30)$$

the maximum lifetime can be estimated as

$$t_0 \sim \varepsilon^{-1/(n+1)}. \quad (31)$$

On the other hand, with increasing m, the lifetime of the localized mode must decrease, because $t_0 \longrightarrow 0$ as $m \longrightarrow \infty$. Therefore, the dependence of t_0 on m at large m becomes nonmonotonic and contains narrow and sharp peaks that refer to resonances at $\omega_0 \sim 1/(2n+1)$. After this preliminary consideration, let us proceed to a quantitative description of the processes under study.

RENORMALIZATION OF THE FREQUENCY OF A TRAPPED MODE

Let us study each type of divergence separately, one by one. At first, let us analyze the strongest divergence, namely, the divergence of the localized wave itself. The undamped trapped mode (21) immediately causes solution (22) to diverge as $t\sin\omega_0 t$, because $(u_1/u_0)|_{t\to\infty} \longrightarrow \infty$. The expression for u_2 already contains terms like $t^2\sin\omega_0 t$ and so on. Thus, it is insufficient to merely seek a solution to the original nonlinear system of equations in the form of expansion (22), because the frequency of the trapped mode depends on the amplitude of the localized wave. Therefore, following the general renormalization theory [16], it is necessary to introduce a new renormalized time s according to the formula

$$t = s(1 - \varepsilon\kappa_1 - \varepsilon^2\kappa_2 - \ldots) \quad (32)$$

and substitute it into the general solution. Then we should choose κ_1, κ_2, etc. so as to make all secular terms equal to zero. If this can be done, we obtain a convergent renormalized solution (otherwise, it is necessary to use another, stronger method to provide the convergence, for example, the multiscale method or the Krylov–Bogolyubov–Mitropol'skiĭ method [16]). Let us perform this procedure. From Eqs. (23), we have

$$u_0(x, t) = -A_0 e^{-m\omega_0^2 x}\sin\omega_0 t, \quad (33)$$

$$A_0 = \frac{2m\omega_0}{1 + 2m^2\omega_0^2}e^{-m\omega_0^2 x_0}. \quad (34)$$

Here, for the sake of simplicity, we neglect the Heaviside step function $H(t - x_0)$ and the damped component (because it produces no secular terms of the type we study). By substituting Eq. (33) into Eq. (24), we obtain

$$u_{1xx} - u_{1tt} - u_1 = -\frac{3A_0^3}{4}e^{-3m\omega_0^2 x}\left(\sin\omega_0 t - \frac{1}{3}\sin 3\omega_0 t\right). \quad (35)$$

Let us seek a solution to this equation with the corresponding boundary and initial conditions in the form

$$u_1(x, t) = q_1(t)e^{-m\omega_0^2 x} + \int_1^\infty p_1(\omega, t) \times \left[\cos(\sqrt{\omega^2 - 1}x) - \frac{m\omega^2}{\sqrt{\omega^2 - 1}}\sin(\sqrt{\omega^2 - 1}x)\right]d\omega. \quad (36)$$

By substituting Eq. (36) into Eq. (35), multiplying it by $(1 + m\delta(x))e^{-m\omega_0^2 x}$, and integrating the result from 0 to ∞ with respect to x, after some algebra we obtain

$$\ddot{q}_1(t) + \omega_0^2 q_1(t) = -B\left(\sin\omega_0 t - \frac{1}{3}\sin 3\omega_0 t\right), \quad (37)$$

$$B = \frac{3A_0^3}{2}\frac{4m^2\omega_0^2 + 1}{2m^2\omega_0^2 + 1}. \quad (38)$$

The solution to Eq. (37) with the corresponding initial conditions has the form

$$q_1(t) = \frac{B}{2\omega}\left[t\cos\omega_0 t - \frac{1}{6\omega_0}\sin\omega_0 t(5 + \cos 2\omega_0 t)\right]H(t - x_0). \quad (39)$$

Substituting Eqs. (32), (33), and (39) into Eq. (22) and collecting terms with equal powers of ε, we obtain

$$u = -A_0 e^{m\omega_0^2 x}\left\{\sin\omega_0 s + \varepsilon\left[\left(\frac{B}{2A_0\omega_0} - \kappa_1\omega_0\right)s\cos\omega_0 s - \frac{B}{12\omega_0^2 A_0}\sin\omega_0 s(5 + \cos 2\omega_0 s)\right]\right\} + O(\varepsilon^2). \quad (40)$$

As can be seen from Eq. (40), to eliminate the secular term $s\cos\omega_0 s$, we must set

$$\kappa_1 = \frac{B}{2A_0\omega_0^2} = \frac{3m^2(4m^2\omega_0^2 + 1)}{(2m^2\omega_0^2 + 1)^3}e^{-2m\omega_0^2 x_0}. \quad (41)$$

Changing from variable s back to variable t, it is easy to obtain the zero-order (with respect to ε) expression for u. In this case, the actually renormalized quantity proves to be the frequency of trapped oscillations. Continuing the calculations in the subsequent orders in ε we can describe the evolution of the localized wave with any accuracy. Here we present the final expression for u in the first order:

$$u(x, t) = -\frac{2m\omega_0}{2m^2\omega_0^2 + 1}e^{-m\omega_0^2(x + x_0)}\sin\omega_* t \times\left[1 - \varepsilon\frac{m^2(2m^2\omega_0^2 + 1/2)}{(2m^2\omega_0^2 + 1)^3}e^{-2m\omega_0^2 x_0} \times(5 + \cos 2\omega_* t) + O(\varepsilon^2)\right], \quad (42)$$

where

$$\omega_* = \omega_0\left[1 + \varepsilon\frac{3m^2(4m^2\omega_0^2 + 1)}{(2m^2\omega_0^2 + 1)^3}e^{-2m\omega_0^2 x_0} + \varepsilon^2\frac{3}{16}\frac{m^4\omega_0^2}{(2m^2\omega_0^2 + 1)^6}(14m^2\omega_0^2 + 1) \times(2m^2\omega_0^2 + 1/2)e^{-4m\omega_0^2 x_0} + O(\varepsilon^3)\right]. \quad (43)$$

Thus, the trapped oscillation frequency becomes dependent on parameter ε, i.e., on the wave amplitude (because, in this case, $\varepsilon = \nu P^2/k\rho T$). The renormalized trapped frequency ω_* increases with ε as a linear function according to Eq. (43). The damped waves being neglected, the amplitude of the trapped wave is described by expression (42).

ATTENUATION OF THE LOCALIZED WAVE: MULTISCALE METHOD

Now, let us describe another key phenomenon: attenuation of the localized wave. As we already noted, the nature of this phenomenon is as follows. If the frequency of the localized wave satisfies the condition $\omega_0 > 1/3$ or, as follows from (13), if $0 < m < 6\sqrt{2}$, the localized wave excites traveling waves at the triple frequency with an amplitude ε. These waves withdraw energy from the localized wave, which leads to its decay with a characteristic time $t \sim \varepsilon^{-2}$ (because the energy withdrawal rate is $\sim\varepsilon^2$). Let us describe the effect quantitatively, using the multiscale method [17]. Consider new time scales T_n:

$$T_0 = t, \quad T_1 = \varepsilon t, \quad T_2 = \varepsilon^2 t, \ldots. \quad (44)$$

Then, $(d^2)/(dt^2) = D_0 + 2\varepsilon D_0 D_1 + \varepsilon^2(2D_0 D_2 + D_1^2) + \ldots$, where $D_n \equiv d/dT_n$. Let us seek a solution to the original equation (7) in the form

$$u = u_0(T_0, T_1, T_2, \ldots) + \varepsilon u_1(T_0, T_1, T_2, \ldots) + \varepsilon^2 u_2(T_0, T_1, T_2, \ldots) + \ldots. \quad (45)$$

By substituting expressions (44) and (45) into Eqs. (7) and equating the coefficients of equal powers of ε, we obtain

$$\begin{cases} u_{0xx} - u_{0T_0T_0} - u_0 = \delta(x - x_0)\delta(t) \\ u_{0x}\big|_{x=0} = m u_{0T_0T_0}\big|_{x=0} \end{cases} \quad (46)$$

$$\begin{cases} u_{1xx} - u_{1T_0T_0} - u_1 = u_0^3 + 2u_{0T_0T_1} \\ u_{1x}\big|_{x=0} = m u_{1T_0T_0}\big|_{x=0} \end{cases} \quad (47)$$

$$\begin{cases} u_{2xx} - u_{2T_0T_0} - u_2 = 3u_0^2 u_1 \\ + 2u_{0T_0T_2} + u_{0T_1T_1} + 2u_{1T_0T_1} \\ u_{2x}\big|_{x=0} = mu_{2T_0T_0}\big|_{x=0} \end{cases} \quad (48)$$

.....

Let us limit our study to the elimination of the secular terms in the second order alone without considering other orders. We also neglect the phase variation of the localized wave under the action of traveling waves, because this effect is weaker (~ε) than that taken into account by the frequency renormalization. In this simplified case, the zero-order solution for the localized wave can be written as

$$u_0 = A(T_2)e^{-m\omega_0^2 x}\sin\omega_0 T_0. \quad (49)$$

The substitution of Eq. (49) into Eqs. (47) yields the equation for traveling waves at the triple frequency:

$$u_{1xx} - u_{1T_0T_0} - u_1 = -\frac{A^3}{4}e^{-3m\omega_0^2 x}\sin 3\omega_0 T_0. \quad (50)$$

The term containing $\sin\omega_0 T_0$, which we have already studied, is omitted here for simplicity. The technique described above can be used to obtain the expression for undamped traveling waves (the remaining terms are neglected for simplicity):

$$u_1 = CA^3\sin(3\omega_0 T_0 - \sqrt{(3\omega_0)^2 - 1}x), \quad (51)$$

where the proportionality coefficient C is

$$C = \frac{1}{48}\frac{1}{(3m\omega_0^2)^2 + (3\omega_0)^2 - 1}. \quad (52)$$

It is clear that the condition $\omega_0 > 1/3$ is associated with the possibility of exciting waves with a wavelength of $2\pi/\sqrt{(3\omega_0)^2 - 1}$. The substitution of Eqs. (49) and (51) into Eqs. (48) yields

$$u_{2xx} - u_{2T_0T_0} - u_2 = 2\omega_0 e^{-m\omega_0^2 x}\cos\omega_0 T_0 \times\left[A'(T_2) + \frac{3C}{8\omega_0}A^5(T_2)e^{-m\omega_0^2 x}\sin(\sqrt{(3\omega_0)^2 - 1}x)\right]. \quad (53)$$

All the remaining terms, which do not contribute to the divergence, are ignored. The solution to this equation contains a localized wave whose divergent part has the form

$$\tilde{u}_2 \sim -\text{const}\,T_0\sin 3\omega_0 T_0 e^{-m\omega_0^2 x} \times\left[A'(T_2) + \frac{1}{4t_*}A^5(T_2)\right], \quad (54)$$

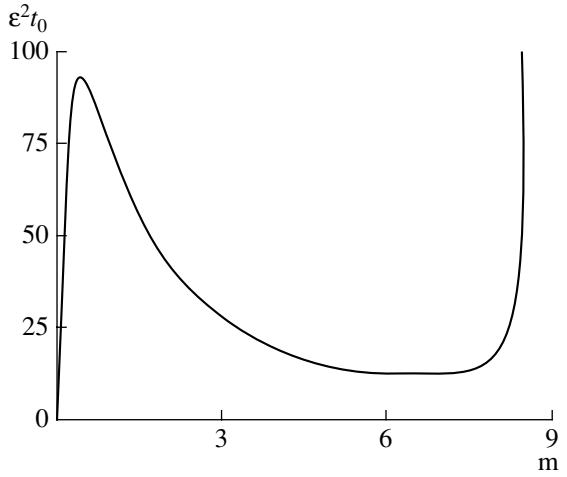

Fig. 2. Decay time versus the dimensionless mass m of the inclusion at $x_0 = 0.75$.

where

$$t_* = \frac{3}{4C}\sqrt{\frac{(3m\omega_0^2)^2 + (3\omega_0)^2 - 1}{(3\omega_0)^2 - 1}}\frac{m^2\omega_0^2 + 1/2}{m\omega_0}. \quad (55)$$

The condition for the secular term to vanish yields the equation that describes the attenuation of the localized wave:

$$A'(T_2) + A^5(T_2)/(4t_*) = 0. \quad (56)$$

At $A(0) = A_0$, its solution has the form $A(T_2) = A_0/\sqrt[4]{A_0^4 T_2/t_* + 1}$. Changing back to the variable t, we obtain

$$A(t) = \frac{A_0}{\sqrt[4]{1 + t/t_0}}, \quad (57)$$

$$t_0 = \left(\frac{4}{\varepsilon A_0}\right)^2\frac{[(3m\omega_0^2)^2 + (3\omega_0)^2 - 1]^{3/2}}{\sqrt{(3\omega_0)^2 - 1}} \times\frac{m^2\omega_0^2 + 1/2}{2m\omega_0}. \quad (58)$$

Evidently, t_0 has the meaning of the characteristic lifetime of the localized mode. Figure 2 shows $\varepsilon^2 t_0$ versus the dimensionless mass of inclusion at $x_0 = 0.75$. This curve reaches its maximum value of 93 at $m = 0.47$ and minimum value of 12.8, at $m = 6.8$. As $\omega_0 \longrightarrow 0$, the lifetime tends to zero and the localization effect disappears. When $\omega_0 \longrightarrow 1/3$, the lifetime t_0 grows without limit. This means that, when $\omega_0 \longrightarrow 1/3$, we must allow for the energy withdrawn by traveling waves of the next order, namely, waves with an amplitude ε^2 and a fivefold frequency $5\omega_0$. As a result, the lifetime will be a nonmonotonic function of $m \longrightarrow \infty$ and it will contain

a number of sharp peaks (the higher the index of the excited mode, the higher and narrower the peak is). In the region $m < 8.4$, one can use formula (58).

Now, let us write the final expression for the localized wave in the principal order of the asymptotic expansion in ε by taking into account all the above effects:

$$u(x, t) = -u_0(t)e^{-m\omega_0^2 x}\sin[\omega_*(t - x_0)]H(t - x_0) + O(\varepsilon), \quad (59)$$

$$u_0(t) = \frac{m\omega_0}{m^2\omega_0^2 + 1/2}\frac{e^{-m\omega_0^2 x_0}}{\sqrt[4]{1 + t/t_0}}, \quad (60)$$

$$\omega_* = \omega_0\left[1 + \frac{3\varepsilon}{4\omega_0^2}\frac{4m^2\omega_0^2 + 1}{2m^2\omega_0^2 + 1}u_0^2 + O(\varepsilon^2)\right]. \quad (61)$$

The lifetime of this mode is rather long. In particular, at $\varepsilon = 0.02$, the characteristic lifetime is $t_0 \sim 10^5\sqrt{k/\rho}$. For example, at $\rho \approx 1$ kg/m and $k \approx 10^8$ kg m/s^2, we have $t_0 \approx 10$ s. For the localization effect to occur, the mass of the inclusion must be small enough. In particular, for $T \sim 10^4$ kg m/s^2, $m = 5$ corresponds to 0.05 kg.

CONCLUSIONS

The following conclusions can be drawn from the above study. The cubic nonlinearity of the elastic base does not eliminate the localization effect and does not distort the form of the localized waves, but causes two characteristic phenomena. First, the frequency of the localized wave becomes dependent on the wave amplitude (formula (61)). Second, the system can produce traveling waves at multiple frequencies ($3\omega_0$, $5\omega_0$, $7\omega_0$, …), which withdraw energy from the localized wave and cause it to decay. The character of the decay is determined by the position of the minimum frequency of the traveling waves relative to the cutoff frequency. In particular, in terms of the dimensionless variables, in which the cutoff frequency is equal to 1, the traveling wave at the triple frequency is excited when the condition $\omega_0 > 1/3$ or $m > 6\sqrt{2}$ is satisfied. In this case, the localized wave decays as $t^{-1/4}$. If $1/5 < \omega_0 < 1/3$, then $u_0 \sim t^{-1/6}$; if $1/7 < \omega_0 < 1/5$, then $u_0 \sim t^{-1/8}$; and so on. The behavior of the lifetime of the localized mode versus the mass of the dynamic inclusion exhibits a number of maxima. In particular, the first maximum corresponds to the minimum amplitude of the traveling wave at the triple frequency (Fig. 2).

ACKNOWLEDGMENTS

This work was supported by the Russian Foundation for Basic Research, project no. 02-01-00879.

REFERENCES

1. V. A. Babeshko, I. I. Vorovich, and I. F. Obraztsov, Izv. Akad. Nauk SSSR, Mekh. Tverd. Tela **3**, 74 (1990).
2. Yu. I. Bobrovnitskiĭ and M. P. Korotkov, Akust. Zh. **37**, 872 (1991) [Sov. Phys. Acoust. **37**, 453 (1991)].
3. G. V. Stupakov and S. S. Kurennoy, Phys. Rev. E **49**, 794 (1994).
4. A. K. Abramian, J. Acoust. Soc. Am. **100**, 2723 (1996).
5. V. L. Andreev, J. Acoust. Soc. Am. **100**, 2686 (1996).
6. A. K. Abramian and D. A. Indeĭtsev, Akust. Zh. **44**, 437 (1998) [Acoust. Phys. **44**, 371 (1998)].
7. D. Indeitchev, J. Acoust. Soc. Am. **105**, 1196 (1999).
8. V. I. Erofeev, *Wave Processes in Solids with Microstructure* (Mosk. Gos. Univ., Moscow, 1991).
9. D. V. Evans, C. M. Linton, and F. Ursell, Q. J. Mech. Appl. Math. **46**, 253 (1993).
10. J. D. Kaplunov and S. V. Sorokin, J. Acoust. Soc. Am. **97**, 3898 (1995).
11. D. A. Indeĭtsev and E. V. Osipova, Zh. Tekh. Fiz. **66** (8), 124 (1996) [Tech. Phys. **41**, 811 (1996)].
12. D. V. Evans and N. Kuznetsov, in *Gravity Waves in Water of Finite Depth* (Comp. Mech., Southampton, 1997), p. 343.
13. D. A. Indeytsev and E. V. Osipova, in *Proceedings of 14th International Workshop on Water Waves and Floating Bodies, Port Huron, Michigan, USA* (1999), p. 41.
14. D. A. Indeĭtsev and E. V. Osipova, Zh. Tekh. Fiz. **70** (12), 1 (2000) [Tech. Phys. **45**, 1513 (2000)].
15. V. A. Babeshko, B. V. Glushkov, and Zh. F. Zinchenko, *Dynamics of Inhomogeneous Linearly Elastic Media* (Nauka, Moscow, 1989).
16. A. H. Nayfeh, *Introduction to Perturbation Techniques* (Wiley, New York, 1981; Mir, Moscow, 1984).

Translated by A. Khzmalyan

Acoustical Physics, Vol. 50, No. 4, 2004, pp. 427–433. Translated from Akusticheskiĭ Zhurnal, Vol. 50, No. 4, 2004, pp. 504–511.

Orientation Phenomena in Nematic Liquid Crystals under a Periodic Compressional Deformation

O. A. Kapustina

Andreev Acoustics Institute, Russian Academy of Sciences, ul. Shvernika 4, Moscow, 117036 Russia

e-mail: bvp@akin.ru

Received May 15, 2003

Abstract—The orientation behavior of homogeneous planar layers of nematic liquid crystals with open and closed ends in the field of compressional deformations caused by an acoustic effect is studied. The mechanisms determining the connection of the optical response of a nematic liquid crystal (the variable component of an optical signal and its spectrum) with the acoustic parameters (the oscillation amplitude and frequency, and the amplitude of sound pressure) and the layer thickness are revealed. The factors responsible for the mechanism and modes of acoustooptic conversion are considered. It is demonstrated that, by varying the layer thickness, it is possible to implement different modes of signal conversion. The possibility of designing a new modification of a sound receiver based on a nematic liquid crystal and the specific features of this design are discussed. Its advantages over conventional sound pressure receivers based on nematic liquid crystals are indicated, in particular, the absence of limitation of the frequency of the received signal in the low-frequency range. © *2004 MAIK "Nauka/Interperiodica".*

An investigation of the optical properties of an anisotropic liquid in a plane capillary under the effect of periodic deformations is interesting not only by itself from a scientific point of view [1–4] but is also important practically, in connection with the development of acoustooptic devices on the basis of liquid crystals for various purposes [5–7]. Physical situations corresponding to the problems of the development of various modifications of such devices can be classified according to the type of boundary conditions at the ends of a capillary filled with a liquid crystal (closed or open ends), the type of deformation (shear or compression) determined by the acoustic action, and the initial orientation of the molecules of the liquid crystal in the layer (planar, twist structure, homeotropic, etc.). The most advanced studies are those of the distortion of the homeotropic macrostructure of a layer of a nematic liquid crystal and its optical response under the conditions, where one of the plates forming a capillary is motionless and the other oscillates in the layer plane, and in this case an oscillating flow of a nematic liquid with a linear profile of velocity is realized between the capillary plates [2]. As for the changes of the orientation state of the homogeneous macrostructure of a nematic liquid crystal in the case of the oscillation of this plate in the direction of the normal to the layer and its periodic compression, these aspects for both cases of homeotropic and planar arrangement of molecules in the layer are studied mainly for the ultrasonic frequency range, where the viscous wavelength in a nematic liquid crystal is considerably smaller than the layer thickness [2–9].

This paper presents the results of an experimental study of the influence of periodic compressional deformations on macroscopically homogeneous planar layers of nematic liquid crystals in capillaries with different boundary conditions at the ends in the frequency range, where the sound wavelength λ, viscous wavelength λ_{vis}, and orientation wavelength λ_{or} correlate with the layer thickness d_0 and the layer length L in such a way that the following inequalities are valid:

$$\lambda_{vis} \ll L \ll \lambda, \quad \lambda_{or} \ll d_0 \ll \lambda_{vis}. \tag{1}$$

Let us consider a planar layer of a nematic liquid crystal in a plane capillary with open ends in the coordinate system with its origin $x = 0$, $z = 0$ at the center of the lower boundary of the layer and the z axis directed along the normal to the layer (Fig. 1a). The layer has a preferred optical axis (the director **n**) lying in its plane and directed along the x axis. The values of the refraction indices of such a "plate" of a uniaxial crystal are given by the optical indicatrix in the form of an ellipsoid of revolution about the principal symmetry axis $O'O'$ [11]. In the initial unperturbed state, the planar layer is birefringent, $\Delta n = n_0 - n_e$, where n_0 and n_e are the indices of light refraction with the polarization vector **E** perpendicular and parallel to the optical axis, respectively. We preset an external action on the nematic layer by the motion of the lower boundary of the capillary in the form $\xi_z(t)|_{z=0} = \xi_{0z}\sin\omega t$. Here ξ_z, ξ_{0z}, and $\omega/2\pi$ are the particle displacement, its amplitude, and the frequency of oscillations.

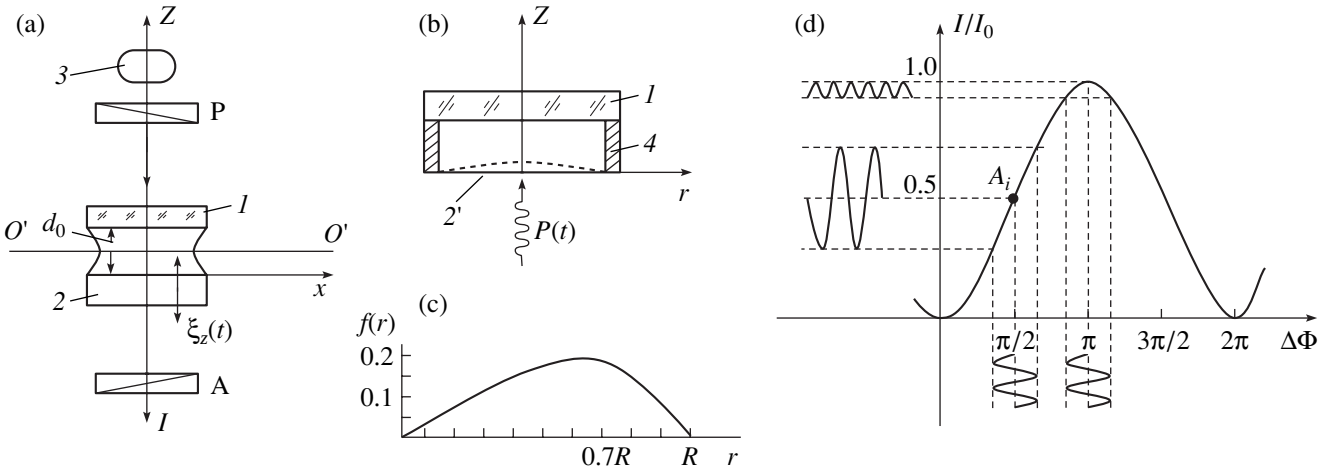

Fig. 1. Schemes of experiments on the effect of a periodic compressional deformation on planar layers of a nematic liquid crystal in a capillary with (a) open and (b) closed ends: (*1*) plate, (*2*) substrate, (*2*') membrane, (*3*) source of sensing radiation, and (*4*) spacer. (c) Radial distribution of the velocity of motion of the nematic liquid in a capillary with closed ends and a membrane with a thickness of 0.1 cm and a radius of 1 cm. $E = 10^{11}$ Pa, $\nu = 0.3$. (d) The conversion characteristic.

The appearance of the following effects is possible in this physical situation:

(i) periodic variation of the layer thickness $d(t) = d_0 + \xi_z(t)$ caused by compression due to the boundary oscillation;

(ii) periodic spreading of the nematic liquid along the layer towards its ends and in the opposite direction ("streaming");

(iii) development of orientation instability in the oscillating flow of the nematic liquid when the oscillation amplitude exceeds a certain threshold value.

Let us give some estimates to understand the general pattern of the phenomenon and determine the individual contributions of the aforementioned factors.

The periodic variation of the layer thickness due to the oscillations of one of its boundaries leads to oscillations of the optical path and, hence, to oscillations of the phase difference between the interfering ordinary and extraordinary waves, which manifests itself in oscillations of light intensity at the output of the system formed by the polarizer (P), the nematic layer, and the analyzer (A) shown in Fig. 1a. This effect can be evaluated proceeding from the classical formula of crystal optics [11], which in the physical situation under investigation in the case of crossed polarizers P and A has the form

$$m = I(t)/I_0 = \sin^2[0.5\Delta n k_0 d(t)]. \quad (2)$$

Here, k_0 is the wave number of light and I_0 and $I(t)$ are the intensities of light transmitted through polarizer P and analyzer A, respectively. The polarization vector of light transmitted through polarizer P and incident upon the nematic layer, **E**, makes an angle of $\pi/4$ with the director. Expanding the function $\sin^2[\text{const}\, d(t)]$ into the Taylor series in particle displacement $\xi_z(t)$ and restricting the consideration to the terms of the second order, we obtain

$$m = I(t)/I_0 \approx \sin^2(0.5\Delta n k_0 d_0) + 0.5\Delta n k_0 \sin(\Delta n k_0 d_0)\xi_z(t) + 0.5(\Delta n k_0)^2 \cos(\Delta n k_0 d_0)\xi_z^2(t) + O[\xi_z^3(t)]. \quad (3)$$

From Eq. (3) it follows that the variable component of the optical signal can be connected with the oscillation amplitude by both linear and quadratic dependences, if the initial thickness of the layer of a nematic liquid crystal is such that one of the conditions given below is satisfied:

$$\cos[\Delta n k_0 d_0] = 0, \quad (4)$$

or

$$\sin(\Delta n k_0 d_0) = 0. \quad (5)$$

The spectral distribution of the optical signal also depends on the layer thickness: either it is represented by even m_{2i} and uneven m_{2i+1} harmonics (at $d_{0i} \cong \pi(i + 0.5)/\Delta n k_0$) or it is the sum of only even harmonics m_{2i} (at $d_{0i} \cong \pi i/\Delta n k_0$). It is necessary to note one more essential fact following from Eq. (3): the coefficients at $\xi_z(t)$ and $\xi_z^2(t)$ do not depend on the layer thickness but are determined by the anisotropy of the nematic liquid crystal and the light wavelength $2\pi/k_0$.

The second effect manifesting itself in the planar layer of a nematic liquid crystal under the conditions of its periodic compression is connected with the inhomogeneity of the distribution of streaming velocity of the nematic liquid over the layer thickness, which causes a director rotation in the plane *xz* through the angle $\varphi \sim \partial V_x/\partial z$. The component of the flow velocity along the *x* axis is equal to $V_x = [6\xi_{0z}\omega xz(d - z)/d^3]\cos\omega t$. This

leads to a periodic variation of birefringence $\Delta n(t)$ and an oscillation of the phase difference between ordinary and extraordinary waves. In this case, the intensity of light after analyzer A that is crossed with respect to the vector **E** is

$$m = I(t)/I_0 = \sin^2[0.5\Delta n(t)k_0 d_0]. \quad (6)$$

From of the form of the function $\Delta n(t) = (n_0 - n_e)\cos\varphi(t) = (n_0 - n_e)[1 - \varphi^2(t)]$ it follows that (i) although the angle $\varphi(t)$ increases with the growth of the oscillation amplitude, the period-average value of ξ_{0z}^2 decreases, which leads to the attenuation of the optical effect connected with the streaming of the nematic liquid; (ii) the variable component of the optical signal, which is connected with the effect of streaming, is proportional to ξ_{0z}^2 at small oscillation amplitudes, and the oscillation of light intensity occurs with a doubled frequency; and (iii) the value of $\Delta n(t)$ is connected with the coordinate x of the sensing point of the optical signal via the velocity V_x determining the rotation angle of the director $\varphi(t)$ due to the streaming.

According to [1], the angle $\varphi(t) = (\alpha_3\cos\Psi/\alpha_2)\varphi_0(t)$, where Ψ is the angle between the director and the vector of streaming velocity, α_2 and α_3 are the Leslie coefficients of viscosity, and $\varphi_0(t)$ is the angle of the director rotation under the same conditions of streaming but in the layer of a nematic liquid crystal with a homeotropic orientation of molecules. In the case of a nematic liquid crystal, the Leslie coefficients of viscosity are such that the ratio α_3/α_2 is within 0.01–0.1 [1]. Therefore, the optical effect connected with the director oscillation is sufficiently small. Moreover, it follows from the form of the function $V_x(x)$ that the value of $\varphi(t)$ is maximal at the open ends of the layer and decreases towards its center. This allows one to assume that a region must exist near the center, where the optical effect caused by the director oscillation may be ignored. Let us evaluate the dimensions of this region in a layer with an axial symmetry and a radius R at an arbitrary value of the angle Ψ between the director and the vector of the flow velocity. The optical phase difference $\Delta\Phi$ of ordinary and extraordinary waves, which accompanies the director oscillation in the case of streaming, with allowance for the change of molecule orientation over the layer thickness is equal to $\Delta\Phi = 0.5\Delta n k_0\int_0^d \varphi^2(t)dz$. Assuming that $\Delta\Phi \le 0.01$ rad and expressing the angle $\varphi(t)$ through the angle $\varphi_0(t) = [6R\alpha_2\xi_{0z}(d - 2z)/\gamma d^3]\sin\omega t$ [12], we determine the critical radius R_1 of the region, where the contribution of the effect caused by the streaming of the nematic liquid to the modulation of optical radiation is minimal:

$$R_1 \le 0.1\gamma d^{3/2}/\alpha_3\xi_{0z}(3\Delta n k_0)^{1/2}\cos\Psi. \quad (7)$$

The effect of orientation instability of a homogeneous planar macrostructure of nematic liquid crystals in oscillating flows of different types has been discussed many times in detail in the literature [13, 14]. This effect is known to manifest itself in the appearance of stationary spatially-modulated structures (one- or two-dimensional) when the oscillation amplitudes exceed a certain threshold value. The consequence of this effect is a change in the spatial characteristics of the luminous flux after its transmission through a layer of a nematic liquid crystal. However, this phenomenon is of a local character and, according to theoretical predictions [14], a region exists in the layer plane where this instability does not occur. In the general case, the radius of this region R_2 depends in a very complex way on the frequency and amplitude of oscillations, on the angle Ψ between the director and the vector of the flow velocity, on the layer thickness, and on the viscoelastic constants of the nematic liquid crystal. However, in the geometry under consideration (Fig. 1a), the radius R_2 can be estimated using the following approximate expression [14]:

$$R_2 \sim d^2[1 + K_1K_2/\alpha_2\alpha_3\omega^2(d/2\pi)^4]^{1/2}/\xi_{0z}\sin\Psi. \quad (8)$$

Here, K_1 and K_2 are the Frank's constants of elasticity, which correspond to transverse flexural and torsional deformations [1].

The estimates given above concern the physical situation given in Fig. 1a, i.e., a layer of a nematic liquid crystal with open ends. As analysis shows, a change in the boundary conditions at the capillary ends does not influence the general pattern of the phenomenon, and the "set" of competing mechanisms and their basic laws persist in a capillary with closed ends. As for some quantitative discrepancies, the most significant one is connected with the mechanism of streaming of the nematic liquid. For example, in the geometry shown schematically in Fig. 1b, the nematic layer is "compressed" between (*1*) a massive plate and (*2*') a flexible membrane and placed into a sound field of the form $P(t) = P_0\exp(-i\omega t)$. The pressure in the sound wave incident upon such a cell deflects the thin membrane in the middle and compresses the liquid at the center of the layer; as a result, the compression gradient causes streaming of the nematic liquid. According to [15], the radial transfer of liquid particles in the layer, U_r, which initiates the director rotation through the angle $\varphi \sim \partial U_r/\partial z$ is determined by the expression

$$U_r = [36P_0Rz(d - z)/d^2\rho c^2(1 + 36Ad/\rho c^2R^4)] \times f(r)\cos\omega t. \quad (9)$$

Here, $A = EH^3/12(1 - \nu^2)$, E is Young modulus, ν is Poisson's ratio of the membrane material, H is the membrane thickness, ρ and c are the density and sound velocity in the nematic liquid crystal, and $f(r)$ is the function describing the radial distribution of U_r in the cell (Fig. 1c). From Eq. (9) it follows that, in a capillary with closed ends, the velocity of spreading of the nematic liquid reaches its maximum at a distance of $0.7R$

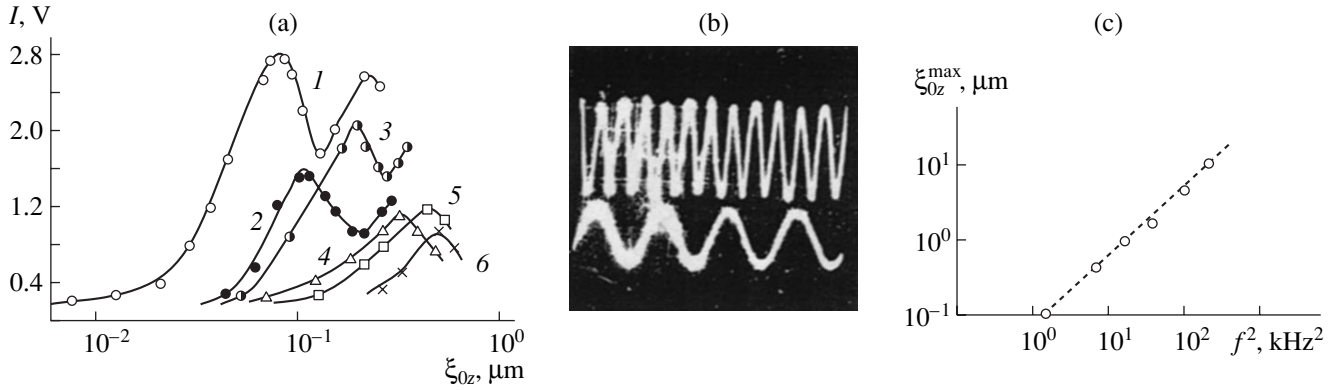

Fig. 2. (a) Intensity of the variable components of an optical signal with the frequencies f, $2f$, $3f$, $4f$, $5f$, and $6f$ versus the amplitude of oscillations at a frequency of 120 Hz for a capillary with open ends in the case of readout within a region with the radius $r < 4$ cm; the layer thickness is 50 μm. (b) Oscillograms of the acoustic (the lower curve, frequency f) and optical (the upper curve, frequency $5f$) signals; the layer thickness is 50 μm, and the frequency is 120 Hz. (c) Oscillation amplitude corresponding to the position of the first maximum of the variable component of the spectrum at the frequency f versus the oscillation frequency; the layer thickness is 50 μm.

from the layer center rather than at its edges, which is characteristic of a capillary with open ends.

The ideas discussed above provide an opportunity to separate independent competing physical effects (periodic variation of the optical path, oscillation of the director, and orientation instability) in the experiment and determine the optimal conditions for their measurement. Performing the measurements within the region with the radius $r < R_1, R_2$, it is possible to minimize the contribution of the effect connected with the director oscillation due to streaming into the modulation of the sensing optical radiation, to eliminate the influence of the orientation instability, and to detect the oscillations of the intensity of the luminous flux that are caused by the periodic variations of the optical path in the layer. Let us estimate the values of the radii R_1 and R_2 at the oscillation amplitude $\xi'_{0z} = 1/\Delta n k_0$ when the modulation depth of the sensing radiation is 100% for typical values of the materials constants of the nematic liquid crystal and typical cell parameters. Assuming $\alpha_2 = -0.8$ P, $\alpha_3 = -10^{-2}$ P, $\Delta n = 0.2$, $\Psi = \pi/4$, $K_1 = 5.5 \times 10^{-7}$ dyn, $K_2 = 4 \times 10^{-7}$ dyn, and $k_0 = 1.5 \times 10^5$ cm^{-1}, for $\omega = 1.9 \times 10^3$ s^{-1} we obtain values of R_1 and R_2 equal to 0.6 and 0.9 cm, respectively, at a layer thickness of 65 μm, and 1.4 and 3 cm for a layer thickness of 100 μm. The calculation demonstrates that, at the oscillation amplitude ξ'_{0z} within the region with the radius R_1, the correction connected with the spreading of the nematic liquid crystal does not exceed 1% of the optical effect caused by the periodic variation of the optical path under the conditions of the quasi-linear conversion determined by Eq. (4). It is essential that, at $\xi_{0z} < \xi'_{0z}$, the contribution of spreading to the modulation is even less significant, since the effect connected with it is proportional to ξ_{0z}^2 and the effect caused by the oscillation of the optical path is connected with ξ_{0z} by a linear dependence.

Two series of experiments were conducted using nematic liquid crystals filling plane capillaries with different boundary conditions. The schemes of experimental setups are given in Figs. 1a and 1b. We used nematic liquid crystals of the H-8 type, i.e., an eutectic mixture of MBBA (4-mexibenzylidene-4'-butylaniline) and EBBA (4-ethoxybenzylidene-4'-butylaniline), in which the nematic phase occurs within 12–54°C. To form planar boundary conditions, the internal surfaces of the plates forming the capillary were cleaned chemically, and a coating of polyvinyl alcohol was applied to them and then polished thoroughly in one direction. The layer thickness in the experiments varied within 50–100 μm. Observation of the orientation state of the nematic liquid crystal in the capillary was conducted by the polarization-optical method using the known schemes [1, 11].

In the first series of experiments, a nematic liquid crystal filled a capillary formed by (*1*) a thick plate (glass) and (*2*) a massive substrate (titanium) with a light-reflecting surface (the scheme in Fig. 1a). Here the plate is motionless and the substrate, being rigidly connected with an electrodynamic driver fed by a generator, performs piston-type vibrations along the normal to the layer plane. The amplitude of these substrate oscillations is detected by a contact accelerometer. The voltage supplied from the generator to the driver and its frequency are monitored with the help of a voltmeter and a frequency meter. The optical part of the setup consists of (*3*) a light source (a polarization illuminator or an LG-59 laser), polarizing filters (polarizer P and analyzer A), and a photomultiplier connected with a dc voltmeter and a spectrum analyzer.

In the second series of experiments, a capillary with closed ends and filled with a nematic liquid crystal had

an axial symmetry (R = 1.2 cm). It was formed by (*1*) a thick plate (glass) and (*2*') a thin membrane (phosphor bronze) with a light-reflecting surface (the scheme in Fig. 2b). This cell was connected through the membrane with a small-volume chamber, where an acoustic radiator and a receiver of sound pressure were located. As in the first series of the experiments, the information readout was performed in polarized light and in the reflection mode, but the optical part of the setup was designed using different devices, i.e., a light-emitting diode as a light source and a photodiode with a photocurrent amplifier as a light sensor.

In both series of the experiments, the optical response of the planar nematic layer to periodic compressional deformation was measured within the frequency range of 0.1–1.5 kHz by detecting the constant and variable components of the luminous flux transmitted through the polarizer P–nematic layer–analyzer A system, and the readout was conducted only within the region determined by the condition $r < R_1, R_2$, where the contribution of the effect caused by the oscillation of the optical path to the modulation was dominant.

Let us discuss the results of these measurements. Figure 2a shows a typical family of curves *1–6* obtained in the first series of experiments. These curves illustrate the change in the intensity I of the spectral components of an optical signal with the frequencies f, $2f$, $3f$, $4f$, $5f$, and $6f$ in the course of an increase in the oscillation amplitude when the thickness of the nematic layer is inconsistent with both conditions (4) and (5). One can see that the content and weight of spectral components depend on the oscillation amplitude: at small oscillation amplitudes, the harmonic with the frequency of the acoustic signal is dominant, but as the amplitude grows, harmonics with higher numbers arise and their overlapping occurs. Note that uneven harmonics prevail over even ones. It is essential that the amplitude dependences of all harmonics have a periodic and attenuating character, the first maximum of each subsequent harmonic coinciding with the first minimum of the preceding one; i.e., an increase in the level of acoustic excitation leads to a pump-over of energy from one harmonic to another. Figure 2b presents an example of oscillograms of an acoustic driving signal and an optical response. Variation of the oscillation frequency at a constant layer thickness leads only to a change in the oscillation amplitude $\xi_0^{\max}$ corresponding to the position of the first maximum of the harmonics (Fig. 2c).

From the experimental data given in Fig. 2a, one can see that, in the most general case of an arbitrary initial layer thickness d_0, the connection of the spectral components of an optical signal with the oscillation amplitude is nonlinear and has a periodic attenuating character, both even and uneven harmonics being present in the spectrum, which agrees with the estimates given above.

It is of interest to verify experimentally the implications that complement the generalized expression (3).

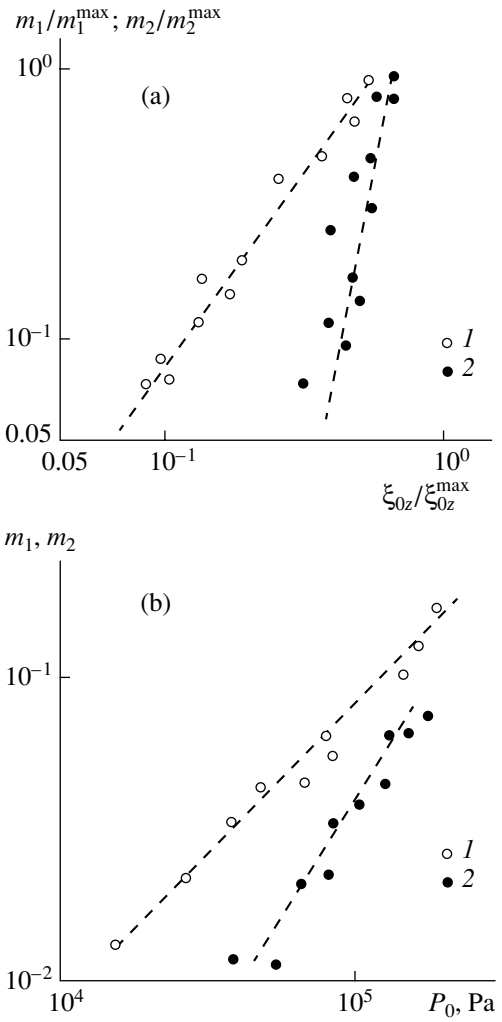

Fig. 3. Optical response of a planar layer of a nematic liquid crystal to a periodic compressional deformation in a capillary with different boundary conditions at r < 0.5 cm. (a) Dependence of the variable components of the spectrum of an optical signal with the frequencies f (a layer thickness of 100 μm, the quasi-linear conversion mode) and $2f$ (a layer thickness of 65 μm, the nonlinear conversion mode) on the oscillation amplitude (notations *1* and *2*, respectively) for a capillary with open ends; the normalization is performed with respect to the maxima of the first and second harmonics $m_1^{\max}$ = 2.8 V and $m_2^{\max}$ = 2 V and the corresponding oscillation amplitudes $\xi_{0z}^{\max}$ = 0.1 μm and $\xi_{0z}^{\max}$ = 0.13 μm; the frequency is 300 Hz. (b) Relation of the variable components of an optical signal, m_1 and m_2, to the sound pressure amplitude for a capillary with closed ends and a nematic layer thickness of 100 and 65 μm (notations *1* and *2*, respectively); the frequency is 430 Hz.

According to Eqs. (4) and (5), at a certain initial layer thickness d_0, such limiting cases are realized in which not only the spectrum of an optical signal changes but also its relation to the acoustic signal. This confirms the experimental data obtained with samples of a nematic liquid crystal with a thickness d_0 of 65 and 100 μm,

which satisfies conditions (4) and (5), respectively (Fig. 3a). The optical signal readout was performed when the condition $r < R_1, R_2$ was satisfied. It is important to note that, in the case of a layer thickness of 100 μm, when Eq. (5) is valid, even and uneven harmonics are present in the spectrum and the harmonic with the frequency f prevails, its relation to the oscillation amplitude being linear (notation *1* in Fig 3a). A transition to a layer thickness of 65 μm satisfying condition (4) manifests itself in the change of the optical signal spectrum (it contains only even harmonics and the harmonic with the frequency $2f$ predominates) and leads to a quadratic amplitude dependence of the second harmonic m_2 (notation *2* in Fig. 3a). To make the representation and comparison of data more convenient, the values of m_1, m_2, and ξ_{0z} are normalized to the values of $m_1^{\max}$, $m_2^{\max}$, and $\xi_{0z}^{\max}$ corresponding to the first maxima of the oscillating functions $m_1(\xi_{0z})$ and $m_2(\xi_{0z})$. Thus, according to theoretical estimates, we observed two types of relation between the acoustic and optical signals: linear and quadratic.

Let us consider the results of the second series of experiments. A layer of a nematic liquid crystal in a capillary with closed ends is positioned in a sound field (the scheme in Fig. 1b). In the general case of arbitrarily selected values of the initial layer thickness, the optical response of the nematic liquid crystal to sound pressure in a wave repeats the laws observed in a similar situation for a capillary with open ends in the case of vibration of its lower supporting plate. The laws characteristic of the limiting cases examined above, which are determined by the selection of the initial thickness of the nematic layer, are also repeated. For example, in the case of validity of condition (4) ($d_0 \cong$ 65 μm), the signal spectrum contains only even harmonics, and the harmonic with the frequency $2f$ related to the amplitude of sound pressure by a quadratic dependence predominates (notation *2* in Fig. 3b). In the case of the layer thickness of 100 μm satisfying condition (5), the signal spectrum (both even and uneven harmonics are present in it, the latter clearly prevailing) and the character of its connection with the amplitude of sound pressure change. As measurements showed, the harmonic with a frequency f demonstrates a linear dependence on the sound pressure amplitude (notation *1* in Fig. 3b).

The above consideration shows that, independent of the type of boundary conditions at the ends of the capillary filled with a nematic liquid and independent of the form of the external acoustic action (particle displacement or sound pressure), the modulated optical signal has a discrete spectrum containing a series of harmonics whose relative weight depends on the oscillation amplitude. It is also found that, in the case of signal readout within a limited region with the radius $r < R_1, R_2$, it is possible to implement different modes of acoustooptic conversion determined by the oscillations of the optical path under periodic compression of the nematic layer in the direction of the z axis (i.e., normally to the layer plane) at the frequencies satisfying condition (1), at a planar orientation of molecules of the nematic liquid crystal in the layer plane. The conversion mode depends on the choice of the initial thickness of the nematic layer, which determines the initial value of the optical phase difference $\Delta\Phi$ and, hence, presets the position of the working point on the conversion characteristic $I/I_0(\Delta\Phi)$ (Fig. 1d). The interesting situation for practice is the one where, according to condition (4), at the layer thickness $d_{0i} = \pi(0.5 + i)/\Delta n k_0)$ corresponding to the optical phase difference $\Delta\Phi_i = 0.5\pi + i\pi$, a quasi-linear mode of conversion is implemented. In this case, the conversion coefficient at $\xi_z(t)$ is determined only by the values of birefringence of the nematic liquid crystal and the wavelength of sensing radiation. This mechanism indicates a unique opportunity to design a new type of receiving linear element on the basis of nematic liquid crystals, which are free of restrictions connected with the conversion mechanism for the upper limiting frequency of the periodic compressional deformation inducing the optical effect. Such a restriction can be introduced only by a violation of the condition $f \ll c/2\pi L$ corresponding to the assumption that, in the process of compression of the layer, the nematic liquid crystal behaves as an incompressible liquid. However the influence of this factor can be eliminated if, in modeling a receiver, we provide soft boundary conditions at the edges of the layer of a nematic liquid crystal so that, in the case of its compression, the spreading of the nematic liquid would occur instead of its uniform compression. It is evident that such conditions are realized in a capillary with open ends. In this connection, the functional scheme given in Fig. 1a is preferable for modeling. Moreover, it provides an opportunity to obtain a higher sensitivity. Let us make some estimates using a characteristic common for modeling acoustic devices employing nematic liquid crystals [2], namely, using the amplitude of particle displacement ξ_0^*, at which the modulation depth of sensing radiation under the conditions of quasi-linear conversion is 1%. The value of $\xi_0^* = 0.005$ μm follows from the experimental data obtained for a capillary with open ends at the layer thickness satisfying Eq. (4), when a quasi-linear conversion mode is implemented near the points A_i on the curve of the conversion characteristic. This is almost one order of magnitude lower than the value of the same parameter for the most advanced model of a sound receiver employing a nematic liquid crystal, which operates using the effect of polarization modulation of light due to a periodic shearing deformation with a homeotropic orientation of molecules in the nematic layer [2]. As for a receiving element with closed ends that is designed according to the scheme given in Fig. 1b, its sensitivity is l/ξ_0 times lower than that of an element with open ends. This is

connected with the fact that, in a receiving element with closed ends, the optical effect depends not only on the oscillation amplitude ξ_0 but also on the deflection l of the membrane $2'$ under the action of the alternating sound pressure $P(t)$ in a wave. According to [15], the maximal displacement of a membrane of radius R at its center is connected with the oscillation amplitude ξ_0 in a wave by the following expression: $l = 3d\omega\xi_0/c(1 + 36dA/\rho c^2R^4)$. In the case of the value of $\xi_0^* = 0.005$ μm, which is the "threshold" for the observation of the optical effect, the membrane deflection is only 2.4×10^{-6} μm. This estimate is obtained for a nematic layer with a thickness of 100 μm and a frequency of 430 Hz for a membrane with the parameters given in the caption of Fig. 1c.

It is necessary to note that the restrictions connected with the self-noise of a nematic liquid crystal and the noise of sensing radiation affect the threshold value of ξ_0^* in real conditions. The noise of a nematic liquid crystal that is caused by surface and volume fluctuations of orientation in the sound frequency range does not exceed $10^{-10}I_0$. As for the noise of the laser source that is caused by the quantum nature of light, according to our data, the noise level for a typical laser like LG-79 is $10^{-2}I_0$. Therefore, in modeling a sound receiver, it is necessary to make arrangements for a correct selection of optical parts and the utilization of optimal readout schemes. For example, it is possible to employ the scheme of differential connection of photodiodes, which provides an opportunity to reduce the noise level down to a value of $10^{-4}I_0$ [5].

Expression (3) allows one to conclude that the conversion mode preset by the position of the working point on the conversion characteristic depends not only on the optical anisotropy, the wavelength of sensing radiation, and the conversion index i but also on the nematic layer thickness. Therefore, providing for a precise control of the layer thickness in the design of a receiving element, which gives an opportunity to preset the values of the phase difference $\Delta\Phi_i$ in the course of the device operation, it is possible not only to control the conversion modes but also to provide adaptation to changes in the operation conditions, which may be connected, for example, with a temperature variation. Although nematic liquid crystals with a very large optical anisotropy ($\Delta n = 0.17$–0.22) and a weak temperature dependence of Δn have been already synthesized, the implementation of this opportunity is of certain interest. It is also necessary to stress that the flexibility of controlling the device parameters can be useful for solving the problems related to various nonlinear operations with received acoustic signals (frequency multiplication, squaring, etc.). It is essential that these operations can be conducted simultaneously and independently, together with a simultaneous reception of signals in the linear mode by a single receiving element.

In conclusion, one more advantage of a sound receiver employing a nematic liquid crystal with a planar orientation of molecules should be mentioned. The receiver performs a conversion of a periodic compressional deformation of a nematic layer into oscillations of the optical path and a modulation of sensing radiation by a direct transformation of the external acoustic action into the oscillatiory motion of the supporting plate of the capillary without employing any intermediate mechanical links (coupling rods, transitional elastic layers, levers, etc.), which are necessary for conventional sound receivers based on nematic liquid crystals. This provides an opportunity to simplify the design of a receiving element and develop a model that is technologically advanced in comparison with the known models and compatible with modern optical devices.

REFERENCES

1. P. de Gennes, *The Physics of Liquid Crystals* (Clarendon Press, Oxford, 1974; Mir, Moscow, 1977).
2. A. P. Kapustin and O. A. Kapustina, *Acoustics of Liquid Crystals* (Nauka, Moscow, 1986).
3. E. Guyon and P. Pieranski, J. Phys. Colloq. **36** (C1-3), 203 (1975).
4. E. Dubois-Violette, E. Guyon, I. Janossy, *et al.*, J. Mech. **16** (5), 733 (1977).
5. Yu. V. Bocharov, I. N. Gurova, and O. A. Kapustina, Mol. Cryst. Liq. Cryst. **209**, 19 (1991).
6. N. M. White and J. D. Turner, Meas. Sci. Technol. **8**, 1 (1997).
7. Yu. V. Bocharov, O. A. Kapustina, and V. N. Reshetov, Akust. Zh. **38**, 616 (1992) [Sov. Phys. Acoust. **38**, 340 (1992)].
8. T. Wolinski and R. Dambrovski, Condens. Matter News **4** (3), 30 (1995).
9. O. A. Kapustina, in *Handbook of Liquid Crystals*, Ed. by D. Demus, J. Goodby, G. W. Gray, H. W. Spiess, and V. Vill (VCH, Weinheim, 1998), Vol. 1, Chap. 7.11.
10. J. V. Selinger, M. S. Spector, V. A. Greanya, *et al.*, Phys. Rev. E **66**, 051708 (2002).
11. A. Sommerfeld, *Optics* (Academic, New York, 1954; Inostrannaya Literatura, Moscow, 1953).
12. O. A. Kapustina, E. N. Kozhevnikov, and G. N. Yakovenko, Zh. Éksp. Teor. Fiz. **87**, 849 (1984) [Sov. Phys. JETP **60**, 483 (1984)].
13. D. I. Anikeev and O. A. Kapustina, Zh. Éksp. Teor. Fiz. **110**, 1328 (1996) [JETP **83**, 731 (1996)].
14. V. N. Reshetov, Akust. Zh. **31**, 639 (1985) [Sov. Phys. Acoust. **31**, 383 (1985)].
15. E. N. Kozhevnikov, Akust. Zh. **28**, 238 (1982) [Sov. Phys. Acoust. **28**, 143 (1982)].

Translated by M. Lyamshev

Acoustical Physics, Vol. 50, No. 4, 2004, pp. 434–437. Translated from Akusticheskiĭ Zhurnal, Vol. 50, No. 4, 2004, pp. 512–515.

Physical Model of Sound Scattering by a School of Fish Located Near an Interface

A. A. Kleshchev

St. Petersburg State Marine Technical University, ul. Lotsmanskaya 3, St. Petersburg, 190008 Russia
e-mail: gakusei@VG2068.spb.edu

Received October 23, 2002

Abstract—Sound scattering by a fairly sparse school of bladder fish is studied in a free medium, near an interface, and in a waveguide. The air bladder of a fish is approximated by a prolate spheroid with an axial ratio of 1:10. Characteristics of the back reflection of sound by a school of fish are calculated for various angles of irradiation, variable number of fish in the school, and various velocities of fish with respect to each other. *© 2004 MAIK "Nauka/Interperiodica".*

It is well known [1, 2] that the scattering of acoustic signals by a bladder fish is mainly determined by the reflecting characteristics of its air bladder. The air bladder is often approximated by a perfectly soft prolate spheroid [2] with a corresponding size and axial ratio. As calculations show, the soft tissues surrounding the bladder can affect the reflected signal only at rather high frequencies [1, 3].

This paper studies sound scattering by a physical model of a fairly sparse fish school; i.e., it considers several (rather than one) scatterers located close to each other and to a boundary between two media. According to [7], the total reflected signal is formed not by the interaction of scatterers but by the interference of signals reflected by individual scatterers if the distance between the scatterers is three or more times greater than the size of the largest scatterer. This criterion was accepted in the calculations. In addition, the school of fish was assumed to be located near one of the boundaries: water–air or water–bottom. For simplicity, the boundaries were assumed to be plane and ideal, the air was replaced by vacuum, and the bottom was assumed to be perfectly rigid. This model allows one to perform the calculations using imaginary scatterers and imaginary sources [7].

The scattering characteristics of individual fish, which were approximated by soft prolate spheroids, were computed using the series expansions in angular and radial spheroidal functions [4–6]. The use of imaginary sources and scatterers makes it possible to eliminate the interface and consider a free medium, in which real and imaginary sources and scatterers are located.

A source and a receiver form a combined system located in the far-field zone (Fraunhofer zone) of a fish school. Therefore, the directions from the centers of all scatterers to the center of the combined source–receiver system are parallel to each other.

A school of six fish of different length is schematically represented in Figs. 1a and 1b. Figure 1a corresponds to a side view, and Fig. 1b shows the top view. Figure 1c displays the side view of a school of three fish. As indicated above, the scatterers are represented by prolate spheroids simulating the air bladders of the fish.

It is easy to show that, as applied to three fish, the total value of the angular characteristic $\Psi_\Sigma(\theta_0, 0)$ in the direction to the real source is given by the expression

$$\begin{aligned}\Psi_\Sigma(\theta_0; 0) &= \Psi_1(\theta_0; 0)\exp[-2ikl_1\sin\theta_0]\\ &+ \Psi_2(\theta_0; 0)\exp[-2ikl_2\cos(\alpha-\theta_0)]\\ &+ \Psi_3(\theta_0; 0)\exp[-2ikl_3\cos(\beta-\theta_0)]\\ &+ \Psi_1(\theta_0; 0)\exp[2ikl_1\sin\theta_0]\\ &+ \Psi_2(\theta_0; 0)\exp[-2ikl_2\cos(\alpha+\theta_0)]\\ &+ \Psi_3(\theta_0; 0)\exp[-2ikl_3\cos(\beta+\theta_0)] \pm 2\Phi_1(\theta_0, \pi)\\ &\pm 2\Phi_2(\theta_0, \pi)\exp[-2ikl_2\cos\alpha\cos\theta_0]\\ &\pm 2\Phi_3(\theta_0, \pi)\exp[-2ikl_3\cos\beta\cos\theta_0],\end{aligned}$$

where the plus sign refers to the Neumann condition (a perfectly rigid bottom) and the minus sign refers to the Dirichlet condition (a perfectly soft surface); the functions $\Psi_1(\theta_0, 0)$, $\Psi_2(\theta_0, 0)$, and $\Psi_3(\theta_0, 0)$ are the angular characteristics of real scatterers, and the functions $\Phi_1(\theta_0; \pi)$, $\Phi_2(\theta_0; \pi)$, and $\Phi_3(\theta_0; \pi)$ are the corresponding angular characteristics of imaginary scatterers. The angles α and β are measured with respect to the interface and characterize the angular positions of the centers of the second and third scatterers; the angles θ_0 and φ_0 represent polar and azimuthal spherical angles (with a polar X axis) of the combined system located at a distance R in the Fraunhofer zone with respect to the school. The angles θ_0 and φ_0 remain constant and do not

1063-7710/04/5004-0434$26.00 © 2004 MAIK "Nauka/Interperiodica"

depend on Z (even when fish move relative to each other in the school) for the following reasons:

(i) the distance R in real situations is three to four orders of magnitude greater than the size of the school and, hence, than the displacements of fish in the school, which are used in the calculations;

(ii) the rotation axes of spheroids are always parallel to the X axis.

In the analytical solution, R is assumed to be equal to ∞; as a result, a plane wave is incident on the school.

The distance Z is measured from the interface for both real and imaginary scatterers. The signal reflected from the school, with fish moving within it, depends on the variations in distances between individual fish (because of their motion with different velocities) and on the changes in the distances between real and imaginary scatterers.

Figure 2 shows the values of the modulus $|\Psi_\Sigma(\theta_0; 0)|$ of back reflection for the angle $\theta_0 = 30°$ (as a function of Z) for six (curve *1*) and three (curve *2*) fish moving away with the same velocity from the boundary between water and a perfectly rigid bottom, where Z is the distance in meters along the normal to the boundary.

In the school of three species, the fish have wave sizes $C = 100$, 65, and 15; in the school of six fish, one fish has a wave size $C = 100$ (the largest one), two fish have a size $C = 65$, and three fish have a size $C = 15$. Straight lines *3* and *4* refer to the schools of six and three fish, respectively, in a free medium. Figure 3 shows the moduli of the back reflection $|\Psi_\Sigma(\theta_0; 0)|$ for a school of three fish, one of which does not move ($C = 100$) and two others ($C = 65$ and $C = 15$) move along the Z axis (the water–vacuum boundary) with different velocities (curve *1*). Curve *2* refers to the same type of motion of the fish, but in a free medium.

Since the air bladder is three to four times smaller than the size of the fish, for the largest air bladder, whose length is 0.8 m ($C = 100$), the minimal distance between the individual fish increased with time.

Unlike the previous study [8], where only vertical movement of fish relative to each other was analyzed, here we consider the general case, when both horizontal and vertical relative motion of fish in the school takes place. As applied to two fish, the geometry of the problem is displayed in Fig. 4.

The notation used in Fig. 4 is as follows: α and α' are the initial and running values of the angle for the center of the second fish relative to the boundary; l_{10} and l_1, l_{20} and l_2 are the initial and running values of the distances from the origin O to the centers of the first and second fish, respectively; Δl_{2x} and Δl_{2z} are the running displacements of the second fish along the X and Z axes with respect to its initial position; and Δl is the running vertical displacement of the first fish. The angles α and β are connected with the z coordinate by the relations $z_2 = l_{20}\sin\alpha$ and $z_3 = l_{30}\sin\beta$, where l_{30} is the initial distance from the center of the third fish to the origin O.

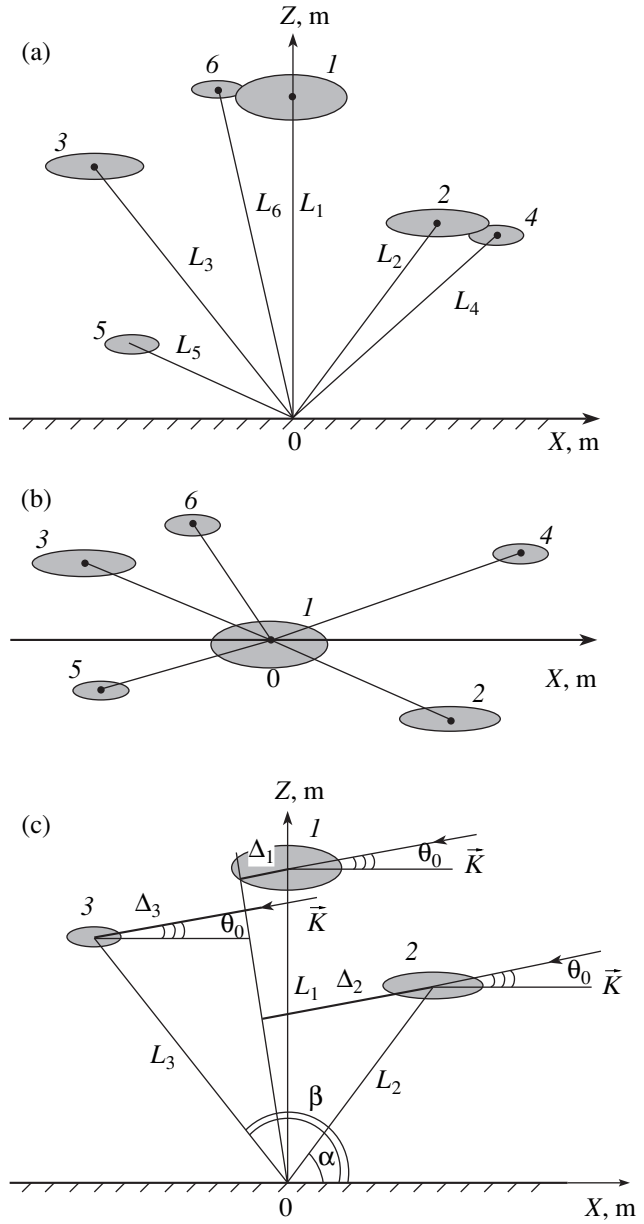

Fig. 1. Schematic representation of a school of fish.

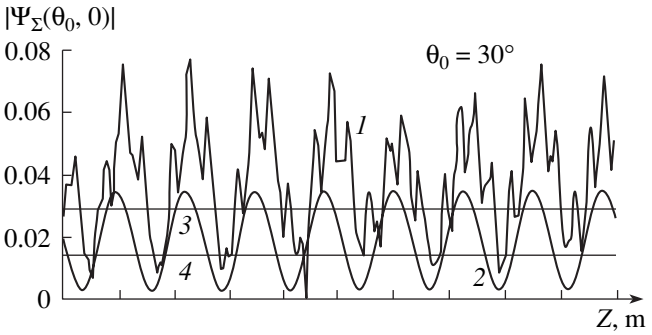

Fig. 2. Modulus of the back reflection $|\Psi_\Sigma(\theta_0; 0)|$ for schools of (*1*) six and (*2*) three fish ($\theta_0 = 30°$) for vertical movement of fish.

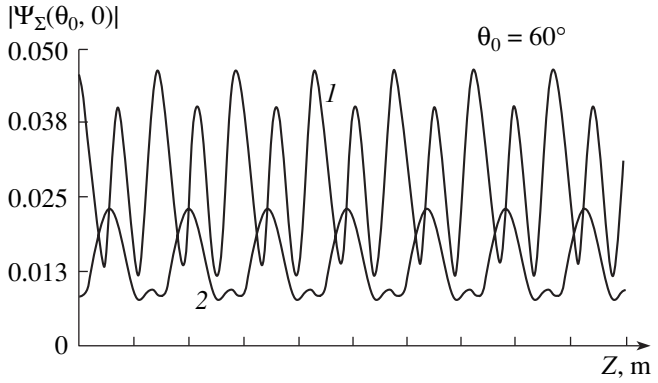

Fig. 3. Modulus of the back reflection $|\Psi_\Sigma(\theta_0; 0)|$ for a school of three fish ($\theta_0 = 60°$) moving along the Z axis with different velocities.

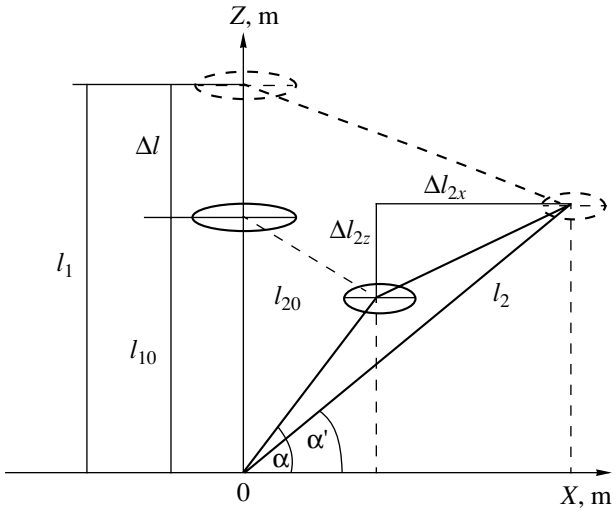

Fig. 4. Schematic representation of the displacement of two fish with respect to the boundary, along the X and Z axes.

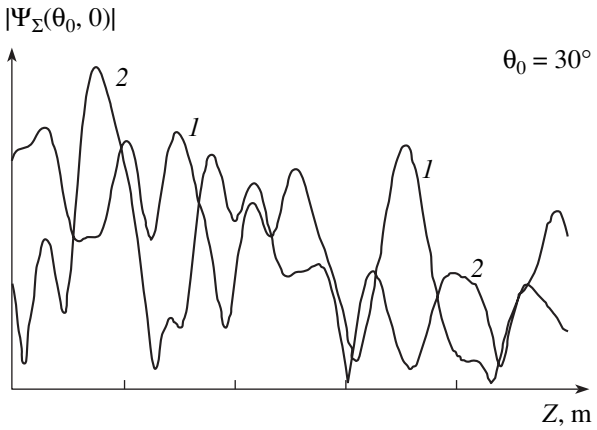

Fig. 5. Modulus of the back reflection $|\Psi_\Sigma(\theta_0; 0)|$ ($\theta_0 = 30°$) for a school of six fish moving along the X and Z axes near (*1*) a perfectly rigid or (*2*) a perfectly soft boundaries.

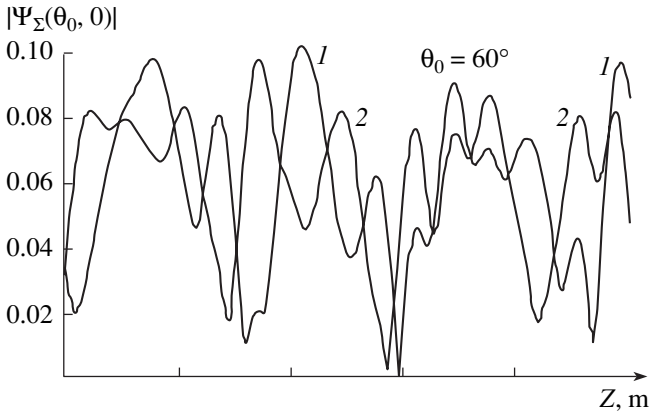

Fig. 6. Modulus of the back reflection $|\Psi_\Sigma(\theta_0; 0)|$ ($\theta_0 = 60°$) for a school of six fish moving along the X and Z axes near (*1*) a perfectly rigid or (*2*) a perfectly soft boundaries.

The moduli of the back reflection $|\Psi_\Sigma(\theta_0; 0)|$ for this kind of fish movement in a school of six fish located near a perfectly rigid (curve *1*) or perfectly soft (curve *2*) medium are shown in Fig. 5 ($\theta_0 = 30°$) and Fig. 6 ($\theta_0 = 60°$).

An analysis of the calculations shows that

(i) for a vertical displacement along the Z axis (without horizontal displacement along the X axis), the modulus of the back reflection $|\Psi_\Sigma(\theta_0; 0)|$ varies periodically for equal and different velocities of individual fish movements in the school;

(ii) for a simultaneous motion in the vertical (along the Z axis) and horizontal (along the X axis) directions, the periodic character of variation of $|\Psi_\Sigma(\theta_0; 0)|$ disappears;

(iii) the value of $|\Psi_\Sigma(\theta_0; 0)|$ is almost independent of the type of the ideal interface (perfectly soft or perfectly rigid);

(iv) a fish school located near a boundary between liquid and an ideal medium gives a greater reflected signal (averaged over Z) in the direction to the source, as compared to a free medium, because of the multiple reflection of sound by the boundary; in actual conditions, this excess should vanish, because the real boundary is not even and smooth and the lower boundary (the bottom) is far from being perfectly rigid;

(v) the oblique angles of irradiation ($\theta_0 = 30°$ and $\theta_0 = 60°$), which were used in the calculations, are of the greatest practical interest, because, in the case of the normal incidence on the boundary ($\theta_0 = 90°$), the reflection of sound by a school is masked by a strong signal reflected from the boundary, and the selection of the

desired signal (from the school) on the background of the boundary is not always possible even by using pulsed signals modulated in amplitude or frequency.

If the influence of tissues and bones of fish on the reflected signal is taken into account, the physical model of each individual fish becomes more complex. However, the problem is quite solvable in this case as well [3, 9, 10].

ACKNOWLEDGMENTS

I am grateful to O.L. Davydova and Yu.Yu. Shkitina for their assistance in the calculations.

REFERENCES

1. I. B. Andreeva and V. G. Samovol'kin, *Scattering of Acoustic Waves from Marine Organisms* (Agropromizdat, Moscow, 1986).
2. D. Weston, in *Underwater Acoustics*, Ed. by V. M. Alberts (Plenum, New York, 1967; Mir, Moscow, 1970), Vol. 2.
3. A. A. Kleshchev and D. M. Rostovtsev, Akust. Zh. **32**, 691 (1986) [Sov. Phys. Acoust. **32**, 432 (1986)].
4. A. A. Kleshchev and L. S. Sheĭba, Akust. Zh. **16**, 264 (1970) [Sov. Phys. Acoust. **16**, 219 (1970)].
5. A. A. Kleshchev and I. I. Klyukin, *Fundamentals of Hydroacoustics* (Sudostroenie, Leningrad, 1987).
6. A. A. Kleshchev, *Hydroacoustic Scatterers* (Sudostroenie, St. Petersburg, 1992).
7. A. A. Kleshchev, Akust. Zh. **25**, 143 (1979) [Sov. Phys. Acoust. **25**, 78 (1979)].
8. A. A. Kleshchev, in *Proceedings of XII Session of the Russian Acoustical Society* (GEOS, Moscow, 2002), Vol. 1, p. 225.
9. V. M. Bel'kovich, V. A. Grigor'ev, B. G. Katsnel'son, and V. G. Petnikov, Akust. Zh. **48**, 162 (2002) [Acoust. Phys. **48**, 133 (2002)].
10. E. L. Shenderov, Akust. Zh. **48**, 684 (2002) [Acoust. Phys. **48**, 607 (2002)].

Translated by A. Svechnikov

Acoustical Physics, Vol. 50, No. 4, 2004, pp. 438–445. Translated from Akusticheskiĭ Zhurnal, Vol. 50, No. 4, 2004, pp. 516–523.

Vector–Phase Characteristics of Acoustic Fields: Statistical Analysis and Measurement Algorithms

V. I. Klyachkin

Morfizpribor Central Research Institute, Chkalovskii pr. 46, St. Petersburg, 197376 Russia

e-mail: mfp@mail.wplus.net

Received June 25, 2003

Abstract—Statistical characteristics of an acoustic field that are based on the data of simultaneous measurements of pressure and acoustic velocity vector are investigated. Conditions of the formation of vector–phase characteristics of acoustic field are formulated in relation to the dispersion properties of the medium. Cross-correlation functions of the components of the vector field are presented. Expressions for the characteristic functionals of vector–phase relationships in acoustic fields and, in particular, for the acoustic energy flux are derived with the use of functional methods. Algorithms of space–time processing of the energy flux vector and the optimum measurement algorithm for a Gaussian vector–phase field are considered. The signal-to-noise ratio is determined as the quality index of vector reception algorithms, and its relation to the corresponding parameter of scalar pressure field measurements is revealed. Indices of relative efficiency of vector algorithms are determined depending on the dispersion characteristics of the medium (the flux algorithm) and the dimension of the input vector of observations (the optimum algorithm). © *2004 MAIK "Nauka/Interperiodica".*

The investigation of statistical properties of vector–phase (V–Ph) characteristics of acoustic fields has attracted considerable interest in recent decades from both scientific and applied points of view, with reference to the development of both systems for studying acoustic waveguides and algorithms for measuring V–Ph fields. Here, the term V–Ph field means the four-component field that combines the acoustic pressure field (scalar) and the particle velocity field (vector).

The purpose of this paper is to study the probability structure of the V–Ph characteristics of an acoustic field and to analyze some algorithms of their measurement and space-time processing, which can be considered as an extension of paper [1] discussed in review [2].

As is known, the equations of acoustics of continuous media in the adiabatic approximation describe the pressure field $P(\bar{\mathbf{x}}, t)$ and the particle velocity field $\bar{\mathbf{V}}(\bar{\mathbf{x}}, t)$ related through the Euler equation

$$\rho_0 \frac{\partial}{\partial t}\bar{\mathbf{V}}(\bar{\mathbf{x}}, t) = -\nabla_x P(\bar{\mathbf{x}}, t);$$
$$\bar{\mathbf{V}}(\bar{\mathbf{x}}, t) = -\rho_0^{-1}\int_{-\infty}^{t} \nabla_{\bar{\mathbf{x}}} P(\bar{\mathbf{x}}, \tau)d\tau, \quad \bar{\mathbf{V}}(\bar{\mathbf{x}}_1 - \infty) = 0. \tag{1}$$

These two fields together completely describe an acoustic medium and are related, in addition to Eq. (1), by the equations of continuity and state:

$$\frac{\partial}{\partial t}\rho(\bar{\mathbf{x}}, t) + \rho_0 \mathrm{div}\bar{\mathbf{V}}(\bar{\mathbf{x}}, t) = 0;$$
$$p(\bar{\mathbf{x}}, t) = c^2\rho(\bar{\mathbf{x}}, t). \tag{2}$$

Here, as usual, the density is $\rho_0 = \text{const}$ (for a homogeneous and nonstratified medium), c is the sound velocity, and $\rho(\bar{\mathbf{x}}, t)$ is the variable acoustic field of density.

Equations (1) and (2) are known to allow the introduction of potential $\Psi(\bar{\mathbf{x}}, t)$

$$p(\bar{\mathbf{x}}, t) = \rho_0 \frac{\partial}{\partial t}\Psi(\bar{\mathbf{x}}, t); \quad \bar{\mathbf{V}}(\bar{\mathbf{x}}, t) = -\nabla_{\bar{\mathbf{x}}}\Psi(\bar{\mathbf{x}}, t), \tag{3}$$

which is a field characteristic that cannot be measured directly. Wave equations for P, $\bar{\mathbf{V}}$, and Ψ follow from Eqs. (1) and (2). In the context of the algorithmic procedures suggested below, we can consider the measurable random fields P and $\bar{\mathbf{V}}$ related through Eq. (1) as the coordinates of the full vector $\bar{\mathbf{A}}$ of the acoustic state of the medium in the four-dimensional phase space (p; V_1; V_2; V_3). The linear independence of the components of vector $\bar{\mathbf{A}}(A_1 \ldots A_L) \equiv A(p; V_1; V_2; V_3)$[1] imposes certain physical conditions on the acoustic characteristics of the medium in which sound propagates. To ensure matching with Eq. (1), the condition has the form

$$\mathrm{Det}U_{kl} \neq 0; \quad k, l = 1 \ldots L, \tag{4}$$

where $\mathrm{Det}U_{kl}$ is the Gramian and $U_{kl} = (A_k, A_l) \equiv \int A_k(\bar{\mathbf{x}}, t)A_l(\bar{\mathbf{x}}, t)d\bar{\mathbf{x}}\,dt$ is the matrix of scalar products of the acoustic vector $\bar{\mathbf{A}}$ in the phase space $(\bar{p}, \bar{\mathrm{v}})$. With this condition, the system of equations of linear acoustics (1), (2) defines the space–time evolution of the four-component vector $\bar{\mathbf{A}}(\bar{p}, \bar{\mathrm{v}})$.

1063-7710/04/5004-0438$26.00 © 2004 MAIK "Nauka/Interperiodica"

For the case $\bar{\mathbf{A}} \equiv \bar{\mathbf{A}}(p, \nu_1)$, we have in particular ($\nu_1 \equiv \nu$):

$$\mathrm{Det}\begin{vmatrix} (p, p); (p, \bar{\nu}) \\ (\bar{\nu}, p); (\bar{\nu}, \bar{\nu}) \end{vmatrix}, \tag{4a}$$

where $(\cdot, \cdot) \equiv \int \ldots d\bar{\mathbf{x}}dt$ is the scalar product.

We have the relationships

$$(p, p) = 2\rho_0 c^2 V; \quad (\bar{\nu}, \bar{\nu}) = 2\rho_0^{-1} T, \tag{5}$$

where V and T are the average potential and kinetic energies in volume $V_0 \times T_0$:

$$V = \frac{1}{2\rho_0 c^2} \int\limits_{V_0 \times T_0} p^2(\bar{\mathbf{x}}, t) d\bar{\mathbf{x}}dt;$$
$$T = \frac{\rho_p}{2} \int\limits_{V_0 \times T_0} \nu^2(\bar{\mathbf{x}}, t) d\bar{\mathbf{x}}dt. \tag{5a}$$

The sum $E = T + V$ makes the total energy; $V = T = \frac{1}{2}E$ for oscillatory motion. Correspondingly, $(P, P) = \rho_0 c^2 E$ and $(\bar{\nu}, \bar{\nu}) = \rho_0^{-1} E$. Similarly, we have

$$(P, \bar{\nu}) = \int\limits_{V_0 \times T_0} p(\bar{\mathbf{x}}, t)\bar{\nu}(\bar{\mathbf{x}}, t) d\bar{\mathbf{x}}dt = \int\limits_{V_0} S(\bar{x}) d\bar{x}, \tag{5b}$$

where $S(\bar{x}) = U_{\mathrm{gr}}\varepsilon(\bar{x})$, ε is the average energy of a unit volume, and U_{gr} is the group velocity. Correspondingly, we have

$$(p, \bar{\nu}) = U_{\mathrm{gr}} E. \tag{5c}$$

From Eqs. (4) and (5), we obtain

$$\mathrm{Det}A \equiv (p, p)(\bar{\nu}, \bar{\nu}) - (p, \bar{\nu})(\bar{\nu}, p) = (c^2 - U_{\mathrm{gr}}^2)E^2. \tag{6}$$

When $c^2 \neq U_{\mathrm{gr}}^2$, i.e., in systems with dispersion of any origin, $\mathrm{Det}A \neq 0$, so that components P and $\bar{\nu}$ appear linearly dependent only for $c = U_{\mathrm{gr}}$, i.e., in systems without dispersion (for example, in an unbounded medium).

In particular, for plane traveling waves $p = F\left(t - \frac{1}{c}\bar{\mathbf{k}}_0\bar{\mathbf{x}}\right)$, where $\mathbf{k}_0$ is the unit propagation vector normal to the wave front, we obtain the relationship

$$\bar{\mathbf{v}}(\bar{\mathbf{x}}, t) = \frac{\bar{\mathbf{k}}_0}{\rho_0 c} p(\bar{\mathbf{x}}, t). \tag{7}$$

Hence, the field of a plane traveling wave is completely determined by the pressure field p and direct measurements of the particle velocity field are unnecessary.

However, for V–Ph characteristics of acoustic fields of the general-type (for which Eq. (7) is unsatisfiable), a direct measurement of fields p and $\bar{\nu}$ becomes necessary to obtain a complete description. This statement is physically obvious because it is known that the solution to the wave equation in a bounded domain depends, in addition to external sources, on pressure fields (monopole fields) and normal components of particle velocity (dipole fields) everywhere on the bounding surface. In these conditions, measurement of vector $(p, \bar{\nu})$ forms the necessary base for a complete description of the V–Ph characteristics of an acoustic field in a bounded domain. An additional physically obvious point is that the passage to the description in terms of vector $(p, \bar{\nu})$ is expedient for neighborhoods of radiation sources, in the Fresnel diffraction region, where Eq. (7) also becomes invalid. Measurement of general-type acoustic fields with the use of the vector description offers physical possibilities for selecting the plane-wave contributions and a direct observation of the group velocity U_{gr} immediately from the measured parameters ε and δ (see Eq. (5)); i.e., possibilities for observing the dispersion structure of the propagation channel. In the application context, it is clear that the change to the vector description must be justified by its practical suitability for designing decision algorithms.

Now, we proceed to the matter of this paper.

Averaging Eq. (1) over an ensemble of realizations, we obtain for the first statistical moments $a_p = MP$ and $\bar{\mathbf{a}}_{\bar{\nu}} = M\bar{\mathbf{V}}$

$$\bar{a}_p(\bar{\mathbf{x}}, t) = Mp(\bar{\mathbf{x}}, t);$$
$$a_\nu(\bar{\mathbf{x}}, t) = -\rho_0^{-1} \int\limits_{-\infty}^{t} \nabla_{\bar{\mathbf{x}}} a_p(\bar{\mathbf{x}}, \tau) d\tau, \tag{8}$$

where M stands for the ensemble expectation. Centrality of field p ($a_p = 0$) causes centrality of field $\bar{\nu}$ ($\bar{a}_\nu = 0$) and centrality of all statistical moments of the vector field $p, \bar{\nu}$.

For the second statistical moments (correlation functions), we have the relationships

$$B_{p\bar{\nu}}(\bar{\mathbf{x}}, t/\bar{\mathbf{y}}, \tau) = -\rho_0^{-1} \int\limits_{-\infty}^{\tau} \nabla_{\bar{\mathbf{y}}} B_{pp}(\bar{\mathbf{x}}, t/\bar{\mathbf{y}}, \varepsilon) d\varepsilon,$$
$$B_{pp}(\bar{\mathbf{x}}, t/\bar{\mathbf{y}}, \tau) = Mp(\bar{\mathbf{x}}, t)p(\bar{\mathbf{y}}, \tau),$$
$$B_{\nu_i\nu_j}(\bar{\mathbf{x}}, t/\bar{\mathbf{y}}, \tau) = \rho_0^{-2} \int\limits_{-\infty}^{t}\int\limits_{-\infty}^{\tau} \frac{\partial^2}{\partial x_i \partial y_j} B_{pp}(\bar{\mathbf{x}}, \sigma/\bar{\mathbf{y}}, \varepsilon) d\sigma d\varepsilon, \tag{9}$$
$$B_{\nu_i\nu_j}(\bar{\mathbf{x}}, t/\bar{\mathbf{y}}, \tau) = M\nu_i(\bar{\mathbf{x}}, t)\nu_j(\bar{\mathbf{y}}, \tau),$$
$$B_{\nu_i, \nu_j}(\bar{\mathbf{x}}, t/\bar{\mathbf{y}}, \tau)$$
$$= -\rho_0^{-1} \int\limits_{-\infty}^{t} \frac{\partial}{\partial x_i} B_{p\nu_j}(\bar{\mathbf{x}}, \sigma/\bar{\mathbf{y}}, \tau) d\sigma; \quad i, j = 1, 2, 3.$$

The differential form of relationships (9) appeared for the first time in the well known paper by Eckart [4] (see also [1–3]).

For statistically stationary fields of pressure, i.e., for $B_{pp}(\bar{\mathbf{x}}, t/\bar{\mathbf{y}}, \tau) \equiv B_{pp}(\bar{\mathbf{x}}, \bar{\mathbf{y}}, \tau - t)$, two relationships follow from Eqs. (9):

$$B_{p\bar{\mathbf{v}}}(\bar{\mathbf{x}}, \bar{\mathbf{y}}, \tau - t) = -\rho_0^{-1} \int_{-\infty}^{\tau - t} \nabla_{\bar{\mathbf{y}}} B_{pp}(\bar{\mathbf{x}}, \bar{\mathbf{y}}, \sigma) d\sigma = B_{\nu p}(\bar{\mathbf{x}}, \bar{\mathbf{y}}, t - \tau), \quad (10)$$

$$B_{\nu_i, \nu_j}(\bar{\mathbf{x}}, \bar{\mathbf{y}}, \tau - t) = \rho_0^{-2} \int_{-\infty}^{\tau - t} d\nu \int_{-\infty}^{\nu} \frac{\partial^2}{\partial x_i \partial y_j} B_{pp}(\bar{\mathbf{x}}, \bar{\mathbf{y}}, \sigma) d\sigma,$$

which means that the steady-state property is extended to mutual statistical moments.

The moment functions form a sufficient base for describing the Gaussian fields p, $\bar{\mathbf{v}}$. In the general case, for example, in describing the energy flux fields $\bar{\mathbf{S}}(\bar{\mathbf{x}}, t) = p(\bar{\mathbf{x}}, t)\bar{\mathbf{v}}(\bar{\mathbf{x}}, t)$, these relationships are insufficient even if p and $\bar{\mathbf{v}}$ are of Gaussian type. This case requires analyzing the whole of the probability structure with the use of probability density functionals (PDF) or characteristic functionals (CF) of the four-dimensional fields (p, $\bar{\mathbf{v}}$). In this approach (see [4, 5]), the CF is the continual Fourier transform of the PDF. According to the procedure used in [6, 7], we introduce the simultaneous PDF $W_{p, \bar{\mathbf{v}}}\{\mu, \bar{\mathbf{v}}\}$ of fields p and $\bar{\mathbf{v}}$, where μ and $\bar{\mathbf{v}}$ are the respective field realizations. For $W_{p, \bar{\mathbf{v}}}$, we have the representation

$$W_{p, \bar{\mathbf{v}}}\{\mu, \bar{\mathbf{v}}\} = W_{\bar{\mathbf{v}}/p}\{\nu/\mu\} W_p\{\mu\}, \quad (11)$$

where $W_{\bar{\mathbf{v}}/p}\{\cdot/\cdot\}$ is the conditional probability density functional of field $\bar{\mathbf{v}}$ for a given field p and $W_p\{\cdot\}$ is the unconditional PDF of field p. Proceeding from Eq. (1), we obtain

$$W_{\bar{\mathbf{v}}/p}\{\bar{\mathbf{v}}/\mu\} = D\left\{\bar{\mathbf{v}} + \rho_0^{-1} \int_{-\infty}^{t} \nabla \mu d\tau\right\}, \quad (12)$$

where $D\{\cdot\}$ is the delta-functional (a continual analog for the multidimensional delta-function) with the properties [8]

$$\int_{D_{\bar{\rho}}} D\{\bar{\boldsymbol{\rho}}\} d\Gamma(\rho) = 1;$$

$$\int_{D_{\bar{\rho}}} D\{\bar{\boldsymbol{\rho}} - \bar{\mathbf{r}}\} G\{\bar{\boldsymbol{\rho}}\} d\Gamma(\rho) = G\{\bar{\mathbf{r}}\}. \quad (12a)$$

In Eqs. (12a), the continual integrations are carried out over functional space $D_{\bar{\rho}}$ with functional volume measure $d\Gamma(\rho)$, and $G\{\bar{\boldsymbol{\rho}}\}$ is an arbitrary functional.

From Eqs. (11) and (12) it follows that

$$W_{p, \bar{\mathbf{v}}}\{\mu, \bar{\mathbf{v}}\} = D\left\{\bar{\mathbf{v}} + \rho_0^{-1} \int_{-\infty}^{t} \nabla_{\bar{\mathbf{x}}} \mu d\tau\right\} W_\rho\{\mu\}. \quad (13)$$

Relationship (13) holds for arbitrary statistical properties of field p.

In particular, the simultaneous CF $\theta_{p, \bar{\mathbf{v}}}$ of fields p and $\bar{\mathbf{v}}$ follows from Eq. (13) as the Fourier transform:

$$\theta_{p, \bar{\mathbf{v}}}\{\alpha, \bar{\boldsymbol{\beta}}\} = \theta_p\left\{\alpha - p_0^{-1} \int_{-\infty}^{t} \mathrm{div}_x \bar{\boldsymbol{\beta}} d\tau\right\}; \quad \theta_{\bar{\mathbf{v}}}\{\beta\} \equiv \theta_{p, \bar{\mathbf{v}}}\{0, \bar{\boldsymbol{\beta}}\}, \quad (14)$$

where θ_p is the CF of the field of pressure, $\alpha = \alpha(\bar{\mathbf{x}}, t)$, and $\bar{\boldsymbol{\beta}} = \bar{\boldsymbol{\beta}}(\bar{\mathbf{x}}, t)$.

Formulas (13) and (14) give a complete probability description of vector field (p, $\bar{\mathbf{v}}$). Any moment function is obtained from Eq. (14) by variational differentiation with respect to functional arguments. We illustrate this general scheme using the determination of the CF of the random field of acoustic power flux $S = p\bar{\mathbf{v}}$ as an example.

Using Eq. (1), we obtain

$$\bar{\mathbf{S}}(\bar{\mathbf{x}}, t) = -\rho_0^{-1} p(\bar{\mathbf{x}}, t) \int_{-\infty}^{t} \nabla_{\bar{\mathbf{x}}} p(\bar{\mathbf{x}}, \tau) d\tau. \quad (15)$$

Introducing a singular kernel

$$\bar{\bar{\mathbf{K}}}(\bar{\mathbf{x}}, t; \bar{\mathbf{r}}, \mu/\bar{\mathbf{r}}', \tau) = \rho_0^{-1} \delta(\bar{\mathbf{x}} - \bar{\mathbf{r}}) \delta(t - \mu) \sigma(t - \tau) \nabla_{\bar{\mathbf{r}}} \delta(\bar{\mathbf{x}} - \bar{\mathbf{r}}'), \quad (15a)$$

we represent Eq. (15) as the quadratic form

$$\bar{\mathbf{S}}(\bar{\mathbf{x}}, t) = \int_{V_{\bar{r}} V_{\bar{r}'}} \int \int \int_{-\infty}^{\infty} \hat{\bar{\mathbf{K}}}_S(\bar{\mathbf{x}}, t; \bar{\mathbf{r}}, \mu/\bar{\mathbf{r}}', \tau) p(\bar{\mathbf{r}}, \mu) p(\bar{\mathbf{r}}', \tau) d\bar{\mathbf{r}} d\bar{\mathbf{r}}' d\mu d\tau, \quad (16)$$

where kernel $\hat{\bar{\mathbf{K}}}_S = \frac{1}{2}[\hat{\bar{\mathbf{K}}} + \hat{\bar{\mathbf{K}}}^+]$ is symmetric and superscript "+" means Hermitian conjugation. In the operator form, Eq. (16) has the form

$$\bar{\mathbf{S}} = (\hat{\bar{\mathbf{K}}}_S p, p). \quad (17)$$

Performing the calculations according to Eqs. (11)–(13), we obtain

$$W_{\bar{S}}\{\bar{\sigma}\} = \int_{D_\varepsilon} D\{\bar{\sigma} - (\hat{\bar{\mathbf{K}}}_S\varepsilon, \varepsilon)\}W_p\{\varepsilon\}d\Gamma(\varepsilon). \quad (18)$$

Passing to the CF in Eq. (18), we obtain ($\boldsymbol{\xi}$ is a vector function)

$$\theta_{\bar{s}}\{\bar{\xi}\} = \int_{D_\eta} \theta_p\{\eta\}T\{\bar{\xi}, \eta\}d\Gamma(\eta), \quad (19)$$

where $\theta_{\bar{s}}$ and θ_p are the CF of fields $\bar{\mathbf{S}}$ and p, respectively.

Functional $T\{\bar{\xi}, \eta\}$ has the form

$$T\{\bar{\xi}, \eta\} = \frac{1}{(2\pi)}\int_{D_\varepsilon} \exp i[((\bar{\xi}, \hat{\bar{\mathbf{K}}}_S)\varepsilon, \varepsilon) - (\eta, \varepsilon)]d\Gamma(\varepsilon). \quad (19a)$$

The integral appearing in Eq. (19) is a continual integral; in the case of functional θ_p with a Gaussian structure, it allows an explicit calculation. After some calculation (see [6, 7]), we obtain

$$\theta_{\bar{s}}\{\bar{\xi}\} = \frac{1}{\sqrt{2\pi}}D_F^{-1/2}\{\hat{I} + 2i\hat{K}_0\} \times \int_{D_\eta} \theta_p\{\eta\}\exp-\frac{i}{4}(\hat{K}_0^{-1}\eta, \eta)d\Gamma(\eta), \quad (20)$$

where $\hat{K}_0 = (\bar{\xi}, \hat{\bar{\mathbf{K}}}_S)$ is again a symmetric kernel; the scalar product is determined, according to Eq. (15a), in the $\bar{\mathbf{x}}$–t space; D_F is the Fredholm determinant of kernel $\hat{I} + 2i\hat{K}_0$; and $\hat{I}_0$ is the unit kernel.

For the Gaussian structure of centered field p, i.e., for

$$\theta_p\{\eta\} = \exp-\frac{1}{2}(\hat{B}_{pp}\eta, \eta) \quad (21)$$

($\hat{B}_{pp}$ is the correlation kernel), we calculate continual integral (20) to finally obtain

$$\theta_s\{\bar{\xi}\} = D_F^{-1/2}\{2i(\bar{\xi}, \hat{\bar{\mathbf{K}}}_S)\hat{B}_{pp}\}. \quad (22)$$

The moment functions of the field of flux $\bar{\mathbf{S}}$ are obtained from Eq. (22) with the use of a routine procedure of variational differentiation [7]. For the two first moments of the field S, we obtain

$$MS_l(\bar{\mathbf{x}}, t) = Mp(\bar{\mathbf{x}}, t)\nu_l(\bar{\mathbf{x}}, t) \equiv B_{p\nu_l}(\bar{\mathbf{x}}, t/\bar{\mathbf{x}}, t) = -\rho_0^{-1}\int_{-\infty}^{t} \frac{\partial}{\partial x_l}B_{pp}(\bar{\mathbf{x}}, t/\bar{\mathbf{x}}, \tau)d\tau, \quad (23)$$

$$MS_l(\bar{\mathbf{x}}, t)S_\sigma(\bar{\mathbf{x}}', t') = B_{S_lS_\sigma}(\bar{\mathbf{x}}, t/\bar{\mathbf{x}}', t') = B_{pp}(\bar{\mathbf{x}}, t/\bar{\mathbf{x}}', t')B_{\nu_l\nu_\sigma}(\bar{\mathbf{x}}, t/\bar{\mathbf{x}}', t') + B_{\nu_lp}(\bar{\mathbf{x}}, t/\bar{\mathbf{x}}', t')B_{p\nu_\sigma}(\bar{\mathbf{x}}, t/\bar{\mathbf{x}}', t') + B_{p\nu_l}(\bar{\mathbf{x}}, t/\bar{\mathbf{x}}', t')B_{p\nu_\sigma}(\bar{\mathbf{x}}, t/\bar{\mathbf{x}}', t'). \quad (24)$$

From Eqs. (23) and (24) we derive the covariance function of flux $\bar{\mathbf{S}}$:

$$\Psi_{l\sigma}(\bar{\mathbf{x}}, t/\bar{\mathbf{x}}', t') = B_{pp}(\bar{\mathbf{x}}, t/\bar{\mathbf{x}}', t')B_{\nu_l\nu_\sigma}(\bar{\mathbf{x}}, t/\bar{\mathbf{x}}', t') + B_{\nu_lp}(\bar{\mathbf{x}}, t/\bar{\mathbf{x}}', t')B_{p\nu_\sigma}(\bar{\mathbf{x}}, t/\bar{\mathbf{x}}', t'). \quad (25)$$

Combining Eqs. (25) and (9), we obtain a useful identity

$$\int_{V_0}\int_{T_0} \Psi_{l\sigma}(\bar{\mathbf{x}}, t/\bar{\mathbf{x}}', t')d\bar{\mathbf{x}}dtd\bar{\mathbf{x}}'dt' = 2\int_{V_0}\int_{T_0} B_{\nu_lp}(\bar{\mathbf{x}}, t/\bar{\mathbf{x}}', t')B_{p\nu_\sigma}(\bar{\mathbf{x}}, t/\bar{\mathbf{x}}', t')d\bar{\mathbf{x}}dtd\bar{\mathbf{x}}'dt'. \quad (26)$$

Certainly, one can obtain expressions (23)–(26) without variational differentiation, by directly averaging the fourth moments of fields p and $\bar{\mathbf{v}}$ under the assumption of their Gaussian structure. However, for higher moments, calculations become laborious even for Gaussian fields. In the case of non-Gaussian fields p, the use of Eq. (20) is preferable. It is clear that the closed expression (22) for the CF of field $\bar{\mathbf{S}}$ becomes the base for designing the optimum algorithms of space–time processing in measuring the energy fluxes S of a V–Ph acoustic field.

Now we proceed to analyzing algorithms and their quality indices (the signal-to-noise ratio) in the case of the vector reception (measurements of fields p and $\bar{\mathbf{v}}$) in comparison with the conventional algorithm based on measuring only the scalar field of pressure. We consider two kinds of algorithms:

(i) the suboptimum algorithm for measuring energy fluxes $\bar{\mathbf{S}}(\bar{\mathbf{x}}, t) = p(\bar{\mathbf{x}}, t)\bar{\mathbf{v}}(\bar{\mathbf{x}}, t)$ and

(ii) the optimum algorithm for measuring fields p and $\bar{\mathbf{v}}$ on the basis of studying the likelihood ratio and analyzing the indicated signal-to-noise ratio.

In the first case, we limit our consideration to evaluative calculations adapted to the physical features of flux propagation in an acoustic medium with considerable spatial dispersion.

In the second case, we perform a more comprehensive analysis based on the Gaussian statistical properties of measured V–Ph fields p and $\bar{\mathbf{v}}$.

For measuring the lth component of energy (power) flux, the simplest (suboptimum) procedure is the weightless processing:

$$Z_l = \iint_{X\,T} p(\bar{\mathbf{x}}, t)\nu_l(\bar{\mathbf{x}}, t)d\bar{\mathbf{x}}dt \equiv \iint_{k\,\omega} \tilde{p}(\bar{\mathbf{k}}, \omega)\tilde{\nu}_l^*(\bar{\mathbf{k}}, \omega)d\bar{\mathbf{k}}d\omega. \tag{27}$$

Integration in Eq. (27) is carried out either in space–time domain (x, t) or in wave vector–frequency domain $(\bar{\mathbf{k}}, \omega)$. The sign ~ denotes the four-dimensional Fourier spectrum. Using the Euler equation (1) in the spectral representation we obtain

$$Z_l = \iint_{\bar{k}\,\omega} \zeta_l(\bar{\mathbf{k}}, \omega)\hat{\Phi}_p(\bar{\mathbf{k}}, \omega)d\bar{\mathbf{k}}d\omega, \tag{28}$$

where

$$\hat{\Phi}_p(\bar{\mathbf{k}}, \omega) = \left|\tilde{p}(\bar{\mathbf{k}}, \omega)\right|^2; \quad \zeta_l = \frac{k_l}{\rho_0\omega}.$$

Since estimate Z_l is a random quantity (process, field), its mean value and variance in the model of a stationary and homogeneous random field can be determined from Eq. (28):

$$\alpha_{Z_l} = MZ_l = \iint_{\bar{k}\,\omega} \zeta_l(\bar{\mathbf{k}}, \omega)\Phi_p(\bar{\mathbf{k}}, \omega)d\bar{\mathbf{k}}d\omega; \quad \Phi_p = M\hat{\Phi}_p; \tag{29}$$

$$DZ_l = MZ_l^2 - \alpha_{Z_l}^2 = \iint_{\bar{k}\,\omega} \zeta_l^2(\bar{\mathbf{k}}, \omega)D_p(\bar{\mathbf{k}}, \omega)d\bar{\mathbf{k}}d\omega, \tag{29a}$$

where

$$D_p(\bar{\mathbf{k}}, \omega) = M\left|\hat{\Phi}_p(\bar{\mathbf{k}}, \omega)\right|^2 - M\left|\Phi_p^2(\bar{\mathbf{k}}, \omega)\right|.$$

To obtain evaluative results of interest, we determine the lower edge of variance D_{Z_l} from the Cauchy–Schwarz inequality:

$$D_{Z_l} \le \Delta_l d_p; \quad \Delta_l = \iint_{\bar{k}\,\omega} \zeta_l^2(\bar{\mathbf{k}}, \omega)d\bar{\mathbf{k}}d\omega; \quad d_p = \iint_{\bar{k}\,\omega} D_p(\bar{\mathbf{k}}, \omega)d\bar{\mathbf{k}}d\omega. \tag{30}$$

If we assume that the final goal of algorithm (27) consists in selecting the plane-wave component of fields p and $\bar{\mathbf{v}}$ (signal S) against the background of noise field N of a general type (i.e., noise caused by different physical mechanisms) and consider $(p, \bar{\mathbf{v}})$- and p-measurements by rejecting the effects of signal processing in time $\sim(\Delta F t)^{1/2}$ in both cases, we obtain the following expression for the indicated (postdetection) signal-to-noise ratio used as the quality index:

$$Q_{Z_l} \equiv Q_{S_l} = (\rho_0 c)^{-1}[DZ_l]_N^{-1/2}MZ_p^S, \quad Q_{pp} = d_{p_N}^{-1/2}MZ_p^S, \tag{31}$$

where we assumed that signal S travels along the horizontal axis of a sea waveguide.

Combining Eqs. (30) and (31), we obtain an estimator for the lower edge of relative efficiency of the algorithms of two types:

$$\eta_p^{S_l} = \frac{Q_{S_l}}{Q_{pp}} \ge (\rho_0 c)^{-1}\Delta_N^{-1/2} = \hat{\eta}_p^{S_l}. \tag{32}$$

From Eq. (32) together with Eqs. (30) and (28), we obtain

$$\hat{\eta}_p^{S_l} = \left[\iint_{\bar{k}\,\omega} \frac{c^2}{c_{\mathrm{ph}lN}^2}(\bar{\mathbf{k}}, \omega)d\bar{\mathbf{k}}d\omega\right]^{-\frac{1}{2}}, \tag{33}$$

where $c_{\mathrm{ph}/N}$ is the phase velocity of noise N. In the case of an ideal waveguide, i.e., for $c_{\mathrm{ph}lN}^2 U_{\mathrm{gr}lN} = c^2$, Eq. (33) gives

$$\hat{\eta}_p^{S_l} = \frac{c}{\langle U_{\mathrm{gr}lN}\rangle}; \quad \langle U_{\mathrm{gr}lN}\rangle = \left[\iint_{\bar{k}\,\omega} U_{\mathrm{gr}lN}^2(\bar{\mathbf{k}}, \omega)d\bar{\mathbf{k}}d\omega\right]^{\frac{1}{2}}, \tag{34}$$

where $\langle U_{\mathrm{gr}lN}\rangle$ is the effective group velocity averaged over $(\bar{\mathbf{k}}, \omega)$ space.

Finally, we obtain the estimator

$$\eta_p^{S_l} = \frac{c}{\langle U_{\mathrm{gr}lN}\rangle}. \tag{35}$$

It is obvious that the strength of inequality (32) is determined by the dispersion structure of the laws governing the propagation of noise fields. One can easily see that the same estimator (35) for relative efficiency $\eta_p^{S_l}$ can be obtained independent of the mechanisms of noise field generation and propagation by using relationship (5) between the energy E of field $(p, \bar{\mathbf{v}})$ and the energy flux.

In the presence of sea noise including noise generated by vibrating structures, noise of hydrodynamic (pseudo-sound) origin, noise of gravity-capillary waves, and dynamic noise of sea surface, we have $U_{\mathrm{gr}} = \frac{d\omega}{dk} < c$, we obtain

$$\eta_p^{S_l} > 1. \tag{36}$$

It is clear that the feasibility of inequality (36) depends on the dispersion structure of propagating noise fields. This fact closely relates the problem of algorithmic usefulness of energy flux measurements to the physical mechanisms of generation and propagation of sea noise.

In conclusion we consider the optimum algorithm of V–Ph processing of $(p, \bar{\mathbf{v}})$ fields, which follows from analyzing the likelihood ratio for Gaussian signals *S* and Gaussian noise *N*. We will carry out the analysis in space–frequency domain.

In the case of V–Ph reception of Gaussian fields $U_k(\bar{\mathbf{x}}, \omega)$, where $\bar{\mathbf{x}} \in X$, $\omega \in \Omega$, and $k = 1\ldots L$, the likelihood ratio has the form

$$\ln\Lambda = \ln\Lambda_0 + (2\pi)^2 \sum_{k=l}^{L}\sum_{l=1}^{L}\int_{-\infty}^{\infty} d\omega \times \iint_{XX} H_{kl}(\bar{\mathbf{r}}/\bar{\boldsymbol{\rho}}, \omega) U_k^*(\bar{\mathbf{r}}, \omega) U_l(\bar{\boldsymbol{\rho}}, \omega) d\bar{\mathbf{r}} d\bar{\boldsymbol{\rho}}, \quad (37)$$

where

$$(2\pi)^2 \hat{H}_{kl} = [\hat{B}^N_{kl} + \hat{B}^S_{kl}]^{-1} - [B^N_{kl}]^{-1}; \quad k, l = 1\ldots L, \quad (37a)$$

$\hat{B}^N_{kl}$ and $\hat{B}^S_{kl}$ are the cross-correlation spectra of signals and noise, $\hat{B}^{N,S}_{kl}(\bar{\mathbf{r}}/\bar{\boldsymbol{\rho}}, \omega) = MU^{N,S}_k(\bar{\mathbf{r}}, \omega) U^{N,S*}_l(\bar{\boldsymbol{\rho}}, \omega)$, and superscript * means complex conjugation.

One can easily see that, in the case of a signal *S* generated by a point source and propagating through a determinate waveguide, the cross-spectrum $\hat{B}^S_{kl}$ can be factorized:

$$B^S_{kl}(\bar{\mathbf{r}}/\bar{\boldsymbol{\rho}}, \omega) = S_k(\bar{\mathbf{r}}, \omega) S^*_l(\bar{\boldsymbol{\rho}}, \omega),$$
$$S_k(\bar{\mathbf{r}}, \omega) = G_k(\bar{\mathbf{r}}/\bar{\mathbf{a}}, \omega)\sigma_S(\bar{\mathbf{a}}, \omega), \quad (38)$$

where G_k $(k = 1\ldots L)$ is a component of Green's vector function and $\sigma^2_S(\bar{\mathbf{a}}, \omega) = F_S(\bar{\mathbf{a}}, \omega) = M|f_S(\bar{\mathbf{a}}, \omega)|^2$ is the power of the source of signal *S* that is located at a point $\bar{a}$.

Using Eqs. (37) and (38), we obtain a factorized representation for $\hat{H}$:

$$H_{kl}(\bar{\mathbf{r}}/\bar{\boldsymbol{\rho}}, \omega) = -h_k(\bar{\mathbf{r}}, \omega) h^*_l(\bar{\boldsymbol{\rho}}, \omega), \quad (39)$$

where

$$h_k(\bar{\mathbf{r}}, \omega) = h_0(\omega) \sum_{m=1}^{L} \int_X R^N_{km}(\bar{\mathbf{r}}/\bar{\boldsymbol{\rho}}, \omega) S_m(\bar{\boldsymbol{\rho}}, \omega) d\bar{\boldsymbol{\rho}},$$

$$h_0(\omega) = (2\pi)\Bigg[1 + (2\pi)^2 \times \sum_{k,l=1}^{L} \iint_{XX} S^*_k(\bar{\mathbf{r}}, \omega) R^N_{km}(\bar{\mathbf{r}}/\bar{\boldsymbol{\rho}}, \omega) S_m(\bar{\boldsymbol{\rho}}, \omega) d\bar{\mathbf{r}} d\bar{\boldsymbol{\rho}}\Bigg]^{-1/2},$$

and

$$R^N_{km} = (B^N_{km})^{-1}. \quad (39a)$$

Representation for the likelihood ratio Λ follows from Eqs. (37)–(39):

$$\ln\Lambda = \ln\Lambda_0 - (2\pi)^2 \int_{-\infty}^{\infty} d\omega \left| \sum_{k=1}^{L} \int_X h_k(\bar{\mathbf{r}}, \omega) U^*_k(\bar{\mathbf{r}}, \omega) d\bar{\mathbf{r}} \right|^2. \quad (40)$$

Structurally, this representation corresponds to space–time processing in the form of weighting summator–quadrator–averager. The corresponding signal-to-noise ratio at the quadrator input has the form

$$Q(\omega) = (2\pi)^2 \sum_{k,l=1}^{L} \iint_{XX} S^*_k(\bar{\mathbf{r}}, \omega) R^N_{kl}(\bar{\mathbf{r}}/\bar{\boldsymbol{\rho}}, \omega) S_l(\bar{\boldsymbol{\rho}}, \omega) d\bar{\mathbf{r}} d\bar{\boldsymbol{\rho}}. \quad (41)$$

Relationships (37)–(41) are known fairly well. We specify these expressions using the vector field U_k in the sourcewise (integral) representation

$$U_k(\bar{\mathbf{r}}, \omega) = \frac{1}{2\pi}\int_X Z_k(\bar{\mathbf{r}}/\bar{\boldsymbol{\rho}}, \omega) W(\bar{\boldsymbol{\rho}}, \omega) d\bar{\boldsymbol{\rho}}, \quad (42)$$

where Z_k $(k = 1\ldots L)$ is some vector kernel. Using Eq. (42) to represent signal and noise fields in the form

$$\begin{matrix} S_k \\ N_k \end{matrix}(\bar{\mathbf{r}}, \omega) = \frac{1}{2\pi}\int_X Z_k(\bar{\mathbf{r}}/\bar{\boldsymbol{\rho}}, \omega) \begin{matrix} W_S \\ W_N \end{matrix}(\bar{\boldsymbol{\rho}}, \omega) d\bar{\boldsymbol{\rho}}, \quad (42a)$$

we reduce Eq. (41) to the equivalent form

$$Q(\omega) = \iint_{XX} W^*_S(\bar{\mathbf{r}}, \omega) T^N(\bar{\mathbf{r}}/\bar{\boldsymbol{\rho}}, \omega) W_S(\bar{\boldsymbol{\rho}}, \omega) d\bar{\mathbf{r}} d\bar{\boldsymbol{\rho}},$$

$$T^N(\bar{\mathbf{r}}/\bar{\boldsymbol{\rho}}, \omega) = \sum_{k,l=1}^{L} \iint_{XX} Z^*_k(\bar{\mathbf{r}}/\bar{\mathbf{z}}, \omega) R^N_{kl}(\bar{\mathbf{z}}/\bar{\boldsymbol{\zeta}}, \omega) Z_l(\bar{\boldsymbol{\zeta}}/\bar{\boldsymbol{\rho}}, \omega) d\bar{\mathbf{z}} d\bar{\boldsymbol{\zeta}}. \quad (43)$$

In a similar way, forming a sourcewise representation for $B^N_{kl}(\bar{\mathbf{r}}/\bar{\boldsymbol{\rho}}, \omega)$ and $R^N_{kl}(\bar{\mathbf{r}}/\bar{\boldsymbol{\rho}}, \omega)$ from Eq. (42a) (see

(39a)), using Eq. (43), and performing some transformations, we obtain

$$Q(\omega) = L^2 \int\limits_{XX} W_S^*(\bar{\mathbf{r}}, \omega) R_W^N(\bar{\mathbf{r}}/\bar{\boldsymbol{\rho}}, \omega) W_S(\bar{\boldsymbol{\rho}}, \omega) d\bar{\mathbf{r}} d\bar{\boldsymbol{\rho}}, \quad (44)$$

where

$$\hat{R}_W^N = [\hat{B}_W^N]^{-1}; \quad B_W^N(\bar{\mathbf{r}}/\bar{\boldsymbol{\rho}}, \omega) = M W_N^*(\bar{\mathbf{r}}, \omega) W_N(\bar{\boldsymbol{\rho}}, \omega).$$

The integral term in Eq. (44) is obviously the signal-to-noise ratio at the output of space–frequency processing channel that is optimum in the sense of the likelihood ratio structure when the field supplied to its input is a Gaussian field $W = W_S + W_N$, where W is some scalar field related to the V–Ph field U_k according to Eq. (42). We can see from Eq. (44) that, in comparison with the measurement of scalar W, the measurement of vector U_k leads to an increase in the signal-to-noise ratio at a frequency ω by a factor of L^2, where L is the dimension of the input vector of observations.

Now, we apply the general results obtained above to the formulated acoustic problem of measuring the V–Ph fields of signal and noise, p and ν.

In this case, it is sufficient to formally set $\bar{U}[U_0, U_1, U_2, U_3] \equiv [p, \nu_1, \nu_2, \nu_3]$, where p is the pressure field and $\bar{\mathbf{v}}[\nu_1, \nu_2, \nu_3]$ is the particle velocity field. As above, all components of vector $\bar{\mathbf{U}}$ are additive mixtures of signal and noise.

We take into consideration the relationship between fields p and $\bar{\mathbf{v}}$ related through the Euler equation (1):

$$\nu_k(\bar{\mathbf{r}}, \omega) = \frac{1}{j\omega\rho_0} \frac{\partial}{\partial r_k} p(\bar{\mathbf{r}}, \omega). \quad (45)$$

Then, representing formally

$$p^{S,N}(\bar{\mathbf{r}}, \omega) = \int \delta(\bar{\boldsymbol{\chi}} - \bar{\boldsymbol{\rho}}) p^{S,N}(\bar{\boldsymbol{\rho}}, \omega) d\bar{\boldsymbol{\rho}},$$
$$\nu_k^{S,N}(\bar{\mathbf{r}}, \omega) = \frac{j}{\omega\rho_0} \int \frac{\partial}{\partial \rho_k} \delta(\bar{\mathbf{r}} - \bar{\boldsymbol{\rho}}) p^{S,N}(\bar{\boldsymbol{\rho}}, \omega) d\bar{\boldsymbol{\rho}} \quad (46)$$

and comparing Eqs. (46) and (42), we obtain an expression for the vector kernel:

$$Z_1(\bar{\mathbf{r}}/\bar{\boldsymbol{\rho}}, \omega) \equiv [Z_0(\bar{\mathbf{r}}/\bar{\boldsymbol{\rho}}, \omega), Z_1(\bar{\mathbf{r}}/\bar{\boldsymbol{\rho}}, \omega), Z_2(\bar{\mathbf{r}}/\bar{\boldsymbol{\rho}}, \omega),$$
$$Z_3(\bar{\mathbf{r}}/\bar{\boldsymbol{\rho}}, \omega)] \equiv \left[\delta(\bar{\mathbf{r}} - \bar{\boldsymbol{\rho}}), \frac{j}{\omega\rho_0} \frac{\partial}{\partial \rho_1} \delta(\bar{\mathbf{r}} - \bar{\boldsymbol{\rho}}), \right.$$
$$\left. \frac{j}{\omega\rho_0} \frac{\partial}{\partial \rho_2} \delta(\bar{\mathbf{r}} - \bar{\boldsymbol{\rho}}), \frac{j}{\omega\rho_0} \frac{\partial}{\partial \rho_3} \delta(\bar{\mathbf{r}} - \bar{\boldsymbol{\rho}}) \right]. \quad (47)$$

In this connection, scalar field W introduced above (see Eq. (42)) is represented as the sum of signal and noise pressure fields given by Eq. (46): $p = p^S + p^N$. Correspondingly, using formal substitutions $B_W^N \longrightarrow B_p^N$ and $R_W^N \longrightarrow R_p^N$ in Eq. (44), we obtain the final expression for the signal-to-noise ratio at a frequency ω at the quadrator input (spatial processing) in the case of the V–Ph measurement of field p, $\bar{\mathbf{v}}$:

$$Q_{p,\bar{\mathbf{v}}}(\omega) = L^2 \int\limits_{XX} p^{S*}(\bar{\mathbf{r}}, \omega) R_p^N(\bar{\mathbf{r}}/\bar{\boldsymbol{\rho}}, \omega) p^S(\bar{\boldsymbol{\rho}}, \omega) d\bar{\mathbf{r}} d\bar{\boldsymbol{\rho}}. \quad (48)$$

Taking into account the fact that the integral in Eq. (48) coincides with the signal-to-noise ratio at the quadrator input in the case of measuring only the scalar field of pressure, we obtain a simple relationship

$$Q_{p,\bar{\mathbf{v}}}(\omega) = L^2 Q_p(\omega), \quad (49)$$

where L is, as earlier, the dimension of the input observation vector (p, ν_1, ν_2, ν_3). In the context of Gaussian fields, result (49) is obviously the potential (upper) estimate of the signal-to-noise ratio for the optimum (in the sense of the likelihood ratio) processing in the case of the V–Ph reception of acoustic fields p, $\bar{\mathbf{v}}$ related through Eq. (1).

In the analysis of the signal-to-noise ratio defined by the formula

$$Q = \frac{E_S}{E_N} = \frac{\int\limits_{-\infty}^{\infty} E_S(\omega) d\omega}{\int\limits_{-\infty}^{\infty} E_N(\omega) d\omega}, \quad (50)$$

where E_S and E_N are the power spectra of signal and noise, the use of the above procedure gives the following result:

$$Q_{p,\bar{\mathbf{v}}} = L^2 \frac{\int\limits_{-\infty}^{\infty} [1 + L^2 Q_P(\omega)]^{-1} Q_P^2(\omega) d\omega}{\int\limits_{-\infty}^{\infty} [1 + L^2 Q_P(\omega)]^{-1} Q_P(\omega) d\omega}, \quad (51)$$

which coincides with Eq. (49) while $Q_p(\omega)$ weakly depends on frequency.

The passage to the indicated signal-to-noise ratio at the quadrator–averager output is performed using standard procedures. The result is

$$Q_{p,\bar{\mathbf{v}}}^U = \frac{1}{2\sqrt{2}} Q_{p,\bar{\mathbf{v}}} [\Delta F T]^{1/2} \cong \frac{1}{2\sqrt{2}} L^2 Q_p [\Delta F T]^{1/2}, \quad (52)$$

where ΔF is the input frequency band, T is the averaging time, and parameter $Q_{p,\bar{\mathbf{v}}}$ is determined in Eqs. (49) and (51).

Comparing the relative increments of the signal-to-noise ratio for the algorithm of flux measurement (35)

and likelihood-ratio algorithm of V–Ph measurement of fields p, $\bar{\mathbf{v}}$ (see Eq. (49)), we obtain

$$\frac{c}{\langle U_{\mathrm{gr}lN}\rangle} \le \eta_p^{p,\bar{\mathbf{v}}} \le L^2 \tag{53}$$

for Gaussian statistical characteristics of V–Ph fields.

Since result (35) refers to the suboptimum algorithm (27) and result (49) refers to the optimum algorithm (37), it is clear that certain prospects appear in investigating algorithms of measuring energy fluxes on the basis of analyzing non-Gaussian structures in the likelihood ratio for the flux algorithm. Such an investigation may start from the above expressions (see Eq. (22)) for the CF of the energy flux as the field characteristic of non-Gaussian structure even if the V–Ph field formed by pressure field p and particle velocity $\bar{\mathrm{v}}$ is Gaussian.

REFERENCES

1. V. A. Gordienko, V. I. Il'ichev, and L. N. Zakharov, *The Vector–Phase Methods in Acoustics* (Nauka, Moscow, 1989).
2. K. J. Ebeling, in *Physical Acoustics: Principles and Methods*, Ed. by W. P. Mason (Academic, New York, 1984; Mir, Moscow, 1984), Vol. 22, pp. 233–310.
3. S. D. Vorob'ev and V. I. Sizov, Akust. Zh. **38**, 654 (1992) [Sov. Phys. Acoust. **38**, 361 (1992)].
4. C. Eckart, J. Acoust. Soc. Am. **25**, 195 (1953).
5. V. I. Tatarskiĭ, *Wave Propagation in a Turbulent Atmosphere* (Nauka, Moscow, 1967).
6. V. I. Klyatskin, *Stochastic Equations and Waves in Randomly Inhomogeneous Media* (Nauka, Moscow, 1980).
7. V. I. Klyachkin, Izv. Vyssh. Uchebn. Zaved., Radiofiz. **17** (1), 134 (1974).
8. V. I. Klyachkin, Izv. Akad. Nauk SSSR, Mekh. Zhidk. Gaza, No. 1, 131 (1979).
9. E. D. Novikov, Usp. Mat. Nauk **16** (2), 135 (1961).

Translated by A. Vinogradov

Acoustical Physics, Vol. 50, No. 4, 2004, pp. 446–453. Translated from Akusticheskiĭ Zhurnal, Vol. 50, No. 4, 2004, pp. 524–532.

Experimental Study of the Effects of Amplitude-Dependent Internal Friction in a Sandstone Bar Resonator

V. E. Nazarov and A. V. Radostin

Institute of Applied Physics, Russian Academy of Sciences, ul. Ul'yanova 46, Nizhni Novgorod, 603950 Russia
e-mail: nazarov@hydro.appl.sci-nnov.ru

Received November 19, 2002

Abstract—Results of an experimental study of the effects of amplitude-dependent internal friction (nonlinear loss, resonance frequency shift, and sound-by-sound damping) in an acoustic bar resonator made of sandstone are presented. The measurements were carried out for the first five longitudinal modes of the resonator. The analytical description of the observed effects is performed within the framework of the phenomenological equations of state that include hysteretic and dissipative components of nonlinearity. The parameters of the hysteretic and dissipative components of sandstone nonlinearity are obtained from a comparison of the experimental data with analytical dependences describing the nonlinear effects. © *2004 MAIK "Nauka/Interperiodica".*

INTRODUCTION

Results of experimental studies of nonlinear acoustic effects in microinhomogeneous media (polycrystalline metals [1–5] and rocks [6–10]) testify to the fact that such media are characterized by strong acoustic nonlinearity, which usually includes a hysteretic component and sometimes a dissipative component. One of the most important distinctive features of these two components consists in the fact that they vary with the frequency of acoustic action in different ways: the hysteretic component usually decreases with increasing frequency while the dissipative component increases [3–5, 9]. Along with the amplitude difference between the hysteretic and dissipative components, this fact offers a possibility to distinguish between their contributions to different nonlinear effects and to carry out experiments so as to emphasize the contribution of one or another nonlinear component to a particular observed effect. A detailed experimental study of nonlinear effects facilitates the determination of the physical mechanisms of acoustic nonlinearity in different media and the construction of models for such media, which, in turn, provides the basis for the development of nonlinear acoustic methods for the diagnostics of structure and state of a medium.

In this paper we present the results of experimental and theoretical studies of the effects of amplitude-dependent internal friction (nonlinear loss, resonance frequency shift, and sound-by-sound damping) in a bar resonator made of sandstone with a grain size of about 0.2–0.3 mm. The analytical description of the observed phenomena is performed within the framework of the phenomenological equations of state that include the hysteretic and dissipative components of nonlinearity. On the basis of these equations, an adequate rheological model of sandstone is proposed.

DESCRIPTION OF THE EXPERIMENT

We experimented on a sandstone bar resonator of length $L = 27$ cm and diameter 2 cm. Figure 1 shows the flow chart of the experiment. Resonator *1* was driven by a low-frequency (LF) piezoelectric ceramic radiator *2* which was glued to a mass load *3* on one side and to the bar end on the other side. To the other, free, bar end, we glued a high-frequency (HF) piezoelectric ceramic

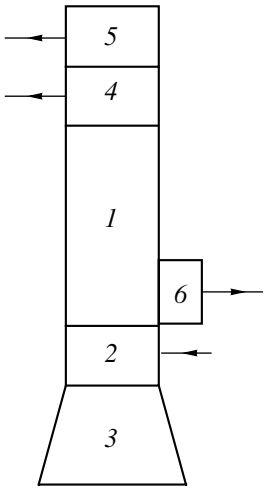

Fig. 1. Flow chart of the experimental setup.

1063-7710/04/5004-0446$26.00 © 2004 MAIK "Nauka/Interperiodica"

radiator *4* used for radiating ultrasonic pulses and an accelerometer *5* used for measuring LF pump waves. Near the LF pump wave radiator, we glued an accelerometer *6* responding to the longitudinal (along the bar) component of acceleration; this accelerometer was used for receiving ultrasonic pulses that passed through the bar and for measuring their amplitudes. Thus, the bar was an acoustic resonator with hard and soft boundaries. The natural frequencies of such a resonator are given by the expression $F_p = \frac{C_0}{4L}(2p - 1)$, where C_0 is the velocity of the longitudinal wave in the bar and p is the mode number. Table 1 shows the resonance frequencies F_p and the Q-factors Q_p of the first five longitudinal modes of the resonator under the conditions of low-amplitude excitation, when nonlinear effects are absent. These resonance frequencies correspond to the velocity of the longitudinal wave $C_0 \cong 2.3 \times 10^5$ cm/s. The errors in measuring the frequencies and amplitudes of LF and HF waves were ±0.5 Hz, $\pm 5 \times 10^{-2}$ dB, and $\pm 1.6 \times 10^{-1}$ dB, respectively.

Before the measurements, reference experiments with a glass bar were carried out. These experiments revealed no nonlinear effects (even for higher LF wave amplitudes). This means that the effects of amplitude-dependent internal friction and their amplitude–frequency behavior were caused exclusively by the physical (i.e., material) nonlinearity of the sample under investigation rather than by the geometric one.

NONLINEAR RESONANCE FREQUENCY SHIFT AND NONLINEAR ABSORPTION OF LF WAVE

In the first series of observations, pump radiator *1* excited in resonator *2* LF acoustic vibrations at one of the first five longitudinal modes, and we measured the nonlinear resonance frequency shift ΔF_{nl} and the attenuation coefficient μ_{nl} as functions of the amplitude [1–4, 6]. Figure 2 shows the strain amplitude ε_m at resonance versus the electric voltage U across the pump radiator for different excitation frequencies. One can easily see that the functional dependence $\varepsilon_m = \varepsilon_m(U)$ is nonlinear, which is indicative of an amplitude-dependent loss. Figure 3 shows the curves for the relative nonlinear resonance frequency shift $\Delta F_{nl}/F_p$ and the relative nonlinear attenuation coefficient μ_{nl}/μ_p, where $\mu_p = (\Omega_p Q_p)^{-1}$ and $\Omega_p = 2\pi F_p$. From these curves it follows that $\Delta F_{nl}/F_p \sim \varepsilon_m^2$ and $\mu_{nl}/\mu_p \sim \varepsilon_m^2$; the relative quantities $\Delta F_{nl}/F_p$ and μ_{nl}/μ_p noticeably decrease with increasing mode number p (at ε_m = const). Note that the quadratic variation of the quantities $\Delta F_{nl}/F_p$ and μ_{nl}/μ_p with ε_m were observed also for lead [3], zinc [4], and marble [6].

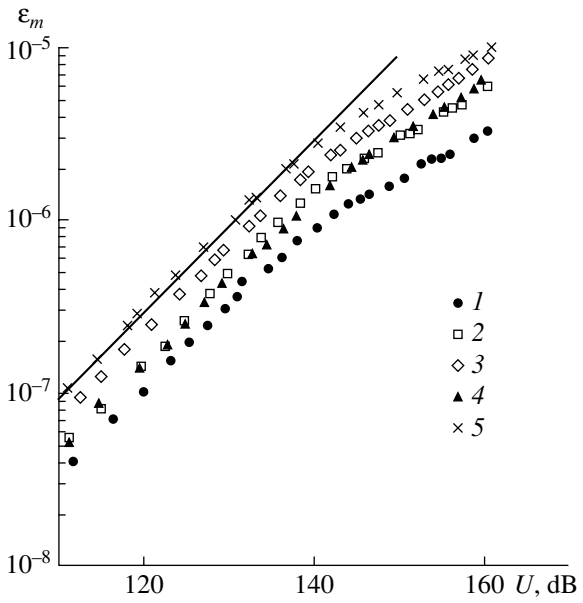

Fig. 2. Amplitude of a wave in the resonator versus the voltage amplitude across the pump radiator (in decibels relative to 1 μV). The straight line corresponds to the function $\varepsilon_m \sim U$.

For each resonator mode, the amplitude dependences $\Delta F_{nl}/F_p \sim \varepsilon_m^2$ and $\mu_{nl}/\mu_p \sim \varepsilon_m^2$ can be described within the framework of the phenomenological equation of state [6]

$$\sigma(\varepsilon) = E[\varepsilon - f(\varepsilon, \dot{\varepsilon})] + \alpha\rho\dot{\varepsilon}, \tag{1}$$

$$f(\varepsilon, \dot{\varepsilon}) = \frac{1}{3}\begin{cases} \gamma_1\varepsilon^3, & \varepsilon > 0, \quad \dot{\varepsilon} > 0; \\ -\gamma_2\varepsilon^3 + (\gamma_1 + \gamma_2)\varepsilon_m^2\varepsilon, & \varepsilon > 0, \quad \dot{\varepsilon} < 0; \\ -\gamma_3\varepsilon^3, & \varepsilon < 0, \quad \dot{\varepsilon} < 0; \\ \gamma_4\varepsilon^3 - (\gamma_3 + \gamma_4)\varepsilon_m^2\varepsilon, & \varepsilon < 0, \quad \dot{\varepsilon} > 0, \end{cases} \tag{2}$$

where σ, ε, and $\dot{\varepsilon}$ are the longitudinal stress, strain, and strain rate of the bar; E is the Young modulus; α is the coefficient of viscosity; ρ is the density; γ_i represents the parameters of hysteretic nonlinearity; and ε_m is the strain amplitude. The two latter parameters satisfy the conditions $|\gamma_i\varepsilon_m^2| \ll 1$ and $|\gamma_i| \gg 1$. For such a resonator, expressions for $\Delta F_{nl}/F_p$ and μ_{nl}/μ_p have the form [6]

$$\Delta F_{nl}/F_p = -b_1\varepsilon_m^2, \quad \mu_{nl}/\mu_p = a_1 Q_p \varepsilon_m^2, \tag{3}$$

Table 1

P	1	2	3	4	5
F_p, Hz	2110	6170	10240	14010	18180
Q_p	73	56	64	69	74

Table 2

P	1	2	3	4	5
$a_1 \times 10^{-9}$	13.4	4.8	2.9	2.7	1.4
$b_1 \times 10^{-9}$	70.4	29.6	15.2	14	5.3
$(\gamma_1 - \gamma_3) \times 10^{-10}$	16	6.9	3.4	3.1	1.1
$(\gamma_2 - \gamma_4) \times 10^{-10}$	3.5	1.1	0.74	0.7	0.42

where $a_1 = \frac{1}{16\pi}(\gamma_1 + \gamma_2 - \gamma_3 - \gamma_4)$, $b_1 = \frac{1}{32}\left\{(\gamma_1 + \gamma_2 - \gamma_3 - \gamma_4) + \frac{3}{4}(\gamma_1 - \gamma_2 - \gamma_3 + \gamma_4)\right\}$, and $Q_p = \frac{C_0^2}{\alpha\Omega_p}$. Comparing the experimental curves of Fig. 3 with expressions (3), we can determine the coefficients a_1, b_1 and the parameters $\gamma_1 - \gamma_3$, $\gamma_2 - \gamma_4$. Table 2 lists the corresponding values for each mode number p.

From Table 2, one can see that the increase in the resonator excitation frequency by a factor of 9 (from 2 kHz to 18 kHz) results in a significant decrease (by a factor of about 10 and 13, respectively) in the coefficients a_1 and b_1 (and the parameters $\gamma_1 - \gamma_3$ and $\gamma_2 - \gamma_4$ as well). Similar regularities were observed for lead [3] and zinc [4]. Thus, the experimental results show that, in such polycrystalline media, the effective parameters $\gamma_1 - \gamma_4$ are frequency-dependent. In this context, the hysteretic equation of state (1) should be modified in such a way as to include the frequency dependence of the nonlinear parameters $\gamma_1 - \gamma_4$.

To illustrate the frequency dependence of the parameters of hysteretic nonlinearity, we use the results of paper [11]. This paper suggests a rheological model of a microinhomogeneous medium in the form of a one-dimensional chain of stiff linear elastic elements and relatively compliant nonlinear viscoelastic defects. In our consideration, we assume that each such defect is characterized by hysteretic nonlinearity (2), relaxation frequency $W = \varsigma_1 E/\eta_1$, and dimensionless parameter $\varsigma_1 \ll 1$. The latter parameter determines the relative elasticity of the defect in comparison with the elasticity of the linear stiff elements, so that the equation of state of the hysteretic defect has the form

$$\sigma(\xi) = \varsigma_1 E[\xi - f(\xi, \dot{\xi})] + \eta_1 \dot{\xi}, \tag{4}$$

where ξ is the strain and η_1 is the coefficient of viscosity. In the case of a low defect concentration, the equation of state of the medium has the form [8]

$$\sigma(\varepsilon) = E\left[\varepsilon - \int_0^\infty\int_0^1 R(\varepsilon)N(\varsigma_1, W)d\varsigma_1 dW - \int_0^\infty\int_0^1 \varsigma_1 R[f(R(\varepsilon))]N(\varsigma_1, W)d\varsigma_1 dW\right],$$
$$\left|\int_0^\infty\int_0^1 \varsigma_1 R[f(R(\varepsilon))]N(\varsigma_1, W)d\varsigma_1 dW\right| \ll \left|\int_0^\infty\int_0^1 R(\varepsilon)N(\varsigma_1, W)d\varsigma_1 dW\right| \ll |\varepsilon|, \tag{5}$$

where $R(\varepsilon) = \frac{W}{\varsigma_1}\int_{-\infty}^t \varepsilon(\tau)e^{-W(t-\tau)}d\tau$ and $N_1 = N_1(\varsigma_1, W)$ is the distribution function describing the distribution of hysteretic defects in the parameters ς_1 and W. In this case, expressions for $\Delta F_{nl}/F_p$ and μ_{nl}/μ_p coincide in form with Eqs. (3); however, the corresponding coefficients now depend on frequency Ω_p and distribution function $N_1 = N_1(\varsigma_1, W)$:

$$a_1(\Omega_p) = \int_0^\infty\int_0^1 \frac{N_1(\varsigma_1, W)}{\varsigma_1^3[1 + (\Omega_p/W)^2]^3} \times \{a_1[1 - (\Omega_p/W)^2] - 2b_1(\Omega_p/W)\}d\varsigma_1 dW, \tag{6}$$

$$b_1(\Omega_p) = \int_0^\infty\int_0^1 \frac{N_1(\varsigma_1, W)}{\varsigma_1^3[1 + (\Omega_p/W)^2]^3} \times \{2a_1(\Omega_p/W) + b_1[1 - (\Omega_p/W)^2]\}d\varsigma_1 dW. \tag{7}$$

These expressions show that a relaxation of hysteretic defects has two consequences: first, the coefficients determining the resonance frequency shift and the nonlinear loss in a microinhomogeneous medium become dependent on frequency and, second, each such coefficient appears to be a linear combination of frequency-independent coefficients a_1 and b_1 determined in Eqs. (3). According to Eqs. (6) and (7), static coefficients of nonlinearity, $a_1(0)$ and $b_1(0)$, of the microinhomogeneous medium are related to nonlinearity parameters a_1 and b_1 of a single hysteretic defect by the formulas

$$a_1(0) = a_1\int_0^\infty\int_0^1 \frac{N_1(\varsigma_1, W)}{\varsigma_1^3}d\varsigma_1 dW,$$

$$b_1(0) = b_1\int_0^\infty\int_0^1 \frac{N_1(\varsigma_1, W)}{\varsigma_1^3}d\varsigma_1 dW.$$

Using Eqs. (6) and (7) and the experimental results (Table 2), we can attempt to determine the distribution function of defects $N_1 = N_1(\varsigma_1, W)$ so as to bring the

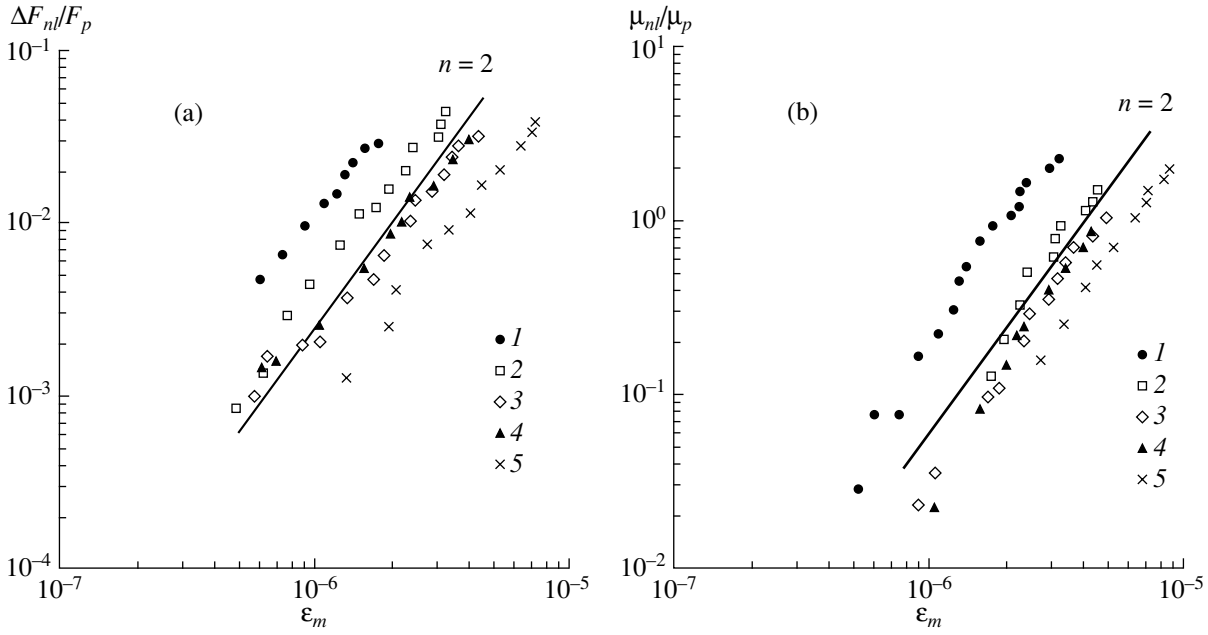

Fig. 3. (a) Relative nonlinear resonance frequency shift and (b) attenuation coefficient as functions of wave amplitude at resonance. The straight lines correspond to functions $F_{nl}/F_p \sim \varepsilon_m^2$ and $\mu_{nl}/\mu_p \sim \varepsilon_m^2$.

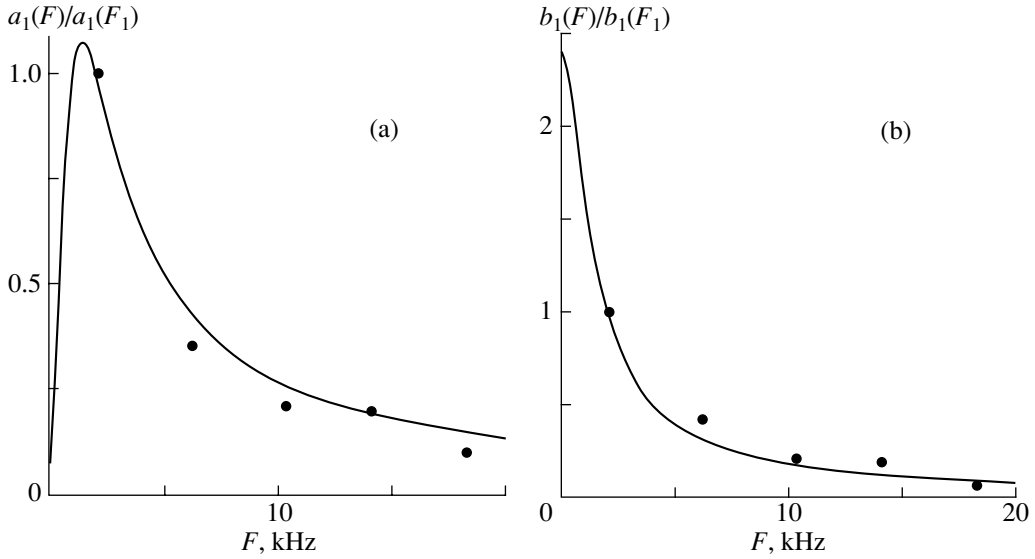

Fig. 4. Parameters (a) $a_1(F)/a_1(F_1)$ and (b) $b_1(F)/b_1(F_1)$ as functions of frequency F.

experimental and analytical results in correspondence. To solve this problem, we assume for simplicity that ς_l = const, so that the distribution function of defects depends only on the relaxation frequency W. Applying the enumerative technique to power functions $N_1 = N_1(W)$, we succeeded in finding such a distribution. Figure 4 shows the experimental points together with the dependences for normalized coefficients $a_1(\Omega_p)/a_1(\Omega_1)$ and $b_1(\Omega_p)/b_1(\Omega_1)$ calculated for the following distribution function:

$$N_1(W) = n_1 W^{-2}/(W_a^{-1} - W_b^{-1}),$$
$$W_a = 12.5 \times 10^3 \text{ s}^{-1}, \quad W_b = 12.5 \times 10^6 \text{ s}^{-1}, \tag{8}$$

where $n_1 = \int_0^\infty N_1(W)dW$ is the concentration of hysteretic defects. One can see that the analytical calculation

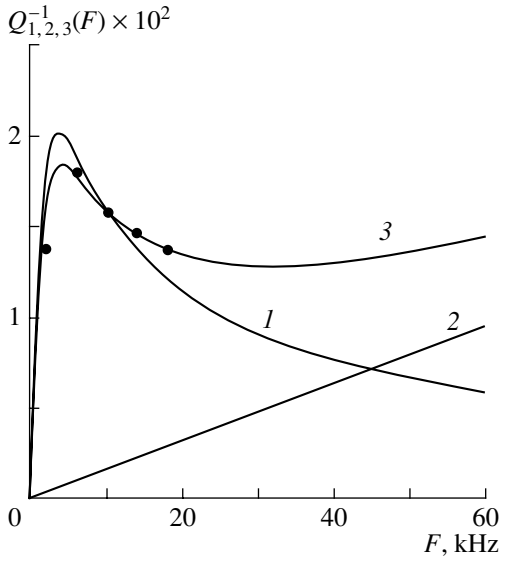

Fig. 5. Inverse Q-factor Q^{-1} as a function of frequency F: loss due to (*1*) hysteretic, (*2*) dissipative, and (*3*) both hysteretic and dissipative defects.

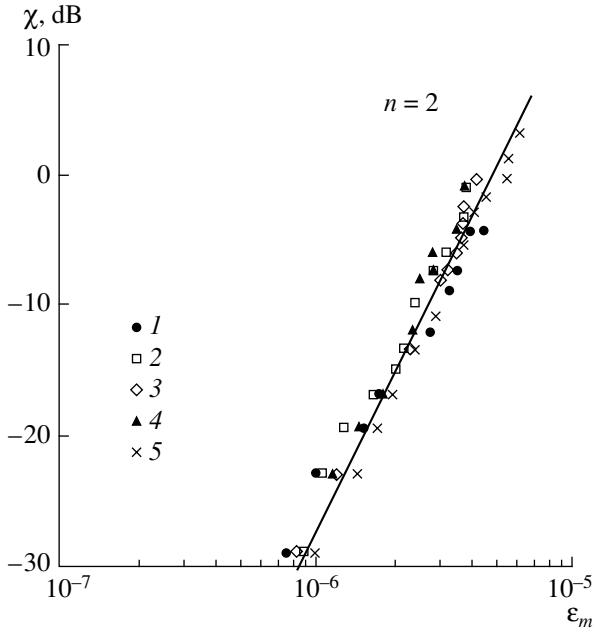

Fig. 6. Coefficient of nonlinear attenuation of the pulse versus the pump wave amplitude. The straight line corresponds to the function $\chi(\varepsilon_m) \sim \varepsilon_m^2$.

with the use of this distribution of hysteretic defects in relaxation frequencies agrees well with the experimental data; in this case, $a_1(0) = 1.3 \times 10^8$ and $b_1(0) = 1.3 \times 10^{10}$.

Using distribution function (8), we can additionally determine the ratio of the defect concentration n_1 to the parameter ς_1. From equation of state (5), we obtain the expression for the Q-factor of the resonator

$$Q_p^{-1} = \frac{1}{\varsigma_1}\int_0^\infty \frac{\Omega_p/W}{1 + (\Omega_p/W)^2} N_1(W)dW. \quad (9)$$

Substituting Eq. (8) in Eq. (9), we find

$$Q_p^{-1} = \frac{n_1}{2\varsigma_1\Omega_p(W_a^{-1} - W_b^{-1})}\ln\left(\frac{1 + (\Omega_p/W_a)^2}{1 + (\Omega_p/W_b)^2}\right). \quad (10)$$

Figure 5 shows the inverse Q-factor, Q^{-1}, versus frequency F for $n_1/\varsigma_1 = 5 \times 10^{-2}$ together with the experimental points. It can be seen that the analytical calculation for this value of n_1/ς_1 agrees well with the experimental results. With this parameter value, we can estimate the ratios of the coefficients a_1 and b_1 to the square of the relative elasticity of defects as $a_1/\varsigma_1^2 = 2.6 \times 10^9$ and $b_1/\varsigma_1^2 = 2.6 \times 10^{11}$.

NONLINEAR ATTENUATION OF AN ULTRASONIC PULSE UNDER THE ACTION OF AN LF WAVE

In the second series of observations, we observed and investigated the sound-by-sound damping related to the dissipative nonlinearity of sandstone. In this case, in parallel with the excitation of the LF pump wave, weak ultrasonic pulses were excited in bar *2* by HF radiator *4*. After passing through the bar, the pulses were received by accelerometer *6*, whose signals were fed to a spectrum analyzer to measure their amplitudes $U_2(\varepsilon_m)$. With increasing strain amplitude ε_m of the pump wave, the amplitude of the received pulse $U_2(\varepsilon_m)$ noticeably decreased. Figure 6 shows the coefficient of nonlinear attenuation $\chi(\varepsilon_m) = \ln[U_0/U_2(\varepsilon_m)]$ (U_0 is the pulse amplitude in the absence of the pump wave) of the pulse at the frequency $f = 180$ kHz versus the strain amplitude ε_m (at resonance) for different frequencies of resonator excitation. It is seen that coefficient $\chi(\varepsilon_m)$ is independent of frequency F_p for all five resonator modes and is a quadratic function of strain amplitude ε_m, i.e., $\chi(\varepsilon_m) \sim \varepsilon_m^2$. Similar dependences were observed for ultrasonic pulses at different frequencies. Figure 7 shows experimental points for the coefficient of nonlinear attenuation of the pulse as a function of frequency f (for a constant strain amplitude $\varepsilon_m = 3.3 \times 10^{-6}$ at the first mode of the resonator). For frequencies ranging from 40 to 400 kHz, this function is approximately the power function $\chi(\varepsilon_m) \sim f^n$, where $n \cong 1/2$.

Comparing Figs. 3 and 4 with Figs. 6 and 7, we see that the hysteretic and dissipative components of nonlinearity of sandstone (and other polycrystalline materials as well) are qualitatively different, because the first component decreases with increasing frequency F_p of

the pump wave and the second is independent of frequency F_p and increases with increasing frequency f of the pulse. From this fact, we can conclude that the origins of the hysteretic and dissipative components of sandstone nonlinearity are different and independent. It should be noted that a small amplitude variation of a weak ultrasonic pulse in the field of an intense LF pump wave is also possible in a medium with a hysteretic nonlinearity. However, in this case, the dependences of the coefficient $\chi(\varepsilon_m)$ on the frequencies Ω_p and ω should differ from the dependences observed in the experiment. Calculations show that, for a resonator with a hysterestic relaxation nonlinearity given by Eq. (5), the coefficient $\chi(\varepsilon_m)$ is determined by the expression

$$\chi(\varepsilon_m) = \frac{(5\gamma_1 - \gamma_2 - 5\gamma_3 + \gamma_4)\varepsilon_m^2}{24\varsigma_1^3} \times \int_0^\infty \frac{(W^2 - \omega^2)W^4 N_1(W)dW}{(W^2 + \Omega_p^2)[W^2 + \omega^2]^2}.$$

We substitute the values of the parameters γ_1–γ_3 and γ_2–γ_4 at the frequency of the first mode of the resonator (Table 1) and the distribution function given by Eq. (8) into the above expression. Using the values found earlier, namely, $n_1/\varsigma_1 = 5 \times 10^{-2}$, $a_1/\varsigma_1^2 = 2.6 \times 10^9$, and $b_1/\varsigma_1^2 = 2.6 \times 10^{11}$, we obtain

$$\chi(\varepsilon_m) = 7 \times 10^8 \varepsilon_m^2 \int_{W_a}^{W_b} \frac{(W^2 - \omega^2)W^2 dW}{(W^2 + \Omega_1^2)[W^2 + \omega^2]^2}.$$

From the numerical analysis of these integrals, it follows that, as the frequencies Ω_p and ω increase, the coefficient $\chi(\varepsilon_m)$ decreases down to zero and may become negative. For example, at $\varepsilon_m = 3.3 \times 10^{-6}$ and $\Omega_p = \Omega_1$, the value of $\chi(\varepsilon_m)$ decreases from 6.5×10^{-5} (at $f = 40$ kHz) to -1.8×10^{-7} (at $f = 400$ kHz), and at $f = 84$ kHz, we have $\chi(\varepsilon_m) = 0$. Hence, in such a resonator, at high frequencies ($f > 84$ kHz), an increase (although a relatively small one) in the amplitude of an ultrasonic pulse rather than a decrease should occur; i.e., an amplification of sound by sound rather than attenuation. In this case, at the frequency $f = 180$ kHz, the value of $\chi(\varepsilon_m)$ is as small as about -10^{-5}, which (in absolute value) is five orders of magnitude smaller than the experimental value (see Fig. 6). All this contradicts the results of the experiment and allows us to neglect the contribution of hysteretic nonlinearity to the attenuation of an HF pulse in the field of an LF wave that occurs due to the dissipative nonlinearity. In this context, an analytical description of sound-by-sound damping requires, in general, another model and another equation of state than those considered above. However, we can again use a similar rheological model of microinhomogeneous medium [11] by assuming that, in addition to hysteretic defects, the medium also includes other defects characterized by dissipative nonlinearity. Here we assume that each dissipative defect can be described by the nonlinear differential equation of second order

$$\sigma(\xi) = \varsigma_2 E\xi + \eta_2[1 + \mu|\dot{\xi}|^S]\dot{\xi} + m\ddot{\xi}, \qquad (11)$$

where ς_2, η_2, μ, and m are the relative elasticity, the coefficient of viscosity, the parameter of dissipative nonlinearity, and the reduced (to unit length) mass of the defect. From this equation, one can obtain the equation of state of the medium and derive the expressions for the coefficients of linear $\beta(\omega)$ and nonlinear $\chi(\varepsilon_m)$ attenuation of the pulse:

$$\sigma(\varepsilon) = E\left(\varepsilon - \frac{2}{\varsigma_2}\int_0^\infty \frac{w^2 N_2(w)dw}{\lambda}\int_{-\infty}^t \varepsilon(t_1)\exp\left(\frac{d}{2}(t_1 - t)\right)\sin\left(\frac{\lambda}{2}(t - t_1)\right)dt_1\right)$$

$$-\frac{2^{S+2}\mu d E}{\varsigma_2^{S+1}}\int_0^\infty \frac{w^{2S+3}N_2(w)dw}{\lambda^{S+2}}\int_{-\infty}^t\int_{-\infty}^{t_1} D[\varepsilon(t_1)]\varepsilon(t_2)\exp\left(\frac{d}{2}(t_2 - t)\right)\sin\left(\frac{\lambda}{2}(t_1 - t_2) - \arctan\left(\frac{\lambda}{d}\right)\right)\sin\left(\frac{\lambda}{2}(t - t_1)\right)dt_2 dt_1, \qquad (12)$$

$$D[\varepsilon(t_1)] = \left|\int_{-\infty}^{t_1}\varepsilon(t_2)\exp\left(\frac{d}{2}(t_2 - t_1)\right)\sin\left(\frac{\lambda}{2}(t_1 - t_2)\right)dt_2\right|^S,$$

$$\beta(\omega) = \frac{dL\omega^2}{2\varsigma_2 C_0}\int_0^\infty \frac{w^2 N_2(w)dw}{(w^2 - \omega^2)^2 + d^2\omega^2}, \qquad (13)$$

$$\chi(\varepsilon_m) = \frac{\mu d\varepsilon_m^S L\omega^2}{2\pi C_0\varsigma_2^{S+1}}\left(\frac{\Gamma[(S+1)/2]}{\Gamma[(S+2)/2]}\right)^2\int_0^\infty \frac{w^{2S+2}[(w^2 - \omega^2)^2 - d^2\omega^2]N_2(w)dw}{[(w^2 - \Omega_p^2)^2 + d^2\Omega_p^2]^{S/2}[(w^2 - \omega^2)^2 + d^2\omega^2]^2}, \qquad (14)$$

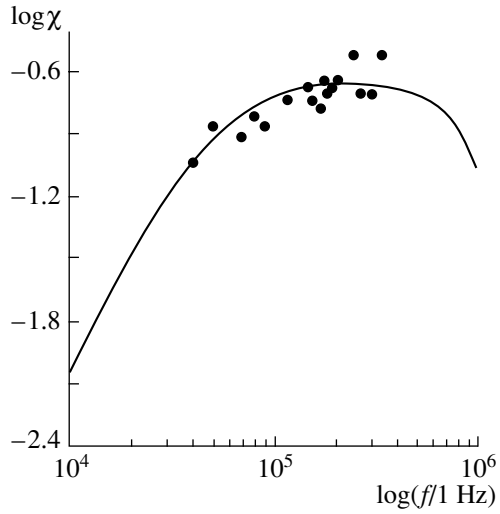

Fig. 7. Coefficient of nonlinear attenuation of the pulse versus the frequency f for $\varepsilon_m = 3.3 \times 10^{-6}$.

where $\lambda^2 = 4w^2 - d^2$, $w = (\varsigma_2 E/m)^{1/2}$ is the defect resonance frequency, $d = \eta_2/m$ is the damping parameter of the defect, and $N_2 = N_2(w)$ is the distribution function of dissipative defects in resonance frequencies. (Here we again assume that $\varsigma_2 = \text{const}$.) It is obvious that $S = 2$ for the sandstone sample under investigation. Fitting the distribution function $N_2 = N_2(w)$, one can achieve a correspondence between the analytical coefficient of nonlinear attenuation (14) as a function of frequency ω and the experimental data. Figure 7 shows coefficient (14) for $N_2(w) = n_2 w^{-1}/\ln(w_2/w_1)$, $w_2 \le w \le w_1$, $w_1 = 4 \times 10^7$ s^{-1}, $w_2 = 10^9$ s^{-1}, $d = 5 \times 10^9$ s^{-1}, $\varepsilon_m = 3.3 \times 10^{-6}$, and $\mu n_2/\varsigma_2^3 = 2.5 \times 10^{10}$. It can be seen that these parameter values provide the agreement between analytical calculations and experimental data. From Eq. (14), using the value of linear attenuation $\beta \simeq 0.7$ measured at a frequency $f = 180$ kHz, we can estimate the ratio of the dissipative defect concentration to parameter n_2 as ς_2: $n_2/\varsigma_2 = 2.4 \times 10^{-1}$. With this value, we obtain $\mu/\varsigma_2^2 = 10^{11}$.

Finally, in the same way as it was shown that hysterestic nonlinearity does not influence the sound-by-sound damping, we can show that the dissipative nonlinearity does not influence the LF effects of resonance frequency shift and the nonlinear loss in the resonator. For this purpose, it is necessary to compare (assuming that $\varepsilon = \varepsilon_m \sin \Omega t$) the hysteretic and dissipative components of nonlinearity. The numerical analysis shows that, when $F < F^* \cong 300$ kHz, the hysteretic nonlinearity predominates over the dissipative one and, hence, in the frequency range $F \ll F_{nl}$, the nonlinear loss μ_{nl}/μ_p and the resonance frequency shift $\Delta F_{nl}/F_p$ are determined by the hysterestic nonlinearity. In the same way, we can determine the boundary frequency F_{lin}, below which the linear loss in the resonator is mainly determined by the hysteretic defects and above which, by the dissipative ones. Curve *2* in Fig. 5 represents the frequency dependence of the linear loss of the resonator, $Q_2^{-1}(F) = \beta(F)C_0/\pi FL$, that is caused by the dissipative defects. The point of intersection of curves *1* and *2* yields $F_{lin} \cong 45$ kHz. Near this frequency, the Q-factor of the resonator is determined by the total loss $Q_p^{-1} = Q_1^{-1} + Q_2^{-1}$. Curve *3* in Fig. 5 represents the frequency dependence of the total linear loss Q_p^{-1} due to the hysteretic and dissipative defects (at $n_1/\varsigma_1 = 4.4 \times 10^{-2}$). One can see that curve *3* agrees even better (than curve *1*) with the results of measuring Q_p. Using the refined value of the parameter $n_1/\varsigma_1 = 4.4 \times 10^{-2}$, we obtain refined values of the ratios of coefficients a_1 and b_1 to the square of the relative elasticity of hysteretic defects: $a_1/\varsigma_1^2 = 2.9 \times 10^9$ and $b_1/\varsigma_1^2 = 2.9 \times 10^{11}$. From curve *3* of Fig. 5, it also follows that, in a fairly wide frequency range (approximately from 2 to 60 kHz), the linear damping decrement of the sandstone sample under investigation is almost frequency-independent, its Q-factor (in this frequency range) being approximately equal to 65. This result agrees well with the previous experimental observations of practically frequency-independent behavior of the Q-factors (in a wide frequency range) of many solids, including rock and metals [12–15]. Outside this range, the Q-factor $Q(\omega)$ of such media should (and does) depend on the frequency ω: at low frequencies, it decreases with increasing ω and, at high frequencies, it increases, so that at medium frequencies, one has $Q(\omega) \approx \text{const}$ [12–15]. Precisely this kind of dependence is shown in Fig. 5 (curve *3*).

CONCLUSIONS

In this paper, we presented the results of experimental studies of the amplitude and frequency dependences of nonlinear effects (nonlinear loss, resonance frequency shift, and sound-by-sound damping) in a sandstone bar resonator. The analysis of the experimental amplitude–frequency behavior of these effects showed that the acoustic nonlinearity of sandstone includes two components: LF hysteretic and HF dissipative ones. Both components exhibit a cubic amplitude dependence, but they have different frequency dependences. The explanation of this fact is based on the assumption that sandstone contains two types of defects, one of which is characterized by a hysteretic nonlinearity and the other, by a dissipative nonlinearity, and the defects of these types are characterized by different relaxation and resonance frequencies. The analytical description of the measured dependences was performed within the framework of the rheological model of a microinhomogeneous medium containing such defects. We derived

equations of state of media with such defects and determined the expressions for the nonlinear loss, the resonance frequency shift, and the nonlinear attenuation coefficient of a weak ultrasonic pulse under the action of an intense LF pump wave. We fitted the distribution functions of both types of defects in relaxation and resonance frequencies to match the analytical calculations with the experimental results and determined the effective parameters of the nonlinearity of sandstone. It was shown that, at frequencies $F \ll 45$ kHz and $F < 300$ kHz, the linear loss and nonlinearity of sandstone, respectively, are mainly determined by hysteretic defects, and at $F \gg 45$ kHz and $F > 300$ kHz, by dissipative ones.

From the experimental and theoretical results obtained in this paper (and earlier [3–7, 9]) it follows that hysteretic and dissipative components of acoustic nonlinearity of many microinhomogeneous media are caused by different kinds of defects characterized by the corresponding nonlinear relaxation and resonance properties. In polycrystalline metals and rocks, such defects may be, for example, dislocations or dislocation clusters, microcracks, and grain boundaries. These defects may differ from one medium to another, and acoustic measurements alone are insufficient for determining exactly which defects are responsible for the manifestations of nonlinearity in the medium. For this purpose, it is necessary to use the physical models of the known defects and the corresponding equations of state. Nevertheless, the above technique is quite appropriate for both qualitative and quantitative determination of the rheological properties and nonlinearity parameters of these defects, which can be used for classification and diagnostics of different microinhomogeneous media.

ACKNOWLEDGMENTS

This work was supported in part by the Russian Foundation for Basic Research, project nos. 01-05-64173, 02-02-16237, and 02-02-08021 INNO.

REFERENCES

1. V. E. Nazarov, L. A. Ostrovsky, I. A. Soustova, and A. M. Sutin, Phys. Earth Planet. Inter. **50** (1), 65 (1988).
2. V. E. Nazarov, Akust. Zh. **37**, 150 (1991) [Sov. Phys. Acoust. **37**, 75 (1991)].
3. V. E. Nazarov, Fiz. Met. Metalloved. **88** (4), 82 (1999).
4. V. E. Nazarov, Akust. Zh. **46**, 542 (2000) [Acoust. Phys. **46**, 186 (2000)].
5. V. E. Nazarov, Akust. Zh. **47**, 509 (2001) [Acoust. Phys. **47**, 438 (2001)].
6. S. V. Zimenkov and V. E. Nazarov, Fiz. Zemli, No. 1, 13 (1993).
7. S. V. Zimenkov and V. E. Nazarov, Fiz. Zemli, No. 5, 62 (1994).
8. R. A. Guyer and P. A. Johnson, Phys. Today, No. 4, 30 (1999).
9. V. E. Nazarov, A. V. Radostin, and I. A. Soustova, Akust. Zh. **48**, 85 (2002) [Acoust. Phys. **48**, 76 (2002)].
10. L. A. Ostrovsky and P. A. Johnson, Riv. Nuovo Cimento **24** (7), 1 (2001).
11. V. E. Nazarov, V. Yu. Zaitsev, and I. Yu. Belyaeva, Acust. Acta Acust. **88** (1), 40 (2002).
12. S. Ya. Kogan, Izv. Akad. Nauk SSSR, Fiz. Zemli, No. 11, 3 (1966).
13. S. Ya. Kogan, Izv. Akad. Nauk SSSR, Fiz. Zemli, No. 11, 17 (1966).
14. L. Knopov, in *Physical Acoustics. Principles and Methods*, Vol. 3: *Lattice Dynamics*, Ed. by W. P. Mason (Academic, New York, 1965; Mir, Moscow, 1968).
15. K. Aki and P. G. Richards, *Quantitative Seismology: Theory and Methods* (Freeman, San Francisco, 1980; Mir, Moscow, 1983), Vol. 1.

Translated by A. Vinogradov

Acoustical Physics, Vol. 50, No. 4, 2004, pp. 454–462. From Akusticheskiĭ Zhurnal, Vol. 50, No. 4, 2004, pp. 533–542.

BIOLOGICAL ACOUSTICS

Echolocation Signals of Wild Dolphins[1]

W. W. L. Au

Marine Mammal Research Program, Hawaii Institute of Marine Biology, P.O. Box 1106, Kailua, Hawaii, 96734 USA

Received December 2, 2003

Abstract—Most of our understanding of dolphin echolocation has come from studies of captive dolphins performing various echolocation tasks. Recently, measurements of echolocation signals in the wild have expanded our understanding of the characteristics of these signals in a natural setting. Measuring undistorted dolphin echolocation signals with free swimming dolphins in the field can be a challenging task. A four hydrophone array arranged in a symmetrical star pattern was used to measure the echolocation signals of four species of dolphins in the wild. Echolocation signals of the following dolphins have been measured with the symmetrical star array: white-beaked dolphins in Iceland, Atlantic spotted dolphins in the Bahamas, killer whales in British Columbia, and dusky dolphins in New Zealand. There are many common features in the echolocation signals of the different species. Most of the signals had spectra that were bimodal: two peaks, one at low frequencies and another about an octave higher in frequency. The source level of the sonar transmission varies as a function of $20\log R$, suggesting a form of time-varying gain but on the transmitting end of the sonar process rather than the receiving end. The results of the field work call into question the issue of whether the signals used by captive dolphins may be shaped by the task they are required to perform rather than what they would do more naturally.

INTRODUCTION

Most of our understanding on echolocation signals used by different species of dolphins has come from research with captive animals (Au, 1993). From these studies, we have learned that dolphins emit high-frequency click signals with peak frequencies as high as 100–130 kHz and with bandwidths between 30–55 kHz. The signals are emitted in a beam that is directed forward and slightly upwards with respect to the longitudinal axis of the animals. The 3-dB transmission beamwidth can vary from 10–16°, depending on the species. Another important characteristic of the transmission system is that signals measured off the axis of the beam are distorted in comparison to signals measured along the beam axis. Finally, the spectrum of the signals may depend on the source level; the higher the source level, the greater the center frequency of the signals [1, 2].

Accurate measurements of echolocation signals used by free-ranging dolphins in the wild can be difficult to obtain because the echolocation beam pattern is relatively narrow. If echolocation signals are not measured close to the axis of the animal's beam, the signals will be distorted. It is also extremely difficult to determine the distance of a moving dolphin from the recording hydrophone in order to determine the source level (sound pressure level 1 m from the dolphin) of the signals. We have successfully overcome these problems by using a short base line array of four hydrophones arranged as a symmetrical star shown schematically in Fig. 1. The array structure resembles the letter "Y", with each 45.7 cm long arm separated by an angle of 120°. A spherical hydrophone was connected to the end of each arm with a fourth hydrophone connected at the geometric center of the "Y." The range of an echolocating dolphin can be determined by measuring the difference in the time of arrival between the center hydrophone and the other hydrophones. The range of the echolocating dolphin can be determined with Eq. (1) [3]:

$$R = \frac{c^2(\tau_{01}^2 + \tau_{02}^2 + \tau_{03}^2) - 3a^2}{2c(\tau_{01} + \tau_{02} + \tau_{03})}, \qquad (1)$$

where τ_{0i} is the arrival time difference between the center hydrophone and the ith hydrophone.

Calibration measurements obtained with the array and a simulated dolphin signal indicate only a 12% error in the range estimation at 25 m, which translated to a propagation loss error of only 1.1 dB. An underwater housing connected to the back of the hydrophone mounting plate contained an amplifier and line-driver for each of the hydrophones. A CCD video camera in an underwater housing was mounted next to the center hydrophone. A multiconductor cable, 77 m in length, consisting of five coaxial lines and two dc power lines connected the array to an adjustable amplifier–filter box containing a power supply.

The symmetrical star array has been used to measure the echolocation signals of the Atlantic spotted dolphin, *Stenella frontalis*, in the Bahama sand banks [3]; white-beaked dolphin, *Lagenorhynchus albirostris*, in the waters of Iceland [4]; killer whale, *Orcinus orca*, in British Columbia [5]; and dusky dolphin, *Lagenorhynchus obscurus*, in the water of Kaikoura, New Zealand [6]. With the exception of the killer whale,

[1] This article was submitted by the author in English.

echolocating dolphins in the wild typically emit broadband, short duration click signals (<80 μs) with a bimodal spectrum; a low-frequency peak occurs between 30–50 kHz and a high-frequency peak between 80–120 kHz. Approximately 70–80% of the signals measured in the field have been bimodal. Killer whales emit echolocation signals that are twice as long in duration and with a frequency content approximately half that of the other dolphins studied.

Echolocation signals were digitized with two Gage-1210, 12-bit dual simultaneous sampling data acquisition boards that were connected to a "lunch box" computer via two EISA slots. The data acquisition system operated at a sample rate of 500 kHz with a pretrigger capability. When the computer signaled the Gage-1210 to collect data, four channels of acoustic signals were simultaneously and continuously digitized with the results going into separate circular memories on each Gage-1210 board. When an echolocation signal was detected by the center hydrophone, it triggered the data acquisition board. Two hundred pre-trigger points and two hundred post-trigger points were collected for each channel and downloaded into the computer. A total of 80 clicks could be downloaded for each episode before the data had to be stored on the hard drive. A specially constructed ISA board was also used to measure the time interval between the clicks being acquired and to cause a light emitting diode to flash indicating that clicks were being captured. The interclick interval data was also downloaded and stored on the hard drive. The time of capture (to the closest 18 ms interval of the computer timing system) of each click was also saved and stored on the hard drive. The clock on a portable VCR was synchronized to the computer's clock, so that the video images could be synchronized with the acoustic data.

During field measurements, with the exception of the killer whale, animals often milled about 30–50 m from our boat and made "runs" towards the array, continuously echolocating as they approached. Killer whales often foraged along the steep cliffs in the Johnstone Strait of British Columbia, Canada. We would position our boat about 100–150 m directly in their path and they rarely deviated from their path except to veer to one side if the array was in their path so as to not strike the array. The range of an echolocating dolphin was determined by measuring the differences in the time of arrival between the signal at the center and the three other hydrophones. Only signals in which the center hydrophone detected the largest amplitude or were within 3 dB of the highest amplitude signals were analyzed. The 3-dB criterion is applicable at ranges of about 5–15 m. As the dolphin approaches within 4 m of the array, the angles between the dolphin and the various hydrophones could increase significantly if the animal approaches along the midline of the array. However, in most cases, the dolphins tend to approach the array at some oblique angle, so that the angles between the dolphin and the different hydrophones tended not to be very large and the 3-dB criterion could be used as an approximation. The video images were used only under special conditions since the quality of the images varies according to lighting and visibility conditions. Also, when dolphins approached the array obliquely, they would be out of the camera's view for various portions of their "run."

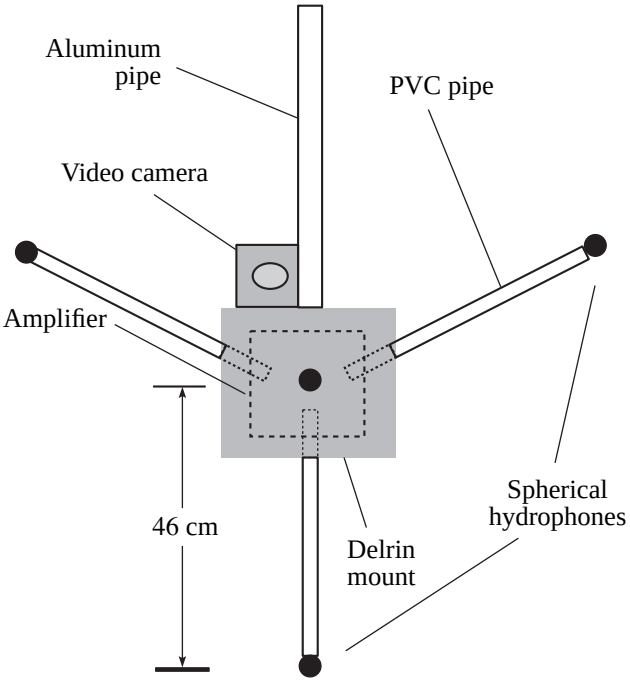

Fig. 1. Symmetrical star array used to measure echolocation signals of dolphins in the field.

WAVEFORM AND SPECTRUM

Echolocation click trains can be highly variable and it is difficult to understand the reasons for these variations. Therefore, echolocation signals should be described statistically in order to understand their basic characteristics. Variations also occur when measuring signals from captive dolphins in highly controlled situations [7] as well as in the wild. The best way to have a glimpse of such variations is to look at the spectra of a click train displayed in a waterfall format. Four examples of click trains are shown in Fig. 2, two examples each for *Orcinus orca* [5] and for *Lagenorhynchus obscurus* [6]. The waterfall display of Fig. 2a for the killer whale shows fairly stereotypical spectra with some slight variations, while Fig. 2c shows much greater variation. The same is true for signals of the dusky dolphin shown in Figs. 2b and 2d. Note that the frequency scale for the dusky dolphin displays is twice as high as that for the killer whale. Similar waterfall displays also exist for the white-beaked and Atlantic spotted dolphins.

Representation echolocation signal waveforms and spectra are shown in Fig. 3. The Atlantic spotted dol-

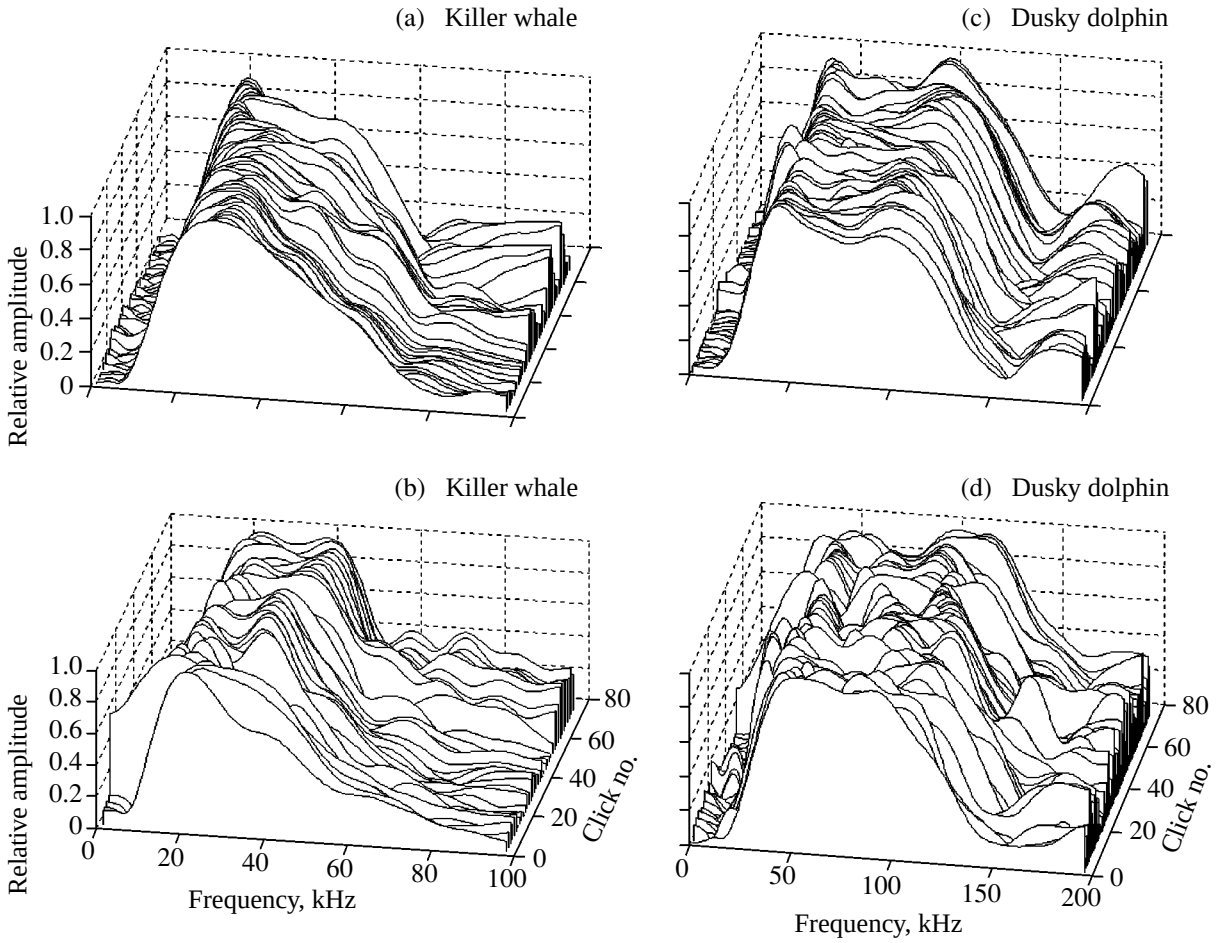

Fig. 2. Waterfall display of the spectra of four several click trains: (a, b) fairly stereotype clicks from the killer whale and dusky dolphin, respectively; (c, d) click trains with considerable variations for the killer whale and dusky dolphin, respectively.

phin, the killer whale, and the dusky dolphin all emitted three basic types of signals. The first signal type had a single primary low-frequency peak in its spectrum, while the two other signal types had bimodal spectra, some with a dominant low-frequency peak and some with a dominant high-frequency peak. The signals with a single low-frequency peak in the spectrum usually occurred 8–15% or less of the time. The bimodal signals occurred between 75 and 89% of the time. The white-beaked dolphin also emitted mainly bimodal signals; however, the single low-frequency peaked signal was rarely observed with this species. The presence of bimodal signals is obvious in the waterfall displays of Fig. 2, and the bimodality contributes to the broadband nature of the signals.

The waveforms and, consequently, the spectra for all the species are very similar except for the specific peak frequencies and signal duration. The axiom that a click is a click seem to be appropriate here and may be related to the notion that there are not many different ways to produce clicks and the mechanism for click production is probably the same for most odontocetes. The signals used by the killer whale are unique among delphinid being about an octave lower in frequency with durations that are twice as long as for the other species.

TIME-VARYING GAIN

The source levels as a function of range for the four delphinid species are shown in Fig. 4 as scatter plots. The solid line through each scatter plot is the best fit of the equation

$$\mathrm{SL} = K + 20\log R, \tag{2}$$

where R is the range of the dolphin from the array and K is a constant that provided the best fit of the equation with the data. The values of the constant K for the difference species are

$$K = \begin{cases} 190.3 \text{ dB } \textit{Lagenorhynchus albirostris} \\ 185.3 \text{ dB } \textit{Stenella frontalis} \\ 181.4 \text{ dB } \textit{Orcinus orca} \\ 177.8 \text{ dB } \textit{Lagenorhynchus obscurus}. \end{cases} \tag{3}$$

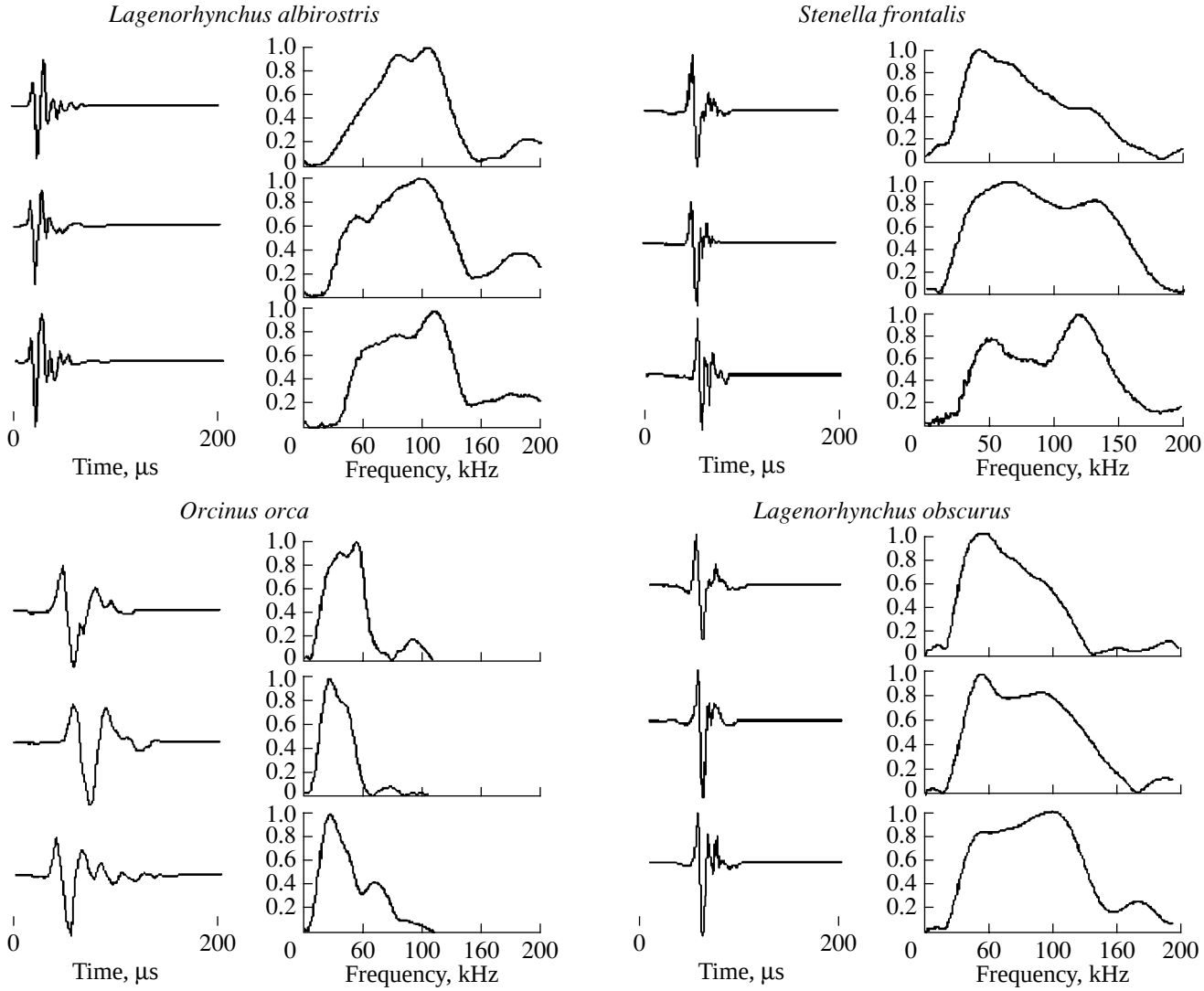

Fig. 3. Representative waveforms and spectra of the four species of dolphins being considered.

The r^2 values are the square of the correlation coefficient between the data points and the solid line in each plot. The r^2 values varied from 0.52 to 0.74, showing a strong correlation between the $20\log R$ curve and the scattered data points.

Au and Benoit-Bird [8] attributed this variation in the source level as a form of time-varying gain. Since the receiving or hearing sensitivity of dolphins is probably fixed and not subject to manipulation, dolphins have evolved to have a time-varying gain implemented in the transmission phase of the echolocation process rather than in the receiving phase as for technological sonars and for some bats [9]. For single sonar targets, an optimal time-varying gain function should vary as a function of $40\log R$, compensating for the two-way spherical spreading loss. However, if the target is a fish school, then the received echo level (RL) of the school can be expressed as [10]

$$\mathrm{RL} = \mathrm{SL} - 20\log R + S_V + 10\log V, \qquad (4)$$

where SL is the source level, R is the range, S_V is the scattering coefficient, and V is the volume factor within the joint transmission and receiving beam of the dolphins. If Eq. (3) for the source level is inserted into Eq. (4), the received echo level will be independent of range. Therefore, dolphins hunting for a fish school with their echolocation system will have an ideal time-varying gain function to keep the echo level relatively constant independent of the range of the school. The ideal situation will not always apply since dolphins also have a specific integration time associated with their

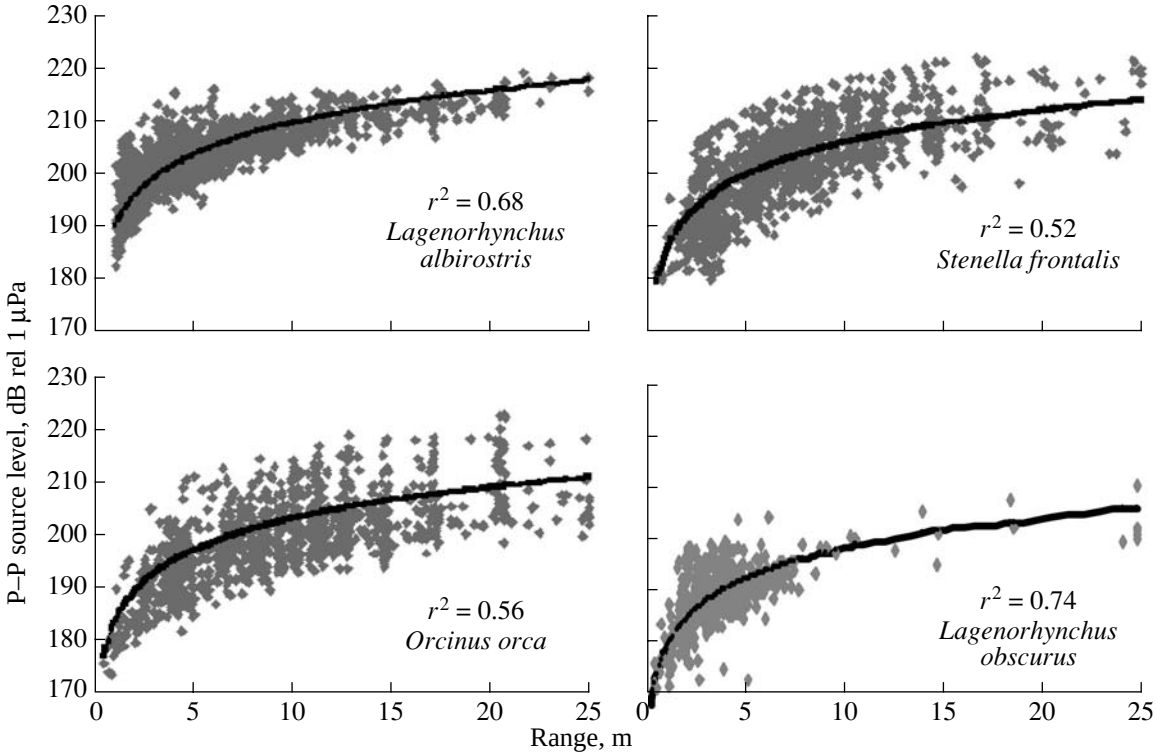

Fig. 4. Scatter plot of source level as a function of the dolphins' range from the measurement array. The solid line is the best fit line for the equation $K + 20\log R$, where K is a constant and R is range.

auditory system so that only a portion of the echoes will be effective in the detection process.

SPECTRAL CHARACTERISTICS

Since most of the signals measured in the wild had bimodal spectra, it is more appropriate to describe the signal spectra by their center frequency rather than peak frequency. Center frequency is defined as that frequency which divides the energy in a frequency spectrum into two equal parts; it is defined mathematically as [11]

$$f_0 = \frac{\int_0^\infty f|S(f)|^2 df}{\int_0^\infty |S(f)|^2 df}, \quad (5)$$

where $S(f)$ is the Fourier transform of the echolocation signal and f is the instantaneous frequency. Histograms of center frequency for the four species are shown in Fig. 5. Also shown are the mean and standard deviation of the center frequency for each species.

The dolphins in the genus *Lagenorhynchus* had the highest center frequencies of the four species discussed here. Most of the signals of the white-beaked dolphin had center frequencies between 90 and 110 kHz. Most of the signals of the dusky dolphin had center frequencies between 80 and 100 kHz, about 10 kHz lower than that of the white-beaked dolphin. This seems rather odd since the white-beaked dolphin is much larger than the dusky dolphin and is almost twice as heavy. One would expect the center frequency of the dusky dolphin to be higher than what was observed. The signals of the Atlantic spotted dolphin tended to spread out in frequency with the center frequencies between 40 and 110 kHz and a peak in the histogram between 50 and 60 kHz. Although the Atlantic spotted dolphin is slightly smaller than the white-beaked dolphin, its center frequencies were also lower than the white-beaked dolphin. The killer whale echolocation signals had the lowest center frequency, with most of the energy between 40 and 50 kHz.

The width of a spectrum can be defined by the 3-dB bandwidth or the root-mean-square (rms) bandwidth about the center frequency. The 3-dB bandwidth for bimodal spectra can often provide a misrepresentation of the width of the signal since the bandwidth might cover only the frequency range about the peak frequency. The rms bandwidth is probably a better measure of the width of signals with bimodal spectra. Histograms of rms bandwidth typically indicate a broader bandwidth than the 3-dB bandwidth [3]. It is a measure

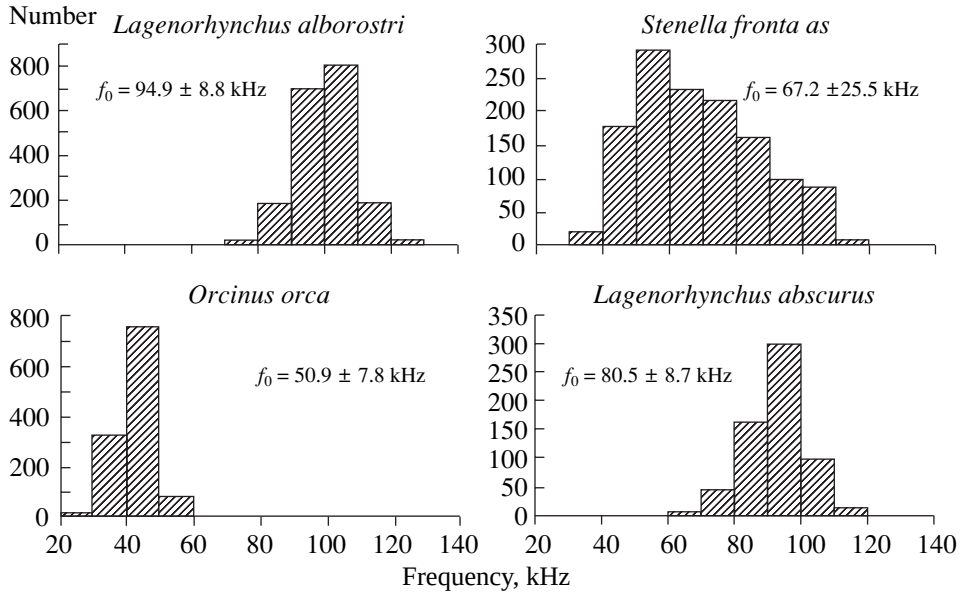

Fig. 5. Histogram of center frequency for the four species of dolphins being considered. The mean and standard deviations are also shown for each species.

of the frequency width about the center frequency and is defined mathematically as [11]

$$\beta = \frac{\int_0^\infty (f - f_0)^2 |S(f)|^2 df}{\int_0^\infty |S(f)|^2 df}, \quad (6)$$

where f_0 is the center frequency given in Eq. (6). Histograms of rms bandwidth for the echolocation signals of the four species discussed here are shown in Fig. 6 along with the appropriate means and standard deviations.

The echolocation signals emitted by the two *Lagenorhynchus* species were the widest, followed by the signals emitted by *Orcinus orca*. The histograms of both *Lagenorhynchus* species are extremely similar, showing that most of the signals had rms bandwidths between 40 and 50 kHz. The average rms bandwidths were also very similar at 42.8 kHz for the white-beaked dolphin and 43.9 kHz for the dusky dolphin. The bandwidth histogram for the Atlantic spotted dolphin showed that most the signals had a bandwidth between 25 and 50 kHz, with a mean of 36.4 kHz. The signals of the killer whale were more tightly spaced with most of the signals having a bandwidth between 20 and 25 kHz.

An appropriate way to define the relative width of a signal is to determine the *Q* of the signal. The *Q* or quality factor of a signal is defined as

$$Q = \frac{f_0}{\Delta f}, \quad (7)$$

where Δf is the bandwidth of the signal and is equal to β if the rms bandwidth is used and f_0 is the center frequency defined by Eq. (5). Using the average center frequency and rms bandwidth, the *Q* values for the different species are as follows:

$$Q = \begin{cases} 2.2 \ \textit{Lagenorhynchus albirostris} \\ 1.9 \ \textit{Stenella frontalis} \\ 1.3 \ \textit{Orcinus orca} \\ 1.8 \ \textit{Lagenorhynchus obscurus}. \end{cases} \quad (8)$$

These *Q* values are relatively low and are indicative of the broadband nature of the echolocation signals used by dolphins. The killer whale had the lowest *Q* value or the broadest bandwidth relative to the value of the center frequency.

DISCUSSION AND CONCLUSIONS

One of the most important results from the field measurements of echolocating dolphins with a short base line array is the discovery of a time-varying gain function for the dolphin echolocation system. The results indicate that, as dolphins close in on a target, the source level of the echolocation signal decreases continuously by 6 dB for every halving of the range. This reduction in source level with decreasing range to the array is a form of dynamic time-varying gain control for the dolphin's echolocation system. Instead of the receiving gain being manipulated, the output level of the system is manipulated. In conventional sonar systems, the amplitude of the emitted signal is held constant while TVG is applied to the receiver. TVG occurs

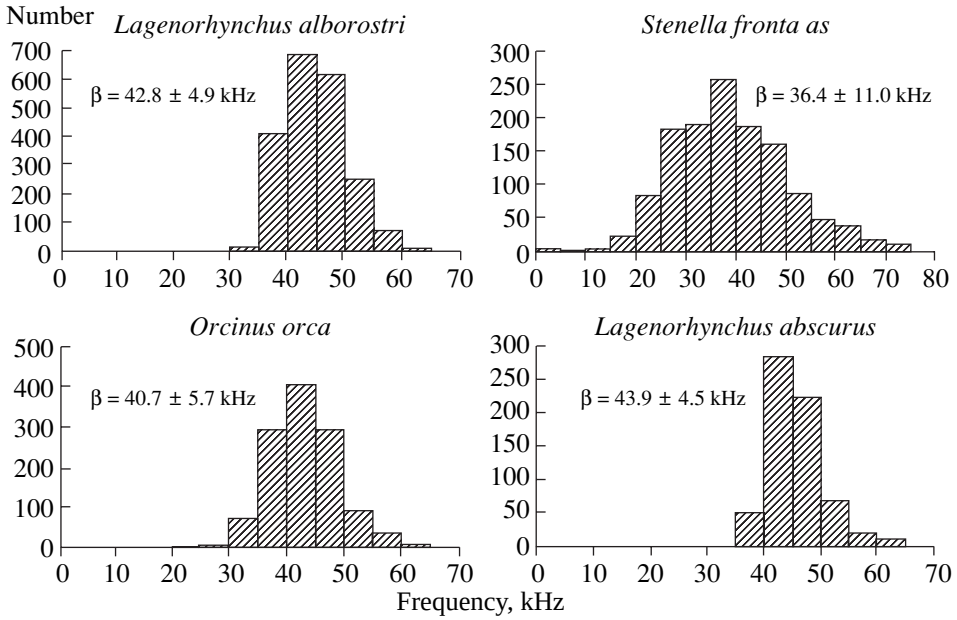

Fig. 6. Histogram of rms bandwidth for the four species of dolphins being considered. The mean and standard deviations are also shown for each species.

in bats during the reception phase because their hearing sensitivity decreases via a middle ear muscle contraction just prior to a signal being transmitted and recovers in a $40\log R$ manner [9]. The middle ear of dolphins is extremely complex and its role in hearing and how it functions is unclear [12]. The ossicular chain is stiffened and tightly bound together with sheaths and annular ligaments, and the ossicles are denser and more massive than for terrestrial mammals of similar size. These adaptations work against any effective middle ear reflex, so that another means of gain control would be needed.

In order to maintain a constant echo level for a single prey item as a dolphin closes in, the gain of the sonar system should vary as $40\log R$ rather than $20\log R$. However, many dolphin species forage on fish schools [13]. Sonar echoes from a fish school would be similar to volume reverberation, consisting of the sum of many individual echoes reflecting from individual fish. The amplitude of echoes from volume reverberation increases with decreasing range as a function of $20\log R$ [11]. Therefore, as a dolphin closes in on a fish school, the amplitude of the echoes will remain constant as the animal dynamically and progressively reduces the amplitude of the outgoing signal at a rate of $20\log R$. When a dolphin closes in on a single prey, the echo level will increase as the distance between dolphin and prey decreases, but not as rapidly as in a situation where there is no gain control.

The dynamic control of the echolocation source level is probably not the result of a cognitive process, but rather a natural consequence of how echolocation clicks are produced. Dolphins typically emit echolocation clicks at a rate that allow the echoes to return to the animal before the next click is emitted [7]. Consequently, the repetition rate increases as an animal closes on a target [14, 15]. The clicks are produced within the nasal system of the dolphins by manipulating the airflow through the phonic lips, previously referred to as the dorsal bursae/monkey lips complex [16, 17]. Dolphins initially pressurize their nasal system [18] and then emit a click train with the clicks occurring at relatively low repetition rate and the animal continually adjusting the rate as targets are located [19]. If the dolphin chooses to keep the amount of acoustic energy emitted relatively constant or within certain limits for each pressurization cycle, then the amplitude of the signal can be high when the repetition rate is low but must continually decrease as the repetition rate increases. The data in Fig. 4 are consistent with the notion that there is a coupling between repetition rate and source level.

An advantage of having a coupling between source level and target range, and subsequently click repetition rate, is that the relative size of a target can be inferred from the reception of a few echoes. The source level of the echolocation signals is coupled to the target range, so that, for a given range, the source level is predictable within some small variation, making comparison of the level of a specific echo with levels of echoes from previous experience relatively simple. The range of a target does not need to be accounted for, but is automatically factored in by the coupling of source level and repetition rate of the signals. At long ranges, scanning of the beam by the dolphin, an effective method at short ranges, will not be useful in determining the size of a

target because the amount of area a sonar beam covers can be much larger than the target. However, a dolphin can still determine the relative size of a target by the levels of the echoes.

The predominance of echolocation signals with bimodal spectra is another interesting finding from measurements of echolocation signals in the field. The only captive animal that showed a preference for emitting bimodal signals was a false killer whale in which 77% of the signals had bimodal spectra [2]. The reason for the lack of bimodal signals in captive animal experiments may be associated with the use of relatively high source levels by some of the dolphins. It seems that, as the source levels of the echolocation signals approach the maximum level for a specific dolphin, the signals tend to be unimodal with a single high-frequency peak [3, 6].

The source levels results given in Fig. 3 seem rather baffling since one would expect a larger animal to produce higher intensity signals than a smaller one. If the killer whale results are momentarily disregarded than the largest of the three dolphins indeed produced the highest source level and the smallest produced the lowest amplitude signals. The killer whale source levels were almost 9 dB lower than that of the white-beaked dolphin. However, it would be more appropriate to consider the source energy flux density since the dolphins auditory system integrates and responds to the energy in acoustic signals [7]. An appropriate means to consider this issue is to consider the role of the signal waveform in contributing to the energy flux density. Let $p(t) = As(t)$ be the waveform of an echolocation click where A is the peak amplitude and $s(t)$ is the normalized form factor describing the shape of the signal in the time domain such that the maximum value of $|s(t)|$ is equal to and less than one. The energy flux density can now be defined as

$$\begin{aligned} E &= 10\log\left(A^2\int_0^T s^2(t)dt\right) \\ &= 20\log(A) + 10\log\left(\int_0^T s^2(t)dt\right). \end{aligned} \tag{9}$$

In Eq. (9), there is a contribution to the energy flux density from both the amplitude of the signal and the normalized waveform. Considering the representative signals shown in Fig. 4, the signal of the killer whale is approximately twice as long as those of the white-beaked dolphin and the normalized waveform contribution for the killer whale is approximately 6 dB greater than for the white-beaked dolphin. Therefore, the source energy flux density of the white-beaked dolphin is only about 3 dB greater than that of the killer whale. Prey type will probably also affect the level of the echolocation signals used by any dolphins. Killer whales in Johnstone Strait prefer to forage on Chinook salmon of lengths that are between 0.6–0.8 m long [5, 20]. These fish are probably much bigger than the herring and cod that white-beaked dolphins are known to prey on and would have much larger target strength. The dorsal aspect target strength for an individual fish is given by Love [21] as

$$TS = 19.1\log(L) + 0.9\log(\lambda) - 35, \tag{10}$$

where L is the length of the fish and λ is the wavelength of the sonar signal. The difference in target strength of a Chinook salmon and the prey of the white-beaked dolphin can be expressed as

$$\Delta TS = 19.1\log\left(\frac{L_s}{L_h}\right) + 0.9\log\left(\frac{f_{oLa}}{f_{0Oo}}\right), \tag{11}$$

where L_s is the length of a Chinook salmon and L_h is the typical length of a herring prey, f_{0La} is the average center frequency of the white-beaked dolphin (94.9 kHz), and f_{0Oo} is the average center frequency of the killer whale (50.9 kHz). If we assume that the typical Chinook salmon prey is about 3–4 times larger than the white-beaked dolphin prey, then the difference in target strength for a single fish in the dorsal aspect will be between 9 and 12 dB higher for the orca. On a single fish basis, echoes in the killer whale situation could be greater by about 6 to 9 dB than those for the white-beaked dolphin. However, the white-beaked dolphin typically forage on schools of fish while the killer whales in British Columbia forage on individual salmon, so that it is highly conceivable that the echo levels for both species might be very similar.

It is difficult to generalize about the properties of echolocation signals used by dolphins in the field from the results associated with only four species of odontocetes. Research performed with wild dolphins seems to suggest that the signal waveform and spectrum are slightly different than what have been measured in controlled experiments with captive dolphins. In order to gain sufficient data to make some generalizations, more species need to be measured in the field. There are approximately 65 species of odontocetes, and this paper discussed results from just 4 species. However, future efforts to record echolocation signals with wild dolphin should be performed with an array of hydrophones, so that source levels and on-axis signals can be measured.

ACKNOWLEDGMENTS

I thank the following individuals for their assistance in collecting data in the field: Dr. D. Herzing (with *S. frontalis*), Dr. L. Miller and Ms. M. Rasmussen (with *L. albirostris*), Dr. J. Ford and Ms. K. Allman (with *O. orca*), and Dr. B. Wursig (with *L. obscurus*). This work was funded by the Office of Naval Research (Dr. R. Gisiner, program manager). This is HIMB contribution 1173.

REFERENCES

1. W. W. L. Au, D. A. Carder, R. H. Penner, and B. L. Scronce, J. Acoust. Soc. Am. **77**, 726 (1985).
2. W. W. L. Au, J. L. Pawloski, P. E. Nachtigall, *et al.*, J. Acoust. Soc. Am. **98**, 51 (1995).
3. W. W. L. Au and D. L. Herzing, J. Acoust. Soc. Am. **113**, 598 (2003).
4. M. H. Rasmussen, L. A. Miller, and W. W. L. Au, J. Acoust. Soc. Am. **111**, 1122 (2002).
5. W. W. L. Au, J. K. B. Ford, J. K. Home, and K. A. Allman, J. Acoust. Soc. Am. (in press).
6. W. W. L. Au and B Wursig, J. Acoust. Soc. Am. (in press).
7. W. W. L. Au, *The Sonar of Dolphins* (Springer, New York, 1993).
8. W. W. L. Au and K. J. Benoit-Bird, Nature **423**, 861 (2003).
9. L. A. Simmons, A. J. M. Moffat, and W. M. Masters, J. Acoust. Soc. Am. **91**, 1150 (1992).
10. R. J. Urick, *Principles of Underwater Sound*, 3rd ed. (McGraw-Hill, New York, 1983; Sudostroenie, Leningrad, 1978).
11. A. W. Rihaczek, *Principles of High-Resolution Radar* (McGraw-Hill, New York, 1969).
12. D. R. Ketten, in *Hearing by Whales and Dolphins*, Ed. by W. W. L. Au, A. N. Popper, and R. R. Fay (Springer, New York, 2000), pp. 43–108.
13. M. R. Heithaus and L. M. Dill, in *Encyclopedia of Marine Mammals*, Ed. by W. F. Perrin, B. Wursig, and J. G. M. Thewissen (Academic, San Diego, 2002), pp. 411–422.
14. W. W. Evans and B. A. Powell, in *Animal Sonar Systems: Biology and Bionics*, Ed. by R. G. Busnel (Laboratoire de Physiologic Acoustique, Jouy-en-Josas, 1967), pp. 363–382.
15. B. P. Morozov, A. E. Akopian, V. Burdin, *et al.*, Biofizika **17**, 139 (1972).
16. T. Cranford, in *Animal Sonar: Processes and Performance*, Ed. by P. E. Nachtigall and P. W. B. Moore (Plenum, New York, 1988), pp. 67–77.
17. T. Cranford, in *Hearing by Whales and Dolphins*, Ed. by W. W. L. Au, A. N. Popper, and R. R. Fay (Springer, New York, 2000), pp. 109–155.
18. S. H. Ridgway, D. A. Carder, T. Kamonick, *et al.*, J. Exp. Biol. **204**, 3829 (2001).
19. R. H. Penner, in *Animal Sonar: Processes and Performance*, Ed. by P. E. Nachtigall and P. W. B. Moore (Plenum, New York, 1988), pp. 707–713.
20. J. K. B. Ford, E. M. Graeme, L. G. Barrett-Lennard, *et al.*, Can. J. Zool. **76**, 1456 (1998).
21. R. H. Love, J. Acoust. Soc. Am. **49**, 816 (1971).

Acoustical Physics, Vol. 50, No. 4, 2004, pp. 463–468. From Akusticheskiĭ Zhurnal, Vol. 50, No. 4, 2004, pp. 543–549.

BIOLOGICAL ACOUSTICS

Modeling of the Dolphin's Clicking Sound Source: The Influence of the Critical Parameters[1]

N. A. Dubrovsky*, A. Gladilin*, B. Møhl, and M. Wahlberg****

** Andreev Acoustics Institute, Russian Academy of Sciences, ul. Shvernika 4, Moscow, 117036 Russia*
e-mail: dubrov@akin.ru
*** Institute of Biological Science, University of Aarhus, Denmark*

Received December 2, 2003

Abstract—A physical and a mathematical models of the dolphin's source of echolocation clicks have been recently proposed. The physical model includes a bottle of pressurized air connected to the atmosphere with an underwater rubber tube. A compressing rubber ring is placed on the underwater portion of the tube. The ring blocks the air jet passing through the tube from the bottle. This ring can be brought into self-oscillation by the air jet. In the simplest case, the ring displacement follows a repeated triangular waveform. Because the acoustic pressure gradient is proportional to the second time derivative of the displacement, clicks arise at the bends of the displacement waveform. The mathematical model describes the dipole oscillations of a sphere "frozen" in the ring and calculates the waveform and the sound pressure of the generated clicks. The critical parameters of the mathematical model are the radius of the sphere and the peak value and duration of the triangular displacement curve. This model allows one to solve both the forward (deriving the properties of acoustic clicks from the known source parameters) and the inverse (calculating the source parameters from the acoustic data) problems. Data from click records of Odontocetes were used to derive both the displacement waveforms and the size of the "frozen sphere" or a structure functionally similar to it. The mathematical model predicts a maximum source level of up to 235 dB re 1 μPa at 1-m range when using a 5-cm radius of the "frozen" sphere and a 4-mm maximal displacement. The predicted sound pressure level is similar to that of the clicks produced by Odontocetest. © *2004 MAIK "Nauka/Interperiodica".*

1. INTRODUCTION

In our previous publications, we have suggested that the clicking source of dolphins is driven by the air pressure created in the upper respiratory tract either by lungs or by air sac muscles [1–3]. The essential feature of this suggestion is the formation of an air jet through the nasal passage that is blocked by a sphincter (a muscle plug, a lip). A physical model of the nasal passage was implemented (Fig. 1). The model consists of (*1*) a displacement sensor attached to (*2*) a rubber ring, which is put on (*3*) a rubber tube opened at one end and attached to a high-pressure gas bottle at the other end [1–3]. The rubber ring blocks the air passage through the tube. When the air pressure in the tube increases, the rubber ring begins to perform typical self-oscillations during which the tube is periodically opened for short periods of time (Fig. 1). The displacement sensor (see Fig. 1) measures the movements of the ring whose surface shows different displacement waveforms. In the simplest case, the displacement waveform is triangular. The oscillating ring is the source of acoustic clicks, which are time-locked to the bends of the displacement curve. This observation is in accord with the acoustic Euler equation stating that the pressure gradient is proportional to the second time derivative of the displacement [4].

A simple mathematical model (MM) based on this physical model has been developed [1–3]. The model is based on the assumption that the ring does not move except for a small spherical portion that performs the above-mentioned self-oscillations. It is also assumed

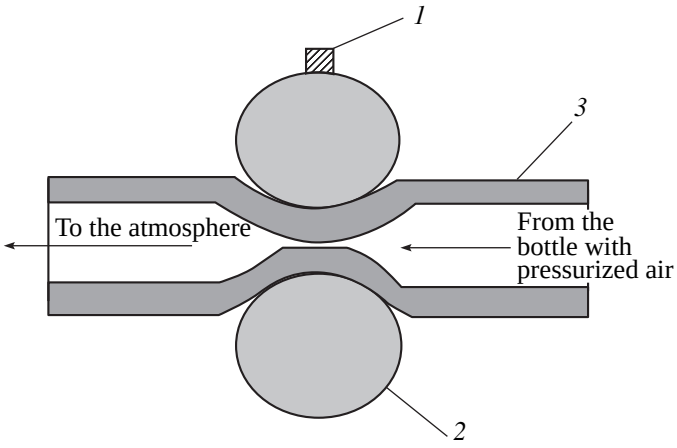

Fig. 1. Schematic view of the underwater part of the physical model: (*1*) a displacement sensor, (*2*) a rubber ring, and (*3*) a rubber tube. The excess air pressure is delivered to the right end of the tube. The left end is connected to the atmosphere. In the state of the model shown in the figure, the expanding forces inside the tube prevail over the compressing forces of the ring.

[1] This article was submitted by the authors in English.

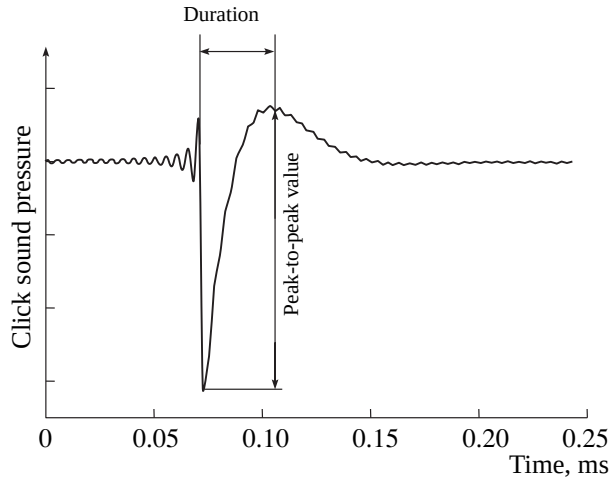

Fig. 2. Calculated click waveform and the definition of the peak-to-peak value and duration of the click in the mathematical model. The duration of the triangular displacement is 1 ms and the maximum of sphere displacement is 2 mm.

that the sphere has no mass. Under these assumptions, the sphere (thereafter called the "frozen sphere") moves in accord with the observed displacement waveform of the ring. The acoustic pressure caused by the sphere displacement (which represents an acoustic dipole) at an angular frequency $\omega = 2\pi f$ can be expressed by the formula [4]

$$p(r, t) = i\rho\omega^2 a^3 \xi(\omega) \times \frac{(ikr-1)\cos\alpha \exp(-ika)\exp(ikr - i\omega t)}{(2 - 2ika - (ka)^2)r^2}. \quad (1)$$

Here, a is the radius of the "frozen sphere," r is the distance from the center of the sphere to the observation point, $k = \omega/c$ is the wave number, c and ρ are the speed of sound and the density of tissue around the source, α is the angle between the dipole axis and the direction to the observation point, and $\xi(\omega)$ is the Fourier transform of the sphere displacement waveform. At this stage of analysis, we assume that the density and the speed of sound propagation in the biological tissue around the delphinid sound source are equal to the corresponding parameters of water, which is at least approximately true [5]. In addition, we disregard the possible distortion of the acoustic click due to the diffraction by the complex structures of the air sacs and passages and the melon [10]. Some comments on these assumptions is given below.

The pressure waveform of the radiated acoustic click is computed by means of the inverse Fourier transform of the click amplitude spectrum density taken from Eq. (1). The computed acoustic clicks are indeed time-locked to the bends of the displacement curve, which agrees well with the physical model [3].

In this paper we further explore the influence of the critical parameters of the mathematical model on the peak-to-peak value of sound pressure, the duration of the simulated clicks, and the maximum (peak) of their amplitude spectral density (SDP). The critical parameters of the MM are the radius of the "frozen sphere" and the duration and maximum (height) of the displacement triangle (MSD). The results of simulation are compared with experimental data for different species of Odontocetes. Here, we consider only the forward problem (deriving the properties of acoustic clicks from the known source parameters). The inverse problem (calculating the source parameters from acoustic data) will be the subject of another paper.

2. RESULTS OF THE SIMULATION STUDY

Let us first examine the waveform of the acoustic click. Figure 2 depicts the calculated click waveform and the definition of the peak-to-peak value and duration of the click for the case when the displacement waveform of the frozen sphere is a triangle. The click has a short positive peak (phase of compression) and a large short negative peak (phase of rarefaction) followed by a prolonged positive peak (the second phase of compression). This click resembles the simplest click waveform (the "typical", "standard" or "direct" click) observed in different species of Odontocetes [6–10] mostly in tanks. However, recently, an observation of the "standard" waveform from killer whales (*Orcinus orca*) in open water has been reported [11].

The "standard" dolphin's click also comprises two compression half-waves separated by a rarefaction half-wave with a higher peak value. Clicks recorded in water contain several oscillations at a frequency roughly corresponding to the frequency of the spectral density peak. The missing first compression half-wave in our mathematical model is due to the ideal triangular displacement waveform.

From Fig. 3, the sound pressure level at 1-m range and re 1 μPa (the source level) of the acoustic click can be assessed for different radii of the "frozen sphere" and different maxima of sphere displacement (MSD). For example, the source level (SL) can be as small as 150 dB at a radius of $a = 0.5$ cm and MSD = 0.1 mm. When the radius of the "frozen sphere" is as big as $a = 5.0$ cm and the MSD runs up to 2 mm, the SL can reach almost 230 dB.

We note that Eq. (1) is valid provided that the displacement maximum h is much less than the radius of the "frozen sphere" a ($h \ll a$) and the wavelength λ ($h \ll \lambda$) [4]. In our case, the maximal value of the MSD is $h = 2$ mm and the minimal value of the radius a is 3 mm. Hence, the maximal value of h at $a = 3$ mm should not exceed 1 mm. In the assessment of the second condition, the wavelength should be the minimal one, which corresponds to the high-frequency boundary of the click spectrum. It implies that, when $h \ll 2$

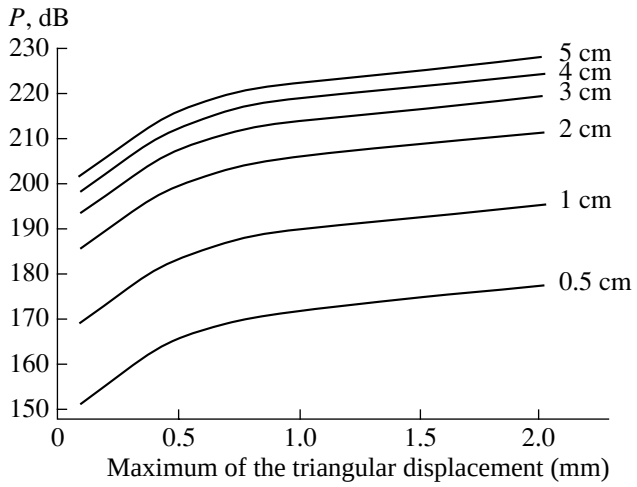

Fig. 3. Source level (SL) of the calculated clicks as a function of the maximum displacement (MSD) and the radius of the frozen sphere (shown as a parameter of the set of curves). The duration of the triangular displacement of the sphere is 1000 μs.

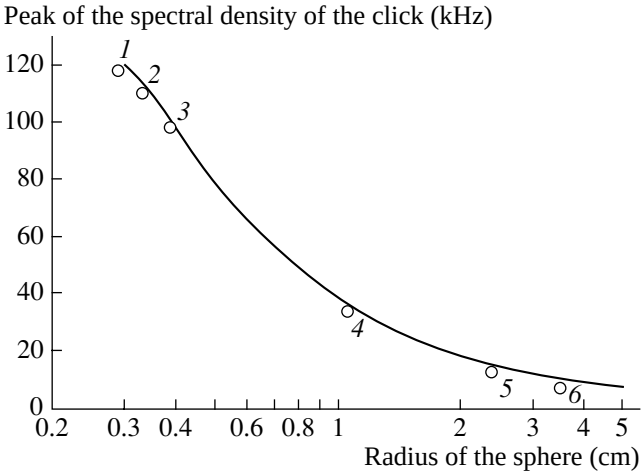

Fig. 4. Peak of the spectral density (SDP) for the calculated click versus the frozen sphere radius. The sphere displacement waveform is a triangle at a fixed MSD = 2.0 mm and duration of 1000 μs. The circles indicate the spectral peak measurements of the Odontocetes clicks fitted to the model: (*1*) Harbor porpoise [12], (*2*) Atlantic bottlenose dolphin [10], (*3*) Beluga whale [15, 16], (*4*) Narwhal [17], (*5*) Killer whale [11], and (*6*) Sperm whale [18].

mm, the condition $h \ll \lambda$ will be fulfilled in the entire frequency range.

The influence of the sphere radius on the click sound pressure level or source level is much more pronounced than the influence of the MSD, which is easily seen from Eq. (1). A tenfold MSD change (from 0.2 mm to 2.0 mm) results in an approximately 25-dB increase in the SL, while a tenfold increase in the sphere radius causes an approximately 50-dB growth of the SL.

Figure 4 depicts how the peak spectral density of the click (SDP) depends on the frozen sphere radius. The SDP shifts to the low frequency range when the sphere radius increases. The most pronounced change in the SDP is observed for 0.3 cm < a < 1.5 cm. The SDP is decreased from 120 kHz down to 30 kHz within this range of radii. The graph in Fig. 4 allows an assessment of the radius of the "frozen sphere" (or sizes of equivalent biological structures presumably responsible for the click radiation) on the basis of the observed SDP for different Odontocetes species. The results of such an assessment are shown in Fig. 4 by the numbered circles, and these results are also presented in the table.

We selected the data for eight species to span the whole range in size and weight of the toothed whales: from one of the smallest toothed whale with the highest SDP (Harbor porpoise [12]) to the biggest one with the lowest SDP (Sperm whale [18]). Our MM predicts that the radius of the frozen sphere (or its biological correlate) varies from 0.25 to 3.5 cm, i.e., by about a factor of 13.

We assume that the assessment of the SDP based on averaging the spectral density is trustworthy, because a superposition of many standard clicks with different delays and peak values results in a rippled SDP but not in a shift of the bandwidth and the SDP itself.

The duration of the simulated click (Fig. 5) varies almost proportionally to the "frozen sphere" radius: from 5 μs at a = 0.3 cm to 53 μs at a = 5.0 cm. The estimates of the standard click duration for six species of Odontocetes (measured from recorded signals) and different sphere radii (from the table) are indicated by circles in Fig. 5. The experimental data for comparison were chosen among the clicks radiated in the frontal direction (zero azimuth and elevation angles).

3. DISCUSSION

Let us first compare the waveform of a simulated click and the actual acoustic clicks of Odontocetes.

The "standard" or "direct" click of dolphins consists of two half-waves of compression separated by a half-wave of rarefaction whose peak value is higher than that of compression half-waves. The first positive half-wave of the modeling click is very small due to the use of the ideal triangular displacement of the "frozen" sphere. Besides, the actual clicks of Odontocetes (contrary to the modeling click) have no such abrupt front with which the rarefaction phase of the modeling click begins. An abrupt front in the actual dolphin clicks would imply a large acceleration of the biological correlate of the "frozen" sphere that would require high air pressure in the nasal passages. Actually, this pressure is rather small, and a smoothing of the click waveform should occur if the sphere under consideration has a mass not equal to zero.

Assessment of the radii of the frozen sphere from the peaks of the spectral density of clicks (SDP) for different toothed whales

Species	Limits of the SDP (kHz)	Radius of the equivalent sphere (cm)	Ref.
Harbor porpoise	120–140	0.25 (extrapolation)	[12]
Atlantic bottlenose dolphin	110–130	0.30	[13]
Risso's dolphin	47.9	0.77	[14]
Beluga whale	100–115	0.35	[15, 16]
Narwhal	40	1.00	[17]
Killer whale	20–30, 40–60	1.3, 0.75	[7]
Killer whale in a tank	14–20	2.35	[11]
Male Sperm whale	10–12	3.50	[18]

Most of the clicks recorded in water deviate from the standard waveform, because they are formed "by a large number of internally reflected pulses that arrive very close together soon after the arrival of the direct pulse, since the melon region is close to the air sacs and the areas of the scull that could reflect acoustic energy into the melon region" [10]. Acoustic clicks recorded in directions that deviate from the longitudinal axis of the dolphin body also contain some oscillations with frequencies roughly corresponding to the peak of click's spectral density [10].

The analysis of Fig. 3 shows that the range of the peak values of clicks in our model varies from 150 dB to 230 dB as the radius of the "frozen" sphere increases from 0.5 cm to 5.0 cm and the maximum of the triangular displacement of the sphere varies from 0.2 mm to 2 mm. At the comparison of these simulation data with actual ones, it is necessary to take into account that the concept of the source level of dolphins [10] includes both the source of clicks and the biological structures (skull bones, melon, air bags, etc.) participating in the formation of the time and spatial structure (directivity) of the click in water. Au [10] has summarized the data on the source level for clicks recorded in tanks and in open water for various species of sea and freshwater dolphins. According to these data, the source level varies from 151 dB for the Hector dolphin to 228 dB for the false killer whale and the Atlantic and Pacific bottlenosed dolphins. This is in a very close agreement with the simulated data shown in Fig. 3 for the sound sources of sizes typical of Odontocetes.

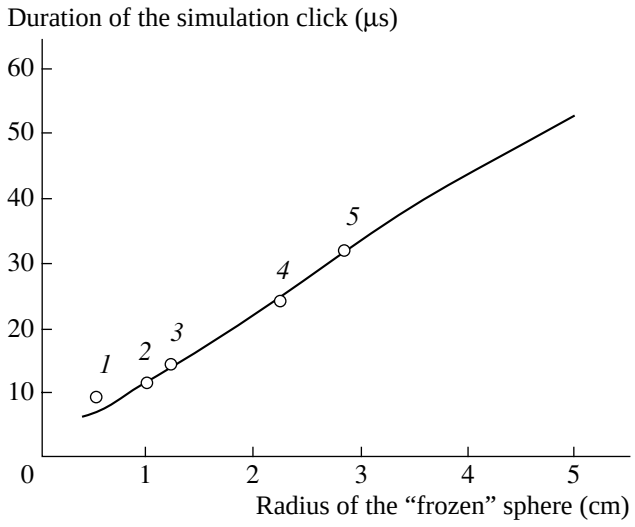

Fig. 5. Duration of the simulated click in microseconds as a function of the radius of the frozen sphere in centimeters. The duration of the triangular displacement is 1000 μs, and the maximum displacement of the frozen sphere is 2 mm. The circles indicate the durations of the dolphin's standard clicks: (*1*) Atlantic bottlenose dolphin [10, 13], (*2*, *3*) Risso's dolphin [14], and (*4*, *5*) Killer whale [11].

The maximal value of the SL among Odontocetes (235 dB) is also observed for the Sperm whale [18]. The values of the radius of the sphere and the maximum of the sphere displacement (MSD) corresponding to this SL are not depicted in Fig. 3. However, by the assessment based on the peak of the spectral density (10–12 kHz), the radius of the equivalent sphere for the Sperm whale is close to 3.5 cm (Fig. 4). To fit this radius estimate with the estimate of the sphere radius based on the SL, it is necessary that the maximum of the triangular sphere displacement be approximately equal to 4 mm.

It is important to take into account that the SL of Odontocetes may considerably vary depending on the echolocation conditions. Babkin and Dubrovsky [19] reported on a gradual increase in the SL by 27 dB at the detection of a target by the Black Sea Tursiops on the background of random noise with an evenly growing level. It also has been shown that, when the target range increased up to 600 m, the level of the click radiation increased on the average by 52 dB: from 170 up to 222 dB [20]. Au and Pawloski [21] have found a change in the source levels by up to 12 dB for a Tursiops truncatus discriminating targets against the background of a masking noise.

As it was already mentioned, the source level in our model grows by no more than 25 dB when the maximum of the triangular displacement of the sphere

increases from 0.2 to 2 mm. Meanwhile, the Black Sea bottlenose dolphin increased the SL of clicks up to 52 dB with an increase in the target range to 600 m [20]. To explain this increase within the framework of the proposed model, it is necessary to admit an opportunity for the Odontocetes to change somehow the radius of the equivalent sphere, i.e., the size of the muscular plug or "lip" performing the dipole oscillation at radiation of a click. According to Fig. 3, such a change allows a variation of the SL by 50 dB. It is possible that the Odontocetes use both possibilities, namely, change both the maximum of the displacement and the size of the equivalent sphere.

Au *et al.* [11] reported on the radiation of acoustic clicks by the Killer whale with a click spectrum containing two pronounced peaks: a low-frequency one with a maximum between 20 and 30 kHz and a high-frequency one with a maximum located between 40 and 60 kHz. The simultaneous emission of low- and high-frequency clicks may testify in favor of the assumption that Odontocetes, either simultaneously or with a delay about the duration of a click, "use" two different equivalent spheres: a larger one for the radiation of low-frequency clicks and a smaller one for the radiation of high-frequency clicks. A possible mechanism for this could be to switch the sound production between the two nasal plugs, which in most delphinids have very different sizes [22]. This assumption, however, needs an additional analysis.

4. CONCLUSIONS

The development of a simulation model of the acoustic click radiation by Odontocetes is presented in this paper. The simulation model is based on the mathematical model of the source of acoustic clicks that was developed and described earlier [1–3]. A software in MathCAD was created to study influence of the critical parameters of the mathematical model (the radius of the "frozen" sphere and the maximum of its triangular displacement) on the sound pressure reduced to 1 m (the source level) and the position of the spectral density peak of the click and its duration.

A comparison of the model predictions with experimental data for various species of Odontocetes is carried out.

It is shown that the waveform of the simulated click generally meets the waveform of the "direct" or "standard" click of the Odontocetes. It consists of the first peak of compression, the peak of rarefaction, and the second peak of compression. Such clicks are observed in directions close to the longitudinal axis of the animal body (at zero azimuth and elevation angles). For a closer agreement of the simulation model with its biological prototype, it is necessary to take into account the mass of the oscillating ("frozen") sphere and to compare the pressure of the air necessary for creating the required displacement of the sphere with the measured values of air pressure in the nasal passages of Odontocetes.

Although the range of the radii of the "frozen" spheres (0.25–5.00 cm) and the maxima (MSD) of the sphere displacement (0.2–2.0 mm) were chosen arbitrarily, i.e., proceeding from the feasible sizes of the biological structures responsible for the generation of the clicks, the range of source levels predicted by our model (150–230 dB) satisfactorily agrees with those observed for various species of Odontocetes.

The maximal changes in the SL (up to 52 dB) observed with an increase in the range of a target to 600 m [20] cannot be explained by a change in sphere displacement alone. It is necessary to assume that, in addition, the animals are able somehow to change the size of the biological equivalent of the "frozen" sphere.

The model of the click generation predicts the size of the sound generating structures throughout a broad size range of Odontocete species. These predictions should be compared with anatomical data of the structures inferred to be involved in the click generation.

ACKNOWLEDGMENTS

This work was supported by the Danish Research Council through the Center for Sound Communication.

REFERENCES

1. L. R. Giro and N. A. Dubrovskiy, in *Proceedings of XXIII International Physiological Congress* (St. Petersburg, 1997).
2. L. R. Giro and N. A. Dubrovskiy, J. Acoust. Soc. Am. **105**, 1263 (1999).
3. L. R. Giro and N. A. Dubrovskiy, in *Echolocations in Bats and Dolphins*, Ed. by J. Thomas, C. Moss, and M. Vater (Chicago Univ. Press, Chicago, 2003), Chap. 10, pp. 59–65.
4. M. A. Isakovich, *General Acoustics* (Nauka, Moscow, 1973), p. 495.
5. K. S. Norris and G. W. Harvey, J. Acoust. Soc. Am. **56**, 659 (1974).
6. K. T. Diercks, R. T. Trochta, C. F. Greenlaw, and W. E. Evans, J. Acoust. Soc. Am. **49**, 1729 (1971).
7. W. E. Evans, J. Acoust. Soc. Am. **54**, 191 (1973).
8. N. A. Dubrovskiĭ and G. L. Zaslavskiĭ, in *Proceedings of VIII All-Union Acoustic Conference* (1973), Section Ts, p. 56.
9. V. M. Bel'kovich and N. A. Dubrovskiĭ, *Sensory Basis of Cetacean Orientation* (Nauka, Leningrad, 1976; Joint Publ. Research Service L/7157, Arlington, VA, 1977).
10. W. W. L. Au, *The Sonar of Dolphins* (Springer, New York, 1993).
11. W. W. L. Au, J. K. B. Ford, J. K. Horne, and K. A. Newman Allman, J. Acoust. Soc. Am. **115**, 901 (2004).
12. B. Möhl and S. Andersen, J. Acoust. Soc. Am. **54**, 1368 (1973).

13. W. W. L. Au, in *Animal Sonar Systems*, Ed. by R. G. Busnel and J. F. Fish (Plenum, New York, 1980), pp. 251–282.
14. J. D. Philips, P. E. Nachtigall, W. W. L. Au, *et al.*, J. Acoust. Soc. Am. **113**, 605 (2003).
15. W. W. L. Au, D. A. Carder, R. H. Penner, and B. L. Scronce, J. Acoust. Soc. Am. **77**, 726 (1985).
16. W. W. L. Au, R. H. Penner, and C. W. Turl, J. Acoust. Soc. Am. **82**, 79 (1985).
17. B. Möhl, A. Surlykke, and L. A. Miller, in *Sensory Abilities of Cetaceans*, Ed. by J. A. Thomas and R. A. Kastelein (Plenum, New York, 1990), pp. 295–303.
18. B. Möhl, M. Wahlberg, P. T. Madsen, *et al.*, J. Acoust. Soc. Am. **114**, 1143 (2003).
19. V. P. Babkin and N. A. Dubrovskiĭ, Tr. Akust. Inst. Akad. Nauk SSSR, No. 17, 29 (1971).
20. M. P. Ivanov, Candidate's Dissertation (St. Petersburg State Univ., St. Petersburg, 1999).
21. W. W. L. Au and D. A. Pawloski, J. Acoust. Soc. Am. **70**, 662 (1988).
22. T. W. Cranford, M. Amundin, and K. S. Norris, J. Morphol. **228**, 223 (1996).

Acoustical Physics, Vol. 50, No. 4, 2004, pp. 469–479. Translated from Akusticheskiĭ Zhurnal, Vol. 50, No. 4, 2004, pp. 550–561.

BIOLOGICAL ACOUSTICS

Dolphin's Echolocation Signals in a Complicated Acoustic Environment

M. P. Ivanov

Ukhtomsky Physiological Institute, St. Petersburg State University, Universitetskaya nab. 7/9, St. Petersburg, 191034 Russia

e-mail: ivanov@MI3453.spb.edu

Received January 20, 2004

Abstract—Echolocation abilities of a dolphin (*Tursiops truncatus ponticus*) were investigated in laboratory conditions. The experiment was carried out in an open cage using an acoustic control over the behavior of the animal detecting underwater objects in a complicated acoustic environment. Targets of different strength were used as test objects. The dolphin was found to be able to detect objects at distances exceeding 650 m. For the target location, the dolphin used both single-pulse and multipulse echolocation modes. Time characteristics of echolocation pulses and time sequences of pulses as functions of the distance to the target were obtained. *© 2004 MAIK "Nauka/Interperiodica".*

In the literature, ample data can be found on the echolocation ability of dolphins to detect and identify underwater objects under laboratory experimental conditions. Experiments were carried out in both closed pools and open water. It was shown that dolphins easily detect and identify underwater objects in a pool even in a complicated acoustic environment (reverberation and signals of other animals). In open cages, the echolocation signals of dolphins were investigated under different acoustic conditions (with receding objects against a background of natural man-made acoustic noise). A review of the results obtained in laboratory experiments in an open cage can be found in [1]. The comparison of the acoustic activity of animals in laboratory experimental conditions with that of animals in the sea shows that the repertory of acoustic activity in natural conditions is much richer than in laboratory experiments [2]. Presumably, the laboratory conditions and the poor selection of methods used in experiments reduce the acoustic repertory required for a dolphin to solve the simple problems proposed by the researchers.

The goal of this investigation is to study the behavior of a dolphin (*Tursiops truncatus ponticus*) in a complicated acoustic environment. The problems to be solved include the development of the experimental procedure for studying the detection of underwater objects at maximal distances from the experimental cage and the investigation of the echolocation radiation used by a dolphin for detecting objects against the natural acoustic background.

Papers concerned with echolocation describe the motor reactions and signals produced by a dolphin during the experiments. The first investigations of the behavior of dolphins in a complicated acoustic environment were performed with *Phocaena phocaena* [3]. In the experiments, the eyesight of the animals was functionally excluded using rubber suckers. It was shown that the smaller the diameter of wires, the greater the number of collisions of the animal with them. The percentage of correct passages through the barrier was practically 100% if barriers were made of wires with diameters from 4 down to 2.8 mm and 90% if barriers were made of wires with diameters from 2.8 down to 0.5 mm. In the case of a wire 0.2 mm in diameter, the percentage of correct passages was only 46%. An echolocation situation typical of detecting bottom foodstuffs was artificially created in [4] by strewing stones of characteristic size varying from 5 to 30 mm over the pool bottom. The dolphin detected the targets positioned at 30 cm from the bottom quite easily and from a long distance. When detecting the targets against the background of stones causing an intense reverberation, the dolphin started from diving to a depth and then moved toward the targets very slowly near the bottom. To reduce the bottom reverberation, the dolphin insonified the target at a small angle relative to the bottom rather than in the downward direction.

In the separating-net experiments on distinguishing between simple geometrical shapes [5], the animal, when solving more difficult problems, often lay on one side upon reaching the net end (i.e., at the point where it had to make the decision) and insonified the objects in this position. The author of paper [5] explains this behavior by the directional pattern of the dolphin's echolocation system. The width of the directional pattern in the vertical plane is smaller by a factor of two than the width in the horizontal plane, and, hence, the dolphin used the favorable conditions to solve the problem.

It was pointed out that, approaching an object, the dolphin not only changed the position of it's whole

1063-7710/04/5004-0469$26.00 © 2004 MAIK "Nauka/Interperiodica"

body with respect to the target but also actively turned it's head. From experiments [6], it was found that, approaching an object, the dolphin activated the motion of the rostrum so that the rostrum end circumscribed an ellipsoidal trajectory in the vertical plane. In view of the fact that the shape and spectrum of the echolocation pulse appreciably depend on the angle with respect to the longitudinal axis of the rostrum, the dolphin can insonify the objects of interest with different pulses by varying this angle; the greater this angle, the lower the frequency corresponding to the peak of the pulse spectrum is. In the case of echolocating an unfamiliar object, the number of scanning motions can reach 57 [6]. After 10–15 echolocation series, the number of such motions decreased to 2–3.

Experiments in which dolphins distinguished spherical targets [7] showed a statistically reliable increase in the repetition rate of echolocation pulses with increasing complexity of the problem. In addition, the repetition rate of echolocation pulses was related to the complexity of the echolocation problem. For relatively simple problems, no statistically significant increase of the repetition rate occurred.

In distinguishing pairs of objects, the peak of the spectrum of location clicks was shifted [8, 9]. In these experiments, dolphins correctly distinguished metallic spheres and cylinders at distances not exceeding 24 m. The study of the trajectory of the animal approaching a target revealed no changes in motor reactions depending on the target type [10].

A large series of laboratory experiments on the simultaneous target detection by two animals was carried out in open waters [11, 12]. The maximum range of detection was 80 m. The mean level of sound pressure was 220.2 dB (relative to 1 μPa, reduced to 1 m) for the first dolphin, and 222 dB for the second one. Typical signals had a duration of 40 μs and were characterized by energy spectra with peaks between 120 and 130 kHz. The pulse-to-pulse temporal interval exceeded the time of signal propagation from the animal to target and back to the animal by a value varying from 30 to 50 ms.

When a dolphin detects underwater objects at distances below 120 m, the pulse-to-pulse temporal interval exceeds the time required for the sounding pulse to travel to the target and return back, and the duration of this interval depends on whether or not the object of detection is available [13–15]. The maximal pulse-to-pulse interval measures 150 ms, and the spectral peaks of all radiated pulses appear to be relatively stable and fall within 120–130 kHz.

In open waters, the animal correctly detected a (steel) sphere 10 cm in diameter at a distance of 120 m and the target with a strength of 1.6 dB (a corner reflector) at a distance as long as 600 m [16].

When the acoustic environment becomes more complicated, the dolphin switches the sonar mode from the single-pulse mode to the multipulse mode (the radiation of pulse bursts) [17]. In a burst, the pulse-to-pulse interval is shorter than the double time of signal propagation to the target. On the contrary, the burst-to-burst interval is longer than the double time of signal propagation to the target.

The most variable acoustic repertory is characteristic of the *Delphinapterus leucas*; however, a comparison analysis [18] showed that, in identical experimental conditions, the echolocation signals of the *Tursiops truncatus* appear to be more stable.

The experience shows that the measurements of dolphin's signals must take into consideration the following factors: the spatial volume of the signal, the hydrophone position with respect to reflecting surfaces, the azimuth-dependent variation of the signal envelope and spectrum, and the body of experimental acoustic data.

Laboratory experiments on echolocation must ensure that the measured parameters of echolocation pulses showed either experiment-to-experiment reproducibility or reproducibility in similar experiments. A laboratory experiment refines the results of acoustic observations of animals in natural conditions and yields unambiguous interpretation of the measured results. However, depending on the experimental method, the data can become more variable, and a statistical processing of large bodies of bioacoustic data not only appears to be complicated but also smoothes out measured data. Considerable contributions to the measurement error are made by the narrow directivity pattern of radiation and the azimuth-dependent pulse structure characterized by an asymmetric shift of the spectral peak in both the vertical and horizontal planes. It is clear that the narrower the target and the point of pulse measurement to the dolphin, the greater the accumulated error. If the animal changes the spectral-time structure of echolocation pulses on purpose, the statistical processing yields an ambiguous interpretation of data on the acoustic behavior of a dolphin in the course of the detection and identification of targets. This is especially true for the experiments in closed pools; these experiments showed that dolphins are capable of advisedly changing the spectral-time structure of echolocation pulses. In the experiments [10–15] on detecting underwater objects in open waters, the animal was fixed in space. In these experiments, the animal could not change the depth when the object of detection changed its depth and the distance to the animal. The search duration and the decision time were also rigidly preset by the experimenter (the beginning and end of echolocation were also preset). No changes in the spectral-time structure of pulses radiated by the dolphin were observed in these experiments.

EXPERIMENTAL TECHNIQUE

Based on the analysis of earlier experiments, an experimental technique was developed that provided the separation of echolocation series into the signals

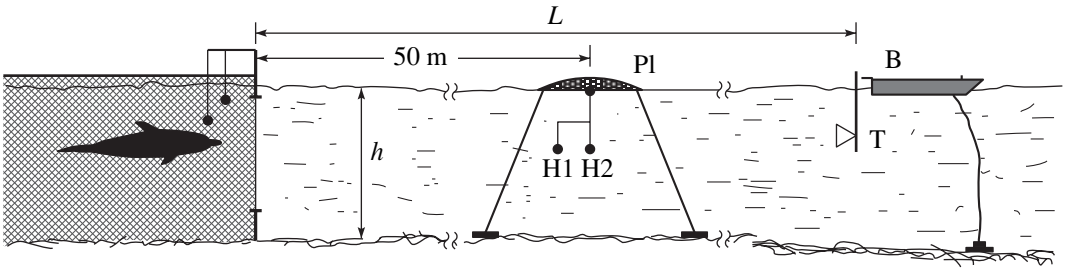

Fig. 1. Experimental geometry: (H1, H2) hydrophones, (Pl) platform, (T) target, and (B) boat; *h* is the depth of the bay and *L* is the distance to the target.

produced by the animal in the presence and the absence of the object of detection. The dolphin was allowed to select the duration of insonifying the coverage sector, the decision time, and the orientation of the body relative to the object of detection, which significantly decreased the volume of acoustic data for further processing. The experimental procedure corresponds to the technique of alternate selection under successive stimulus presentation with an acoustic control over the animal's behavior during the experiment. The technique developed includes the measurement of the parameters, such as the animal orientation in the cage relative to the coverage sector, the alternate selection (yes/no) under successive stimulus presentation, and the motor reaction of the animal to both target presence and target absence. The corroboration of the animal's reaction to all conditional sensory stimuli, including the zero stimulus (corresponding to the target detection problem), is described in the literature as the method of the forced yes/no choice [19] used in psychoacoustic experiments.

Figure 1 schematically shows the geometry of the experiment. The experimental compartment was supplied with a special window looking toward the bay. Unlike the cage nets, the window of size 2×3 m was shielded with a net with a 25×25-cm mesh. The compartment was equipped with the starting manipulator-annunciator at a distance of 1 m from the window and two reaction-token manipulators at distances of 1.5 m to the right and to the left of the starting manipulator. In the direction perpendicular to the window looking out to the bay, along the line of the animal's starting position, a rope was tightened, along which a boat moved with an operator on board. To a distance of 250 m, the boat could be moved to any position along the rope. For experimenting at distances from 300 to 700 m, buoys were placed at every 50 m. In the experiment with distances below 250 m, the depth of the bay measured h = 4 m, and in the experiment with distances up to 700 m, the depth in the cage measured h = 6 m and then gradually increased to 15 m.

The receiving hydrophone was positioned on the line of the animal's starting position, in the middle of the water layer at a distance of 50 m from the cage. Both preamplifier and hydrophone were mounted on an anchored floating platform. For the hydrophone we used a 5-mm-diameter transducer whose average sensitivity was 7 μV/Pa. The preamplifier with a gain equal to 5 was used as the matching device between the acoustic transducer and a 60-m-long cable. Via this cable, the signal from the preamplifier was fed to the amplifier and the recording system.

The above depths and the distance to the receiving point were chosen reasoning from the fact that the structure of the sounding pulse varies only slightly within ±2° at the level of 0.7 of the directional pattern of the dolphin's acoustic field. For the dolphin positions at depths of 0.5, 1, 1.5, 2, 3, and 3.5 m, the respective delays of specular returns were 26.6, 53, 80, 106.5, 159, and 186 μs. The maximal grazing angle of specular returns was 7° and occurred for the dolphin position at a depth of 3.5 m.

In the experiments on target detection at distances up to 700 m, the receiving hydrophone was placed in the middle of the layer at a depth of 3 m. For the dolphin at depths below 5.5 m, the maximal delay of the specular return was 437 μs.

The wind-induced deviation of the receiving point from the axis (for the animal oriented toward the boat) was no greater than ±2 m. In the horizontal plane, the displacement of the receiving point relative to the directional pattern was no greater than ±2.5°. The wind force was in fact unidirectional, so that the platform with hydrophones and the boat were displaced in the same direction. The actual displacement of the hydrophone in the horizontal plane was even smaller, because the tape recording was performed only during periods of calm.

Figure 2 shows the block diagram of the receive-record system. We recorded the signals of the dolphin by an MP-3 tape-recorder and photographed the signal patterns obtained on the screen of an S1-33 oscilloscope by an RFK-5 camera. In the case of the oscilloscope measurements, hydrophone H1, which was closer to the animal, turned on the scanning procedure of the oscilloscope, and hydrophone H2 was used for actual imaging of the signal on the oscilloscope screen and on the tape recorder. The flatness of the amplitude-frequency characteristic of the receiving channel was better than 3 dB in the frequency band of 0.5–200 kHz.

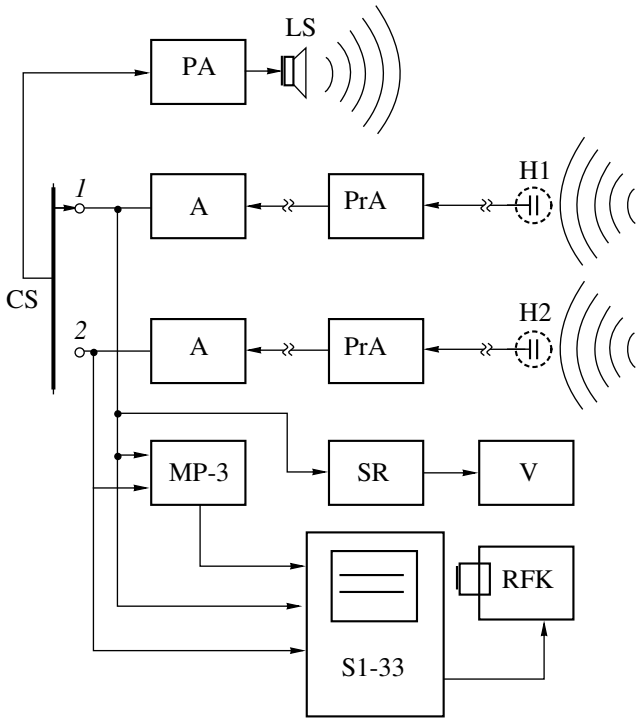

Fig. 2. Block diagram of the receive-record system: H1 is the synchronizing hydrophone, H2 is the measuring hydrophone, PrA is the preamplifier, A is the amplifier, CS is the channel switch, MP-3 is the tape recorder, V is the voltmeter, SR is the selective receiver, S1-33 is the oscilloscope, LS is the loudspeaker, RFK is the camera, and PA is the power amplifier.

At the end of every experimental run, we supplied a calibration signal of frequency 100 kHz or a one-period signal with a 10-μs duration to the preamplifier. This calibration signal recorded on the magnetic medium provided the possibility of controlling the whole of the receiving channel beginning from the preamplifier. To avoid false behavioral reactions of the animal, we controlled the behavior of the dolphin using the channel of hydrophone H1 equipped with a power amplifier PA and a loudspeaker LS. The second channel of the tape-recorder was used to record the report of the experiment. The experimenter communicated with the operator via a radio channel.

We guided the animal's behavior using the annunciator, which generated acoustic signals and transmitted them to water via a radiator (this annunciator served simultaneously as the starting manipulator). The annunciator used four signals (F1, F2, F3, and F4) with a carrier frequency of 50 kHz and respective modulation frequencies of 0.5, 1, 1.5, and 2 kHz. These signals were also fed to the loudspeaker, which indicated the correct operation of the annunciator. We carried out two experiments a day. The duration of an experiment was about two hours.

Five to ten minutes before the beginning of the experiment, we slightly fed the animal in the experimental cage. In the experiments, we used the following test order:

(1) as the experimenter produced the signal F1, the animal stood at the start position near the manipulator M1 in the surface layer and oriented the body at an angle of 90° to the direction of search;

(2) via the radio channel, the experimenter informed the operator about the distance at which the boat should be located, the kind of target to be used, and the target depth in the current experiment;

(3) in accordance with the protocol of the experiment, the target was either submerged in water to the specified depth or left at the surface;

(4) the tape-recorder was turned on for operation in the recording mode, and the experimenter gave the signal F2, which meant the start of search;

(5) on signal F2, the dolphin turned toward the searching sector, went under water and started the location process;

(6) one to three seconds after making a decision, the dolphin pushed the corresponding manipulator;

(7) if the task was fulfilled correctly, the experimenter gave signal F3 to inform the animal about the success; otherwise, the experimenter gave signal F4;

(8) the tape-recorder was turned off.

In the experiment, the dolphin received a food fee for 3 to 10 correctly fulfilled successive tasks, which made it possible to increase the number of tests in one experiment without degrading the food motivation. In one experiment, the number of tests varied from 100 to 200. The duration of every task and the whole of the experiment depended only on the animal participating in the experiment.

We used nine different targets (shapes) in the experiments. The reflectance of the shapes used (i.e., the target strength) was calculated from the experimentally measured sound pressures of radiated and reflected signals in the sea for different distances to the target.

As the radiator, we used a piezoelectric transducer 100 mm in diameter, which was composed of a set of transducers oriented in one plane. As the receiver, we used an omnidirectional piezoelectric receiver 5 mm in diameter. The measurements were carried out for distances of 2, 4, 5, 7, 9, and 11 m from the radiator and receiver. For every kind of target, the distances were selected taking into account the reflected signal amplitude. The calculated results for every target were averaged over 10 measurements. We tested the following shapes: a duralumin sphere 100 mm in diameter, Sh5 (a target strength $T = -27$ dB); a hollow cylinder 120 mm in diameter, 400 mm in height, and with 10-mm thick walls, SH6 ($T = -14$ dB); the same but filled cylinder, Sh7 ($T = -15$ dB); a corner reflector Sh8 composed of triangular hollow plates, 200 mm on a side and 5 mm in thickness, made of 0.2-mm thick tin ($T = -1.6$ dB); and a pair of similar reflectors Sh9 with a distance of 0.5 m between their centers ($T = 0$ (1) dB). (In the case of the

pair of reflectors, the directional pattern is very narrow, which causes an increase in the measurement error.)

For small targets Sh1 to Sh4 (steel spheres of respective diameters 2, 2.7, 4.1, and 4.5 cm), no measurements of target strength were performed.

EXPERIMENTAL RESULTS

The detection of shapes at limiting distances depends on different factors, such as the acoustic background of the environment, the energy performance of the radiating system, the frequency range, the target strength of the object of detection, the performance of the receiving system, the method of animal training, and the experimental procedure.

For objects of large geometrical size and, consequently, great target strength, the detection range could be more than 600 m. The data obtained with the objects of great target strengths showed a good test-to-test reproducibility in one experiment; however, the results can vary from one experiment to another, depending on the season the experiment was carried out (in summer or in autumn). This fact is obviously related to temperature stratification and signal attenuation in water, and this dependence will be the stronger, the greater the distance to the located object is. For shapes Sh5 to Sh9, the respective maximum detection ranges (with a probability of true detection of 0.98) were not less than 100, 300, 450, and 650 m. The dolphin's acoustic activities were recorded for all targets and different target depths. In the case of target Sh9, the signals were recorded only for distances shorter than or equal to 600 m.

The processing of phonograms showed that, when detecting underwater objects, the dolphin varied the signal amplitude depending on the distance to the object of detection. Figure 3 shows the sound pressure level as a function of the distance to the target. The points of this function were obtained as average levels of peak-to-peak sound pressures of signals measured in all experiments with object Sh9 (the realizations corresponded to both the presence and absence of the object). As can be seen, the level of the signal's sound pressure increases practically linearly with the distance to the object of detection. In our experiments, the minimal acoustic pressure of pulses measured 170 dB (the corner reflector at a distance of 5 m from the animal) and could be as great as 222 dB for limiting distances (a pair of corner reflectors at a distance of 650 m from the animal). The linear increase in the amplitude of the signal's acoustic pressure with distance to the object is a general tendency. In particular cases, the sound pressure level of the signal varied depending on the target strength and acoustic environment.

Searching for an object, the dolphin not only varies the sound pressure level of the radiated signal but also changes the pulse distribution in time (the temporal pulse sequence). Figure 4 shows the pulse sequences radiated by the animal during one test for different distances from the located object. It can be seen that pulse sequences appear to not be equidistant in time and depend on the distance to the object, which is especially pronounced for large distances (exceeding 100 m). For distances to the object of detection below 100 m, the duration of the pulse-to-pulse interval depends on the animal–object distance and satisfies the inequality $T > 2L/C$, where C is the velocity of sound in water and L is the distance to the object.

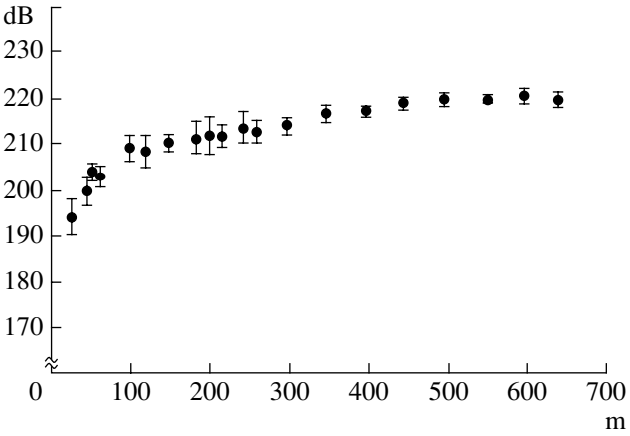

Fig. 3. Sound pressure level of dolphin's echolocation signals as a function of the distance to the object of echolocation. The sound pressure level of the signal in dB (peak-to-peak) relative to 1 μPa reduced to 1 m is plotted as the ordinate, and the distance to the object of detection is plotted as the abscissa.

For distances to the located object above 100 m, the temporal sequences of pulses radiated by the animal become nonequidistant in time and, for this reason, require a more detailed consideration.

Figure 5 shows the dynamics of the echolocation sequence variation versus the order number of a pulse-to-pulse interval in the pulse sequence. The interval number in the pulse sequence order is plotted as the abscissa, and the duration (in milliseconds) of the pulse-to-pulse interval is shown as the ordinate. All sequences shown correspond to situation YY (the target is present, the animal's reaction is correct) for different distances between the dolphin and the object of detection. Every dot shows the actual variation of the period between pulses in one test. The heavy line corresponds to the time required for the signal to travel to the target and return back (calculated by the formula $T_{calc} = 2L/C$).

In the case of the animal–target distance of 10 m, the pulse sequence in time is nonequidistant and the pulse-to-pulse intervals exceed the time of signal propagation to the target and back by a factor of 2–3. With the object of detection receding to a distance of 50 m, the first pulse-to-pulse interval appears to be much greater than the estimated time of signal propagation to the target and back, while subsequent pulse-to-pulse intervals exceed the estimated time (66.7 ms) by 20–40 ms. For

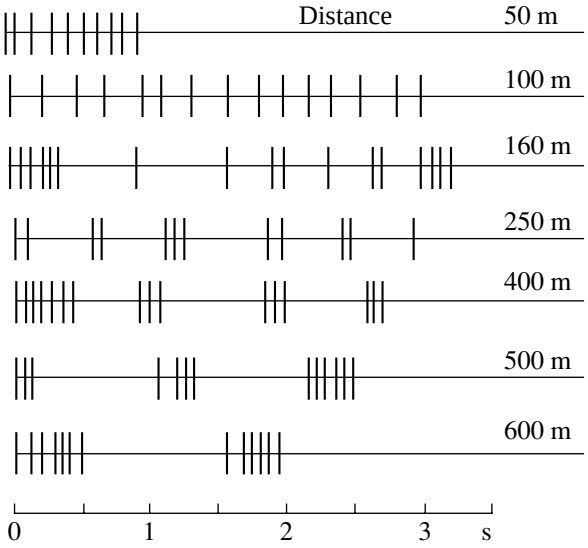

Fig. 4. Pulse sequences radiated by the dolphin detecting underwater objects in a natural acoustic environment for different distances. For every test, the complete fragment is shown.

a distance to the object of 100 m, the pulse-to-pulse interval varies between 170 and 280 ms, which exceeds the estimated time (133.3 ms) by 50–140 ms. For the target at distances exceeding 150 m, the behavior of the pulse-to-pulse intervals drastically changes: pulse subsequences (groups or bursts) appear in which the pulse-to-pulse intervals are much shorter than the estimated time. The dynamics of pulse-to-pulse interval variation with the distance to the target increasing from 150 m to 600 m (Fig. 5) shows a considerable increase in burst-to-burst intervals, the pulse-to-pulse intervals in a burst being much smaller than the estimated time. With increasing distance to the target, the duration of bursts increases due to the correspondingly increased number of pulses in a burst, and the burst-to-burst time intervals exceed the estimated time of signal propagation to the target and back.

The results obtained are evidence of the availability of two operating modes in the animal's radiating system: the single-pulse mode and the mode of transmitting pulse groups (bursts). An intermediate echolocation mode occurs for animal–target distances between 120–150 m, where the pulses are transmitted as a combination of separate pulses (the single-pulse mode) and pulse pairs (bursts). In bursts of two pulses, the pulse-to-pulse interval varies from one burst to another between 50 and 150 ms, while, for the single-pulse mode, the pulse-to-pulse interval varies from 220 to 450 ms.

Switching to the mode of echolocation with pulse bursts definitely occurs at a dolphin–target distance of 200 m; for this distance, bursts are composed of 3–5 pulses with pulse-to-pulse intervals of 10–50 ms. The number of pulses in a burst usually increases at the end of the whole series of echolocation pulse sequence. As the distance to the object of detection increases, the number of pulses in a burst also appreciably increases. For distances from 300 to 600 m, the difference between pulse-to-pulse intervals appeared to be so great that we were forced to use two scales: one (lower) for pulse-to-pulse intervals in bursts and the other (upper) for the interval between the last pulse of a burst and the first pulse of the next burst. As follows from Fig. 5, the pulse-to-pulse interval in long bursts varies from 12 to 50 ms, and the interval between the last pulse of a burst and the first pulse of the next burst can be as long as 1200–1400 ms (for the target at a distance of 600 m).

Figure 6 shows the dynamics of temporal pulse sequence in bursts. The pulse-to-pulse interval in a burst is plotted as the ordinate, and interval number in sequence is plotted as the abscissa. The graphs correspond to the following situations: YY when the target is present and the reaction is correct, NY when no target is present and the reaction is correct, YN when the target is present and the reaction is incorrect, and NN when no target is present and the reaction is incorrect. Figures marking the curve correspond to the number of the burst in the whole series of pulses in one test. From the curves given in Fig. 6, one can see that the pulse sequence in bursts can be both equidistant and nonequidistant; in other words, pulse-to-pulse intervals in bursts appear to be modulated. The pulse-to-pulse interval modulation can both vary significantly from one burst to another (see the NY–Sh8 case) or almost replicate one another (the first and second bursts in the YY–Sh8 and NN–Sh9 cases). The equidistant pulse sequences with minimum pulse-to-pulse interval appear mainly in the last burst of the whole pulse series (the third burst with a pulse-to-pulse interval of 1.7–2 ms in the YN–Sh9 case and the second burst with a pulse-to-pulse interval of 2–3 ms in the NY–Sh9 case). The number of bursts in a test depends on the situation. For example, in the case of the target being present and successfully detected (YY–Sh8), the number of bursts (two) appears to be smaller than in the case of the target being absent and incorrectly detected (NN–Sh9, four bursts). In the majority of cases, pulses in bursts appear to be nonequidistant.

Thus, the measured temporal distributions of pulses in sequences show the availability of two echolocation modes: the single-pulse mode and the multipulse mode (pulse bursts).

Figure 7 shows typical oscillograms of pulses radiated by a dolphin searching for a target at different distances. In the oscillograms in Figs. 7a–7c, the first pulse is the echolocation pulse of the dolphin and the second pulse corresponds to the reflection from the water–air boundary.

The set of features that allow one to distinguish the echolocation pulse of the animal being tested among other possible pulses is as follows. Every sounding

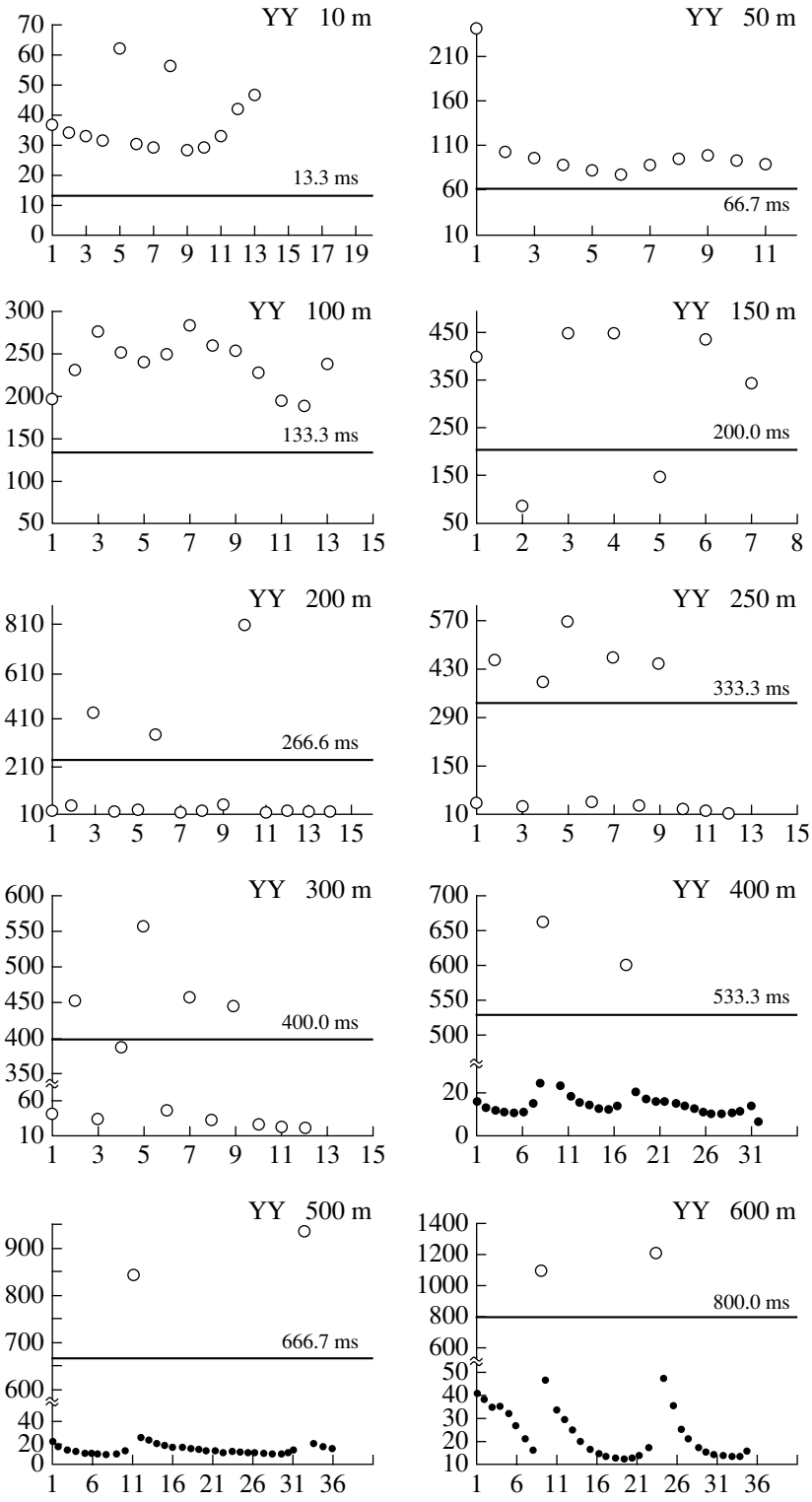

Fig. 5. Dynamics of the temporal pulse sequence versus the pulse-to-pulse interval number in the YY situation (the target is present, the reaction is correct). The heavy line shows the time required for the signal to travel to the target and return back. The pulse-to-pulse interval is plotted as the ordinate, and the interval number in sequential order is plotted as the abscissa.

pulse has a companion pulse (reflected from the water–air boundary). The position of this companion on the time axis relative to the main pulse depends on the depth of the animal position, the hydrophone depth, and the distance from the receiving point to the dolphin. Each reflected pulse changes the phase of the wave to

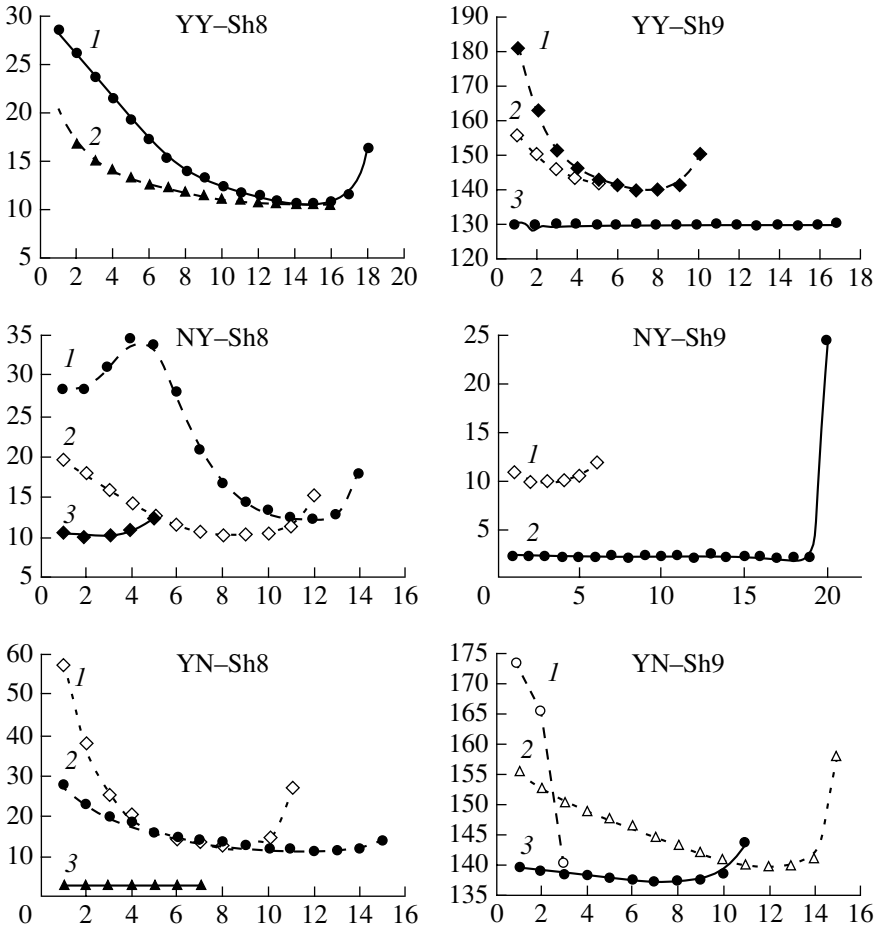

Fig. 6. Dynamics of the temporal pulse sequence in bursts for targets Sh8 and Sh9 versus the pulse-to-pulse interval number in sequential order for targets Sh8 and Sh9 and different situations: (YY) the target is present and the reaction is correct, (NY) no target is present and the reaction is correct, (YN) the target is present and the reaction is incorrect, and (NN) no target is present and the reaction is incorrect. The pulse-to-pulse interval in the burst is plotted as the ordinate, and the interval number in sequential order is plotted as the abscissa.

the value opposite to the phase of the main pulse. The temporal structure of the reflected pulse varies depending on the grazing angle, because the spectral-time structure of a dolphin's acoustic radiation depends on the azimuth. Pulses that the dolphin radiates detecting targets at distances of 650 (Fig. 7a), 500 (Fig. 7b), and 400 m (Fig. 7c) have nearly identical oscillograms in the form of 30-ms-long decaying structures. For comparison, Fig. 7d shows the pulse of the dolphin locating a fish at a distance of 0.7 m. The duration of the main oscillation of this pulse measures 20 μs.

DISCUSSION

The results obtained can be summarized using a situation-dependent analysis of all pulse sequences recorded during all experiments on target detection. Prior to the data processing, we needed to find a parameter that is invariant with respect to switching between the echolocation modes. To generalize the single-pulse and multipulse echolocation modes, we introduce the concept of an overlapping factor defined as the ratio of the pulse-to-pulse or burst-to-burst interval to the calculated time of signal propagation to the target and back: $K = T_{exp}/T_{calc}$. In this formula, the denominator T_{calc} is known and depends on the distance between the dolphin and the target and the numerator T_{exp} is obtained from the experimental data. In the case of the single-pulse echolocation mode (for distances of 120–150 m), the determination of the time T_{exp} is relatively obvious. In the case of the multipulse echolocation mode, the time is determined as $T_{exp} = \Sigma t_i + t_k$, where Σt_i is the sum of pulse-to-pulse intervals in a burst (the burst duration) and t_k is the interval between the last pulse of the burst and the first pulse of the next burst. The pulse sequence characterized by an overlapping factor much smaller than unity can be classified as a burst of pulses. In the case of an overlapping factor of about 0.5–0.7, some uncertainty appears. In this case, the discrimination between a single-pulse sequence and a pulse burst (especially a pulse pair) is hardly possible. We eliminated from further processing the tests in

which the dolphin radiated a single burst of pulses (the overlapping factor was always smaller than unity). Records with uncertain pulse sequences were either not included in calculations or processed more elaborately. In the case of elaborate processing, we must first examine whether the questionable pulse belongs to the pulse sequence radiated by the dolphin employed in the experiment, whether this pulse was radiated by another animal, or whether it is a reflection from random obstacles. Figure 8 shows the results of processing the data obtained in the experiments in which the dolphin detected targets Sh6, Sh7, Sh8, and Sh9 at distances exceeding 120 m. The dots correspond to data averaged over 5 to 60 measurements. The scatter of these values is omitted, because it is insignificant in this case. Depending on the distance to the target, the burst-to-burst interval varies from 220 to 1400 ms (Fig. 8a). The line of measured times T_{exp} (the heavy line in Fig. 8a) lies noticeably higher than the line of calculated times T_{calc} (the light line in Fig. 8a). The mean burst duration varies from 50 to 210 ms depending on the distance to the object of detection (Fig. 8b). The winding behavior of this curve can be considered as evidence of the fact that certain data arrays correspond to situations in which the object of detection was predominantly present or predominantly absent. Nevertheless, the tendency of varying the pulse burst duration depending on the distance to the object of detection is evident. Figure 8c shows the number of bursts radiated by the dolphin versus the distance to the object. The experimental phonograms (Fig. 8c) were processed separately for the situations with the target present and the situations with the target absent. The mean number of bursts in the situation with the target present is much smaller and varies from 2 to 4 bursts. The number of bursts depends on the difficulty of the problem solved by the dolphin. In the situation with the target absent, the dolphin inspects the coverage sector more thoroughly and varies not only the parameters of the radiated bursts but also the burst-to-burst intervals.

Figure 8d shows the number of pulses in the bursts (from 2 to 14) versus the distance to the target. Every dot in the plot was obtained as an average of several measurements (from 5 to 30). In the same acoustic environment, the number of pulses can significantly vary and depends on the success of the previous tests. After unsuccessful previous tests, the animal inspects the coverage sector more thoroughly, which manifests itself in an increase in the burst duration and in the number of bursts in the whole pulse series. In situations with the object being absent, when the search occurs at long distances (550–600 m), the pulse number in bursts can be as high as 30.

Thus, the results of processing allow the interpretation of the pulse bursts as separate signals characterized by the following parameters: amplitude, duration, pulse number, and variation of the pulse-to-pulse interval. The burst-to-burst intervals are longer then the time

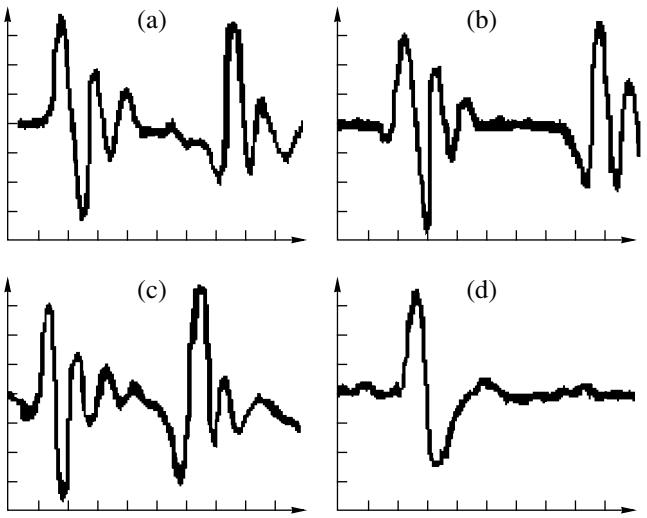

Fig. 7. Oscillograms of pulses radiated by the dolphin: (a–c) the typical signals of the dolphin detecting a target at distances of (a) 650, (b) 500, and (c) 400 m and (d) a typical pulse produced by the dolphin locating a fish at a distance of 0.7 m. In every oscillogram, the first pulse is the dolphin's signal and the second pulse is the reflection from the water–air boundary. The time scale is 10 μs per division.

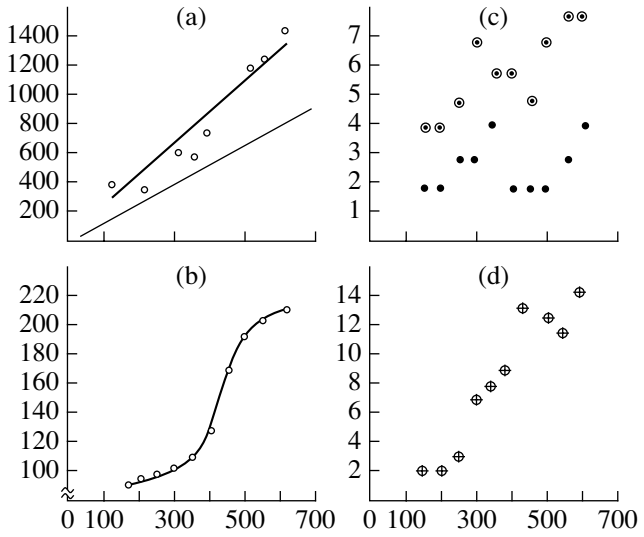

Fig. 8. Characteristics of the echolocation signals of the dolphin detecting objects at large distances: (a) the duration of the burst-to-burst interval versus the distance to the object (the light line corresponds to the calculated time of signal propagation to the target and back, the circles correspond to experimental data); (b) the burst duration versus the distance to the object; (c) the burst number versus the distance to the object (the dotted circles correspond to situations with no target and the dots correspond to situations with the target present); and (d) the pulse number in a burst versus the distance to the object. The objects of detection are Sh7, Sh8, and Sh9. Every dot is obtained as the average over 6 to 20 tests. The distance to the object of detection is plotted as the abscissa in all graphs. The ordinate corresponds to (a) the burst-to-burst interval (in milliseconds), (b) the burst duration (in milliseconds), (c) the mean burst number, and (d) the mean pulse number in a burst.

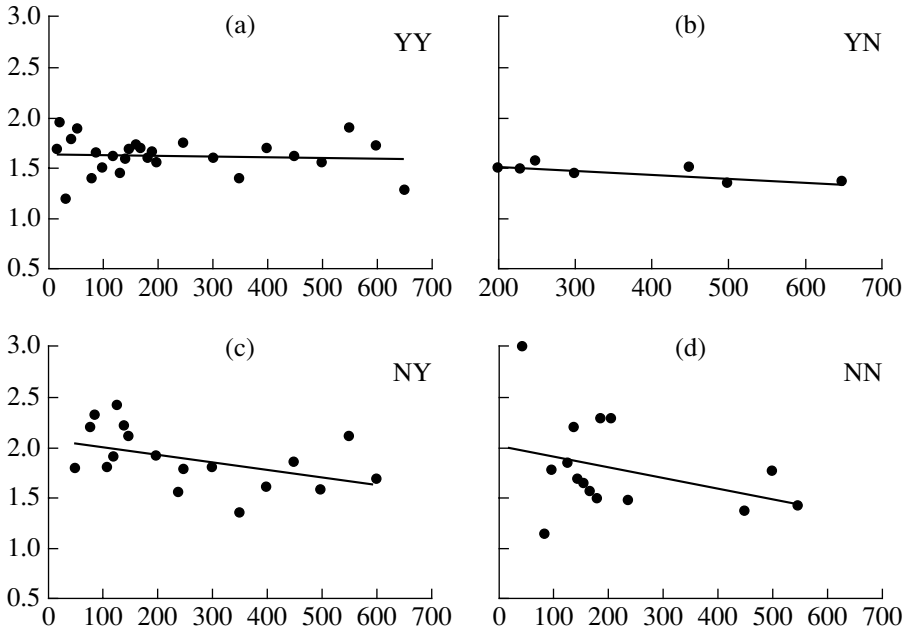

Fig. 9. Dynamics of the mean overlapping factor versus the distance to the object of detection for all targets from Sh1 to Sh9 and different situations: (a) YY (the target is present and the reaction is correct), (b) (no target is present and the reaction is correct), (c) YN (the target is present and the reaction is incorrect), and (d) NN (no target is present and the reaction is incorrect). The overlapping factor is plotted as the ordinate, and the distance to the object of detection (in meters) is plotted as the abscissa in all graphs.

required for a burst to travel to the target and return back.

The revealed regularity offers a possibility of constructing the generalized curve of the overlapping factor as a function of the distance to the object. Figure 9 shows the dynamics of the mean overlapping factor for every situation with all targets used in the experiments (from Sh1 to Sh9). In the YY situation, the mean overlapping factor varies within 1.2–1.9 and the regression line is practically horizontal with a characteristic value of 1.6–1.7. In the YN situation, the overlapping factor varies within 1.3–1.6, i.e., errors in the situation with the target present are seemingly related to the task solved by the animal previously, but not with solving the current task. The NY situation (the absence of the target and a correct reaction of the animal) shows that the overlapping coefficient tends to increase, but does not exceed the value of 2.5. The maximum scatter in data for the mean overlapping coefficient (from 1.1 to 3.0) was obtained in the NN situation, i.e., when the target is absent in the coverage sector but the animal decides that the target is present.

The experimental results showed that the dolphin is able to detect objects at large distances. Phonograms of the acoustic behavior of the animal detecting targets at distances up to 600 m were obtained. Characteristics of temporal pulse sequences were estimated as functions of the distance to the object of detection. The behavioral data of the acoustic experiment showed that, in the case of target Sh9, the maximum detection range can definitely exceed the results obtained. The detection of this target at distances of 650 and 700 m was observed, but no records for these signals were obtained because of bad weather conditions.

The characteristics obtained for the signals of the *Tursiops truncatus ponticus* solving detection problems in a complicated acoustic environment showed that the results of full-scale observations of animals at liberty [2] can be modeled in laboratory experiments. The method of alternate choice under a successive stimulus presentation with an acoustic control over the animal's behavior during the experiment allows one to obtain reliable behavioral and acoustic reactions of the animal. Combining the experimenter's acoustic response to the animal's behavioral reactions with partial food reinforcement makes it possible to control the animal's psychophysiological state during the experiment. The body of acoustic information obtained in one test appears to be much smaller and can easily be interpreted on further processing. The number of pulses radiated by the dolphin depends on geometrical dimensions of the target and on the distance to the target. Indeed, the smaller the volume of space examined by one acoustic pulse, the greater the pulse number required for detecting the target in the water column.

In closing, I thank N.A. Dubrovsky for supporting the experiments described in this paper. Expert discussions of current experimental results have made it possible to arrive at a conclusion that the modeling of a dolphin's acoustic behavior in a laboratory experiment is quite practicable. However, the adequacy of the methods used in laboratory acoustic experiments is still a

topical problem of physiological experiments with superior animals.

REFERENCES

1. A. I. Akopian, Candidate's Dissertation (St. Petersburg, 1995).
2. V. M. Bel'kovich and É. N. Khakhalkina, in *Black Sea Aphaline (Tursiops Truncatus Ponticus)*, Ed. by V. E. Sokolov and E. V. Romanenko (Nauka, Moscow, 1997), pp. 513–543.
3. R. G. Busnel and A. Dziedzic, in *Animal Sonar Systems. Biology and Bionics*, Ed. by R.-G. Busnel (INTRA-CNRZ, Joyen-Josas, 1967), pp. 307–335.
4. A. A. Titov, Candidate's Dissertation (Karadag, 1972).
5. V. A. Vel'min, in *Proceedings of 6th All-Union Meeting on Studies of Marine Mammals* (Naukova Dumka, Kiev, 1975), Part 1, p. 75.
6. N. A. Dubrovskiĭ and P. S. Krasnov, Tr. Akust. Inst. Akad. Nauk SSSR, No. 17, 9 (1971).
7. L. R. Giro and N. A. Dubrovskiĭ, Morsk. Priborostr., Ser.: Akust., No. 2, 84 (1972).
8. É. Sh. Aĭrapet'yants, Yu. V. Ivanenko, M. P. Ivanov, *et al.*, in *Abstracts of V All-Union Meeting on Studies of Marine Mammals* (Makhachkala, 1972), Part 2, p. 234.
9. É. Sh. Aĭrapet'yants, V. A. Voronov, Yu. V. Ivanenko, *et al.*, Zh. Evol. Biokhim. Fiziol., No. 2, 418 (1973).
10. M. P. Ivanov and N. A. Kurganskiĭ, in *Proceedings of All-Union Meeting on Bionics* (Moscow, 1973), p. 54.
11. W. W. L. Au, R. W. Floyd, R. H. Penner, and A. E. Murchison, J. Acoust. Soc. Am. **56**, 1280 (1974).
12. W. W. L. Au, R. W. Floyd, and J. E. Haun, J. Acoust. Soc. Am. **64**, 411 (1978).
13. W. W. L. Au and K. J. Snyder, J. Acoust. Soc. Am. **68**, 1077 (1980).
14. W. W. L. Au, R. J. Schusterman, and D. A. Kersting, in *Animal Sonar Systems*, Ed. by R. G. Busnel and J. F. Fish (Plenum, New York, 1980), pp. 859–862.
15. W. W. L. Au and R. H. Penner, J. Acoust. Soc. Am. **70**, 687 (1981).
16. M. P. Ivanov and V. V. Popov, in *Abstracts of VII All-Union Workshop on Marine Mammals, Simferopol, 1978* (Moscow, 1978), pp. 141–142.
17. M. Ivanov, in *Proceedings of XXXII International Congress of Physiological Sciences* (Leningrad, 1977).
18. C. W. Turl and R. H. Penner, J. Acoust. Soc. Am. **86**, 497 (1989).
19. K. V. Bardin, in *Problem of Sensitivity Thresholds and the Psychophysical Methods* (Nauka, Moscow, 1976), p. 394.

Translated by A. Vinogradov

Acoustical Physics, Vol. 50, No. 4, 2004, pp. 480–484. Translated from Akusticheskiĭ Zhurnal, Vol. 50, No. 4, 2004, pp. 562–567.

BIOLOGICAL ACOUSTICS

Auditory Analysis of the Periodicity of Sound and Its Envelope: A Mathematical Model

S. M. Ishchenko

Andreev Acoustics Institute, Russian Academy of Sciences, ul. Shvernika 4, Moscow, 117036 Russia

e-mail: bvp@akin.ru

Received February 10, 2004

Abstract—A mathematical model of the auditory analysis of periodicity of sound and its envelope is proposed. The model consists of a sequence of mathematical transformations that describe the signal processing stages. The following parameters and properties of the auditory system are taken into account: the crude analysis of the input acoustic signal accurate to the width of the aural critical band; the frequency dependence of the width of the aural critical band; the spectrum of the input signal analysis by a set of 3500 filters closely spaced in frequency; the absolute audibility thresholds at a given frequency; the time-domain analysis of both the output signals of each filter and the envelope profile with the help of the periodicity function; the pulsed activity of auditory neurons; the ability of the auditory system to memorize the spectral–time images of the signal and its individual parameters; the ability of the auditory system to form the perception of the loudness of sound, to memorize and compare the loudness of sound at different time moments, and to conclude which of them is higher or lower or whether they are equal accurate to a certain threshold; the dependence of the critical modulation bandwidth on the modulation frequency; and the dependence of the audibility thresholds of amplitude modulation on the modulation frequency. By an example of processing amplitude-modulated signals with various carrier-to-envelope frequency ratios, the model is shown to give a satisfactory explanation of their pitch and auditory estimate of the envelope period. © *2004 MAIK "Nauka/Interperiodica".*

This paper describes a mathematical model of the auditory analysis of both periodicity of sound and its envelope. The model consists of a sequence of mathematical transformations that describe the functions of the blocks of the diagram given in [1].

According to the block diagram of the model, the input acoustic signal $p(t)$ is applied to 3500 parallel tightly overlapping frequency filters Φ_n1–Φ_nk whose center frequencies fk are spaced uniformly on a logarithmic frequency scale. The frequency band transmitted by these filters is equal to the aural critical band ΔF_{cr} [2, 3]. If the signal's spectral components are spaced apart by a frequency interval wider than the aural critical band, the listener perceives them separately and uses the spectral analysis mechanism. If spectral components of the input signal are concentrated within a single aural critical band, they are perceived together as a single signal or, to be more precise, as a sum of the input signal's spectral components with the corresponding amplitudes and phases. The model implies that, in the latter case, the energy of the signal is distributed over all the tightly frequency-overlapping filters within the aural critical band in accordance with the response of the "auditory filter" and that the time-domain sound analysis mechanism is applied. The frequency interval Δf_{adj} between two adjacent filters inside a single critical band is calculated by the formula

$$\Delta f_{adj} = \Delta F_{cr}(f)/n_f, \tag{1}$$

where f is the frequency in hertz and n_f is the number of filters that fall into a single aural critical band (n_f = 3500/24 ≈ 146, because the number of nonoverlapping aural critical bands that cover the aural frequency band is 24 [2]).

An experimental dependence of the aural critical band $\Delta F_{cr}(f)$ on frequency is given in [2, 3]. In the present paper, we approximate it as follows:

$$\Delta F_{cr}(f) = 40\log(f) \quad \text{for} \quad f \le 250, \tag{2}$$

$$\Delta F_{cr}(f) = f/\log(f + 1.4) \quad \text{for} \quad 250 < f < 1000 \quad \text{and for} \quad f > 3000, \tag{3}$$

$$\Delta F_{cr}(f) = f/[\log(f) + 2.4] \quad \text{for} \quad 1000 \le f \le 3000. \tag{4}$$

The amplitude-vs-frequency responses of the filters are borrowed from [4, 5], where filters called the "auditory filters" are described by the formula

$$W(g) = (1 + pg)^{1/2}e^{-pg/2}, \tag{5}$$

where p is the signal's sound pressure and $g = |f - f_k|/f_k$ is the relative difference between the signal frequency f_k and the current frequency f. When the frequency f_k of the input signal of the kth filter is equal to its center fre-

1063-7710/04/5004-0480$26.00

quency, the amplitude-vs-frequency response of this filter can be represented as

$$W_k(g_k) = (1 + u_k g_k)^{1/2} e^{-u_k g_k/2}, \quad (6)$$

where $u_k = \alpha[p_k(f_k) - p_a(f_k)]$ is the difference between the intensity $\alpha p_k(f_k)$ of the spectral component $\alpha p_a(f_k)$ of the input signal $p_a(f_k)$ at the input of the kth filter and the intensity $\alpha p_k(f_k)$ of the spectral component of the signal at the same frequency at its audibility threshold $\alpha p_k(f_k)$, $g_k = |f - f_k|/f_k$ is the relative difference between frequencies f and f_k, and α is the coefficient of proportionality.

Because the frequency response of the filters depends on the parameter u_k, which in turn depends on the parameter $p_a(f_k)$, their behavior must be calculated with allowance for the frequency dependence of the absolute audibility thresholds $p_a(f_k)$. An averaged experimental frequency dependence of these thresholds is given in [2] and is approximately described by the following five expressions in various frequency bands with $x = \log(f)$ and $\Delta x = |x - x_0|$:

$$p_a(f), \text{dB} = 14.0\Delta x - 51x + 140, \quad \text{where } x_0 = 2.0 \text{ and } 20 < f < 1000; \quad (7)$$

$$p_a(f), \text{dB} = 3.3\Delta x, \quad \text{where } x_0 = 3.3 \text{ and } 1000 < f < 3000; \quad (8)$$

$$p_a(f), \text{dB} = 3.0 f\Delta x, \quad \text{where } x_0 = 3.4 \text{ and } 3000 < f < 12000; \quad (9)$$

$$p_a(f), \text{dB} = 951.56\Delta x, \quad \text{where } x_0 = 4.00688 \text{ and } 12000 < f < 15000; \quad (10)$$

$$p_a(f), \text{dB} = fx, \text{ where } 15000 < f < 20000. \quad (11)$$

Expressions (7)–(11) allow one to approximately calculate the absolute audibility thresholds $p_a(f)$, which will differ from the averaged experimental values by no more than 1.2 dB in the frequency range from 20 Hz to 12 kHz and by no more than 4 dB at frequencies above 12 kHz. The 0-dB level is arbitrarily set at 2 kHz.

According to the block diagram of the generalized model of auditory analysis of sound periodicity [1], a positive constant quantity $A_1 = \min|p(t)|$ equal to the absolute value of the minimum input signal is added to the input signal, which makes all values of the above signals positive while retaining the time profile $\alpha p_k(t)$ of the spectral component of the input signal at the input of the kth filter. As was shown in [6], the time profile of the input signal is stored in the receptor potentials of the hair cells of the Corti organ.

The pulsed nature of the auditory neural network activity was simulated as follows. In the absence of a signal at the input of the model, only a spontaneous pulsed activity is observed at the outputs of the filters $\Phi_n 1$–$\Phi_n k$, the pulse-to-pulse intervals being distributed by the Poisson law

$$p_{m,n} = (Y^m/m)e^{-Y}, \quad (12)$$

where $p_{m,n}$ is the probability that event A occurs m times in n independent trials and $Y = np$.

The density D_s of the spontaneous pulsed activity (firing rate) of human auditory nerve fibers per one aural critical band can be estimated from their total number (30000), the number of aural critical bands (24) that cover the audible frequency band, and the known average spontaneous firing rate (50 pulses per second) for a single fiber. Thus, one aural critical band is covered by 1250 = 30000/24 auditory nerve fibers, and the average spontaneous firing rate of the human auditory nerve per one aural critical band is $D_s = 1250 \times 50 = 62500$ pulses per second. Note that a human with normal hearing does not perceive the spontaneous firing rate of the auditory neurons.

Let $\alpha p_k(\omega_k, t)$ be the input signal of the kth filter and $D_{k0}(\omega_k)$ be the density of the pulsed activity at the output of this filter at the audibility threshold. Then the frequency and time dependence of the pulsed activity density $D_k(\omega_{k,t})$ at the outputs of the filters $\Phi_n 1$–$\Phi_n k$ can be represented as

$$D_k(\omega_k, t) = D_{k0}(\omega_k)[A_1 + \alpha p_k(\omega_k, t)]. \quad (13)$$

The distribution of the pulsed activity density $D_k(\omega_k, t)$ at the outputs of the set of filters $\Phi_n 1$–$\Phi_n k$ at a particular instant can be considered as an instantaneous power spectrum of the input signal, while the variation of this spectrum in time is the spectral–time image of the input signal, which is sometimes referred to as its "full description" [7]. The full description was memorized and the output of each filter was analyzed with the periodicity function $P_k(\tau)$ [8], $P_k(\tau) = S_k(\tau)/S_k(\tau = 0)$, where

$$S_k(\tau) = (1/T_s)\int_0^{T_s} \chi[|D_k(\omega_k, t) - D_k(\omega_k, t + \tau)| - \varepsilon]dt, \quad (14)$$

τ is the delay, T_s is the length of the analyzed signal, t is the current time, $\varepsilon \ll \max[D_k(\omega_k, t)]$, and $\chi(r) = 1$ at $r \le 0$ and $\chi = 0$ at $r > 0$; $r = [|D_k(\omega_k, t) - D_k(\omega_k, t + \tau)| - \varepsilon]$. The period of the signal is extracted from the highest maximum of the periodicity function at the shortest nonzero delay τ. The extracted maxima of the periodicity function in the frequency channels are multiplied by u_k (see expression (6)) with $f = 1/\tau$.

If the level of the spectral component of the input signal at the filter's center frequency f_k was lower than the level of this signal component at the audibility threshold, pulsed activity was generated at the output of the filter, which simulated the spontaneous firing rate of the auditory nerve, whose pulse-to-pulse intervals complied with the Poisson law.

It is assumed that the density of the spontaneous pulsed activity at the filters' outputs gradually decreases from the initial value D_s in the absence of the signal to zero as the density of the forced (under the action of the signal) pulse rate in this frequency channel approaches a particular value $D1 = C1D_s$. Let $C1 \approx 1.5$.

It can easily be shown that, at moderate intensities (20–40 dB), the loudness $L(t)$ of sound reproduces its envelope $M(t)$ accurate to a constant coefficient. Let $p(t)$ be an amplitude-modulated (AM) signal

$$p(t) = [1 + d_m \sin(\Omega t)]\sin(\omega t), \quad (15)$$

where d_m is the modulation index, $M(t) = 1 + d_m \sin(\Omega t)$ is the envelope of the input signal $p(t)$, $\sin(\omega t)$ is the carrier oscillation, Ω is the modulation frequency, and ω is the carrier frequency. The percent AM modulation is $d_{mp} = d_m \times 100\%$.

According to Stevens's law, the loudness $L(t)$ of sound is satisfactorily described by the expression

$$L(t) = Cp(t)^a, \quad (16)$$

where C is a constant coefficient, $p(t)$ is the acoustic pressure, and a is the intensity-dependent exponent. At moderate sound intensities (20–40 dB), the coefficient is $a = 1$ and expression (16) can be written as

$$L(t) = C2[1 + d_m \sin(\Omega t)] = C2M(t), \quad (17)$$

because the loudness of a constant-amplitude sinusoidal signal is constant after a certain time after the pulse is turned on, i.e., $C2 = C\sin(\omega t)$, where $C2$ is a constant factor.

Thus, at moderate intensities, the loudness of sound is proportional to the envelope $M(t)$ of the input signal $p(t)$. Taking this fact into account, we form the envelope $M(t)$ of the input signal by calculating the function $L(t)$ based on the assumption that the loudness of sound is determined by the total pulsed activity of auditory neurons due to the input signal.

A number of experimental data show that the loudness of an acoustic pulse reaches its steady state within 25 to 200 ms after it is turned on. The loudness stabilization time constant of 100 ms is used most often [9]. Let us calculate $L(t)$ from the sum of pulse activity densities at the outputs of the system of filters $\Phi_n 1$–$\Phi_n k$ for each time moment over the time interval $T_{\text{sum}} = 5$ ms.

It may seem that the summation time interval should be equal to 100 ms. In this case, the envelope frequencies higher than 10 Hz will not be fully represented in the function $L(t)$, because this summation acts as a low-pass filter.

With expression (13) for the pulsed activity density $D_k(\omega_k, t)$ at the output of the kth filter, the function $L(t)$ can be represented as

$$M(t_i) \sim L(t_i) = 2\pi/[T_{\text{sum}}(\omega_2 - \omega_1)] \sum_{j=0}^{j_m} \sum_{k=1}^{k_m} D_k(\omega_k, t_i + t1_j), \quad (18)$$

where $t_i = i\Delta t$, $i = 0, 1, \ldots, i_m$; $i_m = T_s/\Delta t$; Δt is determined by the necessary accuracy of calculating $L(t_i)$, T_s is the length of the input signal; $f_1 = 20$ Hz, $f_2 = 20$ kHz; $k_m = 3500$; $j = 0, 1, \ldots, j_m$; $j_m = T_{\text{sum}}/\Delta t1$; $t1_j = j\Delta t_1$; and $\Delta t_1 \approx 0.01 T_{\text{sum}}$.

If frequency and time are continuous variables, expression (18) can be represented as

$$M(t) \approx L(t) = 2\pi/[T_s T_k(\omega_2 - \omega_1)] \times \int_0^{T_{\text{sum}}} \int_{\omega_1}^{\omega_2} D(\omega, t + t_1) d\omega dt_1. \quad (19)$$

The function $M(t) \approx L(t)$ is applied to the set of tightly overlapping modulation filters Φ_{m1}–Φ_{ml}, which are conventionally called the auditory filters for the envelope. The presence of modulation filters [10] and auditory filters, as well as the existence of the aural critical band and aural critical modulation-frequency band [11], allow us to assume that the auditory mechanism of analyzing the envelope periodicity also uses the spectral–time processing and, moreover, its operating principle is similar to that of the auditory analysis of the periodicity of sound. The procedure is such that, if the spectral components of the input signal are concentrated within one aural critical modulation-frequency band, they are combined with allowance for their amplitudes and phases and the energy of the total signal is distributed over the set of modulation filters that fall within the aural critical modulation-frequency band according to the shape of the auditory filters for the envelope.

If the spectral components of the envelope occupy several aural critical modulation-frequency bands, they are processed in each band separately. Let us represent the shape of the auditory filters for the envelope as

$$W_m(g_m) = (1 + p_m g_m)^{1/2} e^{-p_m g_m/2}, \quad (20)$$

where $g_m = \beta|f_m - f_{ml}|/f_{ml}$ is the relative difference between the current amplitude-modulation frequency f_m and the frequency f_{ml} of the envelope's frequency component in the lth frequency channel for the envelope, $\beta = \Delta F_{\text{crm}}/\Delta f_{m,0.7}$, and $\Delta f_{m,0.7}$ is the bandwidth of the modulation filter $W_m(g_m)$ measured between its 0.7 points relative to its maximum response at the center frequency f_{ml}. The coefficient β is introduced to make the experimental bandwidth $\Delta F_{\text{crm}}(f_m)$ equal to $\Delta f_{m,0.7}$, and $p_m = (d_{mp} - p_{ml})$ is the difference between the depth d_{mp} of modulation caused by the lth spectral component of the envelope at the frequency f_{ml} and the

AM audibility threshold $p_a(f_{ml})$ at the same AM frequency f_{ml}.

An experimental dependence of the AM threshold versus the frequency f_m is reported in [11]. Because the dependence of the AM threshold $p_{\text{mn}}(f_m)$ of the AM noise versus the AM frequency significantly differs from that for the tone AM, $p_{\text{mt}}(f_m)$, these modulation functions (in terms of the modulation percentage) are approximated by expressions (21)–(25) for AM noise and AM tone separately:

$$p_{\text{mn}}(f_m) = 3.00 + (3.00 - f_m)^2 \times 0.2 \text{ for } f_m < 3, \quad (21)$$

$$p_{\text{mn}}(f_m) = 3.00 + 0.06 f_m \text{ for } f_m \geq 3, \quad (22)$$

$$p_{\text{mt}}(f_m) = 2.5 + (3.0 - f_m)^2 \times 0.2 \text{ for } f_m < 3.0, \quad (23)$$

$$p_{\text{mt}}(f_m) = 2.5 + (f_m - 3.0)^2 \times 0.1 \text{ for } 3 \text{ Hz} < f_m \leq 11, \quad (24)$$

$$p_{\text{mt}}(f_m) = 3.1 + (f_m - 11.0) \times 0.007 \text{ for } f_m > 11. \quad (25)$$

An experimental dependence of the critical modulation audibility bandwidth ΔF_{crm} versus the modulation frequency f_m is reported in [12]. It is approximated by expressions (26)–(28) for different modulation frequency bands:

$$\Delta F_{\text{crm}}(f_m) = 0.33 f_m \text{ for } f_m \leq 17, \quad (26)$$

$$\Delta F_{\text{crm}}(f_m) = 0.23 f_m \text{ for } 17 < f_m \leq 30, \quad (27)$$

$$\Delta F_{\text{crm}}(f_m) = 5.00 + 0.025 f_m \text{ for } f_m \leq 30. \quad (28)$$

Let us estimate the number n_{fm} of the auditory filters for the envelope that covers one aural critical modulation-frequency band from the deviation of the modulation frequency that is reliably detected by the auditory system. This deviation is 0.07 at a modulation frequency of 1 Hz [8]. Thus, $n_{\text{fm}} = 1/0.07 \approx 14$. The frequency spacing between adjacent modulation filters is calculated as

$$\Delta f_{\text{maf}} = \Delta F_{\text{crm}}(f_m)/n_{\text{fm}}. \quad (29)$$

The output signal of each frequency channel for the envelope, $M_1(t) \approx L_1(t)$, is processed by the periodicity function $P_l(\tau_1) = S_l(\tau_1)/S_l(\tau_1 = 0)$, where

$$S_l(\tau_1) = [1/T_s]\int_0^{T_s} \chi[|L_l(t) - L_l(t + \tau_1)| - \varepsilon_1]dt. \quad (30)$$

Here, $\tau_1 = j_1\Delta\tau_1$ is the delay; $j_1 = 0, 1, \ldots, j_m$; $j_m = T_l/\Delta\tau_1 \approx 100$; T_l is the period of the spectral component in the lth frequency channel; and $\varepsilon_1 \ll \max[L_l(t)]$. The period of the signal $L_l(t)$ was calculated from the highest maximum of the periodicity function $P_l(\tau_1)$ at the shortest nonzero delay r_1. The values of the selected maxima of the periodicity function were multiplied by p_m for the particular frequency channel f_{ml} and projected onto a common frequency axis.

The output signals of the auditory filters and auditory modulation filters in each frequency channel were processed by the periodicity function individually, the result of this analysis for each frequency channel having its individual abscissa (the frequency or delay axis) and ordinate (from 0 to 1). Therefore, to combine the results of analyzing the periodicity of sound, they were displayed on (projected onto) a common frequency axis from 0.01 Hz to 20 kHz. The lower boundary of 0.01 Hz of perceiving the AM frequency was found experimentally. If two maxima overlapped, their values were summed at each frequency individually.

The first 6–7 thus selected highest maxima displayed on the common frequency axis were regarded as an estimate of the periodicity of the input signal. It was shown [13] that the auditory system cannot discriminate more than 6–7 maxima of a complex periodic sound.

Now, let us consider several examples of using the model proposed above to process the AM signal $p(t) = [1 + d_m\sin(\Omega t)]\sin(\omega t)$ given by Eq. (15) for different ratios of the carrier frequency ω to the modulation frequency Ω.

Example 1. Let an AM signal given by Eq. (15) be supplied to the model. When the carrier frequency ω is an integer multiple of the modulation frequency Ω, i.e., $\omega/\Omega = N$, where N is an integer greater than or equal to 10, the spectrum of the signal consists of three spectral components, the amplitude of the central component $\sin(\omega t)$ being equal to 1 and the amplitudes of the side components $\sin(\omega - \Omega, t)$ and $\sin(\omega + \Omega, t)$ being equal to $0.5d_m$. If these spectral components fall within the same aural critical band, the model processes the input signal as a sum of the three spectral components of the input signal. The energy of this signal will be distributed over the auditory filters tightly spaced in one aural critical band according to the form of the auditory filter with the center frequency ω.

Since the period of this signal is T_Ω, a maximum equal to 1 at the frequency Ω will be projected onto the common frequency axis. The envelope of the input signal, $m(t) = 1 + d_m\sin(\Omega t)$, will arrive at the envelope's auditory filter centered at the frequency Ω with its form being projected onto the common frequency axis with a maximum of d_m also at the frequency Ω. A maximum equal to $(1 + d_m)$ will thus be displayed at the frequency Ω on the common frequency axis.

If Ω exceeds the aural critical band, the three spectral components will be processed independently and, therefore, the procedure will display the form of the auditory filter at the frequency ω with a maximum of 1, and at the frequencies $\omega - \Omega$ and $\omega + \Omega$, the forms of the auditory filters with maxima of $0.5d_m$.

There will be no maxima displayed in the envelope, because the intensities of the independent spectral components will be constant in time, as well as their sum, and the periodicity function ignores the constant component of the analyzed signal.

Example 2. Let $N_1 = N + 0.5$ or $N_1 = N - 0.5$. In this case, the period of the signal $p(t)$ is $4\pi/\Omega$. This signal will also have two quasi-periods: $(T_\Omega + T_\omega/2)$ and $(T_\Omega - T_\omega/2)$.

If the three components of the signal fall within the same aural critical band, the model will process them as their sum, and three maxima of 1, $0.5d_m$, and $0.5d_m$ will be projected onto the common frequency axis at $f_1 = 1/2T_\Omega$, $f_2 = 1/(T_\Omega + T_\omega/2)$, and $f_3 = 1/(T_\Omega - T_\omega/2)$, respectively. In the envelope, the model will generate a maximum of $0.5d_m$ at a frequency f_Ω.

If the spectral components of the signal occur in different aural critical bands, i.e., when $\Omega > \Delta F_{cr}$, there will be three maxima of 1, $0.5d_m$, and $0.5d_m$ on the common frequency axis at the frequencies f_ω, $f_\omega + \Omega$, and $f_\omega - \Omega$, respectively. In the envelope, there will also be no maxima projected (see Example 1 for $\Omega > \Delta F_{cr}$).

Example 3. Let the ratio of the carrier frequency ω to the envelope frequency Ω for the signal $p(t)$ gradually increase from $N_1 = N$ to $N_2 = N + 2$.

When the spectral components of this signal lie within the same aural critical band, i.e., at $\Omega < \Delta F_{cr}$, the signal will be processed as a sum of the three spectral components. At $\omega/\Omega = N$, where N is an integer, there will be one maximum of $(1 + d_m)$ produced at the frequency Ω (see Example 1 for $\Omega < \Delta F_{cr}$). As the frequency gradually increases from $N_1 = N$ to $N_1 = N + 0.5$, the length of the quasi-period gradually increases from T_Ω to $(T_\Omega + T_\omega/2)$ and the second quasi-period $(T_\Omega - T_\omega/2)$ appears at $N_1 = N + 0.5$ (see Example 2). As the frequency ω increases further, there will only be one quasi-period of $(T_\Omega - T_\omega/2)$ left, which will gradually increase from $(T_\Omega - T_\omega/2)$ to T_Ω at $N_1 = N + 1$. With a further increase in the frequency ω from $\omega/\Omega = N + 1$ to $\omega/\Omega = N + 2$, the process will be repeated.

When $\Omega > \Delta F_{cr}$, there will be three maxima of 1, $0.5d_m$, and $0.5d_m$ produced at the frequencies ω, $(\omega + \Omega)$, and $(\omega - \Omega)$, respectively. In the envelope, there will be no maxima projected, as before (see Example 1).

Note that the three-dimensional frequency- and time-domain representation of the input signal proves to be efficient not only in the auditory analysis of periodicity of sound but also in extracting the pitch of a speech signal [14]. The above examples of processing AM signals by the mathematical model proposed in this paper show that the model satisfactorily explains their pitch and the auditory estimate of their envelope period.

REFERENCES

1. S. M. Ishchenko, Akust. Zh. **44**, 226 (1998) [Acoust. Phys. **44**, 185 (1998)].
2. E. Zwicker and R. Feldtkeller, *Das Ohr als Nachrichtenempfänger* (Hirzel, Stuttgart, 1967; Svyaz', Moscow, 1971; Acoust. Soc. Am., Woodbury, N.Y., 1999).
3. A. A. Freĭdin, Akust. Zh. **21**, 806 (1975) [Sov. Phys. Acoust. **21**, 496 (1975)].
4. R. Patterson, J. Acoust. Soc. Am. **55**, 802 (1974).
5. R. Patterson, J. Acoust. Soc. Am. **59**, 640 (1976).
6. P. Dallos, J. Neurosci. **5**, 1591 (1985).
7. L. A. Chistovich, in *Recognition of Auditory Images* (Nauka, Novosibirsk, 1970), pp. 98–106.
8. S. M. Ishchenko, Akust. Zh. **34**, 256 (1988) [Sov. Phys. Acoust. **34**, 151 (1988)].
9. V. N. Telepnev, in *Auditory System* (Nauka, Leningrad, 1990), pp. 14–42.
10. S. M. Ishchenko, Akust. Zh. **23**, 64 (1977) [Sov. Phys. Acoust. **23**, 35 (1977)].
11. L. N. Tumarkina and N. A. Dubrovskiĭ, Biofizika **11**, 653 (1966).
12. N. A. Dubrovskiĭ and L. N. Tumarkina, Tr. Akust. Inst. Akad. Nauk SSSR **12**, 48 (1970).
13. R. Plomp, J. Acoust. Soc. Am. **37**, 1110 (1965).
14. S. Granqvist and B. Hammarberg, J. Acoust. Soc. Am. **114**, 2934 (2003).

Translated by A. Khzmalyan

Acoustical Physics, Vol. 50, No. 4, 2004, pp. 485–492. Translated from Akusticheskiĭ Zhurnal, Vol. 50, No. 4, 2004, pp. 568–576.

BIOLOGICAL ACOUSTICS

Auditory Detection of Paired Pulses by a Dolphin in the Presence of a Pulse Jam

M. N. Sukhoruchenko

Andreev Acoustics Institute, Russian Academy of Sciences, ul. Shvernika 4, Moscow, 117036 Russia

e-mail: bvp@akin.ru

Received February 10, 2004

Abstract—From behavioral studies of a bottlenose dolphin (*Tursiops truncatus*), the audibility thresholds were measured for a single pair of equal-amplitude pulses, i.e., clicks, presented to the dolphin in combination with a pulse jam. The pulse jam consisted of pairs of identical pulses with a pulse spacing τ_j within the pairs and a pair repetition rate f_j. Series of pulses were interrupted by a pause $R > 1/f_j$, within which the pulse jam was absent while a pair of test pulses was supplied to one of the two channels at random. Each series had a duration T, and the total stimulation cycle was $J = T + R$. The dependence of the test pair detection threshold on the pulse spacing τ_j was studied at different fixed values of the pulse spacing in the test pair: τ_t = 50, 100, 200, and 500 μs. Preliminary measurements performed with $\tau_j = \tau_t$ = 100 μs were used to adjust the parameters of the pulse jam. The threshold shift at $\tau_j = \tau_t$ = 100 μs reached 35 dB above the audibility threshold of the test pair in the absence of the pulse jam. On both sides of the point $\tau_j = \tau_t$ = 100 μs, the thresholds decreased with varying τ_j to approximately 20 dB above the detection threshold of the test pair in the absence of the jam. However, in the course of training, the threshold curves gradually shifted downwards approaching the detection level of the test pair in the absence of the jam and becoming progressively flatter (the selectivity with respect to the pulse jam vanished). A decrease in the pause duration R restored the dependence of the test pair detection threshold on τ_j. In this case, a statistically significant maximum was obtained at $\tau_j = \tau_t$ for τ_j within the critical interval (for τ_t < 500 μs). Beyond the critical interval (for τ_t > 500 μs), even with the smallest pause duration (R = 15 ms), no dependence of the test pair detection thresholds on τ_j could be observed. *© 2004 MAIK "Nauka/Interperiodica".*

INTRODUCTION

The tone-by-tone and tone-by-noise masking are classical methods of hearing studies. The psychoacoustic literature of the last few decades contains a number of publications concerned with the masking of signals by complex natural stimuli, for example, by speech-like sounds. The masking of pure tones by stimuli with various complex spectra makes it possible to obtain the so-called "auditory spectra" of such maskers.

For a dolphin, a natural type of masker is a pulse jam imitating a multiple reverberation of the dolphin's own echolocating pulses. When a single echolocating pulse of the dolphin hits an underwater target, the echo returning to the animal often has the form of a sequence of several pulses (the so-called primary and secondary echoes) with short pulse spacings and different peak amplitudes [3, 4]. The detection and discrimination of pulse sequences with very short pulse spacings under the actual echolocation conditions is a complicated problem. However, it is surprisingly easily solved by the dolphins. The possibility of explaining the unique echolocation abilities of dolphins by the sensitivity to the pitch produced by a sequence of coherent pulses, i.e., the time separation pitch (TSP), has been much discussed in the literature [5, 6].

According to previous investigations [7–9], the interval of pulse spacings within 200–300 μs contains a boundary where a dolphin changes its behavior in discriminating the paired pulses. If a dolphin perceives stimuli with pulse spacings smaller than 200–300 μs for a sufficiently long time, it ceases being able to discriminate pairs with a pulse spacing of more than 200–300 μs in the standard pair. Moreover, when the pulse spacings are below 200–300 μs, the positive signal used by the dolphin is the pair of pulses with the greater spacing, while when the pulse spacing in the standard pair increases above 200–300 μs, the dolphin begins to use the pair with the smaller spacing as the positive stimulus [8]. In the cited publication, the changes in the behavioral reactions of the dolphin are explained by the fact that, when the pulse spacing in a pair is smaller than 200–300 μs, the pair of pulses is perceived by the dolphin as a single auditory image, while a pair with a greater pulse spacing is perceived as two separate pulses. The pulse spacing of 200–300 μs is called the critical interval. By the method of summary evoked potentials, it was shown that, in the brainstem of a dolphin, in the region of 200–300 μs, responses to individual pulses of a pair begin to separate [10]. An assumption was put forward [6] that, at intervals lying within the critical one, the dolphin perceives the TSP of the

1063-7710/04/5004-0485$26.00 © 2004 MAIK "Nauka/Interperiodica"

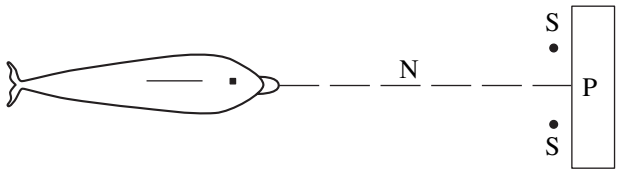

Fig. 1. Schematic diagram of the experiment: the dolphin occupying the starting position, (N) a separating net, (S) two acoustic sources, and (P) the platform from which the test signal was controlled and the animal was rewarded with food.

paired pulses, which is determined by the inverse value of the pulse spacing in pairs.

The effect of a pulse jam on the audibility thresholds of pure tones was studied in [11]. The dependence of the thresholds on the frequency of the test signal had a fairly complex form. This dependence can be considered as a superposition of several components: (i) relatively shallow oscillations of the whole curve of threshold shifts, which correlate with the extrema of the jam spectrum; (ii) a monotonically decreasing component with a high maximum at a frequency of $1/\tau_j$; and (iii) a frequency-independent component. Different components of the masking curve were ascribed to different auditory (subjective) features of the pulse jam [11]. The first component, which reflects the distribution of the neuron excitation level over the frequency channels according to the form of the jam amplitude spectrum, determines the timbre properties of the pulse jam. The second component, which is of special interest, can be explained only by assuming that the pulse sequence is characterized by a pitch corresponding to a frequency of $1/\tau_j$. Then the monotonically decreasing component of the masking curve is the result of the masking of the pure tone by the complex tone of the jam. The first two components are caused by the periodicity of the spectral density of paired pulses. The third component exhibits no traces of periodicity and corresponds to the auditory feature of a quasi-random noise. Its origin is the random neuron activity caused by the pulse jam in different frequency-specific channels.

For the bottlenose dolphin, the effect of the pulse jam on the discrimination between paired and single pulses was studied in [12]. By the conditioned-reflex method of differentiation of paired and single pulses, the detection thresholds were determined for the second pulse in the test pair under the effect of a pulse jam. The selectivity with respect to the pulse spacing in the pairs forming the jam was demonstrated. The threshold curves exhibit one pronounced maximum at the coincidence of the pulse spacing in the test pairs and in the pairs forming the jam. This selectivity was observed for test pairs with pulse spacings from 20 to 200 μs, i.e., within the critical interval. Beyond the critical interval, such a selectivity was absent. Presumably the selectivity is also determined by the sensitivity to the pitch feature of the pulse jam.

This paper reports on the study of the effect produced by a pulse jam in the form of relatively long series of pairs of identical pulses on the detection of a single pair of identical pulses. The detection thresholds were measured for a test pair with a fixed pulse spacing, which was taken to be equal to τ_t = 50, 100, 200, and 500 μs, as functions of τ_j (the pulse spacing in pairs forming the jam). The aim of the study was to find out whether it is possible to obtain a selectivity of the effect of the jam on the detection of paired pulses, as was observed in the case of the discrimination between paired and single pulses [12].

EXPERIMENTAL

The experiments were performed with an adult female bottlenose dolphin (*Tursiops truncatus*) that was caught in the open sea three months before the beginning of its training. The experimental setup is schematically represented in Fig. 1. A separating net N was fastened with its one end to a small platform P. On both sides of the net, at a distance of 1 m, two acoustic sources S (piezoceramic transducers 10 mm in diameter) were suspended at a depth of 1.5 m. The other end of the net was fixed by guy ropes at a distance of 2 m from the platform. The starting position of the animal was at the far end of the separating net. The start signal was a 60-kHz tone produced by a third source not shown in Fig. 1. Figure 2 shows the time diagram of acoustic stimulation. The pulse jam was produced by the two sources that were fed from the same generator and had the form of series of paired pulses with a duration T, a controlled pulse spacing τ_j within a pair, and a pair repetition rate f_j. The series of paired pulses were separated by a pause with a duration $R > 1/f_j$, within which the pulse jam was absent while the test signal appeared at one of the sources (at random) at an instant r. The test signal was a pair of pulses with a fixed pulse spacing τ_t and a controlled pulse amplitude. The total stimulation cycle was $J = T + R$. The peak value of the pulse jam is denoted as L in Fig. 2.

The duration of a single acoustic pulse in water did not exceed 30 μs. Figure 3 shows the acoustic spectrum of single pulses obtained at different sources in response to the same electric pulse together with the averaged spectrum. The latter was calculated by applying the Fourier transformation to the oscillograms of pulses.

By the conditioned-reflex method with food reinforcement, the animal was trained to approach the source at which the test pair of pulses was produced. The period of training was somewhat longer than two months. The thresholds were determined by the adaptive (staircase) method. The peak value of the pulses in the test pair was reduced at steps of 4 dB starting from a value that was preliminarily known to be above the threshold down to the level at which the animal made its first mistake. After this, the level was increased until the dolphin gave a correct response and then again

reduced until it was mistaken, and so on. After a rough determination of the threshold region, the step was reduced to 2 dB and the level was reduced only after two consecutive correct responses. If in two tests one response (or both responses) was wrong, the level was increased. The threshold value obtained in this way corresponded to 70.7% of correct responses [13]. The number of level reversals that were used to obtain one threshold value reached 20 in many cases and was never less than 10. The total number of tests in the threshold region was 30–50. The threshold value was determined by averaging the levels that were intermediate between neighboring reversals. In one experiment, it was possible to obtain two or three (or four to five at best) threshold values.

In the initial experiments, the parameters of the pulse jam were adjusted, and then these parameters were used as fixed. The parameters were as follows: the peak level L above the audibility threshold of the pulse jam, the duration T of the individual series of paired pulses of the jam, the repetition rate of paired pulses f_j, and the duration R of the pause between sequential series of paired pulses of the jam. The parameters of the jam were adjusted at $\tau_j = \tau_t$. At first, the task was to obtain a considerable shift of the detection threshold of the test pair at $\tau_j = \tau_t$ with respect to the detection threshold of the test pair in the absence of the pulse jam.

RESULTS

Figure 4 shows the threshold curves for $\tau_t = 100$ μs. Figure 4a presents the threshold curves obtained with the following parameters of the pulse jam: $1/J = 3$ s^{-1}, $1/f_j = 5$ ms, $R = 10/f_j = 50$ ms, $r = 5/f_j = 25$ ms, and $L \approx 25$ dB above the audibility threshold of the jam. The numbers of the curves indicate the order number of the experiment (one experiment a day). The first three curves (*1–3*) are more or less similar to each other in shape and have a single maximum at $\tau_j = \tau_t = 100$ μs. On both sides of this maximum, the thresholds decrease with varying τ_j to approximately 20 dB above the detection threshold for the test pair in the absence of the jam. The height of the maximum observed in these curves reaches 10–15 dB. However, in the course of training, the threshold curve as a whole moves downwards along the ordinate axis and approaches the detection level of the test pair in the absence of the jam, first without changing its shape (curve *4*) and then ceasing to exhibit any dependence of the threshold on τ_j (curve *5*).

In all subsequent experiments, the peak value of the pulses of the jam was increased by 25 dB, i.e., to 50 dB above the audibility threshold for the jam. Figure 4b shows the test pair detection curves, which were obtained with a new level of the pulse jam and with all other parameters of the jam being invariable, at different stages of training.

Curves *1–3* in Fig. 4b show the average thresholds for every next two sequential experiments as functions

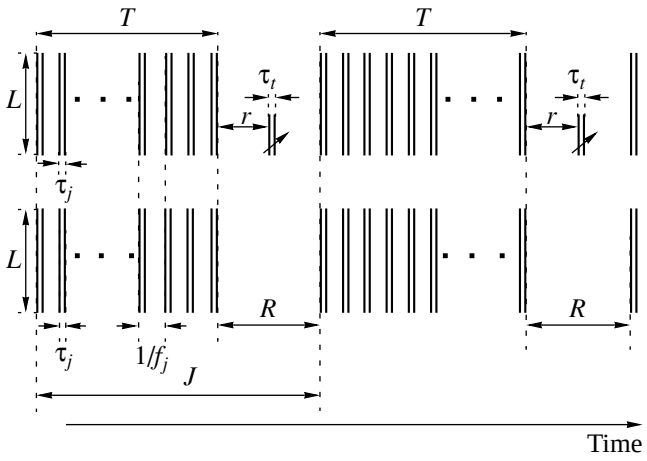

Fig. 2. Time diagram of acoustic stimulation: T is the duration of a single series of paired pulses of the jam; the jam consists of pairs of pulses with a pulse spacing τ_j in each of them and a pair repetition rate f_j; the test signal is a single pair of pulses with a fixed pulse spacing t_t; the test signal is supplied at random to one of the two channels within the pause $R > 1/f_j$ with a time shift r relative to the beginning of the pause; the total cycle of stimulation is $J = T + R$; L is the peak level of the jam pulses above the audibility threshold. The time and amplitude scales are arbitrary.

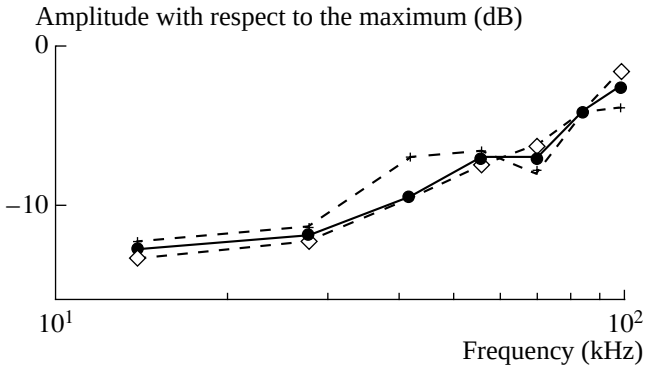

Fig. 3. Spectrograms of the pulses recorded in water from different sources (the dashed lines) in response to the same electric pulse. The solid line shows the average spectrogram for the two sources.

of the pulse spacing in the paired pulses of the pulse jam. Curve *1* in Fig. 4b again exhibits a maximum at $\tau_j = \tau_t = 100$ μs. Its height is approximately the same as in curves *1–3* in Fig. 4a. Curves *2* and *3* in Fig. 4b gradually flatten, and curve *4* in Fig. 4b (the average curve for the last five experiments of the given series) exhibits no dependence of the threshold on τ_j. In the course of the experiments, we again observe a gradual displacement of the threshold curves towards the detection threshold of the test pair in the absence of the pulse jam, which means that the effect of the pulse jam becomes weaker. However, at the jam level of 50 dB, the downward displacement of the curves stopped at the same

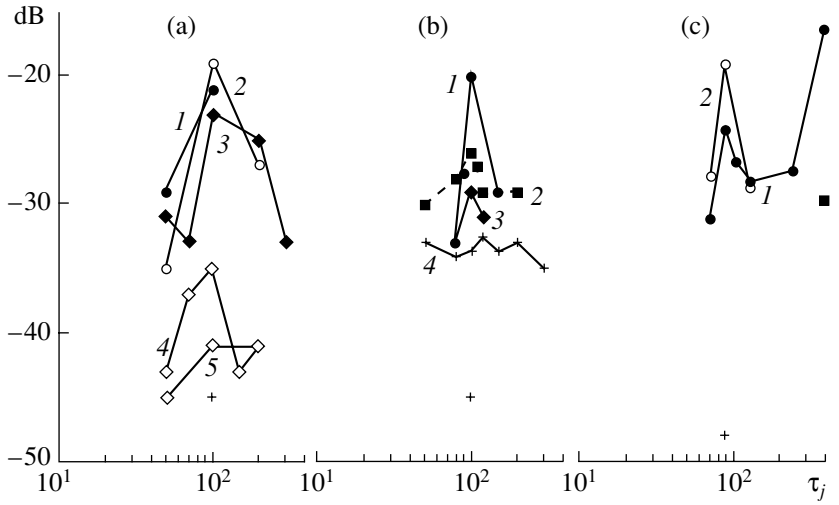

Fig. 4. Detection thresholds of the test pair with a pulse spacing τ_j = 100 μs in the presence of a pulse jam at different stages of training. The pulse jam consists of a series of pairs of pulses with a pulse spacing τ_j, a series duration T, and an interval R between the series. The parameters of the pulse jam are as follows: L = (a) 25 and (b, c) 50 dB; R = (a, b) 50, (c, curve *1*) 30, and (c, curve *2*) 15 ms; r = (a, b) 25, (c, curve *1*) 15, and (c, curve *2*) 5 ms; $1/J$ = (a, b) 3 s^{-1} and (c) 1 s^{-1}; and $1/f_j$ = (a, b) 5 and (c) 1 ms. The numbers of the curves in Fig. 4a indicate the order numbers of the experiments. Curves *1–3* in Fig. 4b show the average thresholds for each two sequential experiments. In Fig. 4c, curve *1* is obtained by averaging over the last 5 experiments out of 18 performed with the pulse jam parameters specified for Fig. 4c, and curve *2* represents the results of a single experiment. The crosses below indicate the detection threshold level for the test pair in the absence of the jam. The decibels along the ordinate axis correspond to the level of the detection threshold of the test pair in the presence of the jam above the threshold of the test pair in the absence of the jam. The abscissa axis represents the pulse spacing in the pairs of pulses forming the jam (in microseconds).

level (approximately 20 dB above the pair detection threshold in the absence of the jam) as that corresponding to curves *1–3* in Fig. 4a (which were obtained at a jam level of 25 dB relative to the threshold in the absence of the jam). Thus, a considerable increase in the jam level does not allow one to obtain a stable selectivity of the effect of the pulse jam on the near-threshold detection of a paired pulse with an equal peak amplitude.

All subsequent experiments were performed at $1/J$ = 1 s^{-1}, $1/f_j$ = 1 ms, and L = 50 dB above the jam audibility threshold. Only the values of R and r were varied. Curve *1* in Fig. 3c was obtained at $R = 30/f_j$ = 30 ms and $r = 25/f_j$ = 25 ms (the threshold dependence on τ_j was averaged over the last 5 experiments out of 18 performed with the indicated jam parameters). At the aforementioned time parameters of the pulse jam, it was possible to obtain a stable maximum at $\tau_j = \tau_t$ = 100 μs, which was retained in the course of the training. The maximum in curve *1* is relatively low. However, the volume of threshold data allowed us to obtain a very high level of statistical significance of the average threshold difference at τ_j = 80 and 150 μs compared to the case of $\tau_j = \tau_t$ = 100 μs: 99.9 and 90%, respectively (according to Student [14]). This suggests that the duration of the pause between sequential series of paired pulses of the jam is more important than the jam level for revealing the selectivity. Concerning the pulse spacing τ_t = 100 μs, it should be added that, when the pulse spacing in pairs of the pulse jam increases beyond the critical interval, at τ_j = 500 μs the threshold proves to be very high (curve *1* in Fig. 4c). However, after the termination of the whole cycle of experiments, at other test pulse spacings, it was found that the threshold at τ_j = 500 μs for τ_t = 100 μs drastically decreased almost to the level observed at τ_j = 80 μs. In Fig. 4c, this value is indicated with number *3*. Curve *2* in Fig. 4c for τ_t = 100 μs was obtained with the pulse jam parameters chosen as the final ones: L = 50 dB, f_j = 1000 s^{-1}, $1/J$ = 1 s^{-1}, $R = 15/f_j$ = 15 ms, and $r = 5/f_j$ = 5 ms. The latter curve also exhibits a maximum at $\tau_j = \tau_t$ = 100 μs but lies somewhat higher than curve *1* (Fig. 4c). Thus, the measurements of the detection thresholds of paired pulses at τ_t = 100 μs showed that a selectivity with respect to the effect of the pulse jam may take place. A sufficiently stable maximum at $\tau_j = \tau_t$ = 100 μs was obtained only for R < 50 ms.

All other threshold measurements in the presence of the pulse jam were performed at τ_t = 50, 200, and 500 μs. The corresponding average threshold curves are shown in Fig. 5. the threshold curve for τ_t = 100 μs is also shown for comparison (curve *1* in Fig. 3c, which was obtained from a sufficiently large array of threshold data). From Fig. 5 it follows that the curves for τ_t = 50 and 200 μs, as well as the curve for τ_t = 100 μs, exhibit a maximum at $\tau_j = \tau_t$. The highest maximum (15 dB) is observed at τ_t = 50 μs, and for this value of the test pulse spacing is no pronounced tendency to a decrease in the height of the maximum in the course of the experiments (during 12 days of experimentation). However, the dif-

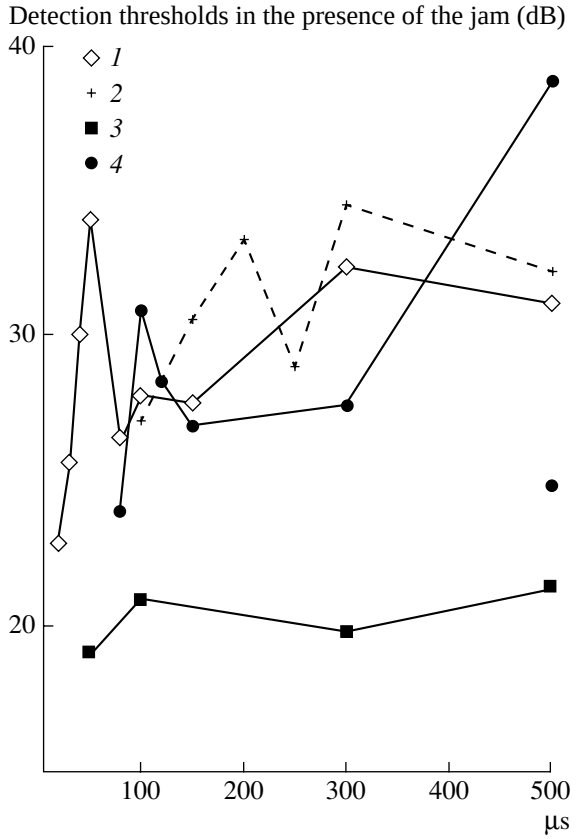

Fig. 5. Detection thresholds of the test pair of pulses in the presence of the pulse jam. The latter consists of pairs of pulses with a pulse spacing τ_j, a series duration T, an interval R between the series, and a pair repetition rate f_j. The parameters of the curves are as follows: the pulse spacing in the test pair τ_t = (*1*) 50, (*2*) 200, (*3*) 500, and (*4*) 100 μs; L = (*1–4*) 50 dB; $1/\tau$ = (*1–3*) 1 s^{-1} and (*4*) 3 s^{-1}; $1/f_t$ = (*1–3*) 1 and (*4*) 5 ms; R = (1–3) 15 and (*4*) 30 ms; and r = (*1–3*) 5 and (*4*) 15 ms. The level of 0 dB corresponds to the detection threshold of the test pair in the absence of the jam. The abscissa axis represents the pulse spacing τ_j in the pairs forming the pulse jam.

ference in the heights of the maximum for τ_t being equal to 50 and 100 μs can to some extent be explained by the fact that the curve for τ_t = 100 μs was obtained with a longer pause between sequential series of paired pulses of the jam (R = 30 ms for τ_t = 100 μs and R = 15 ms for τ_t = 50 μs). The low maximum for τ_j = τ_t = 200 μs is most likely to be determined by the pulse spacing in the test pair for which the measurements were performed with the shortest pause R. Note that the pulse spacing of 200 μs lies near the boundary of the critical interval [7]. Beyond this boundary (at τ_t = 500 μs), no dependence of the test pair detection thresholds on τ_j has been observed. Figure 5 also shows that the threshold curves for the test pulse spacings within 50–200 μs exhibit a rise for the jam pulse spacings τ_j beyond the critical interval. In addition, for τ_t = 100 μs at a jam pulse spacing τ_j = 500 μs, the threshold values are characterized by a fairly large scatter (Figs. 4c and 5).

DISCUSSION

The experimental results have shown that, for the test pairs of identical pulses with a pulse spacing t_t < 500 μs, it is possible to obtain a local selectivity of the masking effect of the pulse jam with respect to the pulse spacing τ_j in the pairs of pulses forming the pulse jam (the pulses of the jam being identical). The masking effect is stronger in the region of coincidence of the pulse spacings in the test pair and in the paired pulses of the jam: $\tau_j = \tau_t$. The maximum of the masking effect occurs exactly at $\tau_j = \tau_t$, and, on both sides of this maximum, the masking effect decreases. This selectivity, which resembles the tone-by-tone masking curves, suggests that, under the effect of the pulse jam, a special kind of masking takes place, namely: the complex tone of the test pair, which corresponds to the time separation pitch (TSP) with a frequency of $1/\tau_t$, is masked by the complex tone of the pulse jam with a frequency of $1/\tau_j$. In the literature, a complex tone is usually understood as a periodic signal consisting of a set of harmonics or an aperiodic signal with a rippled spectral density (pairs or sequences of pulses or noise obtained by combining two identical noise segments with some delay [11]). The pitch of a complex tone corresponds to the fundamental frequency $f_0 = 1/\tau$.

The assumption that masking by a complex tone is possible was first put forward in the paper [11] reporting on a study of the audibility thresholds of simple tones under the effect of a pulse jam. The behavior of the masking curve, which had the form of a monotonically decreasing function of the tone frequency with a high maximum at the fundamental frequency of the pulse jam, was explained by the masking effect of the pitch produced by the pulse jam.

The selectivity observed in our experiments in the masking effect of the jam whose pulse spacings did not exceed the critical interval proved to be stable when the pauses between sequential series of paired pulses were R < 50 ms. The role of the pause duration R that was revealed in our experiments resembles the effect of a combined masking [5, 16]. A combined masking exceeds the sum of the direct and inverse masking taken separately. The effect of the combined masking is explained by the neural processing with a time window within which the average signal-to-noise ratio is estimated. The window can move so as to occupy the position where the signal-to-noise ratio is maximal. A higher signal-to-noise ratio can be obtained when the time window is not centered at the test signal. In the optimal situation, in the case of forward masking, the window is centered after the signal, while in the case of backward masking, it is centered before the signal. When combined masking takes place, the time window is centered at the test signal but includes both maskers (the forward and backward ones). In this case, the sig-

nal-to-noise ratio decreases and an additional masking appears [16].

One can expect that a similar time window exists in the case of the masking by a complex tone. The pitch of a complex tone has a higher or lower strength depending on the value of the delay and the depth of the spectrum ripple [17, 18]. The masking effect of a complex tone due to its pitch strength depends not only on the delay and the depth of the spectrum ripple [17, 18] but, in the case of the pulse jam, also on the duration of the pause R between sequential series of paired pulses. Within a limited time (within $R \approx 15$ ms), the complex tone of the pulse jam has its maximal strength. When $R \leq 30$ ms, the pause proves to be too short for the masking effect of the pitch component of the jam to be completely eliminated by a displacement of the time window. The greater duration $R = 50$ ms is sufficient for the auditory processing system in the course of training to find a position of the time window that provides a complete elimination of the masking effect of the complex tone. Thus, it is possible that the mechanism lying at the heart of the training is the active search for the time window position at which the masking effect of the complex tone is minimal or totally eliminated.

According to [4, 18], for dolphins, the pitch strength of ripple noise reaches its maximum at a delay of 100 μs and decreases on both sides of this value. The masking selectivity curves obtained from our experiments for a test pulse spacing of 100 μs exhibit a similar dependence on the jam pulse spacing. From the similarity of different functions of the pulse spacing, one may surmise that the masking curve for $\tau_t = 100$ μs has the aforementioned form, because precisely this spacing corresponds to the maximal pitch strength of the paired pulses of the pulse jam. However, for the test pulse spacings of 50 and 200 μs, we also obtained a Λ-shaped dependence of masking on the jam pulse spacing with a maximum at $\tau_j = \tau_t$. To explain the observed selectivity of the pulse jam effect on the discrimination of paired pulses and a single pulse, the following hypothesis has been put forward: the auditory system of dolphins may contain specific channels tuned to the pulse spacing in the same way as the frequency-specific auditory channels are tuned to a certain frequency [12]. The data of our experiments do not contradict this hypothesis. It only should be added that the channels with tuning to the pulse spacing actually are pitch-specific channels tuned to the pitch of pulse sequences.

In the literature, one can find psychoacoustic data on the selectivity of the effect of overthreshold amplitude-modulated (AM) or frequency-modulated (FM) tones on the detection thresholds of the tone modulation frequency [19–22]. In [23], an increase in the detection thresholds was observed for a linear FM only when instantaneous frequencies of the overthreshold and test stimuli varied in the same direction. The results of these studies were explained by the adaptation of the system of hypothetical "channels" tuned to certain features of a stimulus. However, the sensory nature of selectivity revealed in [19–23] was questioned in [24]. The doubts expressed by the authors of [24] were caused by the small value of the threshold variations due to the overthreshold exposure and also by the fact that these variations disappeared in the course of training [25, 26]. In the subsequent publication [27], the effect of the overthreshold FM tone has already been called masking, but the authors still believed that special AM and FM channels existed in the human auditory system.

In our experiments, the shift of the detection threshold of a paired pulse in response to the effect of the overthreshold pulse jam reached 15 dB. In addition, we managed to determine the jam parameters at which a stable threshold shift was observed, which also testifies in favor of the presence of pitch-specific pulse sequence channels in the auditory system of a dolphin.

Irrespective of the pulse jam level, most curves in Fig. 4 do not reach below the level of 20–27 dB above the test pair detection threshold in the absence of the jam (indicated by crosses). A pair of pulses has a pitch in the sense that, for each pair, a subject under test may indicate with fair accuracy a simple tone of a close frequency determined by the inverse value of the pulse spacing. However, the subject can always discriminate between a paired pulse and a simple tone. This means that a complex stimulus (for example, a paired pulse or ripple noise) also has other auditory (subjective) features. Psychoacoustic data show that a human individual listening to ripple noise perceives not only the pitch but also the noise component [28]. As was mentioned above, the audibility curve for pure tones in the presence of a pulse jam [11] includes several components. The behavior of two of them may be related to the periodicity of the spectral density of a pair of pulses. The third component, which has a relatively high level, exhibits no traces of periodicity characterizing the spectral density of the jam and may be interpreted as a result of the sensation accompanying the perception of paired pulses of the jam in the form of a random noise. The origin of the third component is the random neuron activity induced by the pulse jam in different frequency-specific channels. The total shift of the threshold curves with respect to the test pair detection threshold in the absence of the jam (shown by crosses in Fig. 4) may also correspond to the noise component in the perception of the pulse jam independently of the pulse spacing τ_j. Figure 4 illustrates the twofold nature of the sensation caused by a paired pulse and also shows that the tone and noise components behave independently of each other. Presumably, the noise and pitch hearing components are related to different levels of signal processing in the auditory system. The noise component is most likely of peripheral origin, while the pitch component, of a more central origin.

In the behavior of the masking curves under the effect of the pulse jam, an unexplained feature is the growth of thresholds for pulse spacings exceeding the

critical interval (more than 200 μs). In the transition zone of pulse spacings, between a paired pulse that is perceived as a single sound with a pitch and a pair of pulses perceived separately without the pitch feature, the pulse jam acquires auditory properties of quasi-random noise. In this case, the masking of the complex tone of the test pair by quasi-random noise takes place. Possibly, in the transition zone of pulse spacings, at low frequencies, the periodicity of the spectral density and the corresponding pitch feature are still retained. In the course of training, the auditory system is adjusted so as to exclude the effect of high-frequency fluctuations of the spectral density of the jam, which explains the sharp threshold change observed at t_t = 500 μs for τ_j = 100 μs after a prolonged experimentation (Fig. 4c). It is of interest that, for a test pulse spacing greater than the critical interval (τ_t = 500 μs), we did not observe any increase in the masking effect of the pulse jam with increasing jam pulse spacing.

CONCLUSIONS

The main results of the studies described in this paper can be formulated as follows:

(1) A stable selectivity of the masking effect of a pulse jam with respect to the pulse spacing in pairs of jam pulses is observed for test pulse spacings of 50–200 μs when the duration of the pause between sequential series of paired pulses forming the pulse jam is $R \le 30$ ms. The selectivity manifests itself as the excess of the masking level in the region of the pulse spacing value at which the pulse spacings in the pulse jam and in the test pair coincide, $\tau_j = \tau_t$. The maximum masking is observed exactly at the coinciding pulse spacings. All masking curves lie at a relatively high level above the detection threshold of a paired pulse in the absence of the pulse jam.

(2) When the interval between sequential series of paired pulses forming the jam is sufficiently large (R = 50 ms), the masking curves flatten in the course of the training.

(3) For a test pulse spacing of 500 μs, no selectivity can be observed.

(4) The detection threshold exhibits another increase beyond the selective masking region around the coincident values of the pulse spacings in the pulse jam and the test pair of pulses.

It is assumed that the perception of paired pulses involves different auditory (subjective) features. Pairs with a pulse spacing less than 500 μs possess a pitch feature, which is perceived by hearing as a tone with a frequency equal to the inverse value of the pulse spacing, and also a noise feature. It is assumed that the noise component is associated with the relatively high level of random neuron activity induced in the auditory filters by the pulse jam, while the tone component is caused by the periodicity of the spectral density of paired pulses. The masking effect observed around the coincident values of the pulse spacings in the test pair and in the paired pulses of the jam is caused by the peculiar kind of masking of the complex tone of the test pair by the complex tone of the paired pulses of the jam. In the course of training, when the pause between the sequential series of paired pulses of the jam is sufficiently large, adaptive mechanisms begin to work, which allows the auditory system to exclude the masking effect of the complex tone. The masking effect associated with the noise feature of a paired pulse is retained in the course of the training.

ACKNOWLEDGMENTS

This work was supported by the Russian Foundation for Basic Research, project no. 03-04-48746.

REFERENCES

1. M. F. Spiegel, J. Acoust. Soc. Am. **82**, 1492 (1987).
2. M. F. Spiegel, J. Acoust. Soc. Am. **84**, 2033 (1988).
3. V. M. Bel'kovich and N. A. Dubrovskiĭ, *Sensory Origin of Orientation in Cetaceans* (Nauka, Leningrad, 1976), p. 204.
4. W. W. L. Au, *The Sonar of Dolphins* (Springer, New York, 1993), p. 277.
5. W. W. L. Au and C. E. Hammer, Jr., in *Animal Sonar Systems*, Ed. by R. G. Busnel and J. F. Fish (Plenum, New York, 1980), pp. 855–858.
6. P. W. B. Moore, R. W. Hall, W. A. Friedl, and P. E. Nachtigall, J. Acoust. Soc. Am. **76**, 314 (1984).
7. V. A. Vel'min and N. A. Dubrovsky, Dokl. Akad. Nauk SSSR **225**, 229 (1975).
8. V. A. Vel'min and N. A. Dubrovsky, Akust. Zh. **22**, 351 (1976) [Sov. Phys. Acoust. **22**, 197 (1976)].
9. N. A. Dubrovsky, in *Black Sea Aphaline*, Ed. by V. E. Sokolov and E. V. Romanenko (Nauka, Moscow, 1997).
10. A. Ya. Supin and V. V. Popov, Dokl. Akad. Nauk SSSR **283**, 740 (1985).
11. N. A. Dubrovsky and M. N. Sukhoruchenko, Akust. Zh. **48**, 504 (2002) [Acoust. Phys. **48**, 441 (2002)].
12. M. N. Sukhoruchenko, in *Marine Mammal Sensory Systems*, Ed. by J. A. Thomas, R. A. Kastelein, and A. Ya. Supin (Plenum, New York, 1991), pp. 277–286.
13. H. Levitt, J. Acoust. Soc. Am. **49**, 467 (1971).
14. V. Yu. Urbakh, *Biometric Metods* (Nauka, Moscow, 1964).
15. L. H. Wilson and R. Carhart, J. Acoust. Soc. Am. **49**, 1254 (1971).
16. C. E. Robinson and I. Pollack, J. Acoust. Soc. Am. **53**, 1313 (1973).
17. W. A. Yost, J. Acoust. Soc. Am. **64**, 485 (1978).
18. W. W. L. Au and J. L. Pawloski, J. Acoust. Soc. Am. **86**, 591 (1989).
19. R. H. Kay and D. R. Matthews, J. Physiol. (London) **225**, 657 (1972).

20. G. G. Green and R. H. Kay, J. Physiol. (London) **234**, 50 (1973).

21. G. G. Green and R. H. Kay, J. Physiol. (London) **241**, 29 (1974).

22. D. Regan and D. Tansley, J. Acoust. Soc. Am. **65**, 1249 (1979).

23. R. B. Gardner and J. P. Wilson, J. Acoust. Soc. Am. **66**, 704 (1979).

24. G. H. Wakefield and N. F. Viemeister, J. Acoust. Soc. Am. **75**, 1588 (1984).

25. B. W. Tansley and J. B. Suffield, J. Acoust. Soc. Am. **74**, 765 (1983).

26. D. B. Moody, D. Cole, L. M. Davidson, and W. C. Stebbins, J. Acoust. Soc. Am. **76**, 1076 (1984).

27. B. Bacon and D. V. Grantham, J. Acoust. Soc. Am. **85**, 2575 (1989).

28. R. D. Patterson, S. Handel, W. A. Yost, and A. J. Datta, J. Acoust. Soc. Am. **100**, 3286 (1996).

Translated by E. Golyamina